STUDIES IN THE USE OF THE ELEMENT-FREE GALERKIN METHOD FOR LINEAR ELASTIC FRACTURE MECHANICS

Submitted in partial fulfillment of the requirements

of the degree of

Doctor of Philosophy

of the
Indian Institute of Technology, Bombay, India
and
Monash University, Australia

by

Nelson Muthu

Supervisors:

Professor S.K. Maiti (IIT Bombay, Mumbai)

Professor Wenyi Yan (Monash University, Melbourne)

Professor B.G. Falzon (Queen's University, Belfast)

2015

Approval Sheet

The thesis entitled *"Studies in the use of the Element-Free Galerkin method for Linear Elastic Fracture Mechanics"* by *Nelson Muthu* is approved for the degree of **Doctor of Philosophy**

(Prof. P. K. Sarkar)
External Examiner
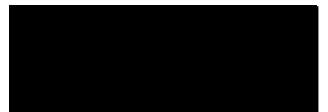
(Prof. Salil Kulkarni)
Internal Examiner

(Prof. S. K. Maiti)
IITB Supervisor
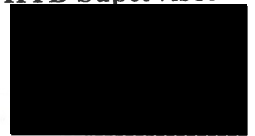
(Prof. Wenyi Yan)
Monash Supervisor
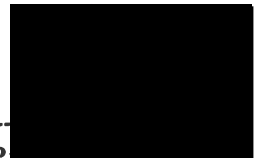
(Prof. ...)
Chairman

Date: 21 December, 2015
Place: IIT Bombay

Declaration

I declare that this written submission represents my ideas in my own words and where others' ideas or words have been included, I have adequately cited and referenced the original sources. I also declare that I have adhered to all principles of academic honesty and integrity and have not misrepresented or fabricated or falsified any idea/data/fact/source in my submission. I understand that any violation of the above will be cause for disciplinary action by the Institute and can also evoke penal action from the sources which have thus not been properly cited or from whom proper permission has not been taken when needed.

Notice 1

Notice 2

Nelson Muthu

IITB ID: 10402402

Abstract

The main aim of the thesis is to expand the scope of the element-free Galerkin (EFG) method in its application to linear elastic fracture mechanics (LEFM). Specific objectives include an accurate assessment of the stress intensity factors (SIFs) for variety of loading and material combinations, and the study of crack propagation in isotropic and composite materials. The present study also deals with modelling interacting cracks that are frequently encountered in fracture of brittle materials.

Two new techniques within the framework of the EFG method have been developed based on the crack closure integral (CCI) to compute the SIFs: CCI with a local smoothing (CCI-LS) technique and modified crack closure integral (MCCI) technique. The first scheme involves extraction of displacement and stress at few locations near a crack tip, and construction of a smooth variation of these parameters in conformity with the crack tip solutions using a suitable smoothing technique. The CCI-LS technique has also been applied to extract the SIFs in FGMs. The second technique is based on computing crack closure forces at some nodes ahead of a crack tip and multiplying with corresponding crack opening displacements (CODs) to determine the potential energy release rate and the SIFs. A novel approach to extract the crack closure forces accurately within the framework of EFG method is proposed. In addition to these techniques, classical SIF extraction methods like the displacement and stress methods have also been used to extract the SIFs. The extracted SIFs are compared with those obtained using the popular M-integral technique to highlight the differences. The dependence of the computed SIFs accuracy, using both the techniques, on nodal density, local refinement at the crack tip, domain of influence and order of Gauss integration have been examined. Varieties of problems including crack face loading and thermal loading have been solved to demonstrate the simplicity and the efficiency of these techniques.

A new variant of the EFG method has been proposed to address the problem of crack propagation through non-homogenous materials. This method eliminates the difficulty associated with the selection of the enrichment functions that are dependent on material properties and location of the crack tip. The SIFs and CODs obtained using this method, for a range of material combinations and interfaces, are compared with published results. The criterion suitable for study of crack propagation has also been investigated. There are a number of criteria to study crack propagation through brittle materials. Noting the

computational advantages offered by the maximum tangential principal stress (MTPS) criterion, it has been selected for the study of the crack propagation in bi-material and composite materials. To facilitate its application, a scheme has been given first to obtain the T-stress and then apply it to bi-materials. Further, the criterion has been amended by bringing in the differences in crack growth resistances. This criterion has been applied to particle-reinforced composites to carry out study at the microscale. Effects of inter particle distance, crack growth resistances of matrix and particle, and location of the initial crack with respect to the particle on the crack path has been presented.

To model multiple interacting cracks, an EFG scheme based on multiple crack weight (MCW) function coupled with level set method has been proposed. Case studies involving crack-crack, crack-microcrack, interface crack-microcrack interaction, and crack propagation have been presented to demonstrate the efficiency of the scheme. This too has been applied to show its usefulness for problems involving knee and crack tip singularities during step-by-strep propagation of a starter crack.

Keywords: *EFG method, SIF, CCI, MCCI, crack propagation, non-homogenous, crack interaction.*

Contents

vi

List of Tables

List of Figures

xiv

xvi

xviii

Chapter 1   Introduction

1.1 Motivation

The history of engineering is full of reports on failed structures, which are directly attributed to initiation and propagation of cracks. In many cases, they have been compounded by the presence of geometric discontinuities such as holes, inclusions, material discontinuities, stress corrosion, thermal loading and fatigue. A US national committee estimated the cost of damages due to fractures to be around 4% of the gross national product (Aliabadi & Rooke, 1991). It is vital, therefore, to develop methods that enable the control and monitoring of the origin and growth of cracks in machines and structural elements.

Although more attention was directed initially toward experiments and analytical investigations, the focus shifted later more toward numerical methods. This was facilitated by the emergence of sophisticated and better modelling techniques and decreasing cost of computational hardware. The development of numerical methods has been driven by the need to decrease developmental costs and increase the reliability of a component and the accuracy of the final solutions. Most engineering problems are governed by a set of ordinary or partial differential equations or integral equations. It is a challenge to solve the equations that are subject to the exacting boundary and initial conditions, and to mimic the observed behaviour of the system under live conditions.

There is a host of numerical methods to analyze problems of deformation mechanics. Some of the well-established and proven methods are the finite element method (FEM), the finite difference method (FDM), the boundary element method (BEM) and the meshfree methods (MMs). The origin of these methods can probably be traced to the fundamental theoretical work by Courant et al. (1928) using finite differences. FEM has proven to be the more widely used method when compared to FDM and BEM in modelling fracture in the past four decades.

In the case of crack propagation, optimization, and large deformation problems, the aspect of meshing in the FEM became tedious and it increased the computational effort. This provided impetus for the development, almost in parallel, of MMs and the eXtended Finite Element Method (XFEM) (Nicolas et al., 1999). In the XFEM, shape functions are enriched by known crack-tip solutions in order to model the displacement and singular stress field

around a crack-tip accurately; the Heaviside function is used to introduce discontinuity in the crack edges away from the crack tip. In the MMs, only points/nodes are to be added, which helps to eliminate the problems associated with meshing. The addition of nodes is much easier than the addition of elements, thus offering advantages for the analysis by the MMs. Further, field singularity can be easily handled because the shape functions of the MMs are higher order continuous (Nguyen et al., 2008). Therefore, they are convenient in the study of moving boundary value problems associated with crack propagation, wave propagation, large deformation, and phase transformation among others.

There are many variations of MMs, based on the way the shape functions are developed. The origin of the MMs can be traced to the 1970s when Smoothed Particle Hydrodynamics (SPH) (Lucy, 1977; Gingold & Monaghan, 1977) was used to solve astrophysical problems. The element-free Galerkin (EFG) (Belytschko et al., 1994) method, which is used to solve solid mechanics problems, is one of the popular formulations in this class. When it comes to modelling cracks, there are two popular approaches within the framework of the EFG method: (1) The first approach is the Partition-of-unity approach based on the XFEM. In this approach, additional degrees of freedom are introduced to model the crack. The meshfree version of it is known as the eXtended element-free Galerkin (XEFG) method (Ventura et al., 2002). (2) The second approach consists of modifying the weight functions of nodes whose domains of influence consist of a crack tip.

Much of the initial developments of the MMs related to crack problems have been driven by applications of the principles of linear elastic fracture mechanics (LEFM) in actual practice. The crucial parameter in this connection is the stress intensity factor (SIF). Only a few techniques based on J-integral (Rice, 1968), such as interaction integral/M-integral (Yau et al., 1980) find their applications frequently in MMs. In contrast, there are variety of techniques available in FEM and BEM, such as the displacement method (Chan et al., 1970), stress method (Watwood, 1969), the stiffness derivative procedure (Parks, 1974), and the crack closure integral technique (Rybicki & Kanninen, 1977; Raju, 1987; Sethuraman & Maiti, 1988; Maiti, 1992). The interaction integral offers advantages in isolating the individual modes. However, it cannot work without the knowledge of the auxiliary displacement and stress field solutions, which are obtained through analytical solutions. Further, they become costlier in the presence of loading on the crack edges, for example, as seen in thermo-mechanical problems, crack face pressure loading situations, etc.

The crack closure integral (CCI), based on Irwin's original CCI, is attractive due to its simplicity and ability to separate the modes in a mixed-mode problem. CCI is seldom used in MMs because they require accurate computation of the asymptotic crack-tip stress field and crack opening displacements (CODs). The basic stress analysis procedure to compute the tractions cannot be implemented because the region close to the crack tip is prone to numerical error. To overcome this issue, Singh et al. (1988) presented a universal crack closure integral (UCCI) technique for adoption in the FEM. It stipulates Gaussian integration over a fraction of the region away from the crack tip to reduce the numerical error. In the BEM, Mukhopadhyay et al. (1999) have suggested a scheme based on the local smoothing of the stress and displacement fields before the integration in order to achieve the same goal. These schemes based on the CCI, can be easily extended to functionally graded materials (FGMs) because the crack-tip stress and the COD field variation are similar to those of isotropic and homogenous materials. A scheme based on the CCI does not exist for MMs. Whether such a scheme can give rise to any advantages is worth investigating.

Another technique based on the CCI is the virtual crack closure technique (VCCT) or modified crack closure integral (MCCI). It has been in existence since the time of early applications of the FEM to fracture mechanics (Rybicki & Kanninen, 1977; Raju, 1987; Ronald, 2002). The MCCI gives the total energy release rate, which includes the effects of higher order terms of the Williams' stress field expansion. The interaction integral, on the other hand, gives the energy release rate associated only with the first term of the stress field expansion.

The MCCI technique calculates the strain energy release rate (SERR) using crack closure forces and the CODs. Although the CODs can be obtained easily, the computation of the real crack closure forces requires special considerations. Therefore, the adoption of the MCCI in the MMs is not straightforward. Previously, Guiamatsia et al. (2009) implemented the MCCI method by using a high stiffness spring at the crack tip, within the framework of the EFG method, in order to determine crack closure forces during the modeling of delamination of composite lamintaes. Later, Chang et al. (2011) constructed an auxiliary finite element mesh around the crack tip to compute the crack closure forces. These techniques are not fully based on MMs and they add extra complexity for studying a problem of extending crack. There is a need to examine how the MCCI can be adopted in MMs.

A crack embedded in isotropic and homogenous material has a square root singularity at the crack tip. Modelling such cracks has been the central focus in most studies. In reality, there are abundant situations with variable order singularity at a point in a domain, for example, at the tip of a two-dimensional crack that meets at an angle to a material interface, at the knee of a kinked crack, at the tip of a notch with a small-included angle, and so on. The fracture of composite materials may also be considered as consisting of variable order singularity as crack propagates. Although fracture is mainly dominated by matrix failure in the transverse directions at the macro scale (Fig. 1.1(a)), the actual failure at a lower scale might be a combination of matrix failure, fiber fracture and interface decohesion (Fig. 1.1(b)). Therefore, further understanding of this type of a fracture is possible through analysis at the micro scale.
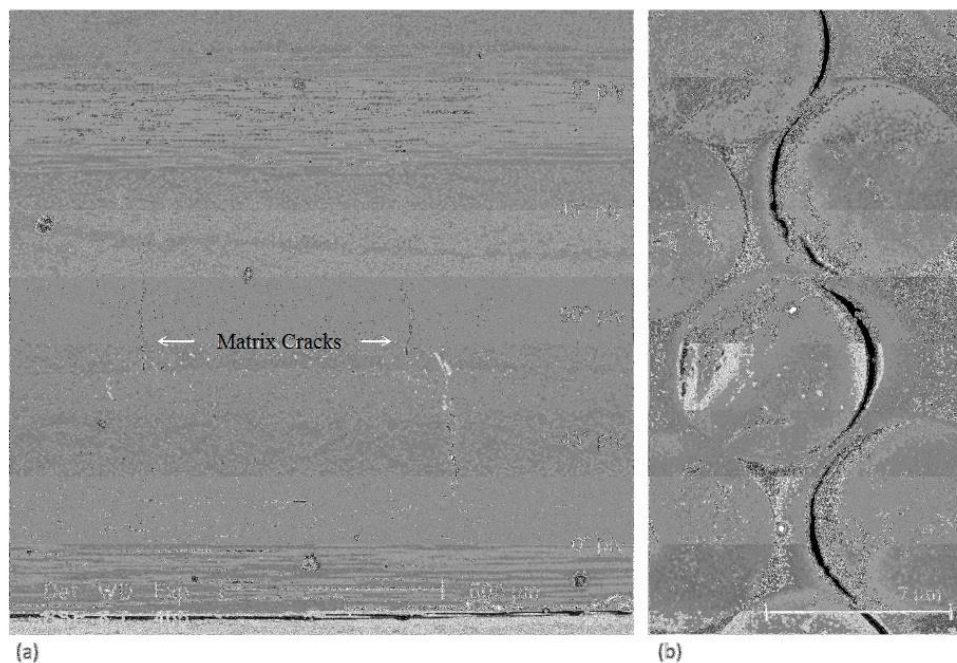
Fig. 1.1 SEM images showing typical damage in carbon fiber/epoxy composites: (a) matrix cracks in transverse plies; (b) magnified region of a matrix crack revealing debonding at the fiber/matrix interface. The composite was loaded under tension along the 0° fibers (Valentin et al., 2015).

Modelling crack growth through non-homogenous materials using the partition-of-unity approach based eXtended element-free Galerkin (XEFG) method is difficult because the enrichment functions change depending on the material under investigation, the location of the crack tip, and the type of loading (Mohammadi, 2012). The alternative approach in which the nodal weight functions are modified also pose difficulties because additional nodes have to be selectively added along the newly formed crack faces/edges, as a crack propagates

further. Any variant of the EFG method, which is capable of overcoming some of these difficulties, may help to broaden the scope of the MMs.

In the LEFM, the study of crack growth is an important issue. Crack propagation at the micro scale would often involve interface crack growth and crack kinking out of an interface. The existing criteria for predicting the kinking angle based on the energy release rate (He & Hutchinson, 1989), or the zero mode II SIF - $K_{II} = 0$ (Akisanya & Fleck, 1992) requires huge computational effort using the EFG method. The maximum tangential stress (MTS) criterion (Erdogan & Sih, 1963; Yuuki & Xu, 1992), which is popular for the same application in isotropic materials does not have such shortcomings. It requires only the evaluation of the SIFs to predict the direction of initial crack growth. It is well known that the accuracy of prediction of crack propagation angle depends not only on the SIFs but also on the higher order terms of Williams' eigenfunction expansion of the crack-tip stress field. The effect of the second term, T-stress, is particularly well known (Kang, 1994). The extraction of T-stress and an assessment of its effect on the kinking angle of interface crack have not yet been reported using the MMs. Even the application of stress-based criterion with the inclusion of the effect of T-stress remains unexplored. This has also provided some motivation for the present work.

Structural/machine elements may give rise to multiple cracks in service due to stress corrosion, creep, impact loading, thermal loading, fatigue, and the like. Often, these cracks interact with each other. Their modelling by the MMs is a problem. Only few studies (Duflot & Nguyen-Dang, 2004; Duflot, 2006; Muravin & Turkel, 2006; Singh et al., 2010; Barbieri et al., 2012; Shi et al., 2013), which are restricted to the analysis of homogenous and isotropic materials, have been reported so far. Any methodology that can help to model crack-crack interaction, crack-microcrack interaction and crack-interface crack interaction will further broaden the scope of the MMs.

1.2 Objectives

In light of the above, the present study has been carried out with the following objectives:

1) To develop a CCI technique for adoption in the XEFG method and to validate its suitability for isotropic and FGMs under mechanical and/or thermal loadings.

2) To develop a method to extract crack closure forces accurately to implement the MCCI technique in the MMs to extract the SIFs.

3) To formulate a new variant of the EFG method that can be used to model crack growth in bi-materials and particulate composites under quasi-static loading.

4) To modify, if needed, the existing crack-kinking criterion appropriately to model an interface crack propagation in particle-reinforced composites and to apply it in conjunction with the proposed EFG method.

5) To develop a scheme to model multiple interacting cracks using the EFG method.

1.3 Outline of the thesis

The relevant literature is reviewed in Chapter 2. This includes an introduction to level-set methods. In Chapter 3, the formulation of the EFG method and its variants, in order to solve the boundary value problem is given. The properties of the shape functions of the EFG method and the difficulties associated with integration of the weak form of the governing equation are discussed. Chapter 4 presents the application of the crack closure integral technique to extract the SIFs for isotropic and functionally graded materials under mechanical, crack-face and thermal loadings. The extracted SIFs are compared with the results obtained by the popular M-integral and other techniques. Chapter 5 describes a MCCI that is useful to extract the SIFs. In connection with the calculation of MCCI, the computation of nodal forces and crack opening displacements are discussed. A parametric study that involves the size of the nodal domain of influence, the nodal density, and the order of Gauss integration on the accuracy of the SIFs is shown. Chapter 6 presents crack propagation in particle-reinforced composites by a variant of the EFG method. An accurate and simple way to find the kinking angle of an interface crack is elaborated, and case studies are presented. Chapter 7 describes a new procedure to model multiple interacting cracks through the level-set method. Several problems, including interface crack and microcrack interactions are studied. Finally, the main conclusions and future scope of this work are presented in Chapter 8.

Chapter 2   Literature Review

2.1 Introduction

In this chapter, a brief development of the MMs is presented. Some aspects of the MMs that contrast with the features of the MMs are presented. The aspect of variable order singularity of a crack tip is discussed. Various techniques that are popular in FEM to extract the SIFs are reviewed. Mechanisms of crack propagation are included to highlight the issues that need special attention to enable application of the MMs in fracture studies. The level-set methods (LSM) that can be helpful in studying crack propagation problems are also presented.

2.2 Meshfree Methods

Although the FEM has been routinely used to model crack and its propagation, it gives rise to difficulties because of the need for meshing and re-meshing. The eXtended finite element method (XFEM) (Belytschko & Black, 1999; Nicolas et al., 1999; Bordas & Moran, 2006; Dunant et al., 2007; Bordas et al., 2008) circumvents the difficulties associated with the meshing through the usage of Heaviside function and crack-tip enrichment functions. The development of the MMs has been driven largely by the difficulties associated with finite element meshing and re-meshing.

There are many formulations of the MMs. The first of them is SPH (Lucy, 1977; Gingold & Monaghan, 1977). It was developed to solve the astrophysical problems, and has been later applied to fluid dynamic problems (Monaghan, 1982; Bonet & Kulasegaram, 2000). In the area of solid mechanics, it was used to solve the impact problem (Libersky et al., 1993). The original SPH lead to numerical instability and therefore improvements have been proposed (Johnson & Beissel, 1996; Bonet & Lok, 1999; Dilts, 2000; Dilts, 2000). The SPH and its corrected versions are based on the strong form.

Many variants of the MMs that are based on the weak form were developed after 1990. The diffuse element method (DEM) (Nayroles et al., 1992) and the EFG method (Belytschko et al., 1994) were based on the Bubnov–Galerkin method. On the other hand, the meshless local Petrov–Galerkin (MLPG) method that was developed by Atluri and Zhu (1998) is based on the local weak form. Although the DEM had some shortcomings, it later

became a popular MM in the area of solid mechanics. The reproducing kernel particle method (RKPM) (Liu et al., 1995), based on wavelets, was developed a year later after the EFG method. The EFG method, DEM and RKPM require higher order Gauss integration because of the non-polynomial nature of their shape functions. In order to overcome this issue, a linearly conforming point interpolation method (LC-PIM) that is based on the polynomial basis functions has been introduced by Liu (2001).

There are also other variants of the MMs, such as particle-in-cell (PIC), which can be used in both the strong and weak forms. The PIC method, when applied to the strong form, is called finite-volume particle-in-cell method (Munz et al., 1999). The PIC method, based on the weak form, is called material point method (Bardenhagen et al., 2000). Similarly, RKPM also has two versions: the collocation strong form (Liu et al., 1995) and the weak form (Aluru, 2000).

The review articles (Fries & Matthies, 2004; Shaofan & Liu, 2008; Nguyen et al., 2008) provide formulations of the versions of the MMs mentioned above. When compared to the popular FEM, the advantages of the EFG method are (Nguyen et al., 2008; Liu, 2010) as follows:

1. h and p adaptivity is much simpler than in FEM. Adding nodes ensures the adaptivity of both h and p (Gavete et al., 2002; Xiaoying et al., 2012).
2. Since adding nodes is not computationally costly, problems with moving boundaries associated with crack propagation, wave propagation, and phase transformation can be treated easily.
3. Impact and large deformation problems can be handled easily.
4. It ensures higher order continuity of the shape functions.
5. It has non-local interpolation character.
6. Retrieving stresses (post-processing) at any arbitrary point is simple, unlike the FEM.
7. To represent discontinuity in domain, it is not necessary to have nodes lying exactly on the boundary.

Although the MMs have many advantages over mesh-based methods, it also has some drawbacks:

1. The shape functions are non-polynomial in nature, and higher order Gauss point integration is needed to compute the stiffness matrix accurately.

2. The imposition of essential boundary conditions is difficult because the shape functions lack the Kronecker delta property.

3. The computational speed is significantly slower than the FEM.

4. The system stiffness matrix is asymmetric depending on the weak form.

2.3 Importance of fracture mechanics

In the first half of the 20th century, the design criteria for structures were based on the yield stress or ultimate stress. Based on this, engineers usually set a high factor of safety (FoS) to ensure a safe design. However, it was found that materials failed even when the applied stress were much less than the gross stress that would cause failure during tensile testing (Roylance, 2001). It was later recognized that embedded cracks lead to an amplification of stress. The fracture, therefore, occurs at a load below the expected level. Fig. 2.1 shows a liberty ship, which was the first all-welded cargo ship, mass-produced in the Unites States during the Second World War. Altogether 2,751 ships were built, only two remain now. Subsequently, many hypotheses (Inglis, 1913; Griffith, 1921) have been put forward by researchers to explain such catastrophic failures due to cracks.

Fig. 2.1 Failure of the Liberty ship due to a crack initiated at the weld (http://www-g.eng.cam.ac.uk/125/1925-1950/tipper3).

Irwin (1948) introduced the concept of SIF and related it to the energy release rate based on Westergaard's solution (1939) for the crack-tip stress field in brittle materials. Since

then, the SIF has become an important parameter to assess the damage tolerance in brittle materials.

Fig. 2.2 shows the geometry of a crack subjected to uniform remote loading. It has an asymptotic stress field ahead of the crack tip, the magnitude of which reaches infinity at the crack tip. Irwin showed that the singular stress field around a crack tip could be described in terms of the SIFs in a particular mode (Fig. 2.3).
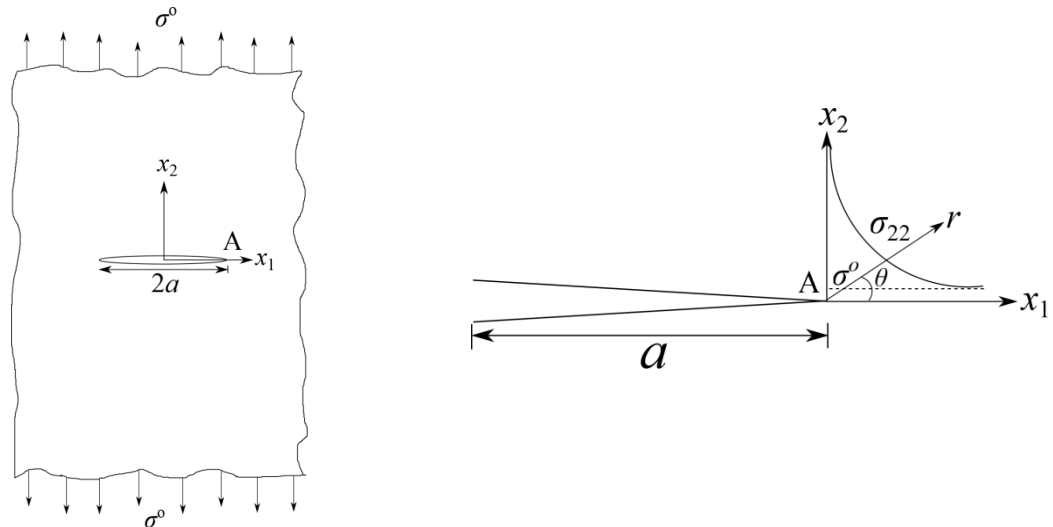
Fig. 2.2 Stress field ahead of the crack tip.

2.3.1 Fracture modes

The stress distribution $\sigma_{ij}(r,\theta)$ can be expressed as

$$\sigma_{ij}(r,\theta) = \frac{K}{\sqrt{2\pi r}} f_{ij}(\theta) + O(r) \tag{2.1}$$

where K is the stress intensity factor and $f_{ij}(\theta)$ is a function of θ only.

Mode I: Mode II: Mode III:
Opening   In-plane shear   Out-of-plane shear
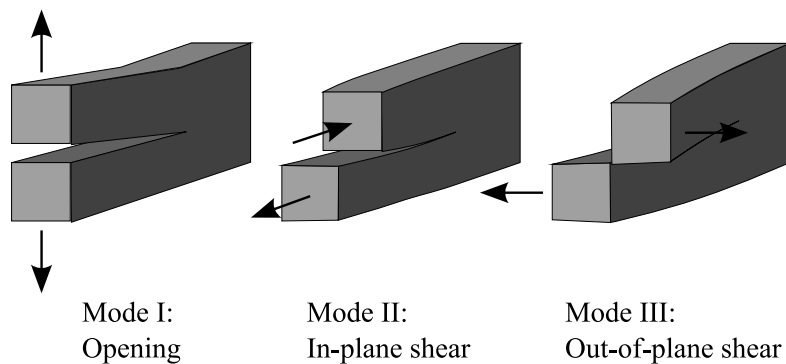
Fig. 2.3 Fracture modes.

For a crack in a homogenous material, the stress distribution has a square root singularity at the crack tip. The effect of loading and the geometry on the crack-tip stress field is included in the SIF parameter. Due to this, the stress field is characterized by a single parameter—SIF. In reality, plastic deformation occurs due to high stresses close to the crack tip where a linear elastic solution is no longer strictly valid. However, if the plastic zone size is small, the relation mentioned above can still be used to describe the stress state that occurs ahead of the crack tip.

The mode I crack driven by the tensile stress corresponds to the opening mode. The mode II and mode III crack correspond to in-plane and out-of-plane shear modes, respectively. The relation between the individual mode SIF and its corresponding energy release rate, in an isotropic material, is given by

$$G_I = K_I^2 / E^*$$
$$G_{II} = K_{II}^2 / E^*$$
$$G_{III} = K_{III}^2 / 2\mu$$

(2.2)

where K_i, $i = \mathrm{I, II}$ and III, are individual mode SIFs. μ is the shear modulus, and E^* is given by

$$E^* = \begin{cases} E & \text{plane stress} \\ E / (1-v^2) & \text{plane strain} \end{cases}$$

(2.3)

where E is Young's modulus and v is Poisson's ratio. The total energy release rate for a combined mode problem is as follows

$$G = G_I + G_{II} + G_{III}$$

(2.4)

2.4 Modelling fracture of materials

For a crack in an isotropic and homogenous material, the crack-tip stress field has a fixed singularity of order 1/2. It is different for bi-materials and composites. A crack propagating through a non-homogenous material (Fig. 2.4) has crack-tip stress field characterized by a complex order of singularity, which depends on the location of the crack tip with respect to the various material phases and the adjoining material properties.

In general, the stresses around the crack tip are proportional to $r^{\lambda-1}$ and are non-linear functions of θ. λ is called the order/strength of the singularity. λ depends on material

properties, the location of the crack tip, and the orientation of the crack with respect to the material interface, if any.
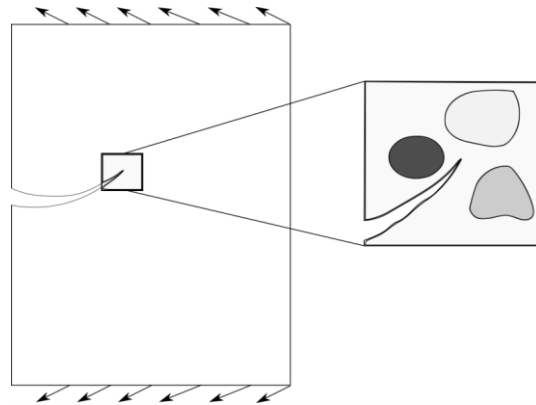
Fig. 2.4 Crack propagation through the composite with a zoomed view of the region around the crack tip showing different materials.

2.4.1 Isotropic and functionally graded materials

Most of the metals and glass are examples of isotropic materials. Although the individual grains are anisotropic, the property is homogenous at the macro level. If the material properties vary spatially and smoothly, they are called FGM. FGMs have a heterogeneous microstructure with no sharp discontinuity in material properties.
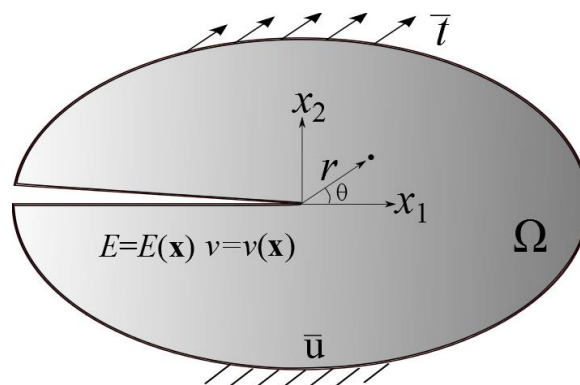
Fig. 2.5 A crack in an isotropic functionally graded material.

The concept of FGMs was introduced in Japan during a space plane project in 1984. Such a material was required to withstand a very high temperature gradient of 1000 K across a section of less than 10mm, and a surface temperature of around 2000 K (AZoM.com, 2015). FGMs were used as thermal barriers in weight-critical applications in the nuclear industry and in bioengineering applications (Marin, 2005; Mortensen & Suresh, 1995;

Cherradi et al., 1994; Neubrand & Rode, 1997). An overview of the various aspects of FGMs, with emphasis on their fracture behaviour is presented by Shanmugavel et al. (2012).

If Young's modulus and Poisson's ratio vary spatially with $\mathbf{x} = (x, y)$ (Fig. 2.5), in the absence of body forces, the Airy stress function $F(\mathbf{x})$ satisfies the following equation (Eischen, 1987).

$$\nabla^2\left(\frac{\nabla^2 F}{E^*(\mathbf{x})}\right) - \frac{\partial^2}{\partial x_2^2}\left(\frac{1+\nu^*(\mathbf{x})}{E^*(\mathbf{x})}\right)\frac{\partial^2 F}{\partial x_1^2} - \frac{\partial^2}{\partial x_1^2}\left(\frac{1+\nu^*(\mathbf{x})}{E^*(\mathbf{x})}\right)\frac{\partial^2 F}{\partial x_2^2} + 2\frac{\partial^2}{\partial x_1 x_2}\left(\frac{1+\nu^*(\mathbf{x})}{E^*(\mathbf{x})}\right)\frac{\partial^2 F}{\partial x_1 \partial x_1} = 0 \quad (2.5)$$

where $E^*(\mathbf{x})$ and $\nu^*(\mathbf{x})$ are given by

$$E^*(\mathbf{x}) = \begin{cases} E(\mathbf{x}) & \text{plane stress} \\ E(\mathbf{x})/(1-\nu(\mathbf{x})^2) & \text{plane strain} \end{cases}$$

$$\nu^*(\mathbf{x}) = \begin{cases} \nu(\mathbf{x}) & \text{plane stress} \\ \nu(\mathbf{x})/(1-\nu(\mathbf{x})) & \text{plane strain} \end{cases} \quad (2.6)$$

It has been shown that for such piecewise differentiable material property variations, the stress function is identical to the case of the crack in an isotropic and homogenous material (Jin & Noda, 1994) whose crack-tip stress field in a two-dimensional situation is given by

$$\sigma_{11} = \frac{1}{\sqrt{2\pi r}}\left[K_I f_{11}^I(\theta) + K_{II} f_{11}^{II}(\theta)\right]$$

$$\sigma_{22} = \frac{1}{\sqrt{2\pi r}}\left[K_I f_{22}^I(\theta) + K_{II} f_{22}^{II}(\theta)\right] \quad (2.7)$$

$$\sigma_{12} = \frac{1}{\sqrt{2\pi r}}\left[K_I f_{12}^I(\theta) + K_{II} f_{12}^{II}(\theta)\right]$$

and the displacement field is given by

$$u_1 = \frac{1}{\mu_{tip}}\sqrt{\frac{r}{2\pi}}\left[K_I g_1^I(\theta) + K_{II} g_1^{II}(\theta)\right]$$

$$u_1 = \frac{1}{\mu_{tip}}\sqrt{\frac{r}{2\pi}}\left[K_I g_2^I(\theta) + K_{II} g_2^{II}(\theta)\right] \quad (2.8)$$

where $\mu_{tip} = E_{tip}/(2+2\nu_{tip})$. E_{tip} and ν_{tip} are Young's modulus and Poisson's ratio at the crack tip.

The functions $f_{ij}^I(\theta)$ and $f_{ij}^{II}(\theta)$ $(i, j = 1, 2)$, $g_i^I(\theta)$ and $g_i^{II}(\theta)$ $(i = 1, 2)$ (Anderson, 1995) are the universal functions of θ, which are the same for the isotropic and

homogenous materials. Similar to the case of homogenous and isotropic materials, the crack-tip stress field in FGMs has a square root singularity too, that is, $\lambda = 0.5$.

The crack embedded in a homogenous material is relatively simpler than the cases that include cracks lying along the material interface or whose tip is at the interface (Akisanya & Fleck, 1997; Reedy, 2000; Mohammed & Liechti, 2000; Labossiere et al., 2002). In such cases, the crack-tip stress field consists of a superposition of two singular fields. The orders of singularity can be either two unequal real numbers $(\lambda_1 \neq \lambda_2)$ or a pair of complex conjugates $\lambda = \lambda_1 \pm i\lambda_2$ (Zhen & Zhigang, 2007). In some special cases, the two unequal real numbers may degenerate to a single value.

2.4.2 Bi-material
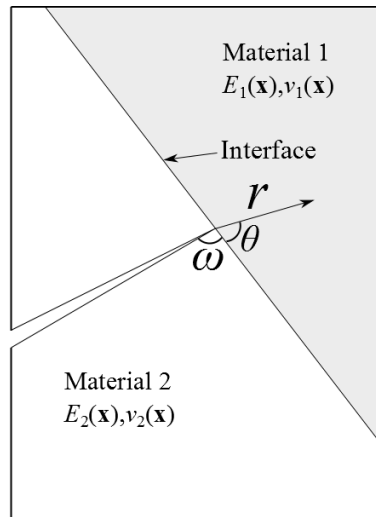
Fig. 2.6 Crack inclined toward material interface at an arbitrary angle.

When the crack is inclined at an angle to a material interface (Fig. 2.6), the order of singularity (λ) is a variable, which is the root of a transcendental equation (Bogy, 1971) . It depends on the angle (ω) at which a crack meets the interface and the material properties characterized by Dundurs' parameters, α and β .

$$\alpha = \frac{\mu_1\left(1-\nu_2\right) - \mu_2\left(1-\nu_1\right)}{\mu_1\left(1-\nu_2\right) + \mu_2\left(1-\nu_1\right)}$$

$$\beta = \frac{1}{2}\left[\frac{\mu_1\left(1-2\nu_2\right) - \mu_2\left(1-2\nu_1\right)}{\mu_1\left(1-\nu_2\right) + \mu_2\left(1-\nu_1\right)}\right]$$

(2.9)

where μ is the shear modulus of the material and v_1 and v_2 are Poisson's ratios of the two materials.

Fig. 2.7 shows the contours of the order of singularity for a crack meeting at an angle $\omega = 45^o$ to the material interface. This contour plot shows four regions separated by dark lines. For various material combinations characterized by the Dundurs' parameters, α and β, the order of singularity varies. In the upper-left and lower-right regions of the plot, the roots of the transcendental equation are unequal real numbers. The larger root (λ_1) is labelled horizontally and the smaller root (λ_2) vertically. In such a case, the stress field is given by

$$\sigma_{ij}(r,\theta) = \frac{k_1}{(2\pi r)^{\lambda_1}} Z_{ij}^1(\theta) + \frac{k_2}{(2\pi r)^{\lambda_2}} Z_{ij}^2(\theta) \tag{2.10}$$

where k_1 and k_2 are stress intensity coefficients that correspond to the order of singularity λ_1 and λ_2, respectively. $Z_{ij}^1(\theta)$ and $Z_{ij}^2(\theta)$ $(i = 1, 2)$ are functions of θ.
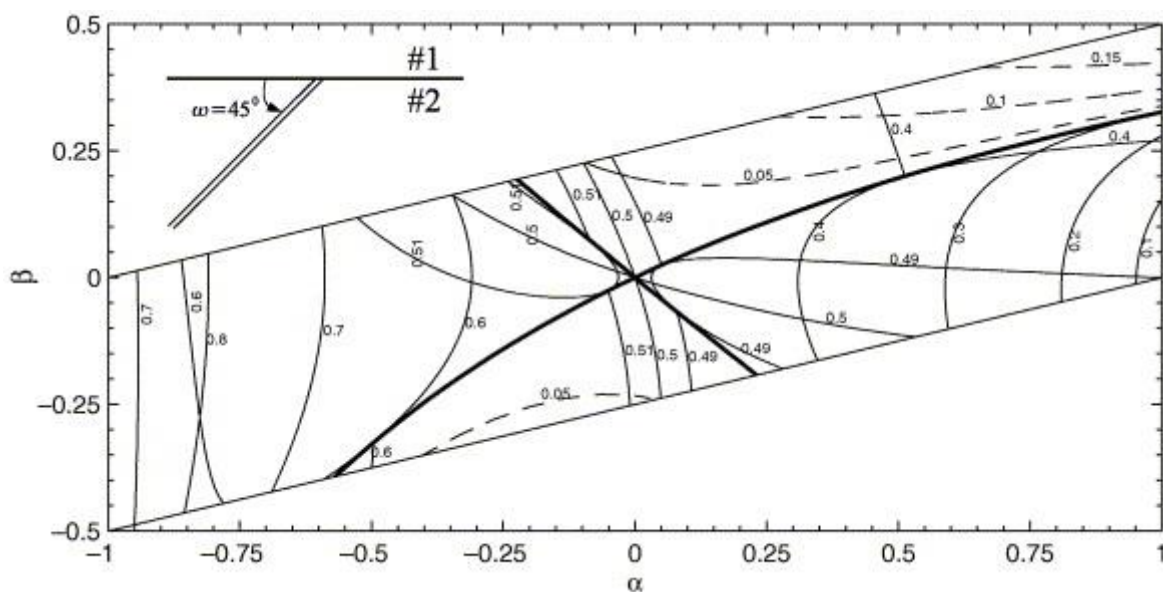
Fig. 2.7 Orders of singularity for different combinations of materials (Zhen & Zhigang, 2007).

In the upper-right and lower-left regions, the roots are a pair of complex conjugates $\lambda_{1,2} = (\xi \pm i\eta)$. The real part ξ is plotted by solid curves and the imaginary part η is plotted by dashed curves. The dark curves indicate that the roots are equal numbers.

(a) Bi-material interface crack: As a special case, when the crack lies along the interface $\omega = 0^o$ or 180° as shown in Fig. 2.8, the roots are a pair of complex conjugates given by

$$\lambda_{1,2} = \left(0.5 \pm i \frac{1}{2\pi} \ln \left(\frac{1-\beta}{1+\beta} \right) \right) \tag{2.11}$$

In the case of a bi-material interface crack (Rice, 1988; Hutchinson & Suo, 1992), the stress state is given by

$$\sigma_{ij}^m = \frac{f_{ij}^m(\theta)}{\sqrt{r}} \text{Re} \left[\mathbf{K} r^{i\varepsilon} \right] + \frac{g_{ij}^m(\theta)}{\sqrt{r}} \text{Im} \left[\mathbf{K} r^{i\varepsilon} \right] + T_m \delta_{i1} \delta_{j1} + O(\sqrt{r}) \tag{2.12}$$

where $\mathbf{K} = K_1 + iK_2$ (complex SIF) and T_m is the T-stress for material m, $m = 1$ and 2. T-stress is the first non-singular stress term of the Williams' eigenfunction expansion of a crack-tip stress field. The angular functions $F_{ij}^m(\theta)$ and $G_{ij}^m(\theta)$ are given in the work by Hongjun at al. (2012). The stresses σ_{22} and σ_{12} along the interface in front of the crack tip (Fig. 2.8) are given by

$$\boldsymbol{\sigma} = (\sigma_{22} + i\sigma_{12})_{\theta=0} = \frac{K_1 + iK_2}{\sqrt{2\pi r}} r^{i\varepsilon} \tag{2.13}$$
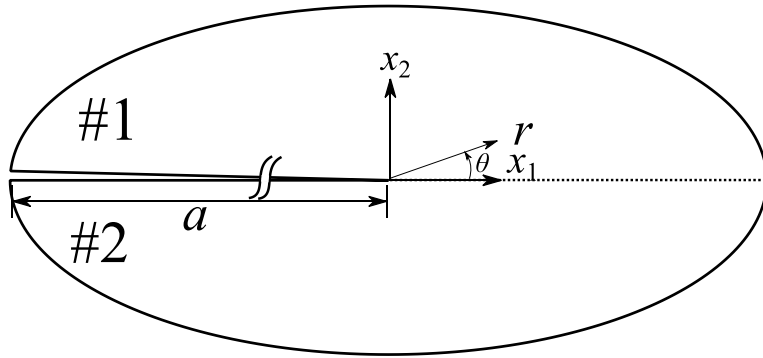
Fig. 2.8 Interface crack.

(b) Crack perpendicular to the interface: Another special case arises when $\omega = 90^o$, the two orders of singularities degenerate to one single value (Zak & Williams, 1963; Lu & Erdogan, 1983; Chen, 1994). It can be obtained by solving the following equation:

$$\cos(\lambda\pi) = \frac{2(\beta - \alpha)}{(1+\alpha)}(1-\lambda)^2 + \frac{\alpha + \beta^2}{1 - \beta^2} \tag{2.14}$$

2.5 SIF extraction techniques

The most important parameter that facilitates the application of the principles of LEFM into actual practice comprises of the SIFs and energy release rate (ERR). While interaction integral/M-integral serves as a routine method to extract the SIFs in the MMs, several other

methods such as the stress method, the displacement method and the CCI have been used frequently in the FEM and BEM to compute the SIFs. The ERRs are related to the SIFs.

The problems that involve crack face loading due to pressure or temperature are rarely studied by MMs. Such problems occur in hydraulic fracturing of the dam (Qing et al., 2009), oil pipelines, subsea production risers and flowlines (Cerkovnik & Akhtar, 2013) subjected to high temperatures and pressures that can range from 70 to 100 MPa. The pipe walls are usually thick, with a radius-to-thickness ratio of below 3. Most often, the fluid inside the pipe is corrosive and causes pitting. Often, a crack will quickly nucleate at this pit and lead to failure (Fig. 2.9). In such cases, determination of the SIF is necessary to check the safety of the element.
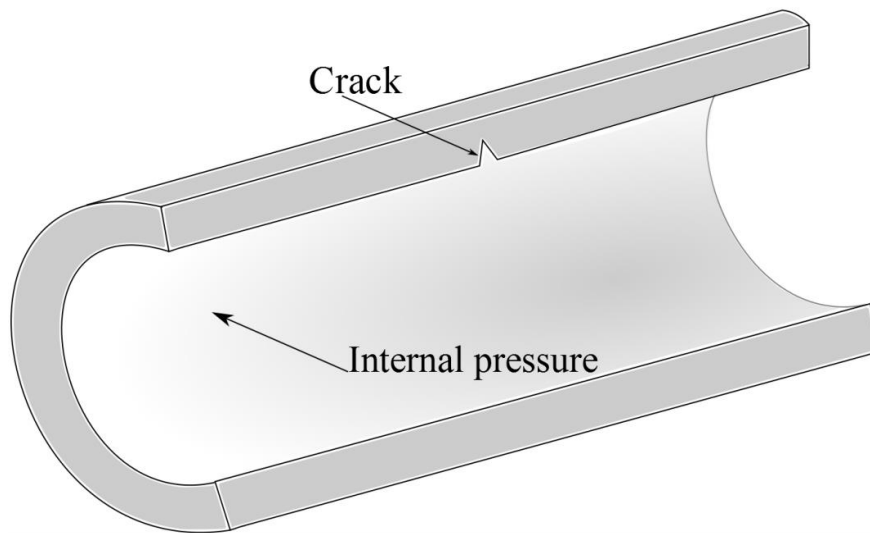
Fig. 2.9 Pipe with internal crack.

The evaluation of SIFs in the presence of crack edge loading requires special consideration. The usage of the interaction integral involves an extra term in the integral, the computations of which are relatively cumbersome when compared to the methods based on the displacements and the CCI.

2.5.1   Stress method

The stress method is the simplest and earliest of the methods used to extract the SIFs (Watwood, 1969). In this method, the stress is computed at location r_c, which is ahead of the crack tip, and is then compared with the theoretical solution for SIF calculation (Fig. 2.10). The mode I SIF can be obtained by

$$K_I = \sqrt{2\pi r_c}\, \sigma_{22|r_c} \tag{2.15}$$

where ($\sigma_{22|r_c}$) is computed at r_c, ahead of the crack tip ($\theta = 0$). Similarly, mode II SIF can be computed by computing the shear stress, $\sigma_{12|r_c}$ ahead of the crack tip.
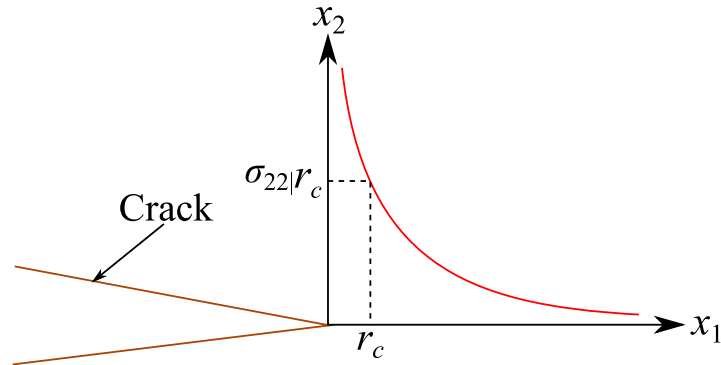
Fig. 2.10 Stress field ahead of the crack tip.

2.5.2 Displacement method

In the displacement method (Chan et al., 1970), the COD obtained numerically behind the crack tip is related to the theoretical COD solution according to Eq. (2.16), in order to extract the SIF. The theoretical solution for COD for a Mode I crack can be written as follows.

$$\begin{pmatrix} u_{COD} \\ v_{COD} \end{pmatrix} = \frac{K_I}{2\mu} \sqrt{\frac{r}{2\pi}} \begin{pmatrix} \cos\dfrac{\theta}{2}(\kappa\text{-}\cos\theta) \\ \sin\dfrac{\theta}{2}(\kappa\text{-}\cos\theta) \end{pmatrix} \tag{2.16}$$

where κ is the Kolosov's constant, $\kappa = 3 - 4v$ for plane strain, and $\kappa = (3-v)/(1+v)$ for plane stress. μ is the shear modulus.

Generally, the COD is measured within a distance of 5% of the crack length a behind the crack tip (Fig. 2.11), for an estimation of Mode I SIF. The SIF is given by

$$K_I = \frac{2\mu v_{COD|r_c}}{(\kappa+1)} \sqrt{\frac{2\pi}{r_c}} \tag{2.17}$$

where r_c is the location behind the crack tip where v_{COD} is evaluated. K_{II} is also found following a similar procedure using the sliding or u_{COD} for the mode II problem.

The COD is important not only in connection with the evaluation of the SIFs in the LEFM, but also in deciding on the extension of a crack in elastic plastic material.
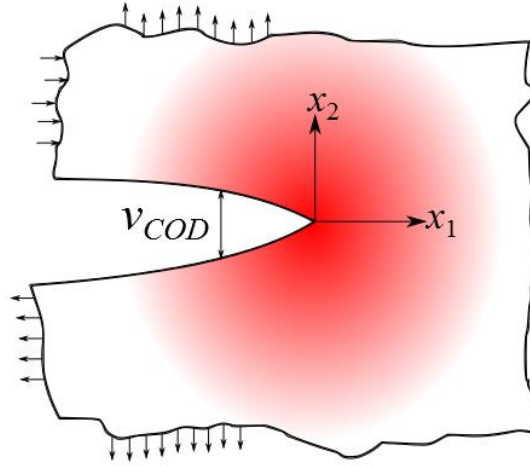
Fig. 2.11 COD behind the crack tip.

The displacement method and the stress method are the simplest of the methods used to extract the SIFs. Between these two, the displacement method gives superior results because the numerical method's formulation is mostly based on the displacement approximation. The accuracy of the SIFs obtained through these methods is dependent on the mesh or nodal density.

Another simple method to extract the SIFs within the framework of the FEM is stiffness derivative (Parks, 1974) procedure. It involves modifying the mesh in the region surrounding a crack tip in the crack extension direction in order to obtain the SIFs.

2.5.3 *J*-integral

The *J*-integral is a path-independent integral around the crack tip. It was first developed by Rice (1968). It is given by

$$J = \int_{\Gamma} \left(W n_1 - \sigma_{ij} \frac{\partial u_i}{\partial x_1} n_j \right) d\Gamma \tag{2.18}$$

where W is the strain energy density, n_i ($i = 1,2; n = n_1 \hat{i} + n_2 \hat{j}$) is the component of the unit normal vector of the line contour Γ (Fig. 2.12), and u_i denotes the displacement. The *J*-integral is also called J_1 integral. In general, the J_k integral can be written as

$$J_k = \int_{\Gamma} \left(W n_k - \sigma_{ij} \frac{\partial u_i}{\partial x_1} n_j \right) d\Gamma \tag{2.19}$$
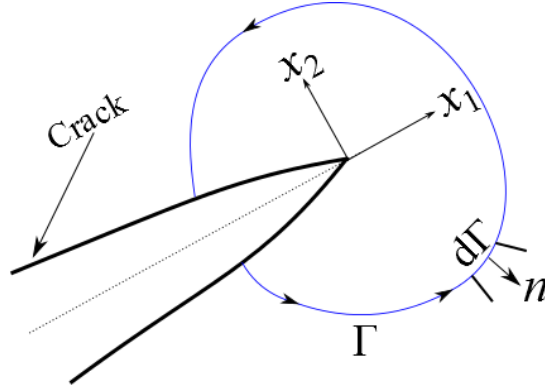
Fig. 2.12 *J*-integral contour for a crack.

For linear elastic materials, J_1 integral is the potential energy release rate (PERR) associated with a crack $(J_1 = J = G)$. For 2D problems, the J_1 integral can be split into two terms (Cherepanov, 1979) that correspond to each mode:

$$J_1 = J^I + J^{II} \tag{2.20}$$

where J^I and J^{II} are the mode I and mode II energy release rates. In the same fashion, J_2 integral is also expressed as

$$J_2 = -2\sqrt{J^I J^{II}} \tag{2.21}$$

From Eq. (2.20) and Eq. (2.21), the individual mode SIF can be obtained through the following relations:

$$
\begin{aligned}
K_I &= \pm\sqrt{\frac{E^* J_1}{2}\left[1 \pm \sqrt{1 - \left(\frac{J_2}{J_1}\right)^2}\right]} \\
K_{II} &= \pm\sqrt{\frac{E^* J_1}{2}\left[1 \mp \sqrt{1 - \left(\frac{J_2}{J_1}\right)^2}\right]}
\end{aligned}
\tag{2.22}
$$

However, computing J_2 integral is tricky because it involves singular terms when the sampling points lie in the region close to the crack tip, because n_2 is non-zero.

One of the popular approaches to compute SIFs is to decompose the mixed-mode J_1 integral (Kitagawa et al., 1976; Rigby & Aliabadi, 1998). It was first successfully applied

using dual BEM (Portela et al., 1992). This was then extended to the 3D case by Huber et al. (1993). This decomposing technique is tedious because the stress, strain and the displacement corresponding to each mode has to be extracted.

The other popular technique is based on the Betti's reciprocal theorem. In this case, auxiliary stress and displacement fields are employed to determine the SIFs (Huber et al., 1993; Wen & Aliabadi, 1995; Gosz & Moran, 2002). This technique is advantageous over the technique of decomposing the symmetric and anti-symmetric terms of the displacement and the stress. Moreover, the SIFs K_I and K_{II} can be calculated independently.

Nikishkov et al. (1987) converted the contour integral to domain integral and calculated the SIFs. Later, the idea of adopting auxiliary stress and displacement field solutions to calculate the SIFs was executed in planar and non-planar cracks (Moran & Shih, 1987; Gosz & Moran, 2002). This technique is popularly known as the M-integral or interaction domain integral method. M-integral is widely used in the extraction of mixed-mode SIFs in the MMs.

In addition to these techniques, there exist other methods such as the body force method (Nisitani & Chen, 1987; Nisitani & Chen, 1992) for the computation of SIFs.

2.5.4 Crack closure integral

Irwin showed that the PERR associated with formation of new surfaces due to an extended crack is equal to the specific work required to close the extended crack. This became the basis for the calculation of the CCI.

The following crack closure integrals give the expression for computing PERRs in mode I (G_I) and mode II (G_{II}):

$$G_I = \lim_{\Delta a \to 0} \frac{1}{2\Delta a} \int_0^{\Delta a} \sigma_{yy}(x) v_{COD}(\Delta a - x) dx$$

$$G_{II} = \lim_{\Delta a \to 0} \frac{1}{2\Delta a} \int_0^{\Delta a} \tau_{xy}(x) u_{COD}(\Delta a - x) dx \tag{2.23}$$

where G_I and G_{II} are mode I and mode II energy release rates, respectively. The stresses and displacements are shown in Fig. 2.13. The total energy release rate G is the sum of G_I and G_{II}. The SIFs associated with the individual modes can be extracted using Eq. (2.2).
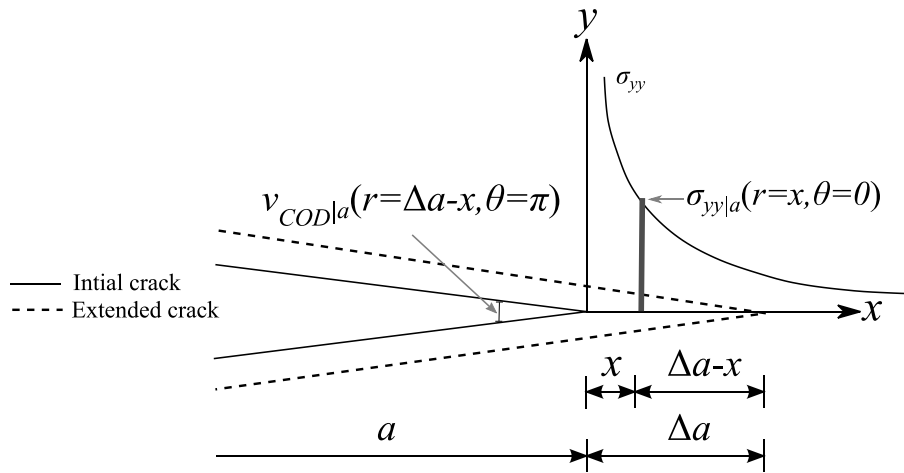
Fig. 2.13 Self-similar crack extension.

The integral in Eq. (2.23) can be evaluated by numerical integration or Gauss quadrature using the computed displacements and stresses. Because of steep gradients in stress near the crack tip, it is necessary to divide the span Δa into a large number of divisions, and to use a high order of Gauss quadrature to obtain good accuracy. Table 2.1 shows the percentage of error in SIF calculation using Gauss integration for various Gauss order and cell divisions. As the number of divisions Ndiv and order of Gauss quadrature increases, the error in the SIF calculation decreases.

Table 2.1 The percentage of error in SIF calculation using Gauss integration (Singh et al., 1988).

Ndiv	2 Point	3 Point	4 Point	5 Point
10	−3.57976	−2.53881	−1.96812	−1.60703
110	−1.06671	−0.75899	−0.58947	−0.48189
210	−0.77091	−0.54875	−0.42628	−0.34854
310	−0.63412	−0.45143	−0.35072	−0.28678
410	−0.55112	−0.39242	−0.30490	−0.24932
510	−0.49404	−0.35178	−0.27333	−0.22351
610	−0.45160	−0.32161	−0.24990	−0.20435
710	−0.41853	−0.29807	−0.23161	−0.18940
810	−0.39177	−0.27904	−0.21683	−0.17732
910	−0.36960	−0.26324	−0.20455	−0.16728
1010	−0.35079	−0.24985	−0.19415	−0.15878

In order to minimize the numerical error associated with the integration, Singh et al. (1988) proposed mid-fractional domain integration in the BEM and termed it as the UCCI. The Gauss integration over a certain fractional domain can be written as

$$G = \frac{2}{\Delta a} \int_0^{\Delta a} \frac{1}{2} \sigma_{(r,0)} v_{COD(\Delta a - r, \pi)} dr = \frac{2M}{\Delta a} \int_{r_1}^{r_2} \frac{1}{2} \sigma_{(r,0)} v_{COD(\Delta a - r, \pi)} dr \tag{2.24}$$

where M is a constant that depends on the fractional length of the domain and can be obtained from Eq. (2.24). The crack-tip stress field and crack opening displacement near the tip can be written as

$$\sigma_{(r,0)} = \frac{K}{\sqrt{2\pi r}}$$

$$v_{COD(\Delta a - r, \pi)} = \frac{K}{\sqrt{2\pi}} \sqrt{r} C_{COD} \tag{2.25}$$

where K is the SIF, C_{COD} equals $4/E(1-v^2)$ for plane strain and $4/E$ for plane stress. The energy release rate for a small crack extension of length Δa using Eq. (2.25) can be written as

$$G = \frac{K^2}{\Delta a 2\pi} C_{COD} \int_0^{\Delta a} \sqrt{\left(\frac{\Delta a}{r} - 1\right)} dr \tag{2.26}$$

The integral in Eq. (2.26) can be simplified to

$$\int_0^{\Delta a} \sqrt{\left(\frac{\Delta a}{r} - 1\right)} dr = \Delta a \frac{\pi}{2} = M \int_{r_1}^{r_2} \sqrt{\left(\frac{\Delta a}{r} - 1\right)} dr \tag{2.27}$$

M is obtained from Eq.(2.27) by choosing a suitable span r_1 to r_2 as

$$M = \frac{\pi/2}{V_{r_2} - V_{r_1}} \tag{2.28}$$

where $V_{r_i} = \varpi_i + \frac{1}{2}\sin\varpi_i$ and $\sin\varpi_i = \sqrt{\frac{r_i}{\Delta a}}$. For the mid half of the domain ranging from $r_1 = \Delta a/4$ to $r_2 = 3\Delta a/4$, M is equal to 3.

Table 2.2 shows the percentage of error in the SIF using BEM calculation by Gauss integration over the mid-half domain for various Gauss order and cell divisions. The error in the SIF calculation is significantly reduced by performing the integration over a

fractional domain. As long as the crack-tip stresses and displacements are extracted within a reasonable level of accuracy, the UCCI method gives the SIFs with very good accuracy.

Table 2.2 The percentage of error in SIF calculation using Gauss integration over the mid-half domain (Singh et al., 1988).

Ndiv	2 Point	3 Point	4 Point	5 Point
1	−0.13052	−0.00804569	−0.00051478	−0.00003356
2	−0.01398	−0.00033300	−0.00000879	−0.00000024
3	−0.00327	−0.00004057	−0.00000068	−0.00000002
4	−0.00111	−0.00000839	−0.00000014	−0.00000001
5	−0.00048	−0.00000238	−0.00000006	−0.00000001
6	−0.00023	−0.00000084	−0.00000004	−0.00000001
7	−0.00012	−0.00000035	−0.00000003	−0.00000001
8	−0.00008	−0.00000016	−0.00000002	−0.00000001
9	−0.00005	−0.00000008	−0.00000002	−0.00000001
10	−0.00003	−0.00000005	−0.00000002	−0.00000001

Alternative approach to improve the accuracy of the SIFs

When the crack-tip stresses and CODs are not smooth, a smoothing function of a known variation can be used to smoothen out the field variation (Maiti et al., 1997). Various smoothing functions that depend upon the displacement variation, such as linear, quadratic, and asymptotic variation using a quarter point compatible with square root singularity in the BEM, have been suggested.

MCCI or VCCT

The MCCI or VCCT is routinely used within the context of the FEM. In this method, the crack closure forces are extracted using the stiffness matrix and nodal displacement. Fig. 2.14 shows a four-node quadrilateral FE mesh in the region around the crack tip, which is used to compute the crack-tip nodal force and the crack opening displacement. The mode I and mode II components of the SERR G_I and G_{II} are then calculated using the following relation:

$$G_I = \frac{-1}{2\Delta a}.F_y.v_{COD}$$
$$G_{II} = \frac{-1}{2\Delta a}.F_x.u_{COD}$$

(2.29)

where Δa is the length of the elements at the crack front and F_x and F_y are the nodal forces at the crack tip (nodal point *i*). The CODs behind the crack tip are calculated from the nodal displacements at the upper crack face and the lower crack face.
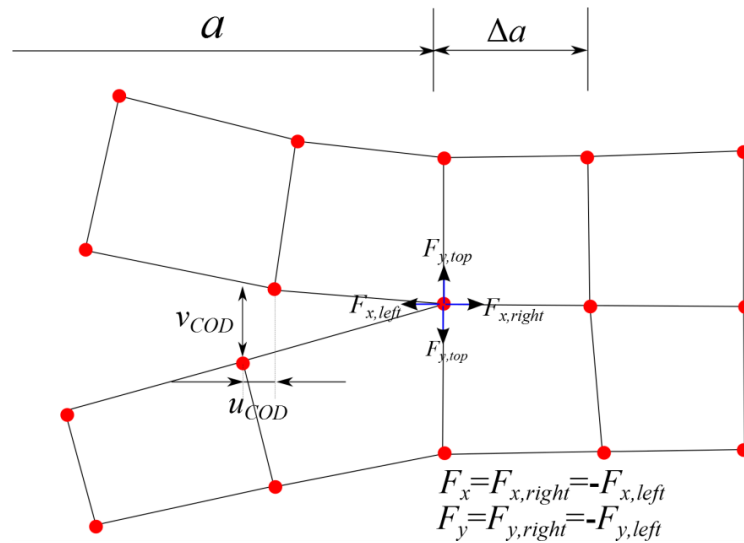
Fig. 2.14 Modified crack closure integral in FEM.

Eq. (2.29) is very convenient to extract the mixed-mode SIFs, because it does not involve cumbersome computations. The crack face loading due to pressure or temperature can also be easily handled by the MCCI. Moreover, the energy release rate associated with the MCCI includes the contribution due to a singular term plus the higher order terms. The direct adoption of the method in the MMs is beset by only the problem of computation of the crack closure forces to implement the MCCI technique.

Since the variation of the crack-tip stress and displacement fields are the same for the isotropic and functionally graded materials, the expressions given in this section are applicable to the latter group of materials.

2.6 Crack Propagation Criteria

There are many theories (Kumar, 2013) to predict the direction of crack extension. It can be broadly classified into categories: stress and energy based criterions. The crack propagates when the stress or the maximum energy release rate along the crack extension direction reaches a critical value.

2.6.1 Maximum tangential stress (MTS) criterion

The MTS criterion was proposed by Erdogan and Sih (1963). They proposed that the crack extension would occur from the crack tip in the radial direction perpendicular to the direction of maximum tangential stress (MTS). The criterion was based on the stress field approximated by the first term of the Williams' stress function expansion given by Eq. (2.7). The direction of crack extension $(\theta_c)_{MTS}$ is given by the following condition:

$$
\frac{\partial \sigma_{\theta\theta}}{\partial \theta} = 0
$$
$$
\frac{\partial^2 \sigma_{\theta\theta}}{\partial \theta^2} < 0
$$

(2.30)

where $\sigma_{\theta\theta}$ is the tangential stress around the crack tip. Substituting Eq. (2.7) in Eq. (2.30), $(\theta_c)_{MTS}$ can be expressed in terms of SIFs as

$$
\theta_c = 2 \tan^{-1} \left(\frac{-2K_{II}/K_I}{1 + \sqrt{1 + 8(K_{II}/K_I)^2}} \right)
$$

(2.31)

The condition for the crack to propagate in the $(\theta_c)_{MTS}$ direction is given by

$$
\sigma_{\theta\theta}^{\max} = \frac{K_I}{\sqrt{2\pi r_c}} \cos^3 \frac{(\theta_c)_{MTS}}{2} - \frac{3}{2} \frac{K_{II}}{\sqrt{2\pi r_c}} \cos \frac{(\theta_c)_{MTS}}{2} \sin(\theta_c)_{MTS} = \sigma_c
$$

(2.32)

where σ_c is the critical stress. It is a material property that can be obtained from pure Mode I fracture tests where

$$
\sigma_c = \frac{K_{Ic}}{\sqrt{2\pi r_c}}
$$

(2.33)

K_{Ic} is the Mode I fracture toughness and r_c is the radial distance from the crack tip at which $\sigma_{\theta\theta}$ is computed using Eq. (2.32).

The MTS criterion does not take into account the higher order terms of the eigenfunction expansion. Therefore $(\theta_c)_{MTS}$ is not a principal direction when more than one term (singular term) of the Williams' stress function expansion is used to predict the direction of crack extension.

2.6.2 Maximum tangential principal stress (MTPS) criterion

According to the MTPS criterion, a crack extends in a radial direction corresponding to the maximum tangential principal stress on a circle of finite radius from the crack tip. This extension occurs when this maximum reaches a critical value, which is defined as a material constant. It can be easily obtained from mode I fracture tests.
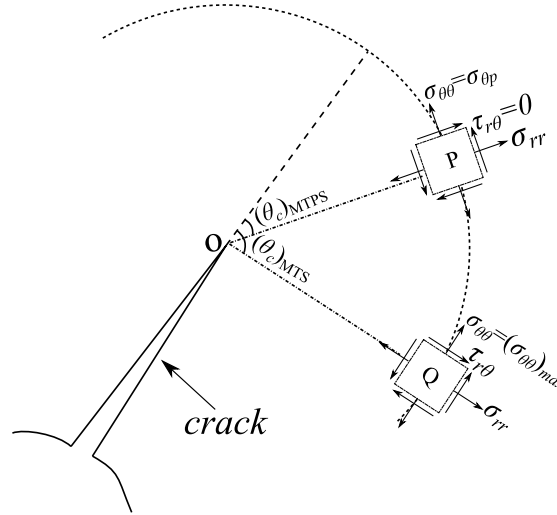
Fig. 2.15 MTS and MTPS criteria.

When a finite number of terms of the Williams' eigenfunction expansion are used to express the crack-tip stress field, the condition $\partial\sigma_{\theta\theta}/\partial\theta = 0$ does not give a principal direction. There is a direction close to this and is given by $\tau_{r\theta} = 0$, which corresponds to a principal direction. The corresponding tangential stress is a principal stress. According to the MTPS criterion, the crack extends in the $(\theta_c)_{MTPS}$ direction, which is given by $\tau_{r\theta} = 0$. The condition for the onset of extension is given by $\sigma_{\theta P}$ (Fig. 2.15), which reaches a critical value σ_c (Maiti & Smith, 1983a). σ_c is equal to, $K_{Ic}/\sqrt{2\pi r_c}$, where r_c is the radius of the circle considered for plotting. This is also called the shear stress criterion.

2.6.3 Maximum tangential strain (MTSN) criterion

This criterion was first proposed by St.Venant (Timoshenko, 1953). It has received considerable attention; this has been accepted as a theory of failure. This theory was later successfully adapted in the study of the failure of concrete (Wu, 1974). When applied to an elliptical angled crack problem, along the line of the MTS criterion, the MTSN criterion σ_c (Maiti & Smith, 1983a) yielded results that matched published data (Wu & Chang, 1978; Chang, 1981). It was also applicable to slit cracks (Maiti & Smith, 1983b).

The variation of tangential strain can be obtained from the asymptotic stress field in the region close to the crack tip using Hooke's law. Alternatively, the strain field can also be obtained from the numerical simulation by multiplying the strain-displacement matrix with the displacement vector. This computed strain would include the effects due to both singular and non-singular terms. According to the MTSN criterion, the crack initiates when the $\varepsilon_{\theta\theta}^{\max}$ reaches the critical value that can be obtained from the mode I test.

2.6.4 Minimum strain energy density (SED) criterion

The strain energy density criterion was proposed by Sih (1974). According to this criterion, a crack extends in a radial direction from the crack tip corresponding to the minimum strain energy density W on a circle of finite radius from the crack tip. The extension occurs when the minimum SED value reaches a critical value, which is a material parameter. The total strain energy is given by

$$U = \int_{V} \left(\int_{0}^{\varepsilon_{ij}} \sigma_{ij} d\varepsilon_{ij} \right) dV \tag{2.34}$$

where V is the volume of the body. The strain energy density is given by

$$W = \frac{dU}{dV} = \int_{0}^{\varepsilon_{ij}} \sigma_{ij} d\varepsilon_{ij} = \frac{(1+v)}{2E} \left[\frac{\kappa+1}{4} \left(\sigma_{11} + \sigma_{22} \right)^2 - 2 \left(\sigma_{11}\sigma_{22} - \sigma_{12}^2 \right) \right] \tag{2.35}$$

where $\kappa = 3 - 4v$ for plane strain, and $\kappa = (3-v)/(1+v)$ for plane stress. Substituting Eq. (2.7) in Eq.(2.35), the SED can be expressed as

$$W = \frac{1}{\pi r} \left[g_{11} K_I^2 + 2 g_{12} K_I K_{II} + g_{22} K_{II}^2 \right] \tag{2.36}$$

where

$$g_{11} = \frac{1}{16\mu} \left(1 + \cos\theta \right) \left(\kappa - \cos\theta \right)$$

$$g_{12} = \frac{1}{16\mu} \sin\theta \left[2\cos\theta - (\kappa - 1) \right] \tag{2.37}$$

$$g_{22} = \frac{1}{16\mu} \left[(\kappa + 1)(1 - \cos\theta) + (1 + \cos\theta)(3\cos\theta - 1) \right]$$

Since the SED function poses singularity, Sih proposed another function $S(\theta)$ that is independent of the radius r, given by

$$S(\theta) = Wr \tag{2.38}$$

The direction of the crack extension $(\theta_c)_{SED}$ is given by the following condition.

$$\frac{\partial S}{\partial \theta} = 0$$
$$\frac{\partial^2 S}{\partial \theta^2} > 0 \tag{2.39}$$

By combining Eq.(2.37), (2.38), and (2.39), the direction of crack propagation $(\theta_c)_{SED}$ can be obtained by solving the following equations:

$$\begin{aligned}
&\left[2\cos\theta - (\kappa-1)\right]\sin\theta K_I^2 + 2\left[2\cos 2\theta - (\kappa-1)\cos\theta\right]K_I K_{II} \\
&+ \left[(\kappa-1-6\cos\theta)\sin\theta\right]K_{II}^2 = 0 \\
&\left[2\cos 2\theta - (\kappa-1)\cos\theta\right]K_I^2 + 2\left[(\kappa-1)\sin\theta - 4\sin 2\theta\right]K_I K_{II} \\
&+ \left[(\kappa-1)\cos\theta - 6\cos 2\theta\right]K_{II}^2 > 0
\end{aligned} \tag{2.40}$$

Eq. (2.40) can be solved to determine the direction of crack extension when the SIFs are known. The material parameter S_c is obtained from Mode I fracture test, as follows:

$$S_c = \frac{(1+v)(\kappa-1)}{4\pi E} K_{Ic}^2 \tag{2.41}$$

Fig. 2.16 shows crack paths predicted by four criteria, MTS, MTPS, MTSN, and SED, for an elliptical crack with $b/a = 0.2$. The crack paths predicted by each of the criterion are different; the difference between them increases with an increase in the inclination of the crack to the loading angle. For instance, for $\beta = 75°$, the crack extension direction predicted by the SED criterion is very different from those obtained by the MTS, MTPS and MTSN criteria.
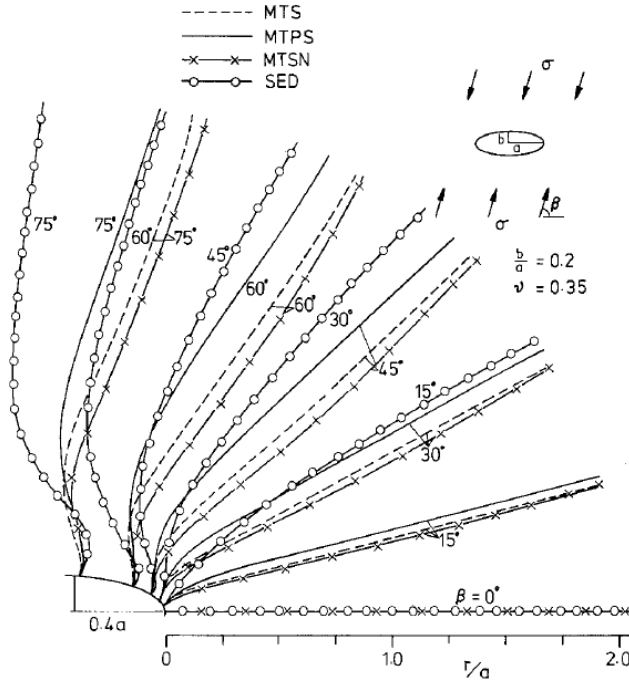
Fig. 2.16 Crack paths predicted by four criteria (Maiti & Smith, 1983a).

2.7 Interface Crack-Kinking Criterion

A propagating crack in non-homogenous materials often encounters the material interface. The crack may propagate along the interface or kink into the adjoining materials, depending upon the loading angle and the properties of the adjoining material. The criteria governing the kinking out of an interface are different from those used to determine the crack propagation angle in homogenous materials. There are three popular criteria to predict the interface crack kinking angle.

2.7.1 G_{max} criterion

He and Hutchinson (He & Hutchinson, 1989) proposed that the kink angle ω of an interface crack (Fig. 2.17(a)) is dictated by the maximum ERR (G_{max}) of the kinked crack. In order to find the maximum energy release rate $G_{m\omega}$ $\left(G_{m\omega}=G_{max}\right)$, the crack is extended by Δa in various directions θ, as shown in Fig. 2.17(b). The direction θ, which corresponds to the maximum energy release rate $G_{m\omega}$ is the angle of crack propagation ω into the material m (#1 or #2).
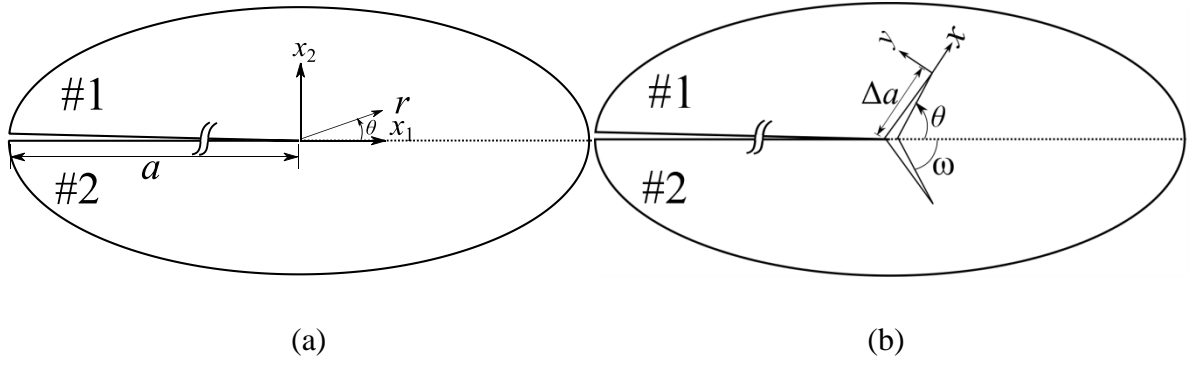
Fig. 2.17 (a) Interface crack. **(b)** Kinking of an interface crack.

The tendency of the interface crack to kink out of the interface or to grow along it is determined by the following ratio:

$$\frac{G_{m\omega}}{\Gamma_f^m} > \frac{G_I}{\Gamma_f^I} \tag{2.42}$$

where Γ_f^m and Γ_f^I are the fracture toughness of the adjoining material m and the interface, respectively. The ERR G_I along the interface and ERR $G_{m\omega}$ along the kinking angle ω are related to SIFs and is given by

$$G_I = \frac{1}{E^*}\frac{K_1^2 + K_2^2}{\cosh^2(\pi\varepsilon)}$$

$$G_{m\omega} = \frac{1}{E_m^*}\frac{K_I^2 + K_{II}^2}{2} \tag{2.43}$$

$$1/E^* = 1/E_1^* + 1/E_2^*$$

where E_m^* is the Young's modulus of the material m (#1 or #2). The crack is likely to penetrate the homogenous neighboring material if the inequality in Eq. (2.42) holds. Otherwise, it is likely to extend along the interface.

This theory can also be extended to an arbitrary crack located in any material. The crack extends in the direction of the maximum energy release rate. In order to find the energy release rate $G(\theta)$, the crack is extended by Δa in various directions, θ, as shown in Fig. 2.18. The θ_c corresponding to the maximum energy release rate G_θ^{max} is the crack propagation direction.
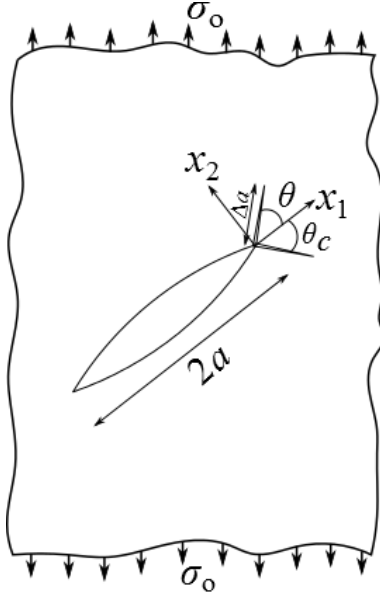
Fig. 2.18 Crack extension Δa to find the energy release rate $G(\theta)$.

The crack propagates when $G_\theta^{\max}$ reaches the critical energy strain energy release rate G_c. That is,

$$G_\theta^{\max} \geq G_c \qquad (2.44)$$

where $G_c = K_{Ic}^2 / E^*$; K_{Ic} is the critical SIF of the material.

Although the energy-based criterion can be used to determine both the crack-kinking angle and the load that leads to initiation of interface crack kinking, it requires substantial computational effort. This is because the criterion requires multiple analyses to generate a variation of the ERR with the possible kinking direction θ. In general, for an accurate computation of ERR, Δa of the kinked crack is kept very small when compared to the parent interface crack.

2.7.2 $K_{II} = 0$ criterion

The $K_{II} = 0$ criterion, proposed by Akisanya and Fleck (Akisanya & Fleck, 1992), stipulates that the interface crack kinks in the direction that corresponds to zero mode II SIF of the kinked crack. The mixed-mode SIFs of a kinked crack of length Δa is related to the parent crack (He & Hutchinson, 1989; Akisanya & Fleck, 1992) by the following relation.

$$K_I + iK_{II} = c\mathbf{K}(\Delta a)^{i\varepsilon} + \bar{d}\mathbf{K}(\Delta a)^{i\varepsilon} + gT_m\sqrt{\Delta a} \qquad (2.45)$$

where $c, \overline{d}$ and g are complex functions that are dependent on material parameters α, β, and the kink angle, ω.

Given the complex functions $c, \overline{d}$, and g, the complex SIF of the interface crack, calculated from the interaction integral or from any other SIF extraction technique is substituted in the Eq. (2.45) to determine ω. In the absence of the data of $c, \overline{d}$, and g, the kinked crack of length Δa is extended in various directions, θ. The kink angle ω corresponds to the direction in which mode II SIF of the kinked crack is zero.

2.7.3 MTS criterion

Yuuki and Xu (1992) proposed that the interface crack would extend in the direction of the maximum tangential/hoop stress given by the singularity term; they did not consider T-stress in their analysis. The angle θ corresponding to $\sigma_{\theta\theta}^{\max}$ gives the kinking angle ω. The tangential/hoop stress variation for an interface crack is given by

$$\sigma_{\theta\theta} = \frac{|\mathbf{K}|}{\sqrt{2\pi r_c}} \left(\cos\left(\hat{\psi} + \varepsilon \ln \frac{r_c}{L} \right) \Sigma_{\theta\theta}^{I}(\theta) + \sin\left(\hat{\psi} + \varepsilon \ln \frac{r_c}{L} \right) \Sigma_{\theta\theta}^{II}(\theta) \right) \qquad (2.46)$$

where $\mathbf{K} = K_1 + iK_2$ is a complex SIF associated with an interface crack, r_c is radius at which tangential stress is determined, and ε is oscillation index parameter defined by

$$\varepsilon = \frac{1}{2\pi} \ln\left(\frac{1-\beta}{1+\beta} \right) \qquad (2.47)$$

$\hat{\psi}$ is the phase angle defined by

$$\hat{\psi} = \tan^{-1}\left(\frac{\mathrm{Im}\left(\mathbf{K}L^{i\varepsilon} \right)}{\mathrm{Re}\left(\mathbf{K}L^{i\varepsilon} \right)} \right) \qquad (2.48)$$

where L is some fixed value, and usually set close to $100\,\mu\mathrm{m}$.

Although, $K_{II} = 0$ and the MTS criterion are used to determine the kinking angle, they cannot be used to judge whether crack would kink or grow along the interface. Only when the interface is assumed to be tough, the crack can be forced to propagate into the adjoining material. Eq. (2.42) is still needed to ascertain the direction of crack propagation.

Fig. 2.19 shows a Brazil-nut-sandwich specimen made of aluminum and epoxy, which is used to determine the kink angle of an interface crack. The experimental results are compared with the kink angle of an interface crack obtained using the three criteria in Fig. 2.20. It is observed that the MTS criterion performs better than the two other criteria.
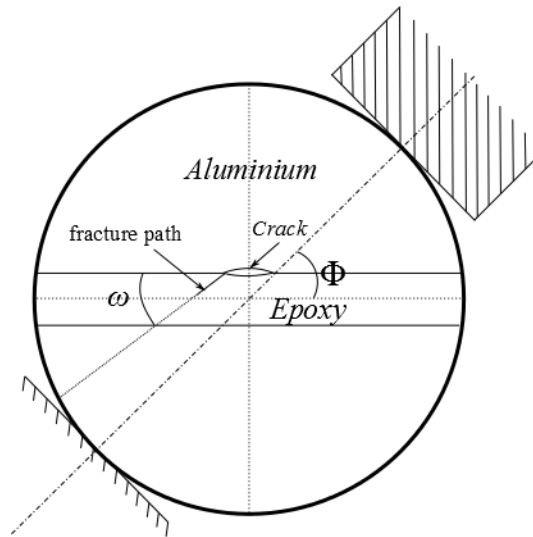
Fig. 2.19 Brazil-nut-sandwich fracture specimen (Kang, 1994).

The MTS criterion is the simplest among all the criteria, but does not take into account T-stress. It is well known that in non-homogenous materials the first non-singular term (T-stress) of the Williams' expansion affects the crack propagation angle (Kang, 1994). When T-stress is taken into account, the $\sigma_{\theta\theta}^{\max}$ based on the MTS criterion is no longer the principal stress.
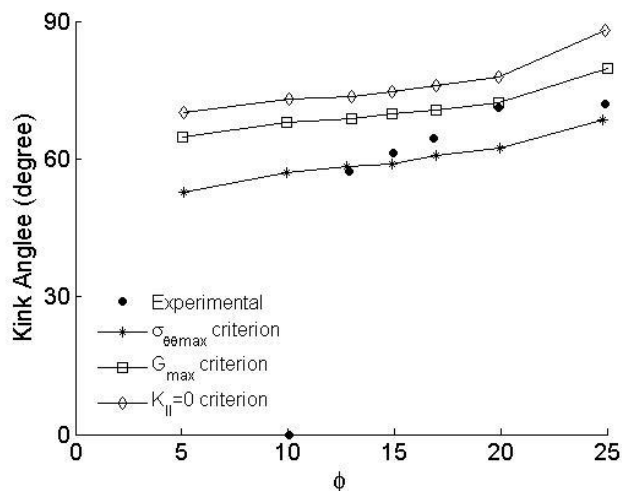
Fig. 2.20 Comparison of kinking angle obtained using three criteria, with the experimental results in brazil-nut-sandwich specimen (Kang, 1994).

2.8 Level-Set Methods

The LSM was developed by Osher et al. (1988) to model the motion of interfaces or moving boundaries. It has been used in a wide range of applications (Sethian, 1999). The combination of LSM and the numerical method such as the XFEM or MMs provided a simple way of implicitly tracking crack growth in two and three dimensions (Xiaoying, 2010). The level-set data that corresponds to a crack is generally stored at FE nodes or meshfree nodes. These values are updated using evolution equation when crack propagates.

There are different techniques to track crack propagation using level sets, which can be classified into four groups. In the first group, the level-set values stored in the background grid points are updated using the solution of an evolution equation, the Hamilton–Jacobi PDE (Moës et al., 2002; Gravouil et al., 2002; Sukumar et al., 2002). In the second group, algebraic relations between the coordinates of a given point, the coordinates of the crack front, and the crack advance vector is stored as level-set data and used to track crack propagation (Stolarska et al., 2001). The third group is based on the vector level set (Ventura et al., 2002; Ventura et al., 2003), in which the information about magnitude of the distance of a point to the crack curve and its sign is stored. The fourth group tracks the crack by algebraic and trigonometric equations that involve the initial value of the level-set functions and the crack advance vector. The first and the fourth group suit any 3D tracking of crack growth. An efficient crack-tracking algorithm in the framework of MMs has been presented by Zhuang et al. (2011; 2012).

A 3D crack has two level-set functions (Fig. 2.21)—normal and tangential level set— defined at each background grid point. The normal level set $\varphi(\mathbf{x})$ corresponds to the signed normal distance from the crack surface to the grid point. Therefore, the set $\varphi(\mathbf{x}) = 0$ describes the surface that contains the crack. The tangential level set $\varsigma(\mathbf{x})$ corresponds to signed distance of the crack front from a given grid point. Therefore, the set $\varsigma(\mathbf{x}) = 0$ describes the crack front curve. Therefore, it becomes easy to track the crack with these two level sets without explicit representation.

In the case of a 2D crack, a single level-set function (normal level-set- $\varphi(\mathbf{x})$), is sufficient for crack description because the crack front is just a point. The third group of the method based on the vector level set is particularly suitable for 2D cracks. It does not require the solving of the evolution PDE. When a crack propagates, the vector level-set function and

the crack-tip location are updated using simple algebraic equations. Since the MMs allow modeling of curved cracks with ease, it becomes all the more advantageous to combine them with the vector level set to track any crack extension.
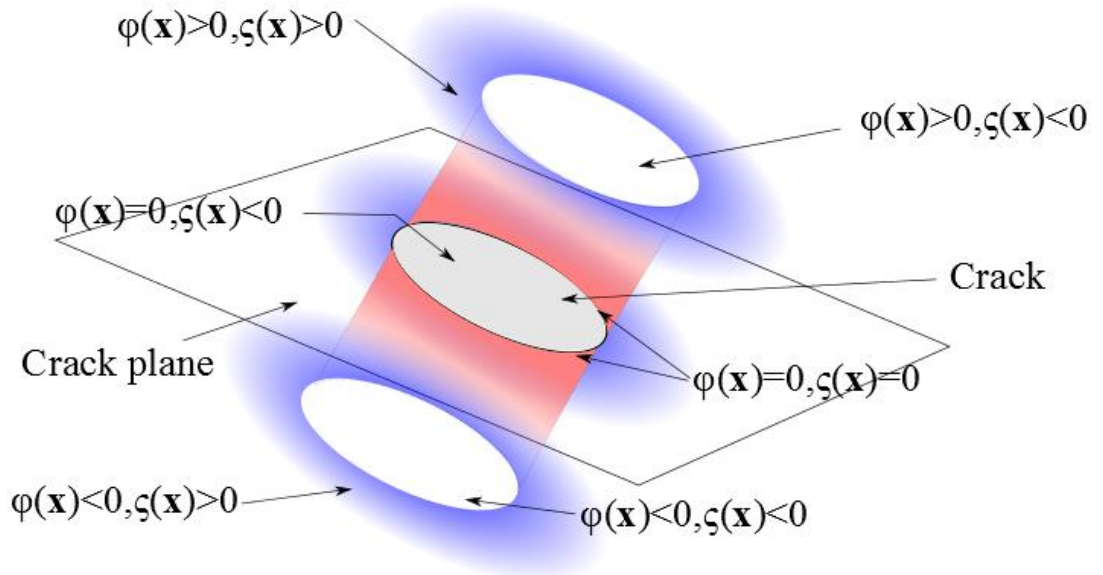
Fig. 2.21 Level-set methods for a 3D crack.

The vector level-set function $f(\mathbf{x})$ in a 2D case is defined on a narrow band of nodes, as shown in (Fig. 2.22). Usually, the level-set values are stored in the grid points that coincide with nodes and fall within a distance of r_f from the crack line. The r_f is usually related to the domain of influence d_I; it is slightly bigger than the d_I for a regular node in the MMs.
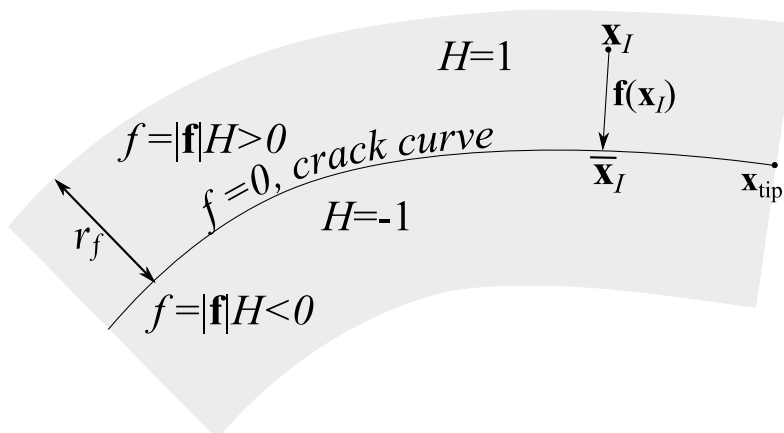
Fig. 2.22 Level-set method for a 2D crack.

In the case of a 2D crack, a compound object $\tilde{f}(\mathbf{x})$ is defined by Ventura et al. (2002) such that it consists of vector level set and Heaviside function of $f(\mathbf{x})$

$$\begin{aligned}
\tilde{f}(\mathbf{x}) &= \{\mathbf{f}(\mathbf{x}), H(f(\mathbf{x}))\}^T \\
\mathbf{f}(\mathbf{x}) &= \bar{\mathbf{x}} - \mathbf{x}
\end{aligned} \qquad (2.49)$$

where $\bar{\mathbf{x}}$ is the foot of perpendicular from $\mathbf{x}$ to the crack curve. The signed distance function required for representing the crack can be computed using

$$f(\mathbf{x}) = \|\mathbf{f}(\mathbf{x})\| H(f(\mathbf{x})) \qquad (2.50)$$

During the calculation of the stiffness matrix, the signed distance at grid points has to be extrapolated to any generic point p, which can be a Gauss point. This is done by identifying the grid point closest to p (Fig. 2.23(a)). Then the signed distance $f(\mathbf{x}_p)$ (Fig. 2.23(b)) is then given by

$$\begin{aligned}
f(\mathbf{x}_p) &= f(\mathbf{x}_I) + (\mathbf{x}_I - \mathbf{x}_p) \\
H(f(\mathbf{x}_p)) &= H(f(\mathbf{x}_I)) \operatorname{sign}(f(\mathbf{x}_p).\hat{f}(\mathbf{x}_I))
\end{aligned} \qquad (2.51)$$

where I is the node closest to p and $\hat{f}(\mathbf{x}_I)$ is the normalized vector distance of point $\mathbf{x}_I$ to the crack. As the crack propagates, the level-set values are easily updated using geometric expressions in the background grid points (Ventura et al., 2002).
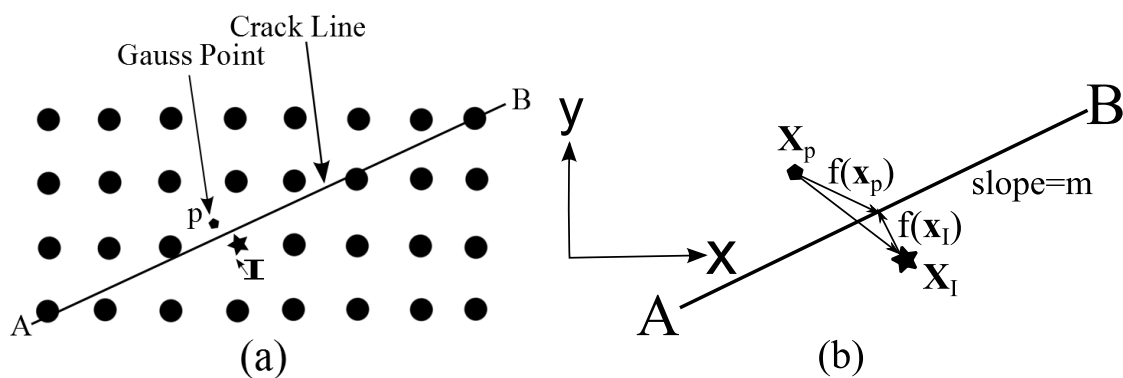
Fig. 2.23 (a) Gauss point p near the crack line. **(b)** Vector extrapolation.

2.9 Closure on the review

The literature review indicates a variety of ways of exploiting MMs. Most of the techniques that have been used for extraction of the SIFs are based on the J-integral

technique. Many other techniques such as the displacement method, the stress method, and the CCI technique are much simpler than this approach, and are routinely used in the FEM and BEM. The use of such techniques in MMs to extract the SIFs has not yet been studied. Further, whether the cases of crack face loading and thermal loading can be incorporated easily into these methods, for extraction of the SIFs, needs fresh examination.

Crack propagation study through non-homogenous materials is greatly facilitated by MMs. The criteria that are usually employed in such investigations are based on the energy criterion of fracture mechanics. This method is computationally expensive for the study of the kinking of an interface crack. Even the criterion $K_{II} = 0$ belongs to the same category. The other criterion, which offers some advantages, is the MTS criterion. It can help in reducing the computational cost. However, this criterion is not sufficient on its own to study the kinking of an interface crack. How this criterion can be made sufficient is an issue open to investigation.

In the case of homogenous and heterogeneous materials, the first non-singular term or T-stress has significant influence on the direction of crack propagation. In order to evaluate the influence of the T-stress using EFG methods, it is first necessary to develop suitable methods for extraction of T-stress in the case of bi-materials, particulate composites, and functionally graded materials. In addition, it is necessary to evaluate the influence of this T-stress on the direction of crack propagation. The method of predicting the direction of crack propagation by considering that the crack-tip stress field is given by a combination of the singular and non-singular terms is the same as the prediction based on the MTPS criterion or the zero shear stress criterions.

LSMs greatly reduce the effort in tracking the extension of a crack. Whether LSM can be combined with crack modelling techniques in the realm of the EFG method and adopted to model multiple interacting cracks needs fresh investigations. Keeping all these in view, the present investigations have been carried out with the objectives given in section 1.2.

Chapter 3   Element-free Galerkin Method

3.1   Introduction

In this chapter, the details of the element-free Galerkin (EFG) method are described. The properties of the shape functions, which are obtained using the moving least-squares technique, are discussed. Although the EFG method is called a meshfree method, it is not truly devoid of a mesh. A background mesh is needed for integration. Some aspects of integration are discussed in this chapter. A preliminary case study that shows the effect of the number of Gauss points, the nodal density, and the domain of influence on the accuracy of the solution is presented.

In the later part of this chapter, different methods of modelling cracks by using the EFG method are presented. The issues related to the use of the XEFG method to model fracture in a non-homogenous material are discussed. Finally, the formulation of the interaction integral to extract the SIFs is described.

3.2   Parameters of the EFG Method

The key parameters that affect the solution in the EFG method are the domain of influence, nodal density and order of Gauss integration. The study of these parameters is crucial to understanding and controlling the approximating errors.

3.2.1   Doman of influence and its size

Fleming (1997) defined domain of influence as a region on which a node exerts influence. Fig. 3.1(a) shows three nodes with circular domains of influence of support sizes d_1, d_2 and d_I. d_I is size of the domain of influence/support of node I. This is also known as the dilatation parameter. It is analogous to the element size in the FEM. The bigger the domain of influence, the bigger will be the bandwidth of the global stiffness matrix. In general, d_I is kept neither large nor too small; it is related to the average nodal spacing (δ) by $d_I = \tilde{\alpha}\delta$. A larger value of d_I will increase the bandwidth and artificially smoothen out the solution. This is not preferable, especially, in the region that contains a crack tip. On the other hand, a smaller d_I leads to ill conditioning of the stiffness matrix. Fig. 3.1(b) shows

different shapes of the domain of influence. In a particular problem, it can be of any shape and size. Circular domains of influence have been widely employed (Fig. 3.2).
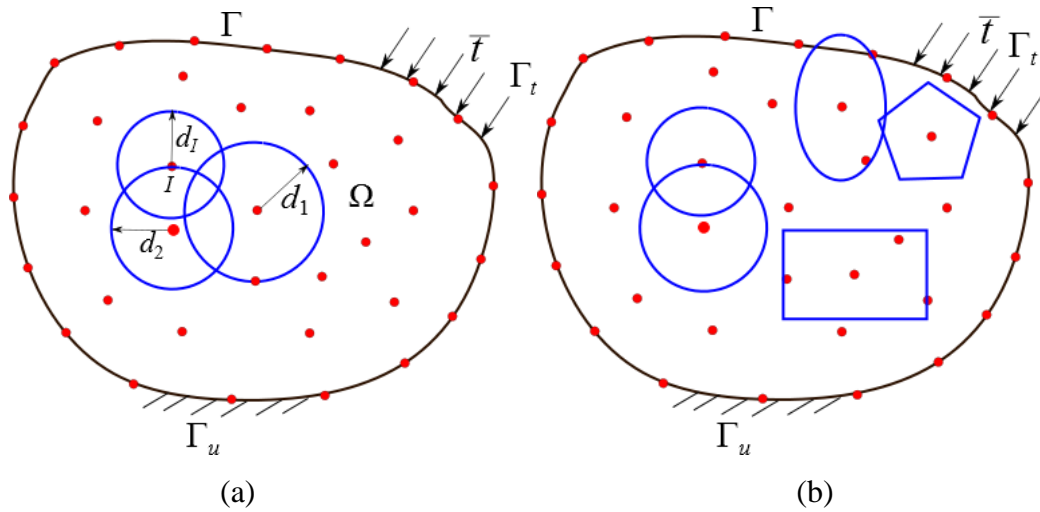
Fig. 3.1 (a) Domain of influence. **(b)** Shape of the domain of influence.

The size of the domain of influence is usually constant or varied in a domain. For example, the nodal domain of influence is relatively small when a node is close to a crack tip or lies in a region where the gradient in the field variable (for example, displacement) is very high. This is done to capture the displacement variation accurately. In the case of a regular nodal discretization with no refinement for modelling a crack, $\tilde{\alpha}$ has been chosen ranging from 1.75 to 2.5 (Fig. 3.2) (Organ et al., 1996; Muravin & Turkel, 2006; Muthu et al., 2013; Tuan & Fei, 2014).
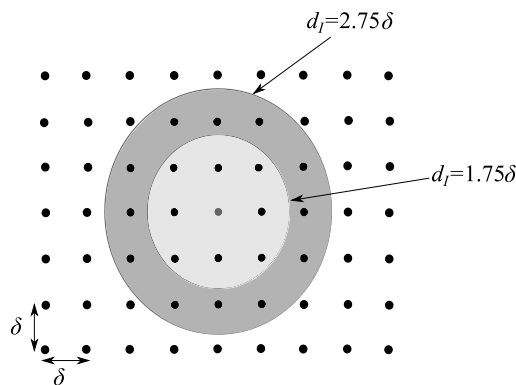
Fig. 3.2 d_I for a node in the case of a regular nodal discretization.

3.2.2 Weight function

Weight/window or the kernel functions are necessary to obtain the shape functions. They provide a local behavior to the solution. Weight functions have compact support associated with it. They are continuous and positive in their support. Weight functions tend to

- 40 -

be used with a support domain associated with a point of interest whereas a domain of influence is associated with a node. Functional forms of the weight function that are commonly used for interpolation are

Cubic Spline

$$w(s) = \begin{cases} 2/3 - 4s^2 + 4s^3 & s \leq 1/2 \\ 4/3 - 4s + 4s^2 - 4s^3/3 & 1/2 < s \leq 1 \\ 0 & s > 1 \end{cases} \tag{3.1}$$

Quartic spline

$$w(s) = \begin{cases} 1 - 6s^2 + 8s^3 - 3s^4 & s \leq 1 \\ 0 & s > 1 \end{cases} \tag{3.2}$$

Conical formula

$$w(s) = \begin{cases} 1 - s^2 & s \leq 1 \\ 0 & s > 1 \end{cases} \tag{3.3}$$

Exponential function

$$w(s) = \begin{cases} e^{-(s/\hbar)^2} & s \leq 1 \\ 0 & s > 1 \end{cases} \tag{3.4}$$

Negative exponential function

$$w(s) = \begin{cases} \dfrac{e^{-(\hbar s)^2} - e^{-\hbar^2}}{(1 - e^{-\hbar^2})} & s \leq 1 \\ 0 & s > 1 \end{cases} \tag{3.5}$$

where $s = r_I / d_I$ and d_I are the domain of influence. The parameter $\hbar$ affects the shape of the exponential functions.

In the case of 2D problems, circular and rectangular shapes for generally used as weight functions. In this work, the circular shape of d_I is used. The distance r_I of a sampling/Gauss point at location $\mathbf{x}$ from a node at location $\mathbf{x}_I$ is given by

$$r_I = \|\mathbf{x} - \mathbf{x}_I\| \tag{3.6}$$

3.2.3 Nodal Density and Gaussian integration

Increasing the nodal density increases the order of the approximating nodal shape functions (Xiaoying et al., 2012). Unlike the FEM, the EFG method gives both h-adaptivity and p-adaptivity as the nodal density is increased. Therefore, it is difficult to control the error in the EFG method. In addition, the shape functions are rational functions; they behave more like non-polynomial functions in the case of non-uniformly distributed nodes. In order to demonstrate this effect, a set of six nodes in $x \in (0,1)$ was considered by Dolbow et al. (1999), as shown in Fig. 3.3.
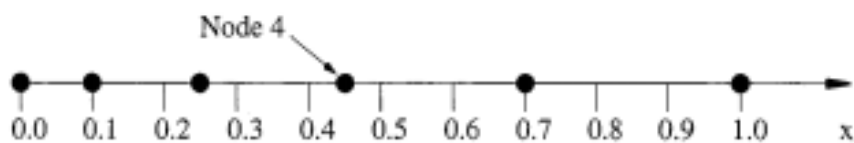
Fig. 3.3 1D non-uniform grid (Dolbow & Belytschko, 1999).

Fig. 3.4 shows the shape function, its first derivative, and the square of the derivative at the 4th node. The square of the derivative is considered for the plot because it appears in the computation of the stiffness matrix. It can be observed that the derivative and the square of the derivative are complex functions and therefore, demands a high order of Gauss integration for an accurate evaluation of the stiffness matrix.
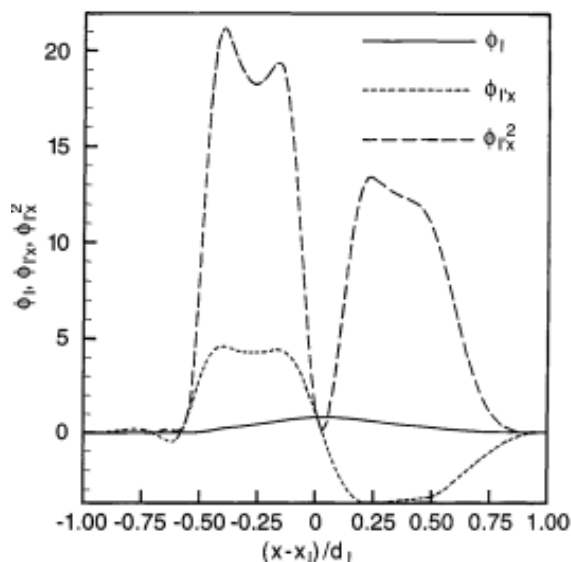
Fig. 3.4 Shape function, derivative, and square of the derivative for node 4 (Dolbow & Belytschko, 1999).

In order to understand the effect of Gaussian integration on the accuracy, a rational function that behaves as a regular type of EFG shape function, was considered by Dolbow et al. (1999). It is of the form given by

$$f(\Omega) = \begin{cases} 0 & -1 \le \Omega < 0 \\ \dfrac{3\Omega^2 + 2\Omega}{\Omega^3 + \Omega^2 + 1} & 0 \le \Omega < 1 \end{cases} \qquad (3.7)$$

In order to integrate the function in Eq.(3.7) accurately, two cases were considered. In the first case, an integration cell that covers the entire span was used. In the second case, the span was subdivided into two sub-intervals $[-1,0] \cup [0,1]$. Table 3.1 shows that the accuracy is high if the number of subdivided background cells is higher. It can be further improved by increasing the order of Gauss integration.

Table 3.1 Comparison of Gauss quadrature accuracy (Dolbow & Belytschko, 1999).

Gauss Order	% error (1 cell)	% error (2 cells)
2	28.5	-1.8
3	-17.9	1.3×10^{-1}
4	5.3	-6.5×10^{-3}
5	-5.4	4.5×10^{-5}
6	1.9	3.4×10^{-5}
7	-2.7	-4.8×10^{-6}

(a)   (b)
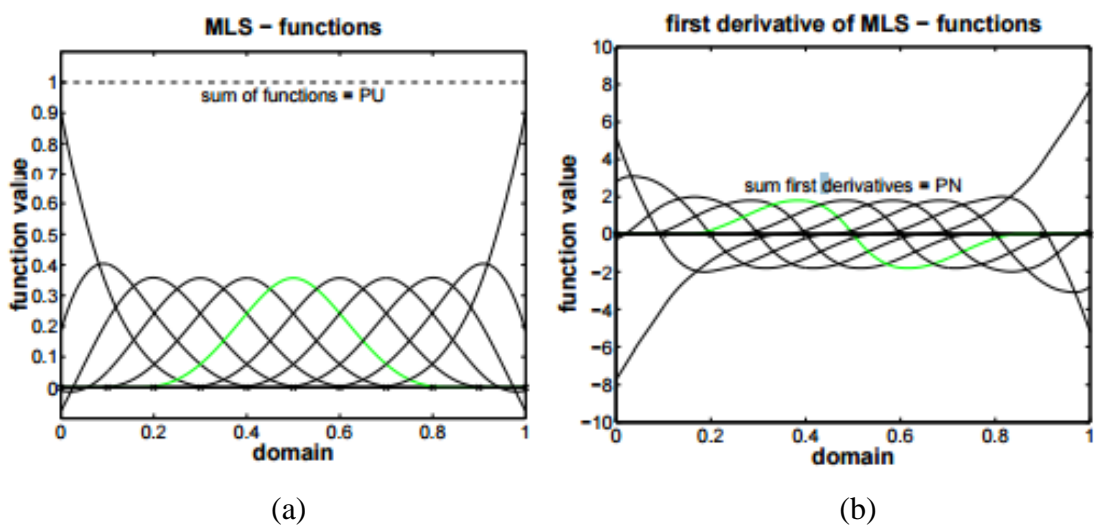
Fig. 3.5 (a) Shape function. **(b)** Its derivative (Fries & Matthies, 2004).

Fig. 3.5(a) shows the variation of the shape function, and Fig. 3.5(b) shows the derivative of the shape functions for a 1D domain with 11 equally spaced nodes. Although the nodes can be arranged randomly inside the geometry, the computational efforts involved in integrating the derivatives of shape functions in regular nodal distribution are less than that of non-uniform distribution. Therefore, a regular nodal distribution that results in smooth variation of shape functions and its derivatives is preferred over irregular nodal distribution.

3.3   Shape Function

The shape functions of the EFG method are obtained by the moving least-squares (MLS) interpolation technique (Lancaster & Salkauskas, 1981). The term "moving" in MLS refers to the varying coefficients with spatial coordinates. There are many variants of least squares for interpolation of data (Onate et al., 1996): the standard least-square method, the fixed least-square method, and the multiple fixed least-squares method. These techniques are based upon minimization of the residual, which is a weighted square of the error at any point. The residual is given by

$$\mathbf{J} = \sum_{I=1}^{N} w\left(u^h(\mathbf{x}_I) - u(\mathbf{x}_I)\right)^2 \tag{3.8}$$

where $u(\mathbf{x}_i)$ is the actual value at node I and $u^h(\mathbf{x}_I)$ is the approximated value. N is the total number of nodes that influence the node $\mathbf{x}_I$. w is the weight function.

Let us consider 1D formulation of the EFG method, which can be generalized to higher dimensions. The approximated field variable $u^h(x)$ at any generic point x can be represented by

$$u^h(x, x_I) = \mathbf{P}^{\mathrm{T}}(x_I)\boldsymbol{a}(x) \tag{3.9}$$

Where $\boldsymbol{a}(x)$ is the coefficient vector given by $\boldsymbol{a}^T(x) = \begin{bmatrix} a_0(x) & a_1(x) & a_2(x) & ... & a_m(x) \end{bmatrix}$ and $\mathbf{P}(x)$ is a standard complete polynomial of order m . It is given by

$$\mathbf{P}^{\mathrm{T}}(x) = \begin{bmatrix} P_0(x) & P_1(x) & P_2(x) & ... & P_m(x) \end{bmatrix} = \begin{bmatrix} 1 & x & x^2 & ... & x^m \end{bmatrix} \tag{3.10}$$

$\mathbf{P}(x)$ and $\boldsymbol{a}(x)$ when substituted in Eq. (3.8), gives rise to

$$\mathbf{J}(\boldsymbol{a}(x)) = \sum_{i=1}^{N} w(x - x_I) \left[\begin{bmatrix} 1 & x_I & x_I^2 & \dots & x_I^m \end{bmatrix} \begin{bmatrix} a_0(x) \\ a_1(x) \\ a_2(x) \\ \vdots \\ a_m(x) \end{bmatrix} - u_I \right]^2 \quad (3.11)$$

In order to find the unknown coefficients, the residual $\mathbf{J}$ is minimized with respect to each unknown coefficient of vector $\boldsymbol{a}(x)$

$$\frac{\partial \mathbf{J}(\mathbf{a}(x))}{\partial a_i} = 0; \ i = 0 : m \quad (3.12)$$

This results in

$$\frac{\partial \mathbf{J}(\mathbf{a}(x))}{\partial a_0} = 0; \ \sum_{I=1}^{N} w(x - x_I) 2 P_0(x_I) \left[\mathbf{P}^T(x_I) \boldsymbol{a}(x) - u_I \right] = 0$$

$$\frac{\partial \mathbf{J}(\mathbf{a}(x))}{\partial a_1} = 0; \ \sum_{I=1}^{N} w(x - x_I) 2 P_1(x_I) \left[\mathbf{P}^T(x_I) \boldsymbol{a}(x) - u_I \right] = 0 \quad (3.13)$$

$$\vdots$$

$$\frac{\partial \mathbf{J}(\mathbf{a}(x))}{\partial a_m} = 0; \ \sum_{I=1}^{N} w(x - x_I) 2 P_m(x_I) \left[\mathbf{P}^T(x_I) \boldsymbol{a}(x) - u_I \right] = 0$$

Eq. (3.13) can be rearranged to yield

$$\sum_{I=1}^{N} w(x - x_I) \mathbf{P}(x_I) \mathbf{P}^T(x_I) \boldsymbol{a}(x) = \sum_{I=1}^{N} w(x - x_I) \mathbf{P}(x_I) u_I \quad (3.14)$$

$$\mathbf{A}(x)\boldsymbol{a}(x) = \mathbf{B}(x)\mathbf{u}$$

where

$$\mathbf{A}(x) = \sum_{I=1}^{N} w(x - x_I) \mathbf{P}(x_I) \mathbf{P}^T(x_I)$$

$$\mathbf{B}(x) = \begin{bmatrix} w(x - x_1) \mathbf{P}(x_1) & w(x - x_2) \mathbf{P}(x_2) & \cdots & w(x - x_N) \mathbf{P}(x_N) \end{bmatrix}$$

For example, in a 1D system with a linear basis- $\mathbf{P}^T(x) = \begin{bmatrix} 1 & x \end{bmatrix}$, $\mathbf{A}(x)$ and $\mathbf{B}(x)$ will be

$$\mathbf{A}(x) = w(x-x_1)\begin{bmatrix} 1 & x_1 \\ x_1 & x_1^2 \end{bmatrix} + w(x-x_2)\begin{bmatrix} 1 & x_2 \\ x_2 & x_2^2 \end{bmatrix} + \ldots + w(x-x_N)\begin{bmatrix} 1 & x_N \\ x_N & x_N^2 \end{bmatrix} \quad (3.15)$$

$$\mathbf{B}(x) = \begin{bmatrix} w(x-x_1)\begin{Bmatrix} 1 \\ x_1 \end{Bmatrix} & w(x-x_2)\begin{Bmatrix} 1 \\ x_2 \end{Bmatrix} & \cdots & w(x-x_N)\begin{Bmatrix} 1 \\ x_N \end{Bmatrix} \end{bmatrix} \quad (3.16)$$

Replacing the term $a(x)$ in Eq. (3.9) with the solution of $a(x)$ from Eq. (3.14), $u^h(x)$ can be written as

$$u^h(x) = \mathbf{\Phi}^T(x)\mathbf{u} = \sum_{I=1}^{N} \Phi_I(x)u_I \quad (3.17)$$

where $\mathbf{\Phi}^T(x) = \mathbf{P}^T(x)\left[\mathbf{A}(x)\right]^{-1}\mathbf{B}(x)$. $\Phi_I(x)$ is the MLS shape function associated with node I.

An important term during the derivation of the MLS shape function is the moment matrix $\mathbf{A}(x)$. Its size is $m \times m$. The size of the polynomial basis vector $\mathbf{P}^T(x)$ is m. This matrix should be inverted whenever the MLS shape function $\Phi_I(x)$ is to be calculated at any point x. For example, if the polynomial basis is quadratic $\mathbf{P}^T(x) = \begin{bmatrix} 1 & x & x^2 \end{bmatrix}$, that is, $m = 3$, then the moment matrix is given by

$$\mathbf{A}(x) = w(x-x_1)\begin{bmatrix} 1 & x_1 & x_1^2 \\ x_1 & x_1^2 & x_1^3 \\ x_1^2 & x_1^3 & x_1^4 \end{bmatrix} + w(x-x_2)\begin{bmatrix} 1 & x_2 & x_2^2 \\ x_2 & x_2^2 & x_2^3 \\ x_2^2 & x_2^3 & x_2^4 \end{bmatrix} + \ldots +$$
$$w(x-x_N)\begin{bmatrix} 1 & x_N & x_N^2 \\ x_N & x_N^2 & x_N^3 \\ x_N^2 & x_N^3 & x_N^4 \end{bmatrix} \quad (3.18)$$

Since the derivation of the shape function and its derivative involves the inversion of the moment matrix $\mathbf{A}(x)$ at each Gauss point during the computation of the global stiffness matrix, the computational cost of the EFG method becomes enormous. Secondly, the domain of influence d_I has to be increased depending upon the size of the polynomial $\mathbf{P}^T(x)$ vector.

This is done to avoid the occurrence of a singular moment matrix. For example, if $m = 2$, then the number of nodes (N) within a domain of influence must be at least equal to $m (N \geq 2)$. When N increases, the bandwidth of the stiffness matrix also increases. Consequently, the computational costs increase drastically with the increase in the polynomial basis. Therefore, in this work, a linear basis is chosen and efforts are made to increase the accuracy without any significant increase in the computational cost.

3.4 Properties of the Shape Function

The shape functions obtained through the MLS technique differ from the FEM shape functions in some aspects.

3.4.1 Approximants

Although shape functions are built upon the concept of partition-of-unity (PU), they do not interpolate like the shape functions of the FEM. They do not possess the Kronecker delta property. At every node, there are more than one shape function that have values other than zero. This feature makes imposition of essential boundary conditions (EBC) difficult and, hence, adds more computational cost.

3.4.2 Non-polynomial nature of the shape functions

Although the weight functions can be polynomial in nature, the resulting shape functions are non-polynomial (Askes et al., 2003). The derivatives are even more non-polynomial in nature. This becomes a problem in integrating the expressions of the weak form (Hegen, 1996). However, for a regular nodal discretization, the shape functions and its derivatives can be treated as polynomial-like functions (Section 3.2.3).

3.5 Imposition of Dirichlet Boundary Conditions

One of the difficulties associated with the EFG method is imposition of Dirichlet or EBCs due to the lack of Kronecker delta property for the shape functions. A number of techniques have been proposed to overcome this problem. It is to be noted that there would be loss in the convergence order for most of the imposition techniques (Han & Meng, 2002).

3.5.1 Boundary collocation

This is the simplest approach when it comes to imposing the EBC in the framework of MMs (Mukherjee & Mukherjee, 1997). However, using this technique, one cannot enforce

the EBC at points other than nodal locations (Atluri & Shen, 2002). If the displacement value u_{g_I} is to be imposed at node, *I*, at the location x_I, then an extra row and column will be added in the global stiffness matrix $[\mathrm{K}]$, given by

$$
\begin{bmatrix}
& & \cdots & & \\
\cdots & \Phi_{i-1}(x_I) & \Phi_i(x_I) & \Phi_i(x_I) & \cdots \\
& & \cdots & &
\end{bmatrix} \rightarrow \begin{Bmatrix} \cdots \\ u_{g_I} \\ \cdots \end{Bmatrix}
\tag{3.19}
$$

where $\Phi_i(x_I): i = 1, 2, ..., n$ are shape functions of the *n* nodes that influence the point x_I.

3.5.2 Lagrange multiplier

This concept of Lagrange multipliers (Belytschko et al., 1996) is derived from the equality constrained optimization problem. The EBC are the constraints. The minimization problem becomes a saddle point problem (Brezzi, 1974). A new set of interpolation functions, such as FE shape functions, are needed for the Lagrange multipliers.

The Lagrange multiplier technique introduces additional unknowns in the system. Because of this, the final matrix structure becomes $\begin{bmatrix} \mathrm{K} & \mathrm{G} \\ \mathrm{G}^{\mathrm{T}} & 0 \end{bmatrix}$, where K is the global stiffness matrix, and G is due to Lagrange multipliers. The final structure is no more positive definite (because of zeros on the main diagonal.). Therefore, equation solvers that take advantage of positive definiteness no longer be used (Belytschko et al., 1994; Lu et al., 1994).

3.5.3 Penalty approach

EBC can also be weakly imposed by a penalty formulation (Noguchi et al., 2000). The main advantage of the penalty method is that it does not introduce additional unknowns in the system. However, the choice of the penalty parameter α_p is important. A very high value of α_p may lead to ill conditioning of the resulting stiffness matrix.

3.5.4 Nitsche's method

Nitsche's method (Babuška et al., 2002; Fernández-Méndez & Huerta, 2004) is an improvement of the penalty method. In this method, a number of terms are added to the weak form, depending on the problem considered. The value of α_p can be small and, thus, ill conditioning of the resulting stiffness matrix is avoided. It is claimed that this method is superior to both, the Lagrange multiplier and the penalty method.

3.5.5 Finite element coupling

The sole aim of coupling the MMs and FEM is to avoid the difficulties in imposing the EBC. Since FE shape functions possess the Kronecker delta property, this coupling might seems effective. However, the challenge remains in modelling the interface as shown in Fig. 3.6, because the derivatives become discontinuous. Several approaches to overcome this issue exist (Rabczuk et al., 2000): the master-slave coupling approach (Johnson, 1994; Belytschko et al., 2000), compatibility coupling (Belytschko et al., 1995), the bridging domain coupling method (Belytschko & Xiao, 2004), coupling with Lagrange parameters (Hegen, 1996; Rabczuk & Belytschko, 2006), and hybrid approximation (Sauer, 2000). If a point lies inside a domain in which the EBC have to be imposed, such a coupling would be even more costly computationally.
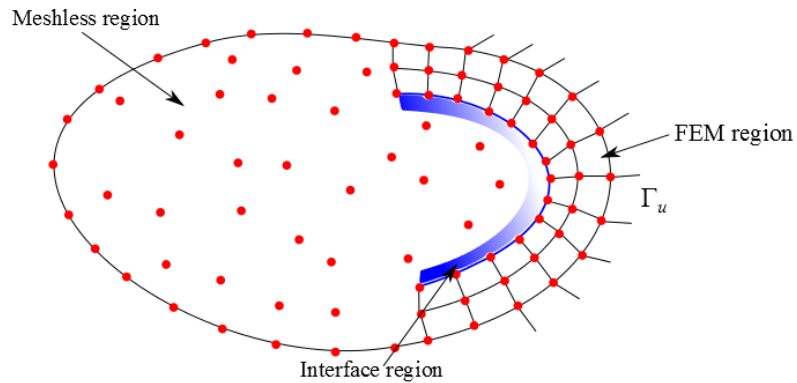
Fig. 3.6 Coupled meshless finite element method.

In addition to the approaches mentioned above, there are also other complex approaches (Fries & Matthies, 2004) such as the Transformation method (Chen et al., 1997; Chen & Wang, 2000), singular weighting functions (Kaljevic & Saigal, 1997) and D'Alembert's principle (Gunther & Liu, 1998) to overcome the problem associated with the imposition of EBCs.

3.6 System of Equations for Elastic Problems

In this work, only two-dimensional problems are considered and, therefore, the effect of mode III in the case of crack problems is neglected. Nevertheless, the formulations presented here can be easily extended to 3D problems. Consider a 2D geometry subjected to traction $\mathbf{t}_\Gamma$ and the EBC $\mathbf{u}_\Gamma$ as shown in Fig. 3.7. It shows the background mesh for integration and nodal distribution. There are four nodes that are in the support domain of the

point $\mathbf{x}$. The governing partial differential equation for 2D solid mechanics problem is given by

$$\mathbf{L}_{d}^{T}\boldsymbol{\sigma}+\mathbf{b}=0 \qquad (3.20)$$

where $\mathbf{b}=\{b_1 \quad b_2\}^{T}$ is the body force vector and $\boldsymbol{\sigma}=\{\sigma_{11} \quad \sigma_{22} \quad \sigma_{12}\}^{T}$ is the stress vector. The operator $\mathbf{L}_d$ is given by

$$\mathbf{L}_d = \begin{bmatrix} \dfrac{\partial}{\partial x_1} & 0 \\[2mm] 0 & \dfrac{\partial}{\partial x_2} \\[2mm] \dfrac{\partial}{\partial x_2} & \dfrac{\partial}{\partial x_1} \end{bmatrix}_{3\times 2} \qquad (3.21)$$
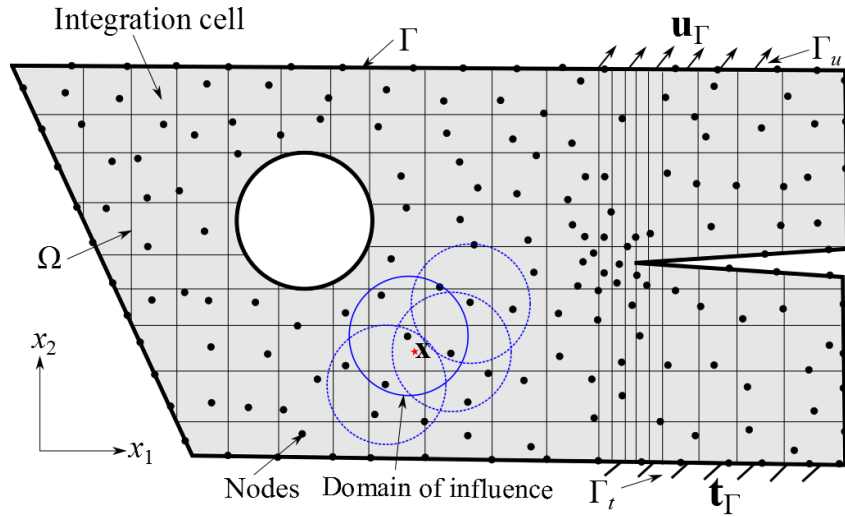
Fig. 3.7 EFG method discretization with background mesh for integration.

For this 2D problem, the Galerkin weak form in the presence of Lagrange multipliers (λ) for the constraints is given by

$$\int_{\Omega}\delta(\mathbf{L}_d\mathbf{u})^{T}\mathbb{C}(\mathbf{L}_d\mathbf{u})\,d\Omega-\int_{\Omega}\delta\mathbf{u}^{T}\mathbf{b}\,d\Omega-\int_{\Gamma_t}\delta\mathbf{u}^{T}\mathbf{t}_{\Gamma}\,d\Gamma-$$
$$\int_{\Gamma_u}\delta\lambda^{T}(\mathbf{u}-\mathbf{u}_{\Gamma})\,d\Gamma-\int_{\Gamma_u}\delta\mathbf{u}^{T}\lambda\,d\Gamma=0 \qquad (3.22)$$

The last two terms arise due to the adoption of Lagrange multipliers. It can be viewed as the force required to impose the condition $\mathbf{u}=\mathbf{u}_{\Gamma}$ on Γ_u .

For an isotropic material, the material property matrix $\mathbb{C}$ is given by

$$\mathbb{C} = \frac{E}{1-v^2}\begin{bmatrix} 1 & v & 0 \\ v & 1 & 0 \\ 0 & 0 & \dfrac{1-v}{2} \end{bmatrix} - \textit{for plane stress};$$

$$\mathbb{C} = \frac{E(1-v)}{(1+v)(1-2v)}\begin{bmatrix} 1 & \dfrac{v}{1-v} & 0 \\ \dfrac{v}{1-v} & 1 & 0 \\ 0 & 0 & \dfrac{1-2v}{2(1-v)} \end{bmatrix} - \textit{for plane strain}$$

(3.23)

where E is the Young's modulus and v is the Poissons' ratio.

The displacement approximation at any generic point x in terms of MLS shape functions is given by

$$\mathbf{u}^h(\mathbf{x}) = \begin{Bmatrix} u \\ v \end{Bmatrix}^h = \sum_{I \in S_n} \underbrace{\begin{bmatrix} \Phi_I & 0 \\ 0 & \Phi_I \end{bmatrix}}_{\mathbf{\Phi}_I} \underbrace{\begin{Bmatrix} u_I \\ v_I \end{Bmatrix}}_{\mathbf{u}_I} = \sum_{I \in S_n} \mathbf{\Phi}_I^H \mathbf{u}_I$$

(3.24)

where S_n is the set that contains the nodes in the support domain of point $\mathbf{x}$. It is to be noted that at node location $\mathbf{x}_I$, $\mathbf{u}^h(\mathbf{x}_I) \neq \mathbf{u}_I$. This is because the MLS shape functions lack the Kronecker delta property. $\mathbf{L}_\mathrm{d}\mathbf{u}$ can be further simplified using Eq. (3.24) as follows

$$\mathbf{L}_\mathrm{d}^\mathrm{T}\mathbf{u}^h = \mathbf{L}_\mathrm{d}\sum_{I \in S_n} \mathbf{\Phi}_I \mathbf{u}_I = \sum_{I \in S_n} \mathbf{L}_\mathrm{d}\mathbf{\Phi}_I \mathbf{u}_I = \sum_{I \in S_n} \begin{bmatrix} \dfrac{\partial}{\partial x_1} & 0 \\ 0 & \dfrac{\partial}{\partial x_2} \\ \dfrac{\partial}{\sigma x_2} & \dfrac{\partial}{\partial x_1} \end{bmatrix} \begin{bmatrix} \Phi_I & 0 \\ 0 & \Phi_I \end{bmatrix} \mathbf{u}_I$$

(3.25)

$$= \sum_{I \in S_n} \underbrace{\begin{bmatrix} \Phi_{I,x_1} & 0 \\ 0 & \Phi_{I,x_2} \\ \Phi_{I,x_2} & \Phi_{I,x_1} \end{bmatrix}}_{\mathbf{B}_I} \mathbf{u}_I = \sum_{I \in S_n} \mathbf{B}_I \mathbf{u}_I$$

In order to impose the boundary conditions, the Lagrange multiplier is expressed by

$$\lambda(\mathbf{x}) = \sum_{I \in S_\lambda} N_I(\mathbf{x})\lambda_I \quad \mathbf{x} \in \Gamma_u \tag{3.26}$$

where S_λ is the set containing the nodes whose shape functions are used to interpolate at the location $\mathbf{x}$ (Fig. 3.8). $N_I(\mathbf{x})$ in Eq. (3.26) in one dimensional FEM shape functions or Lagrange interpolation functions
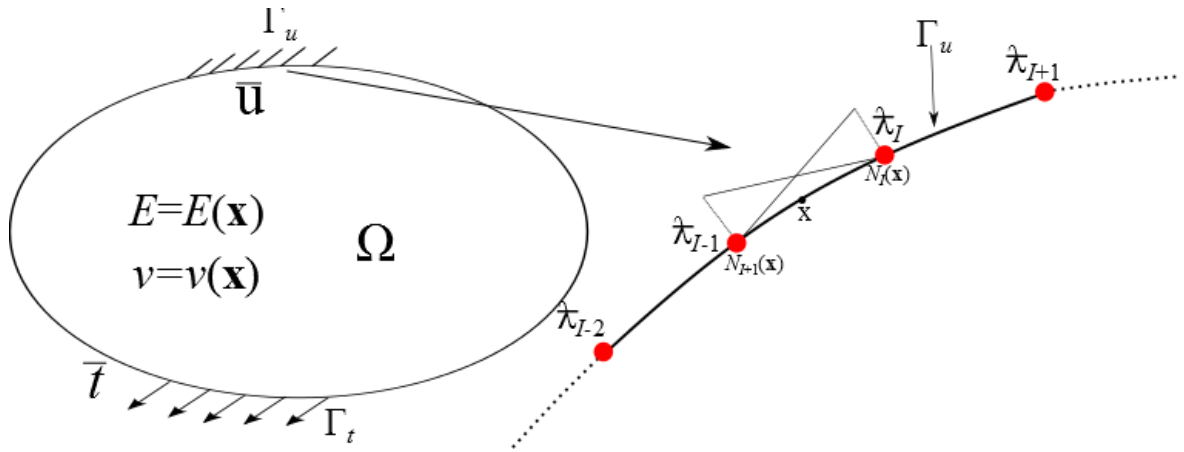
Fig. 3.8 Boundary on which the EBCs are imposed.

. Substituting Eqs. (3.24), (3.25) and (3.26) in Eq. (3.22), the following equation is obtained.

$$\underbrace{\int_\Omega \delta\left(\sum_{I \in S_n} \mathbf{B}_I \mathbf{u}_I\right)^T \mathbb{C}\left(\sum_{J \in S_n} \mathbf{B}_J \mathbf{u}_J\right) d\Omega}_{\delta\mathbf{U}^T\mathbf{K}\mathbf{U}} - \underbrace{\int_\Omega \delta\left(\sum_{I \in S_n} \mathbf{\Phi}_I \mathbf{u}_I\right)^T \mathbf{b}\, d\Omega - \int_{\Gamma_t} \delta\left(\sum_{I \in S_n} \mathbf{\Phi}_I \mathbf{u}_I\right)^T t_\Gamma\, d\Gamma}_{\delta\mathbf{U}^T\mathbf{F}} - $$

$$\underbrace{\int_{\Gamma_u} \delta\lambda^T \left(\left(\sum_{I \in S_n} \mathbf{\Phi}_I \mathbf{u}_I\right) - \mathbf{u}_\Gamma\right)^T d\Gamma}_{\delta\lambda^T[\mathbf{G}^T\mathbf{U}-\mathbf{q}]} - \underbrace{\int_{\Gamma_u} \delta\left(\sum_{I \in S_n} \mathbf{\Phi}_I \mathbf{u}_I\right)^T \lambda\, d\Gamma}_{\delta\mathbf{U}^T\mathbf{G}\lambda} = 0 \tag{3.27}$$

Eq. (3.27) can be alternatively represented as

$$\delta\mathbf{U}^T[\mathbf{K}\mathbf{U} + \mathbf{G}\lambda - \mathbf{F}] + \delta\lambda^T[\mathbf{G}^T\mathbf{U} - \mathbf{q}] = 0 \tag{3.28}$$

Since $\delta\mathbf{U}$ and $\delta\lambda$ are arbitrary, Eq. (3.28) gives

$$\begin{bmatrix} \mathbf{K} & \mathbf{G} \\ \mathbf{G}^T & 0 \end{bmatrix} \begin{Bmatrix} \mathbf{U} \\ \lambda \end{Bmatrix} = \begin{Bmatrix} \mathbf{F} \\ \mathbf{q} \end{Bmatrix} \tag{3.29}$$

where

$$\mathbf{K}_{IJ} = \int_{\Omega} \mathbf{B}_I^{\mathrm{T}} \mathbb{C} \mathbf{B}_J \, d\Omega$$

$$\mathbf{B}_I = \mathbf{L}\mathbf{\Phi}_I = \begin{bmatrix} \Phi_{I,x_1} & 0 \\ 0 & \Phi_{I,x_2} \\ \Phi_{I,x_2} & \Phi_{I,x_1} \end{bmatrix}$$

$$\mathbf{G}_{IJ} = -\int_{\Gamma_u} \mathbf{N}_I^T \mathbf{\Phi}_J \, d\Gamma \qquad (3.30)$$

$$\mathbf{\Phi}_I = \begin{bmatrix} \Phi_I & 0 \\ 0 & \Phi_I \end{bmatrix}$$

$$\mathbf{N}_I = \begin{bmatrix} N_I & 0 \\ 0 & N_I \end{bmatrix}$$

It is clear from Eq. (3.29) that the stiffness matrix in the EFG method will be much larger than the FEM stiffness matrix, for the same nodal degrees of freedom, because of the presence of the $\mathbf{G}$ matrix. The efficiency of the solution depends significantly on the number of nodes on which the EBCs are imposed.

3.7 Numerical Study: Rectangular Cantilever

A numerical study is conducted considering a cantilever subjected to external load P (Fig. 3.9). This is done to understand the effect of Gaussian integration, nodal density and domain of influence on the accuracy of the solution. The specific data considered are the length of the cantilever, $L = 48$ m, the height of the cantilever, $D = 12$ m, Poisson's ratio, $v = 0.3$, Young's modulus, $E = 3 \times 10^7 \, N/m^2$, and load, $P = \dfrac{-1000}{2I}\left[\dfrac{D^2}{4} - y^2\right]$; the thickness of the cross section is unity.
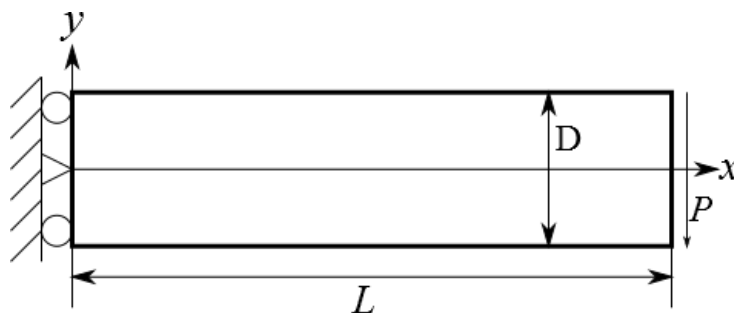
Fig. 3.9 Rectangular cantilever subjected to external load P.

The exact solutions are available in the work by Timoshenko and Goodier (1970). The displacement in the x direction

$$u_x = \frac{-Py}{6EI}\left[(6L-3x)+(2+v)\left[y^2-\frac{D^2}{4}\right]\right]$$ (3.31)

where $I = D^3/12$ is the area moment of the inertia of the rectangular cross section beam. The displacement in the y direction

$$u_y = \frac{P}{6EI}\left[3vy^2(L-x)+(4+5v)\frac{D^2x}{4}+(3L-x)x^2\right]$$ (3.32)

The stress at any generic point on the cantilever is given by

$$\begin{Bmatrix}\sigma_{xx}\\\sigma_{yy}\\\tau_{xy}\end{Bmatrix} = \begin{Bmatrix}-\dfrac{P(L-x)y}{I}\\0\\\dfrac{P}{2I}\left(\dfrac{D^2}{4}-y^2\right)\end{Bmatrix}$$ (3.33)

Initially, a coarser discretization of 11×5 nodes (Fig. 3.10(a)) with a background mesh (Fig. 3.10(b)) is used to solve the problem. The domain of influence d_I is set to three times the nodal spacing ($\bar{\alpha}=3$).
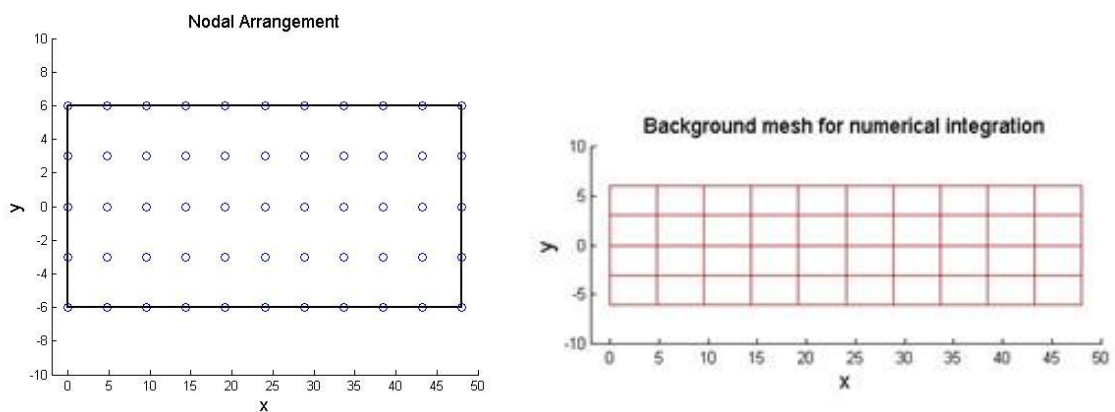
Fig. 3.10 (a) Nodal discretization. (b) Background mesh.

The deformed shape obtained using the 4×4 Gauss point quadrature is shown in Fig. 3.11. The normal and shear stresses obtained are compared with the theoretical stress values

(Fig. 3.12). Although there is a good match between the computed and the theoretical normal stress, there is a mismatch between the computed and theoretical shear stress. The mismatch does not reduce with an increasing order of Gauss integration.
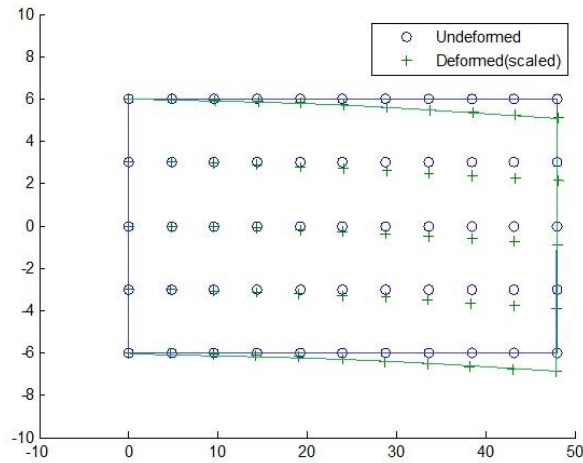
Fig. 3.11 Deformed geometry with a structured nodal discretization.
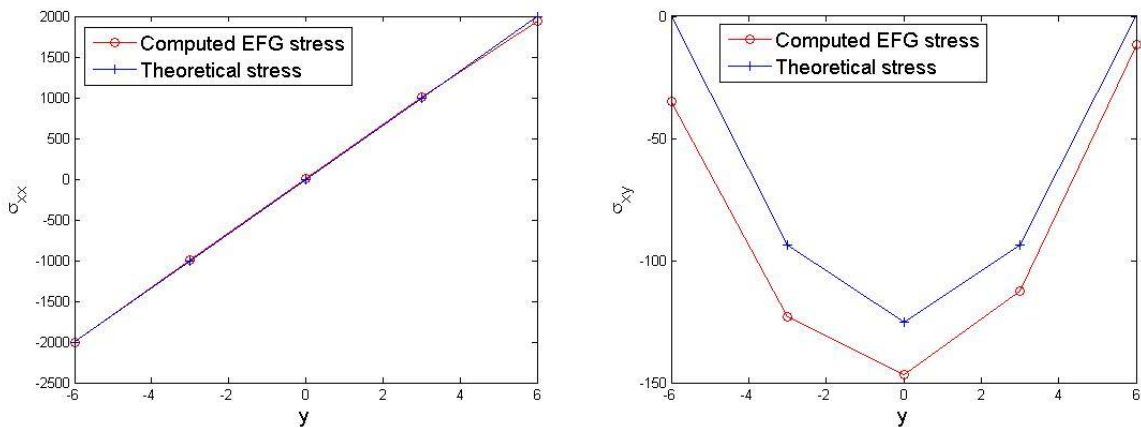
Fig. 3.12 Position $x = L/2$ **(a)** Normal stress; **(b)** Shear stress.

Next, the nodal discretization is increased to 31×11, as shown in Fig. 3.13(a). The background mesh for integration coincides with the nodes. A Gauss quadrature of order 4×4 is used to obtain the results. The computed shear stress plot (Fig. 3.13(b)) at $x = L/2$ shows a better agreement with the theoretical results. In order to quantify the results, the strain energy error $\left(S_{error} \right)$ is measured. It is given by

$$S_{error} = \left\{ \frac{1}{2} \int_{\Omega} \left(\varepsilon^{EFG} - \varepsilon^{theory} \right)^T \mathbb{C} \left(\varepsilon^{EFG} - \varepsilon^{theory} \right) d\Omega \right\}^{1/2} \tag{3.34}$$

where $\mathbb{C}$ is the plane stress material property matrix. ε^{EFG} and ε^{theory} are the computed and theoretical strain matrices, respectively.
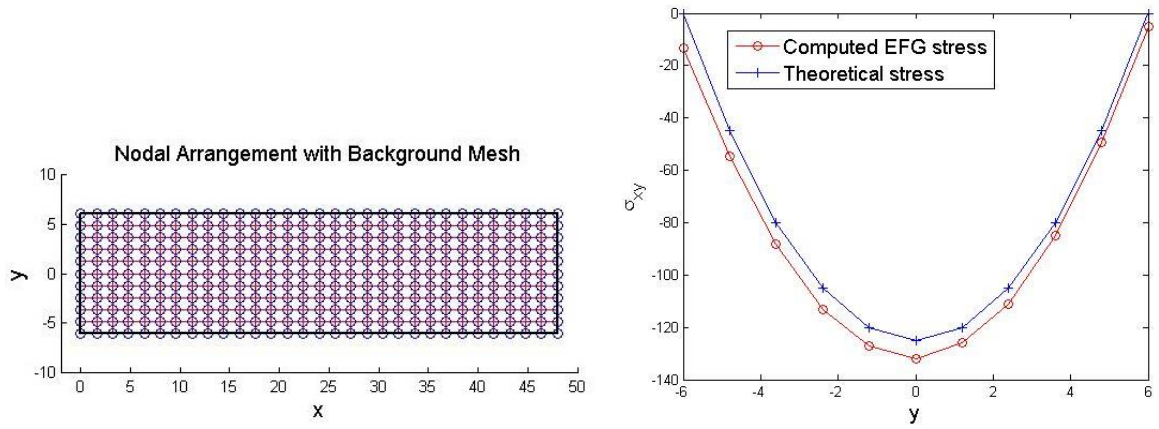
Fig. 3.13 (a) Nodal arrangement with background mesh. **(b)** Shear stress at $x = L/2$.

The effect of an unstructured nodal discretization has also been studied. While the structured nodal discretization has regular nodal spacing, the present unstructured nodal discretization does not have a truly random nodal spacing. The unstructured nodal discretization have been generated by the Delaunay triangulation of the domain Ω (Fig. 3.14). Inter-nodal distance in the structured mesh and average nodal spacing in the unstructured mesh are comparable parameters for this study.
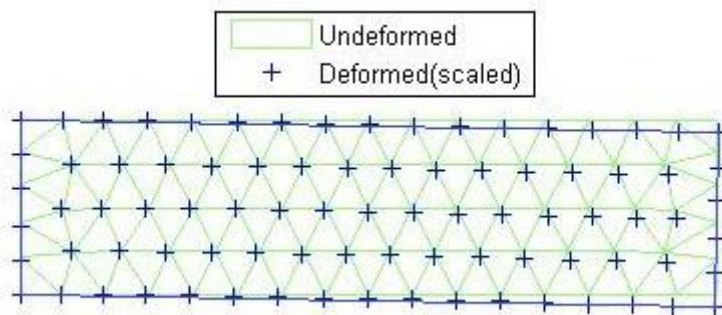
Fig. 3.14 Deformed geometry with an unstructured nodal discretization.

Table 3.2 shows a comparison of the errors in strain energy with different Gauss quadratures. 31×11 nodes have been used in the structured mesh. The $\bar{\alpha}$ (scaling factor) is set to three. The average nodal spacing in the unstructured mesh is 1m. The average nodal spacing of the unstructured mesh is kept slightly lesser than that of the structured mesh nodal spacing. The same regular background mesh is used for the structured and unstructured

meshes. As the order of Gauss quadrature increases, the S_{error} in both the structured and unstructured nodal discretization decreases. However, the error in the case of structured mesh is lesser than the unstructured mesh.

Table 3.2 Strain energy error with Gauss quadrature.

Gauss Point Quadrature	S_{error}	
	Structured	Unstructured
1×1	0.1103	7.11E+27
2×2	1.04E-04	1.07E+06
4×4	8.95E-05	0.1028
10×10	8.94E-05	0.0310

Table 3.3 shows the variation of error in the strain energy with size of the domain of influence. 31×11 nodes have been used in the structured mesh. The average nodal spacing of the unstructured mesh is 1m. A Gauss quadrature of 4×4 is used in the background mesh for integration of the weak form. The error in strain energy S_{error} decreases with the increase in the size of the domain of influence ($\bar{\alpha}$) for the structured discretization. However, the behavior oscillates in the case of the unstructured arrangement of nodes.

Table 3.3 Strain energy error with domain of influence ($d_I = \bar{\alpha}\delta$).

Scaling factor ($\bar{\alpha}$)	S_{error}	
	Structured	Unstructured
1.5	0.0122	5.74E-04
2	0.0012	1.17E-04
3	8.95E-05	0.1028
5	4.40E-05	0.1198

The maximum domain of influence ($\bar{\alpha}$) cannot be arbitrarily increased. A very high $\bar{\alpha}$ leads to a larger bandwidth of the global stiffness matrix. In problems that involve a crack, a large $\bar{\alpha}$ leads to a spread of the error in the region around the crack tip. This is not desirable in the computation of SIFs. There are many criteria for the selection of $\bar{\alpha}$. Most of them are based on ensuring an invertible moment matrix (Liu, 2010; Guiamatsia et al., 2009).

Table 3.4 shows the strain energy error with the increase in the nodal density. A background mesh that coincides with the nodes is used for integration in the structured and unstructured discretizations. A Gauss quadrature of the order 4×4 is used in the integration cells. The $\bar{\alpha}$ (scaling factor) is set as 3m. This is done to show the poor results of the unstructured mesh despite the usage of relatively higher nodal spacing. As the nodal density increases, S_{error} decreases in the structured discretization. However, such convergence is not observed in the case of the unstructured discretization.

Table 3.4 Strain energy error with nodal density.

S_{error}			
Nodal density (Structured)	**Structured**	**Nodal density (Average nodal distance)**	**Unstructured**
11×5	0.0015	3	0.0785
21×11	1.61E-04	2	0.0034
31×11	8.95E-05	1	0.1028
51×26	2.17E-05	0.65	6.2435

Based on the observations above, it can be concluded that the pattern of S_{error} is relatively random for an unstructured discretization. This is mainly attributed to an increase in the non-polynomial nature of the MLS shape functions that arise out of unstructured nodal arrangement. In such case, a very high order of Gauss quadrature is needed for accurate integration. This makes the process computationally more cumbersome. Therefore, only structured discretization is used in the advanced studies in this thesis.

3.8 Modelling Cracks

There are two popular approaches to model strong discontinuities that arise out of the crack in the EFG method: (1) Modification of the weight function and (2) Enrichment using special functions through the PU approach.

3.8.1 Modification of the weight function

The first technique to account for strong discontinuities in the MMs is the visibility method. In this technique, a node is considered a point source of light and the crack is treated

as an opaque object. Fig. 3.15 shows the domain of weight functions of nodes in the presence of a crack according to the visibility method.
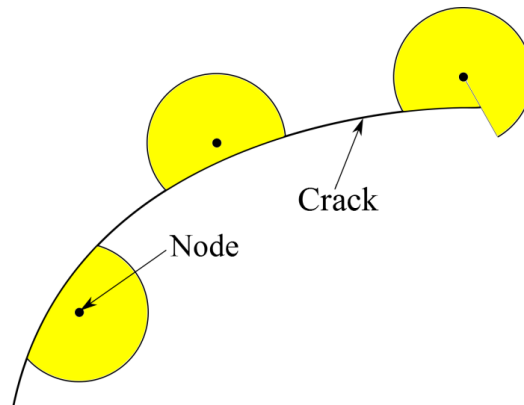
Fig. 3.15 Visibility method.

Any line from a node to a generic point is imagined to be line-of-sight (LOS). If a LOS is intercepted by a crack, then the nodal weight function has zero value at that point. This method has the following advantages: (1) It is a very simple technique and does not involve much computational cost; and (2) Modelling a 3D crack is also simpler.

The disadvantage of this technique is that there is an artificial lengthening of the crack (Nguyen et al., 2008). In addition, the computations near the crack tip are not smooth because a crack is modelled using discontinuous functions.

In order to overcome these shortcomings, the diffraction method has been proposed (Rabczuk, 2013). It stipulates continuous modelling of a crack (Fig. 3.16). This facilitates smooth computations. In this technique, the principle of diffraction of light from a point source provided the basis for the decision of what the domain of influence of a nodal weight function would be.
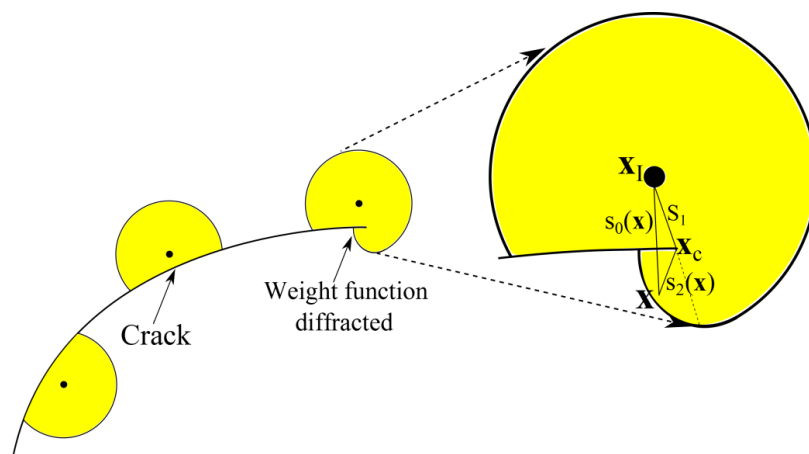
Fig. 3.16 Diffraction method.

The modified distance r_I of a generic point in the diffracted region is amplified by a factor, as given below.

$$r_I = \left(\frac{s_1 + s_2(\mathbf{x})}{s_0(\mathbf{x})} \right)^{\lambda} s_0(\mathbf{x}) \tag{3.35}$$

where $\mathbf{x}$ is the sampling point, $\mathbf{x}_I$ is the node and $\mathbf{x}_c$ is the crack tip. $s_0(\mathbf{x}) = \|\mathbf{x} - \mathbf{x}_I\|$, $s_1 = \|\mathbf{x}_I - \mathbf{x}_c\|$ and $s_2(\mathbf{x}) = \|\mathbf{x} - \mathbf{x}_c\|$. The parameter λ is either to 1 or 2. For the present study $\lambda = 2$ was employed throughout. The advantages of the diffraction method are (1) cracks are modelled with continuous functions, (2) there is no artificial lengthening of the crack.

In the diffraction approach, the stress singularity at the crack tip is not properly captured. The maximum stress shifts to a small distance behind the crack tip, which leads to an artificial shortening of the crack. In addition, modelling a 3D crack becomes a cumbersome process.

In order to extend the diffraction method to 3D cracks, the transparency method has been developed (Rabczuk, 2013). It is also based on the smooth modelling of the weight function around the crack tip (Fig. 3.17).
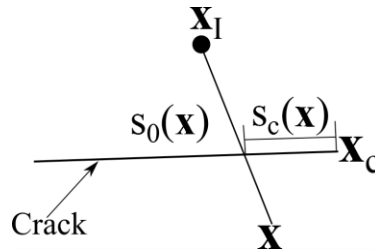
Fig. 3.17 The transparency method.

In this method, the modified distance r_I of a generic point from the source node is given by

$$r_I = s_0(\mathbf{x}) + d_I \left(\frac{s_c(\mathbf{x})}{\overline{s}_c} \right)^{\lambda} \tag{3.36}$$

where $s_0(\mathbf{x}) = \|\mathbf{x} - \mathbf{x}_I\|$ and $s_c(\mathbf{x})$ is the distance between the crack tip and the intersection point of LOS with the crack line. The parameter $\overline{s}_c$ sets the distance at which the crack

segment behaves completely like an opaque object. The crack tip behaves like a transparent point and the transparency diminishes as one moves away from the crack tip on the crack line.

The contours of the weight functions along with the surface plot of the shape function, for three methods, are shown in Fig. 3.18.
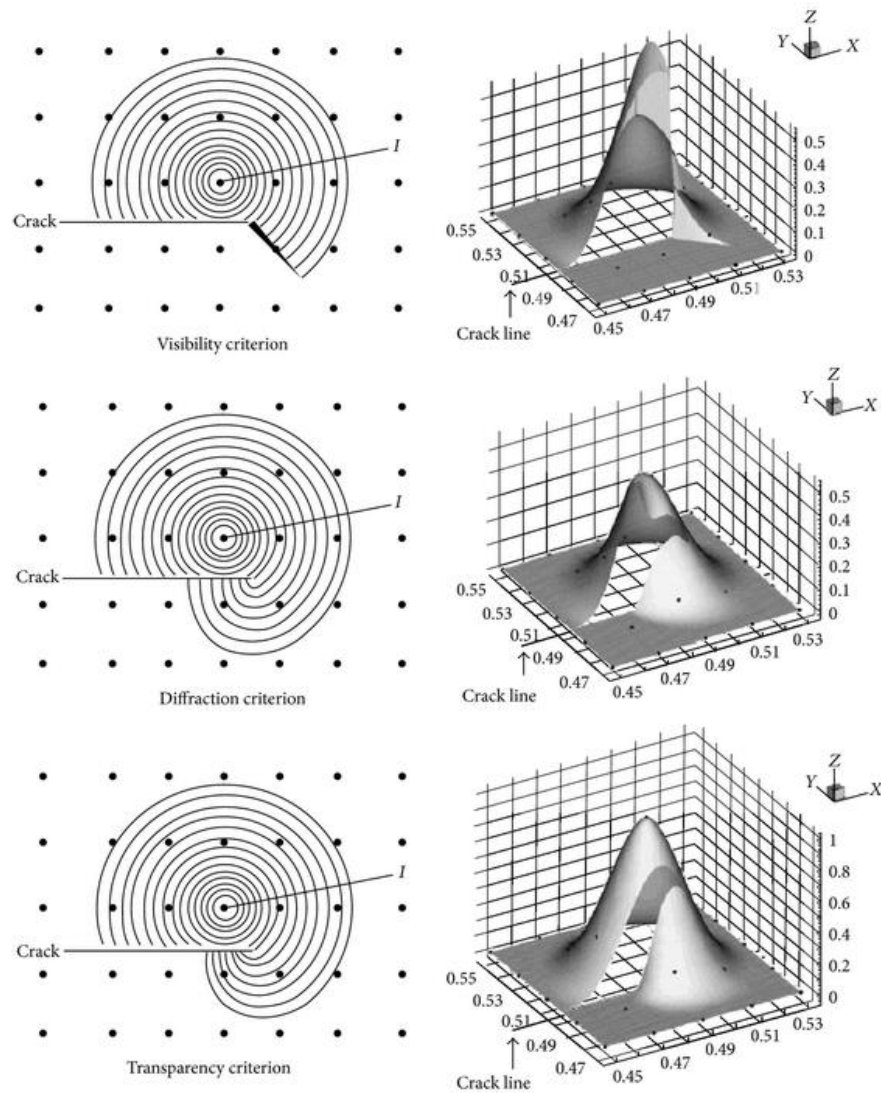
Fig. 3.18 Altered weight function of the visibility, diffraction, and transparency methods, with corresponding shape functions (Belytschko et al., 1996; Rabczuk, 2013).

There are also other methods such as the "see-through" method and the "continuous line" method. The "see-through" method proposed by Terry (1994) was used to model features such as interior holes and is not suitable for cracks. The "continuous line" (Duarte & Oden, 1996; Krysl & Belytschko, 1997) is also based on ensuring continuous shape

functions; however, it artificially shortens the crack significantly. Modifications were proposed to increase the accuracy of the solutions (Rabczuk, 2013).

3.8.2 Extrinsic PU enrichment (XEFG method)

In the eXtended element-free Galerkin (XEFG) method, the displacement approximation is done using a PU approach by enriching the MLS shape functions. The Heaviside function is used to describe the displacement discontinuity, and Williams' expansion is used to reproduce asymptotic displacement variation in the region around the crack tip.

$$\mathbf{u}(\mathbf{x}) = \sum_{I \in w(\mathbf{x})} \Phi_I(\mathbf{x})\mathbf{u}_I + \sum_{I \in w_j(\mathbf{x})} \Phi_I(\mathbf{x})\{\mathbf{a}_I H(f(\mathbf{x}))\} + \sum_{I \in w_b(\mathbf{x})} \Phi_I(\mathbf{x})\sum_{k=1}^{4} \mathbf{b}_{Ik}\xi_k^{\mathrm{enr}}(r,\theta) \quad (3.37)$$

where $f(\mathbf{x})$ is the signed distance function from the crack line.

The Heaviside or jump-enriched function $H(f(\mathbf{x}))$ and branch-enriched function $\xi^{\mathrm{enr}}(r,\theta)$ are given by

$$H(f(\mathbf{x})) = \begin{array}{ll} 1 & \text{if} \quad f(\mathbf{x}) \geq 0 \\ -1 & \text{if} \quad f(\mathbf{x}) < 0 \end{array}$$
$$\xi^{\mathrm{enr}}(r,\theta) = [\sqrt{r}\sin\frac{\theta}{2}, \sqrt{r}\cos\frac{\theta}{2}, \sqrt{r}\sin\frac{\theta}{2}\sin\theta, \sqrt{r}\cos\frac{\theta}{2}\sin\theta] \quad (3.38)$$

where r and θ are the coordinates of $\mathbf{x}$ in the polar reference frame centered at the crack tip. The set $w(\mathbf{x})$ includes all the nodes in the support domain of a point located at $\mathbf{x}$, $w_b(\mathbf{x})$ is the subset of branch-enriched nodes, and $w_j(\mathbf{x})$ the subset of jump-enriched nodes. Fig. 3.19 shows geometry with a crack and adjacent nodal point locations.

The enrichment functions change with materials. The common type of enrichment functions used for isotropic materials and FGMs (Ventura et al., 2002) are

$$\xi^{\mathrm{enr}}(r,\theta) = [\sqrt{r}\sin\frac{\theta}{2}, \sqrt{r}\cos\frac{\theta}{2}, \sqrt{r}\sin\frac{\theta}{2}\sin\theta, \sqrt{r}\cos\frac{\theta}{2}\sin\theta] \quad (3.39)$$
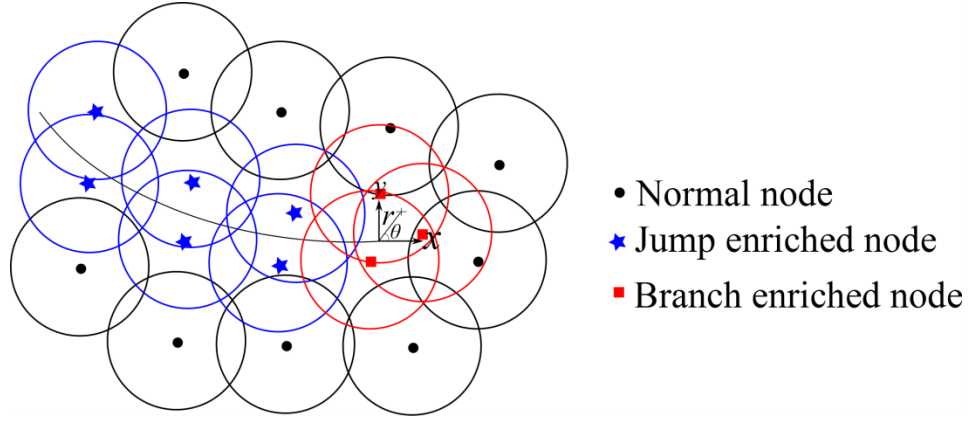
Fig. 3.19 Enriched nodes in the XEFG method.

In the case of a crack meeting at an angle oblique to the bi-material interface, $\xi^{\text{enr}}(r,\theta)$ is given by (Bouhala et al., 2013)

$$[r^{\lambda_1}\sin(\lambda_1+1)\theta, r^{\lambda_1}\cos(\lambda_1+1)\theta, r^{\lambda_1}\sin(\lambda_1-1)\theta, r^{\lambda_1}\cos(\lambda_1-1)\theta,$$
$$r^{\lambda_2}\sin(\lambda_2+1)\theta, r^{\lambda_2}\cos(\lambda_2+1)\theta, r^{\lambda_2}\sin(\lambda_2-1)\theta, r^{\lambda_2}\cos(\lambda_2-1)\theta] \tag{3.40}$$

λ_1 and λ_2 are roots of a transcendental equation given by (Bogy, 1971). Eq. (3.40) is only applicable when the roots are real. The branch enrichment function is more complicated and consists of 16 functions when the roots are complex.

For an interface crack, $\xi^{\text{enr}}(r,\theta)$ is given by (Sukumar et al., 2004)

$$[\sqrt{r}\cos(\varepsilon\log r)\,\mathrm{e}^{-\varepsilon\theta}\sin\frac{\theta}{2}, \sqrt{r}\cos(\varepsilon\log r)\,\mathrm{e}^{\varepsilon\theta}\sin\frac{\theta}{2}\sin\theta, \sqrt{r}\cos(\varepsilon\log r)\,\mathrm{e}^{-\varepsilon\theta}\cos\frac{\theta}{2},$$
$$\sqrt{r}\cos(\varepsilon\log r)\,\mathrm{e}^{\varepsilon\theta}\cos\frac{\theta}{2}\sin\theta, \sqrt{r}\cos(\varepsilon\log r)\,\mathrm{e}^{\varepsilon\theta}\sin\frac{\theta}{2}, \sqrt{r}\sin(\varepsilon\log r)\,\mathrm{e}^{\varepsilon\theta}\sin\frac{\theta}{2}\sin\theta,$$
$$\sqrt{r}\cos(\varepsilon\log r)\,\mathrm{e}^{\varepsilon\theta}\cos\frac{\theta}{2}, \sqrt{r}\sin(\varepsilon\log r)\,\mathrm{e}^{\varepsilon\theta}\cos\frac{\theta}{2}\sin\theta, \sqrt{r}\sin(\varepsilon\log r)\,\mathrm{e}^{-\varepsilon\theta}\sin\frac{\theta}{2}, \tag{3.41}$$
$$\sqrt{r}\cos(\varepsilon\log r)\,\mathrm{e}^{-\varepsilon\theta}\sin\frac{\theta}{2}\sin\theta, \sqrt{r}\sin(\varepsilon\log r)\,\mathrm{e}^{\varepsilon\theta}\sin\frac{\theta}{2}, \sqrt{r}\sin(\varepsilon\log r)\,\mathrm{e}^{\varepsilon\theta}\sin\frac{\theta}{2}\sin\theta]$$

where ε is the oscillation index parameter, and is given by

$$\varepsilon = \frac{1}{2\pi}\ln\left(\frac{\kappa_1\mu_2+\mu_1}{\kappa_2\mu_1+\mu_2}\right) \tag{3.42}$$
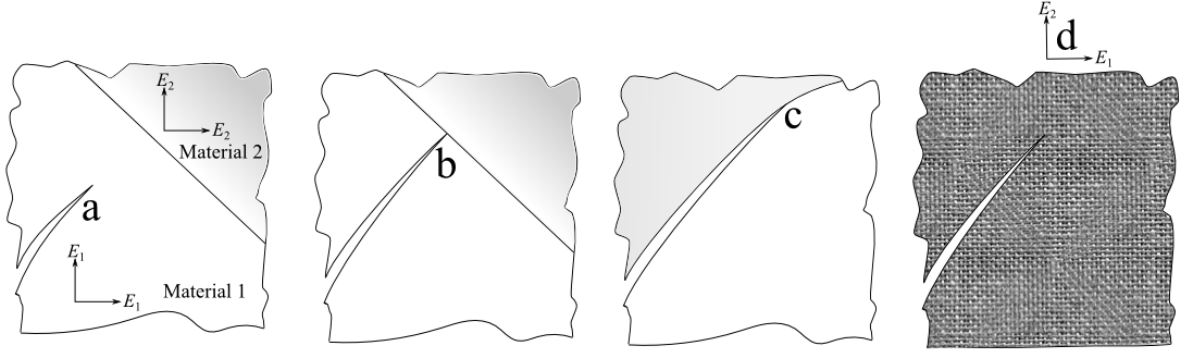
Fig. 3.20 Various locations of the crack tip at **(a)** isotropic and homogenous mediums; **(b)** the material interface at an arbitrary angle; **(c)** the interface parallel to it; and **(d)** orthotropic and homogenous mediums.

One of the difficulties associated with the use of the XEFG method is the implementation of appropriate enrichment functions, which depends upon the location of the crack tip, the orientation of the crack, and the material properties. Fig. 3.20 shows various locations of crack tips. For case (a), the enrichment functions given by Eq. (3.39) are sufficient. Eq. (3.40) is suitable for case (b), where the crack tip meets the material interface. For a crack parallel to the interface (c), the enrichment functions given by Eq. (3.41) are suitable. If the crack tip lies in an orthotropic medium, as shown in configuration (d), then the enrichment functions are as follows (Ghorashi et al., 2011).

$$\xi^{enr}(r,\theta)=[\sqrt{r}\cos\frac{\theta_1}{2}\sqrt{g_1(\theta_1)},\sqrt{r}\cos\frac{\theta_2}{2}\sqrt{g_2(\theta)},\sqrt{r}\sin\frac{\theta_1}{2}\sqrt{g_1(\theta)},\sqrt{r}\sin\frac{\theta_2}{2}\sqrt{g_2(\theta)}] \quad (3.43)$$

where $g_j(\theta)=\sqrt{\left(\cos\theta+s_{jx}\sin\theta\right)^2+\left(s_{jy}\sin\theta\right)^2}$ and θ_j is given by

$$\theta_j=\tan^{-1}\left(\frac{s_{jy}\sin\theta}{\cos\theta+s_{jx}\sin\theta}\right) \quad (3.44)$$

with $j=1,2$. In the above equations s_{jx} and s_{jy} are real and imaginary parts of the characteristic roots s_j of the fourth-order partial differential equation (Lekhnitskii, 1963) given by

$$\mathbb{C}_{11}s^4-2\mathbb{C}_{16}s^3+\left(2\mathbb{C}_{12}+\mathbb{C}_{66}\right)s^2-2\mathbb{C}_{26}s+\mathbb{C}_{22}=0 \quad (3.45)$$

where $\mathbb{C}$ is the compliance matrix. It was shown by Lekhnitskii that the roots of the above equation are always complex or purely imaginary.

The XEFG method is based on an extrinsic enrichment scheme, in which the additional functions are incorporated through the PU approach. There is another scheme based on intrinsic enrichment, in which the extra functions are added to the polynomial basis $\mathbf{P}^{\mathrm{T}}(x)$, which is normally required for constructing the EFG method shape functions. Fleming et al. (1997) used this scheme to model cracks. The disadvantage of this method is that it increases the computational cost because all the nodes in the domain are enriched. Duflot& Nguyen-Dang (2004) proposed a meshfree method based on intrinsic enrichment of kernel functions. This approach is relatively cheaper computationally, but less accurate.

3.9 Domain Form of *J*-Integral

The *J*-integral was developed by Rice (1968) to potential energy release rate for a crack. The contour form of *J*-integral is given by

$$J = \int_{\Gamma}\left(Wn_1 - \sigma_{ij}\frac{\partial u_i}{\partial x_1}n_j\right)\mathrm{d}\Gamma \tag{3.46}$$

Eq. (3.46) can also be written as

$$J = \lim_{\Gamma_s \to 0}\oint_{\Gamma_s}(W\delta_{1j} - \sigma_{ij}u_{i,1})n_j d\Gamma \tag{3.47}$$

where $W = \sigma_{ij}\varepsilon_{ij}/2$ is the strain energy density, δ_{ij} is the Kronecker delta, and n_i is the unit outward normal to the contour Γ. A contour integral $\aleph$ is defined such that

$$\aleph = \oint_{\Gamma}(W\delta_{1j} - \sigma_{ij}u_{i,1})m_j q d\Gamma \tag{3.48}$$

where $\Gamma = \Gamma_o + \Gamma_{c+} - \Gamma_s + \Gamma_{c-}$. m_j is the unit outward normal vector at point to the corresponding contour (Fig. 3.21). q is a smooth function such that $q = 1$ on Γ_s and $q = 0$ on Γ_o. There are many forms of the q function (Anderson, 1995; Kim & Paulino, 2003). The following q function is used.

$$q = \left(1 - \frac{abs\left(x_1 - x_{ctip}\right)}{d_s}\right)\left(1 - \frac{abs\left(x_2 - y_{ctip}\right)}{d_s}\right) \tag{3.49}$$

where $\left(x_{ctip}, y_{ctip}\right)$ is the coordinate of the crack tip and $\left(x_1, x_2\right)$ is the coordinate of the sampling point. d_s is the half of the length of the integral domain (Fig. 3.22).
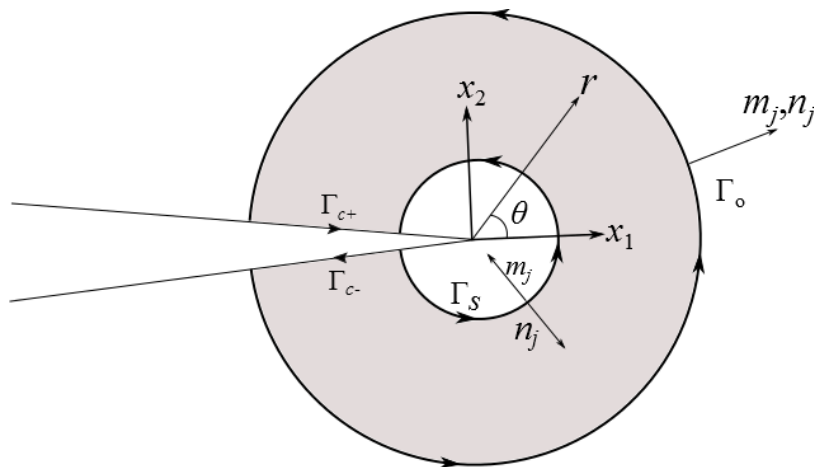
Fig. 3.21 Contour Integral to a domain form of the integral. ($m_j = n_j$ on Γ_o and $m_j = -n_j$ on Γ_s).

As $\Gamma_s \to 0$, Eq. (3.48) can be rewritten as

$$\lim_{\Gamma_s \to 0} \aleph = \lim_{\Gamma_s \to 0} \oint_{\Gamma_o + \Gamma_{c+} - \Gamma_s + \Gamma_{c-}} (W\delta_{1j} - \sigma_{ij}u_{i,1})m_j q d\Gamma$$
$$= \lim_{\Gamma_s \to 0} \oint_{\Gamma_o + \Gamma_{c+} + \Gamma_{c-}} (W\delta_{1j} - \sigma_{ij}u_{i,1})m_j q d\Gamma - \lim_{\Gamma_s \to 0} \oint_{\Gamma_s} (W\delta_{1j} - \sigma_{ij}u_{i,1})m_j q d\Gamma$$

(3.50)

In the absence of crack face loading, Eq. (3.50) becomes

$$\lim_{\Gamma_s \to 0} \aleph = \lim_{\Gamma_s \to 0} \oint_{\Gamma_o} (W\delta_{1j} - \sigma_{ij}u_{i,1})m_j q d\Gamma - \lim_{\Gamma_s \to 0} \oint_{\Gamma_s} (W\delta_{1j} - \sigma_{ij}u_{i,1})m_j q d\Gamma \qquad (3.51)$$

The first term in Eq.(3.51) is zero because $q = 0$ on Γ_o. The second term is equal to the J-integral because $m_j = -n_j$ on Γ_s. That is,

$$J = -\lim_{\Gamma_s \to 0} \aleph = -\lim_{\Gamma_s \to 0} \oint_{\Gamma_s} (W\delta_{1j} - \sigma_{ij}u_{i,1})m_j q d\Gamma$$
$$= \lim_{\Gamma_s \to 0} \oint_{\Gamma_s} (W\delta_{1j} - \sigma_{ij}u_{i,1})n_j d\Gamma$$

(3.52)

Applying the divergence theorem to Eq.(3.52), the domain form of the J-integral is obtained

$$J = \int_A (\sigma_{ij}u_{i,1} - W\delta_{1j})_{,j} q dA + \int_A (\sigma_{ij}u_{i,1} - W\delta_{1j})q_{,j} dA \qquad (3.53)$$

Eq.(3.53) is the most general form of the equivalent domain J-integral.
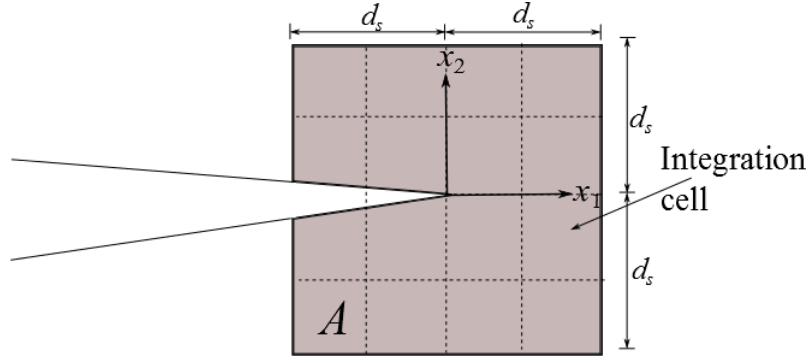
Fig. 3.22 Square integral domain for calculation of *J*-integral.

In the present work, a square domain of size d_s, centered at the crack tip, is used to compute the domain form of *J*-integral. The size of the square domain ($2d_s$) usually ranges from 10% to 25% of the crack length.

3.9.1 Interaction Integral for Isotropic materials

The interaction integral were developed by Yau et al. (1980) to separate different modes associated with a crack field. This was developed by considering the first term in the Eq.(3.53) that arises due to heterogeneity. It can be written as

$$I_{nonh} = \int_A (\sigma_{ij} u_{i,1} - W\delta_{1j})_{,j} q dA = \int_A (\sigma_{ij,j} u_{i,1} + \sigma_{ij,j} u_{i,1j} - W_{,j}\delta_{1j}) q dA \qquad (3.54)$$

In the absence of the body force $\sigma_{ij,j} = 0$. Since $W_{,j}\delta_{1j} = W_{,1}$, the derivative of the strain energy density is given by

$$W_{,1} = \sigma_{ij}\varepsilon_{ij,1} + \frac{1}{2}\mathbb{C}_{ijkl,1}\varepsilon_{kl}\varepsilon_{ij} \qquad (3.55)$$

For an isotropic and homogenous material, $\mathbb{C}_{ijkl,1} = 0$. The I_{nonh} expression in Eq. (3.54) will become zero under small strain assumption $\varepsilon_{ij,1} = u_{i,1j}$. I_{nonh} is not zero for non-homogenous materials such as FGMs. It is also not zero when the crack tip is close to a material interface.

Let us consider two independent fields: the actual field $(\mathbf{u}, \boldsymbol{\varepsilon}, \boldsymbol{\sigma})$ and the auxiliary field $(\mathbf{u}^{aux}, \boldsymbol{\varepsilon}^{aux}, \boldsymbol{\sigma}^{aux})$. The *J*-integral of the superimposed fields can be written as

$$J^s = \int_A \left\{ (\sigma_{ij} + \sigma_{ij}^{aux})(u_{i,1} + u_{i,1}^{aux}) - \frac{1}{2}(\sigma_{ik} + \sigma_{ik}^{aux})(\varepsilon_{ik} + \varepsilon_{ik}^{aux})\delta_{1j} \right\} q_{,j} dA \qquad (3.56)$$

For an isotropic and homogenous material, the auxiliary stress and displacement field solution is given in Appendix A. Eq. (3.56) can be decomposed into three terms

$$J^s = J + J^{aux} + M \tag{3.57}$$

where J is given by Eq. (3.53), J^{aux} can be written as

$$J^{aux} = \int_A (\sigma_{ij}^{aux} u_{i,1}^{aux} - W^{aux} \delta_{1j}) q_{,j} dA \tag{3.58}$$

The *M*-integral is given by

$$M = \int_A (\sigma_{ij} u_{i,1}^{aux} + \sigma_{ij}^{aux} u_{i,1} - \sigma_{ik} \varepsilon_{ik}^{aux} \delta_{1j}) q_{,j} dA \tag{3.59}$$

The *M*-integral is also known as the interaction integral. In the presence of crack face loading (Matthew et al., 2005) and thermal loading (Amit & Jeong, 2008), Eq. (3.59) is modified to the following

$$M = \int_A (\sigma_{ij} u_{i,1}^{aux} + \sigma_{ij}^{aux} u_{i,1} - \sigma_{ik} \varepsilon_{ik}^{aux} \delta_{1j}) q_{,j} dA + \\ \int_A \sigma_{ij}^{aux} \alpha (\Delta T)_{,1} \delta_{ij}) q dA - \int_{\Gamma_{c+}+\Gamma_{C-}} t_j u_{j,1}^{aux} q d\Gamma \tag{3.60}$$

For a 2D problem, the *M*-integral is equal to

$$M = \frac{(2 K_I K_I^{aux} + 2 K_{II} K_{II}^{aux})}{E^*} \tag{3.61}$$

where E^* is E for plane stress and $E/(1-v^2)$ for plane strain. K_I is evaluated by setting K_I^{aux} to unity and K_{II}^{aux} to zero. Similarly K_{II} is evaluated by setting K_{II}^{aux} to unity and K_I^{aux} to zero.

3.9.2 Interaction Integral for crack in an orthotropic material

The auxiliary functions in case of a crack in an orthotropic material are given in Appendix B (Ghorashi et al., 2011). The *M*-integral is then equal and is given by

$$M = 2 e_{11} K_I K_I^{aux} + e_{12} \left(K_I K_{II}^{aux} + K_I^{aux} K_{II} \right) + 2 e_{22} K_{II} K_{II}^{aux} \tag{3.62}$$

where

$$e_{11} = -\frac{\mathbb{C}_{22}}{2} \operatorname{Im}\left(\frac{s_1 + s_2}{s_1 s_2}\right)$$

$$e_{12} = -\frac{\mathbb{C}_{22}}{2} \operatorname{Im}\left(\frac{1}{s_1 s_2}\right) + \frac{\mathbb{C}_{11}}{2} \operatorname{Im}\left(s_1 s_2\right) \tag{3.63}$$

$$e_{12} = \frac{\mathbb{C}_{11}}{2} \operatorname{Im}\left(s_1 + s_2\right)$$

The SIFs can be obtained by considering the two states: state 1: $K_I^{aux} = 1, K_{II}^{aux} = 0$; and state 2: $K_I^{aux} = 0, K_{II}^{aux} = 1$. Then, the following systems of linear algebraic equations are solved to obtain the SIFs.

$$M^{(\text{act,state } I)} = 2e_{11}K_I + e_{12}K_{II}$$

$$M^{(\text{act,state } II)} = e_{12}K_I + 2e_{12}K_{II} \tag{3.64}$$

3.9.3 Interaction Integral for bi-material interface crack

In case of an interface crack in bi-materials (Fig. 3.23) subjected to mechanical and thermal load, ΔT, the interaction integral is given by

$$I = \sum_{m=1}^{2} \int_{A_m} (\sigma_{ij} u_{i,1}^{aux} + \sigma_{ij}^{aux} u_{i,1} - \sigma_{ik}\varepsilon_{ik}^{aux}\delta_{1j})q_{,j}dA + \sum_{m=1}^{2} \varphi_m \int_{A_m} \varepsilon_{kk}^{aux}(\Delta T)_{,1}qdA \tag{3.65}$$
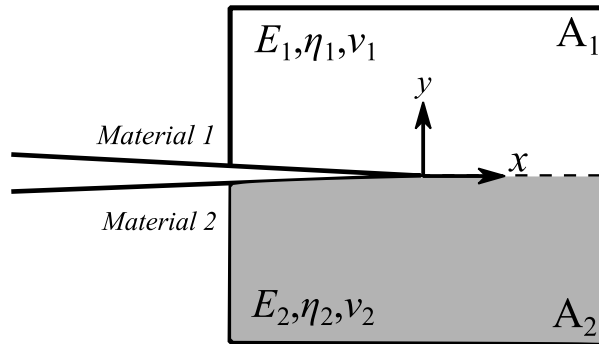
Fig. 3.23 Interaction integral for interface crack.

σ_{ij}^{aux}, ε_{ik}^{aux} and u_i^{aux} are obtained from the crack-tip solutions for an auxiliary state with an interface crack (Appendix C). The complex SIF can be computed through the following relation,

$$M = \frac{(1/E_1^* + 1/E_2^*)(2K_1 K_2^{aux} + 2K_2 K_2^{aux})}{2\cosh^2(\pi\varepsilon)} \tag{3.66}$$

ε is the bi-material oscillatory parameter given by,

$$\varepsilon = \frac{1}{2\pi} \ln\left(\frac{1-\beta}{1+\beta}\right) = \frac{1}{2\pi} \ln\left(\frac{\kappa_1 \mu_2 + \mu_1}{\kappa_2 \mu_1 + \mu_2}\right) \tag{3.67}$$

where μ_m is the shear modulus and κ_m is the Kolosov's constant, $m = 1$ and 2. κ_m is $(3-4v_m)$ in the case of plane strain and $(3-v_m)/(1+v_m)$ in the case of plane stress.

The stress intensity factor amplitudes, K_1 and K_2, associated with an interface crack are different from mode I and mode II SIFs for a crack in isotropic and homogenous materials. The dimension of $\mathbf{K} = K_1 + iK_2$ is $\text{MPa(m)}^{0.5-i\varepsilon}$; the dimension of mode I (K_I) or mode II SIF (K_{II}) is $\text{MPa(m)}^{0.5}$.

For a crack tip impinging at an angle to the material interface, the explicit expression of the interaction integral to compute the SERR or the SIFs is not available in the literature. Further, the expression for CCI cannot be easily defined. In such situations, the SIFs can be still determined using the stress or displacement methods, provided the crack-tip displacement field solutions are available.

3.9.4 Interaction Integral for a crack close to a material interface

When a crack is close to the interface of a material, as shown in Fig. 3.24, I_{nonh} in the Eq. (3.53) is not zero. The interaction integral I is given by

$$I = \int_A \left(\sigma_{ij}^{aux} u_{j,1} + \sigma_{ij} u_{j,1}^{aux} - \sigma_{jk}^{aux} \varepsilon_{jk} \delta_{1i} \right) q_{,i} dA + \\ \int_A \left(\sigma_{ij}^{aux} u_{j,1} + \sigma_{ij} u_{j,1}^{aux} - \sigma_{jk}^{aux} \varepsilon_{jk} \delta_{1i} \right)_{,i} q dA \tag{3.68}$$
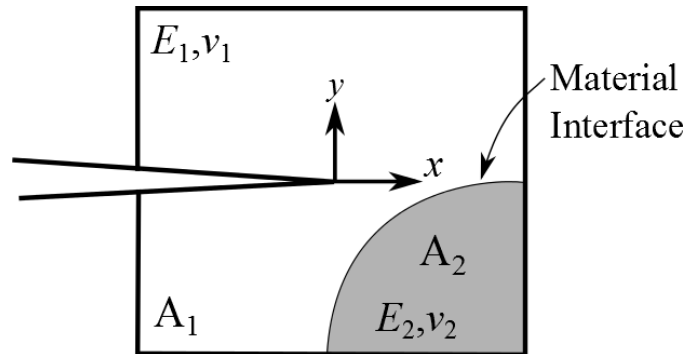
Fig. 3.24 Crack close to a material interface.

The second term in Eq. (3.68) is I_{nonh}. It can be expanded as follows

$$I_{nonh} = \int_A \left(\sigma_{ij,i} u_{j,1}^{aux} + \sigma_{ij,i}^{aux} u_{j,1} + \sigma_{ij} u_{j,i1}^{aux} + \sigma_{ij}^{aux} u_{j,i1} - \sigma_{ij,i}^{aux} \varepsilon_{ij,1} - \sigma_{ij,1}^{aux} \varepsilon_{ij} \right) q dA \qquad (3.69)$$

Note that $\sigma_{ij,i} u_{j,1}^{aux} = 0$ and $\sigma_{ij,i}^{aux} u_{j,1} = 0$ because of equilibrium conditions in the absence of body forces and $\sigma_{ij}^{aux} u_{j,i1} = \sigma_{ij,i}^{aux} \varepsilon_{ij,1}$ because of the symmetry of the auxiliary stress tensor, Eq.(3.69) can be further simplified to give

$$I_{nonh} = \int_A \left(\sigma_{ij} u_{j,i1}^{aux} - \sigma_{ij,1}^{aux} \varepsilon_{ij} \right) q dA \qquad (3.70)$$

Defining $\varepsilon_{ij}^{aux0} = S_{ijkl}^{tip} \sigma_{kl}^{aux}$, where S_{ijkl}^{tip} is the compliance tensor at the crack tip, and noting that $\sigma_{ij} u_{j,i1}^{aux} = \sigma_{ij} \frac{1}{2} (u_{j,1}^{aux} + u_{j,1}^{aux}) = \sigma_{ij} \varepsilon_{ij,1}^{aux} = \sigma_{ij} (S_{ijkl}^{tip} \sigma_{kl}^{aux})_{,1} = \sigma_{ij} S_{ijkl}^{tip} \sigma_{kl,1}^{aux}$ due to symmetry of the stress field, Eq. (3.70) can be further simplified to

$$I_{nonh} = \int_A \sigma_{ij} \left[S_{ijkl}^{tip} - S_{ijkl}(\mathbf{x}) \right] \sigma_{kl,1}^{aux} q dA \qquad (3.71)$$

Substituting Eq. (3.71) for Eq. (3.68), the following expression is obtained:

$$I = \int_A \left(\sigma_{ij}^{aux} u_{j,1} + \sigma_{ij} u_{j,1}^{aux} - \sigma_{jk}^{aux} \varepsilon_{jk} \delta_{1i} \right) q_{,i} dA + \int_A \sigma_{ij} \left[S_{ijkl}^{tip} - S_{ijkl}(\mathbf{x}) \right] \sigma_{kl,1}^{aux} q dA \qquad (3.72)$$

Eq. (3.72) is advantageous because it is valid for materials with continuous variation in properties, as is in the case of FGMs, and discontinuous variation in the material properties, as is in the case of bi-materials. More details of the derivation are presented in Yu et al. (2009).

3.10 EFG Procedure

The algorithm for the procedure of the EFG method based on the weak formulation is outlined in Fig. 3.25. The primary difference between the FEM and the EFG method is generation of the approximation shape functions. Secondly, in the case of the XEFG method, the construction of the strain field equation takes into account the enrichment functions. Thirdly, the imposition of boundary conditions in the EFG method is not trivial, as is in the case of FEM.

All the analysis in the present study are carried in the MATLAB2013A (8.1.0.604) under the license number 724504 environment.
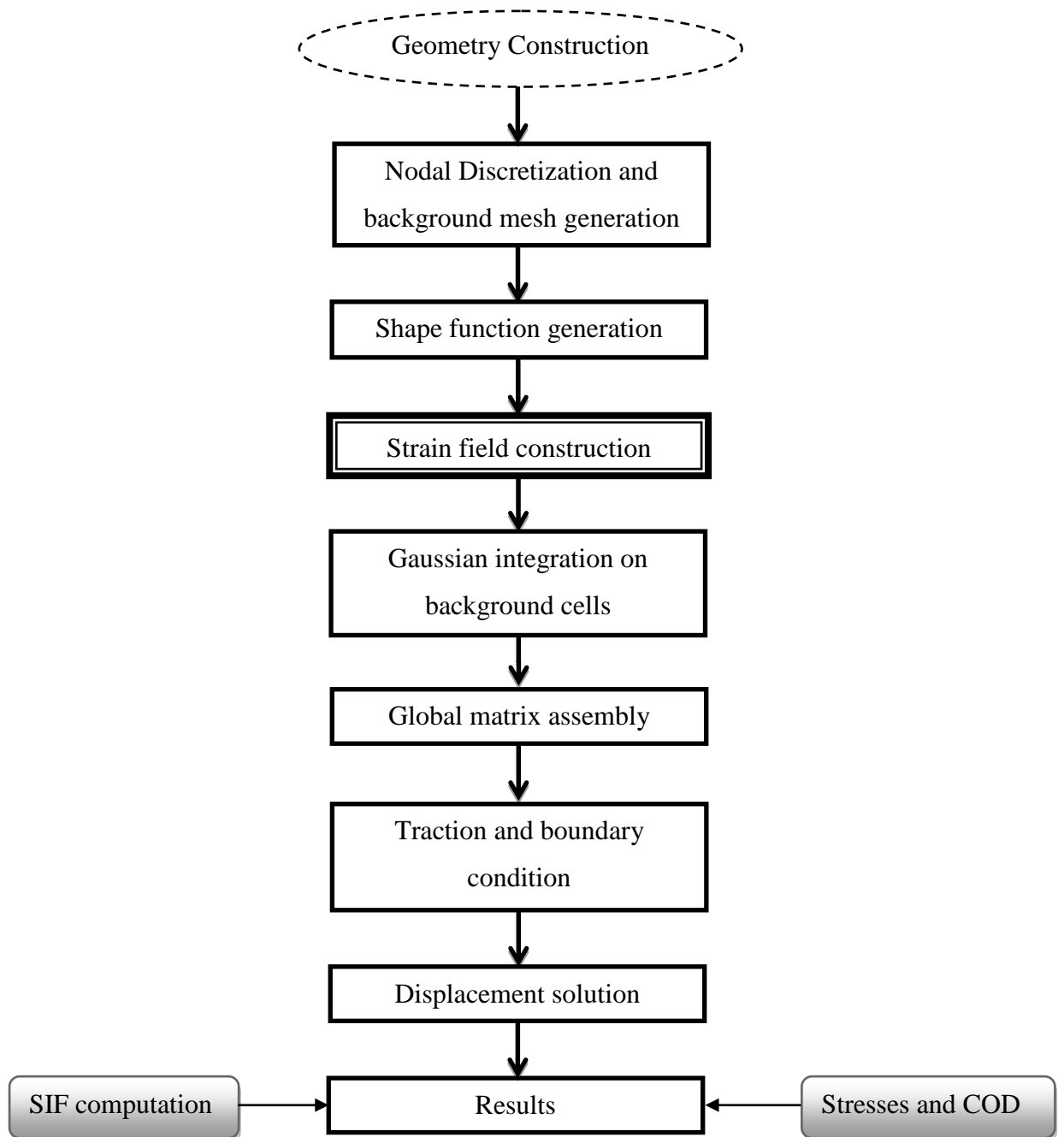
Fig. 3.25 Flowchart for the EFG method.

3.11 Closure

In this chapter, the formulation of the EFG method has been given. Method parameters such as the order of Gauss integration, size of the domain of influence and nodal density are studied in order to control the error in the solutions. A 2D case study concerning a bending problem is presented in order to study the effects of these parameters on the accuracy of the solution. It is observed that an irregular nodal discretization leads to an increase in the non-

polynomial behavior of the shape functions. This leads to unnecessary accumulation of errors during the numerical integration. Therefore, a regular nodal discretization is preferable; it has been used in the subsequent analysis.

Different methodologies available to model a crack in a material has been presented. Modelling crack propagation in a non-homogenous material using the XEFG method is difficult if analytical solutions for the crack-tip stress field are not available.

The interaction integrals that are useful in the determining of the SIFs in varieties of situations have been presented. Wherever possible, the SIFs obtained by the interaction integral are kept as benchmark solution. A flowchart of the full procedure of the EFG method has been presented.

Chapter 4   Computing Stress Intensity Factors

4.1 Introduction

In this chapter*, a method that exploits the advantages of both the crack closure integral (CCI) and MMs to evaluate the SIFs is given. The variations of elastic singular fields near the crack tip are modelled using mathematical approximation and the SIFs are extracted. Since it is relatively straightforward, with an element-free discretization, to obtain (1) the traction along any radial direction from the crack tip, and (2) the crack opening displacement (COD) from the enriched nodal displacement field, the calculation of energy release rate associated with crack extension can be easily obtained with the XEFG method. This offers a possibility of applying the CCI to crack problems easily.

The CCI is combined here with a local smoothing technique (Maiti et al., 1997) to arrive at simpler expressions for calculation of the SIFs, eliminating the need for integration. This approach helps to improve the accuracy of the computed SIFs obtained using the original CCI. Various straight crack problems including those involving external traction on the crack faces and loading with a temperature gradient, are studied using the proposed CCI technique and the results are compared with other techniques such as M-integral, displacement method and stress method. In addition, a problem involving a curved crack in an infinite medium is studied to show the performance of the various schemes.

4.2 CCI with Local Smoothing Technique

The following crack closure integrals give the expression for computing SERRs in mode I (G_I) and mode II (G_{II}):

$$G_I = \lim_{\Delta a \to 0} \frac{1}{2\Delta a} \int_0^{\Delta a} \sigma_{yy}(x) v_{COD}(\Delta a - x) dx$$

$$G_{II} = \lim_{\Delta a \to 0} \frac{1}{2\Delta a} \int_0^{\Delta a} \tau_{xy}(x) u_{COD}(\Delta a - x) dx$$

(4.1)

where G_I and G_{II} are mode I and mode II energy release rates.

Fig. 4.1 shows a crack of length a and a virtual crack advance of Δa. For an elastic material, the potential energy release rate or strain energy release rate (SERR) during crack extension is equal to the energy required to close the crack by the same distance.
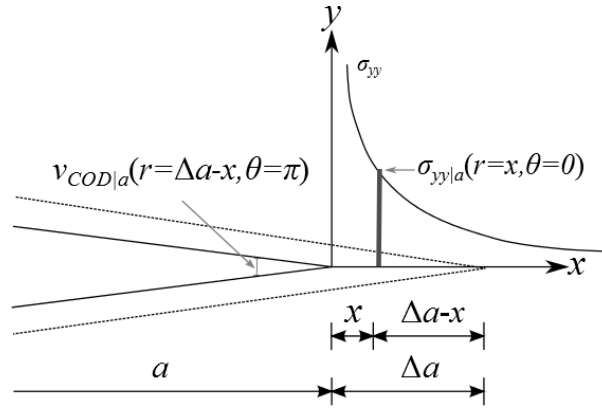
Fig. 4.1 Self similar virtual crack extension.

The integral in Eq.(4.1) can be evaluated by resorting to numerical integration like Gauss quadrature from the computed values of displacements and stresses. However, because of steep gradients in stress near the crack tip, it is necessary to divide the span Δa into a large number of divisions and use a high order of Gauss quadrature, to obtain a good accuracy. In the MMs, the virtual crack extension length Δa can be set by the user and is equal to the size of crack tip elemental in the FEM. Typically Δa is kept within $1-5\%a$ (Maiti, 1992; Sethuraman & Maiti, 1988).

The advantage of the MMs when computing the SIFs through the CCI is linked to the smoothness of the MLS shape functions. Because of this property, the stress field can be evaluated more accurately at any location in the domain, as opposed to the FEM where the stresses are most accurate at the Gauss/Barlow points.

In this work, the COD varies as a square root function of distance from the crack tip because of the enrichment functions. Substituting x by $\xi - \Delta a$, the COD variation can be expressed as

$$\begin{Bmatrix} u_{COD} \\ v_{COD} \end{Bmatrix} = \begin{Bmatrix} u_{COD}^{+} - u_{COD}^{-} \\ v_{COD}^{+} - v_{COD}^{-} \end{Bmatrix} = \begin{bmatrix} a_u & b_u & c_u \\ a_v & b_v & c_v \end{bmatrix} \begin{Bmatrix} 1 \\ \xi \\ \sqrt{\Delta a - \xi} \end{Bmatrix} \tag{4.2}$$

where $\{u_{COD}, v_{COD}\}^{\mathrm{T}}$ is the COD vector. In the above expression, the unknown coefficients $a_i, b_i, c_i \; i = u,v$ can be calculated from the displacement values at nodes $j, j-1$ and $j-2$ as shown in Fig. 4.2. The COD at the crack tip (j) is assumed zero. The nodes $j-1$ and $j-2$ are located at a distance of $\Delta a/4$ and Δa, respectively, behind the crack tip. Thereby the COD variation in the span, Δa, is obtained as follows:

$$\mathbf{u}_{COD} = 2(\mathbf{u}_{COD}^{j-2} - 2\mathbf{u}_{COD}^{j-1})(1 - \xi/\Delta a) + (4\mathbf{u}_{COD}^{j-1} - \mathbf{u}_{COD}^{j-2})\sqrt{1 - \xi/\Delta a}, 0 \le \xi \le \Delta a \qquad (4.3)$$

where $\mathbf{u}_{COD} = \{u_{COD}, v_{COD}\}^{\mathrm{T}}$.
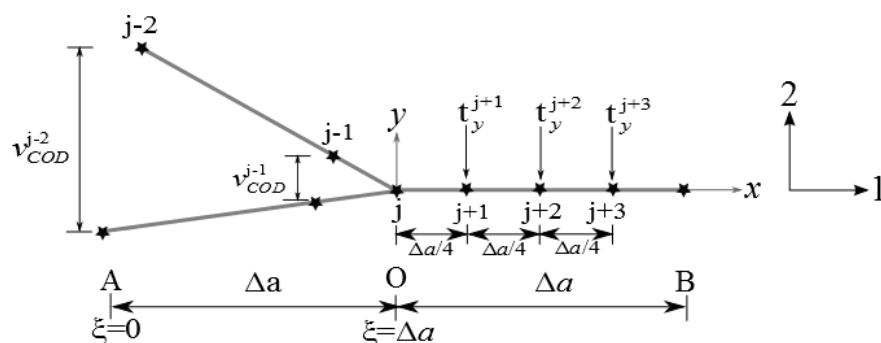
Fig. 4.2 Locations at which displacements and tractions are computed for mode I SIF.

The tractions $t_x = \tau_{xy}$ and $t_y = \sigma_{yy}$, along the crack plane, vary as a function of $1/\sqrt{x}$ due to the local enrichment functions and its variation ahead of the crack tip can be expressed as follows:

$$\begin{Bmatrix} t_x \\ t_y \end{Bmatrix} = \begin{bmatrix} a_{t_x} & b_{t_x} & c_{t_x} \\ a_{t_y} & b_{t_y} & c_{t_y} \end{bmatrix} \begin{Bmatrix} 1 \\ 1/\sqrt{x/\Delta a} \\ \sqrt{x/\Delta a} \end{Bmatrix} \qquad (4.4)$$

The above constants can be obtained from the computed traction, t_y, at locations $j+1, j+2$ and $j+3$.

$$\begin{Bmatrix} a_{t_y} \\ b_{t_y} \\ c_{t_y} \end{Bmatrix} = \begin{bmatrix} 1 & 2 & 1/2 \\ 1 & \sqrt{2} & 1/\sqrt{2} \\ 1 & 2/\sqrt{3} & \sqrt{3}/2 \end{bmatrix}^{-1} \begin{Bmatrix} t_y^{j+1} \\ t_y^{j+2} \\ t_y^{j+3} \end{Bmatrix} \qquad (4.5)$$

The approximated traction field is not affected significantly by the choice of the points at which tractions are obtained. This effect is studied in a later section. The three points selected to evaluate the traction coefficients are equally distributed along the span Δa and are located at some distance from the crack tip or point of singularity, where the evaluated value would be less accurate.

The local smoothing technique consists of taking the average traction over the crack extension length and yields a simpler expression for the CCI. The average value is given by

$$t_y^{avg} = \frac{1}{\Delta a} \int\limits_0^{\Delta a} t_y \, \mathrm{dx} = (a_{ty} + 2b_{ty} + 2/3c_{ty}) \tag{4.6}$$

To conform to the singularity variation, the local traction is normalized and is assumed to have the form:

$$t_y = t_y^{avg} / (2\sqrt{x/\Delta a}) \tag{4.7}$$

Eq. (4.3) and (4.7) are substituted into Eq. (4.1) to obtain the mode I SIF. The Mode II SIFs can also be obtained in a similar fashion. The expressions for mode I and II SIFs are given by

$$
\begin{aligned}
G_I &= 0.5 \, t_y^{avg} [v_{COD}^{j-2}(4/3 - \pi/4) + v_{COD}^{j-1}(\pi - 8/3)] \\
G_{II} &= 0.5 \, t_x^{avg} [u_{COD}^{j-2}(4/3 - \pi/4) + u_{COD}^{j-1}(\pi - 8/3)]
\end{aligned}
\tag{4.8}
$$

Similar expressions for G_I and G_{II} for the classical EFG method can be obtained without enrichment. This method can be easily extended to crack problems in 3D. In this case, the CCI with local smoothing can be applied for the calculation of the SIFs at a point on the crack front considering a local plane normal to the crack front. The span, Δa, could then be taken in the local normal direction.

4.2.1 Crack Face Loading

Most of the literature deals with load-free crack surfaces. The crack faces loaded with traction are considered here. Consider a body with a crack, described by Γ_c ($\Gamma_{c+} \cup \Gamma_{c-}$), as shown in Fig. 4.3. The body is subjected to displacement constraints $\bar{u}$ on Γ_u part of the boundary. Traction $\bar{t}$ is applied on Γ_t part of the boundary. The upper and lower crack edges are subjected to tractions t_{e+} and t_{e-} respectively.
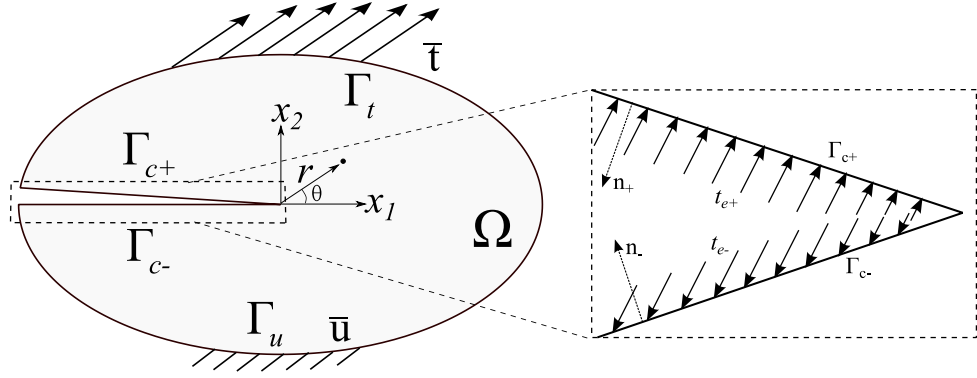
Fig. 4.3 Domain subjected to constraints with crack face traction.

A self-similar expansion of the crack is shown in Fig. 4.4. If the crack faces are subjected to constant external traction $\mathbf{t}_e$, as the crack extends from $x = 0$ to $x = \Delta a$, the newly formed crack faces will also be subjected to this traction. The COD will be larger compared to the case when the crack faces are traction free.
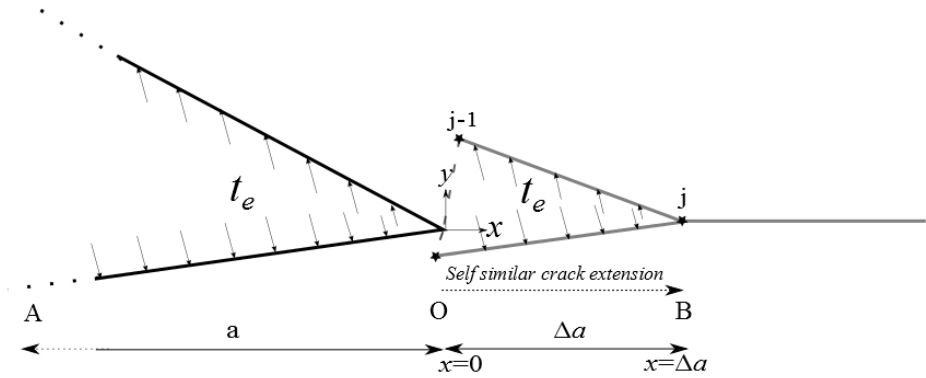
Fig. 4.4 Crack face subjected to loading.

In such a case, additional energy is released during crack extension due to crack face loading. This extra energy released is equal to additional energy required to close the crack which is given by,

$$\mathbf{W}_e = \frac{1}{2} \int_0^{\Delta a} \mathbf{t}_e . \mathbf{u}_{COD} dx \tag{4.9}$$

The extra energy release rate, during crack extension, is given by

$$\mathbf{G}_e = \frac{1}{2\Delta a} \int_0^{\Delta a} \mathbf{t}_e^{avg} . \mathbf{u}_{COD} dx$$
$$= \mathbf{t}_e^{avg} . [\mathbf{u}_{COD}^{j-2} + 2\mathbf{u}_{COD}^{j-1}] / 6 \tag{4.10}$$

- 78 -

where $\mathbf{G}_e = \{G_I, G_{II}\}^T$. The additional work by the external load is then added to Eq. (4.8) to yield the expression for the SERRs in the presence of crack face loading:

$$G_I = 0.5 t_y^{avg}[v_{COD}^{j-2}(4/3 - \pi/4) + v_{COD}^{j-1}(\pi - 8/3)] + 0.5 t_{ey}^{avg}[(v_{COD}^{j-2} + 2v_{COD}^{j-1})/3]$$
$$G_{II} = 0.5 t_x^{avg}[u_{COD}^{j-2}(4/3 - \pi/4) + u_{COD}^{j-1}(\pi - 8/3)] + 0.5 t_{ex}^{avg}[(u_{COD}^{j-2} + 2u_{COD}^{j-1})/3] \qquad (4.11)$$

4.2.2 Thermal Loading

In the case of thermal loading, the mechanical strain is related to total strain by

$$\varepsilon_{ij}^m = (\varepsilon_{ij}^t - \alpha^* \Delta T \delta_{ij}) \qquad (4.12)$$

where ε_{ij}^m is the mechanical strain, ε_{ij}^t is the total strain, α is the coefficient of thermal expansion and ΔT is the temperature difference. The stress developed is related to strain by the standard fourth order constitutive tensor.

$$\sigma_{ij} = \mathbb{C}_{ijkl} \varepsilon_{kl}^m \qquad (4.13)$$

The computed stresses are smoothed by the local smoothing scheme described earlier to obtain a new average traction including the thermal effects, $t_{\Delta T}^{avg}$, Substituting into Eq. (4.6) yields the required mode I and II SERRs.

$$G_I = 0.5 \, t_{y/\Delta T}^{avg}[v_{COD}^{j-2}(4/3 - \pi/4) + v_{COD}^{j-1}(\pi - 8/3)]$$
$$G_{II} = 0.5 \, t_{x/\Delta T}^{avg}[u_{COD}^{j-2}(4/3 - \pi/4) + u_{COD}^{j-1}(\pi - 8/3)] \qquad (4.14)$$

Upon any crack extension, the newly formed crack edges OB (cf. Fig. 4.2 and Fig. 4.4) are subjected to crack face loading due to the thermal traction. The contribution of this thermal traction to the energy release rate has been accounted for in Eq.(4.14). As the crack tip advances from O to B, if the temperature field over the span OB before and after the crack extension remains the same. Under such circumstances, the thermal field does not contribute to any extra work (Mukhopadhyay et al., 1999).

The CCI with local smoothing technique is an energy-based approach just like the *J*-integral or interaction integral. It is derived from Irwin's two-step crack closure method. In order to calculate SERR associated with a crack extension two geometries are analyzed. In the first case, the geometry with a given crack is analyzed and the strain energy U_i is calculated. In the second case, the same geometry with the given crack extended in-plane by an infinitesimal amount Δa (Fig. 4.4) is analyzed and the strain energy U_f is calculated. The

SERR G is then obtained through $G = \left(U_i - U_f \right) / t.\Delta a$, where t is thickness of specimen. Since the two energies U_i and U_f contain similar order of error, the SERR is obtained with a good accuracy because of the finite difference process involved. The CCI method is also based on the same approach; it offers good accuracy and it helps to eliminate the need for any calculation of U_i and U_f without any loss of accuracy of the SERR, hence the SIFs.

4.3 Results for Isotropic Materials

In this section, the CCI in conjunction with the local smoothing technique has been applied to a number of crack problems involving thermal-mechanical loadings and crack face pressure loading. The SIFs computed using the proposed CCI method and other standard methods are compared with the results available in the literature.

All the materials considered here are isotropic with Young's modulus $E = 210 GPa$ and Poisson's ratio $v = 0.3$. The domain of influence is kept as 1.75 times the nodal spacing unless otherwise mentioned.

4.3.1 Mixed-Mode Edge Crack in Finite Plate
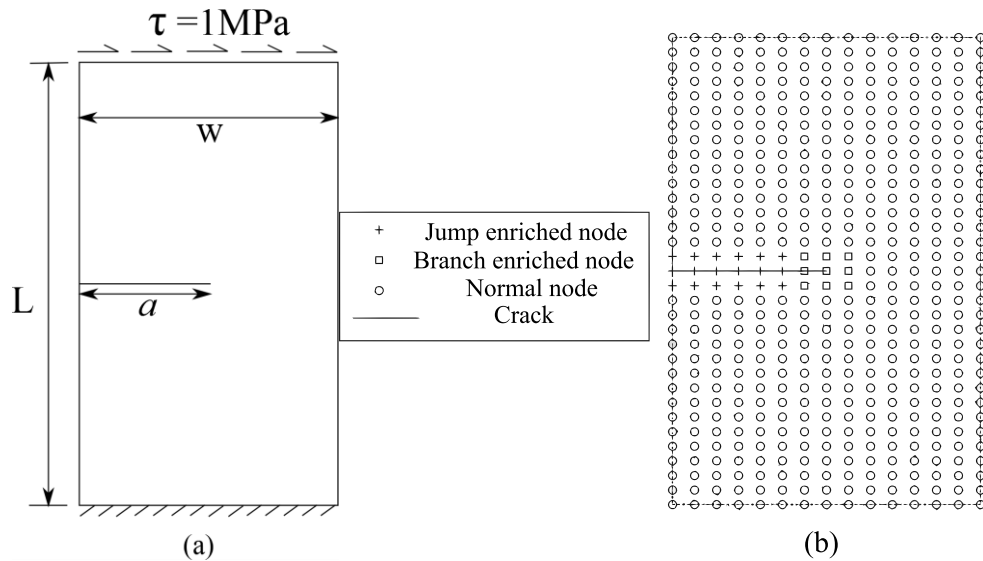
Fig. 4.5 Mixed-mode edge crack **(a)** Geometry. **(b)** Nodal Discretization.

The dimensions of the plate(Fig.4.5(a)) are Width, $w = 7$ m (width) and Length $L = 16 / 7 w$. The plate contains an edge crack and is subjected to a traction of $1 MPa$. It is discretized with 15×33 nodes. Wilson (1969) gave the solution as $K_I = 34$ MPa $\sqrt{m}$ and

$K_{II} = 4.55 \, \text{MPa} \sqrt{\text{m}}$. Here the SIFs have been obtained using five techniques: the CCI with local smoothing, the CCI without local smoothing, the M-integral, the displacement method and te stress method.

The crack opening displacement (COD), required for the displacement method, can be obtained by the jump and branch enriched nodal degrees of freedom. This is given by

$$\mathbf{u}_{COD} = \mathbf{u}_{COD}^+ - \mathbf{u}_{COD}^- = 2\left\{ \sum_{I \in w_j(\mathbf{x})} \Phi_I(\mathbf{x})\mathbf{a}_I + \sum_{I \in w_b(\mathbf{x})} \Phi_I(\mathbf{x})\mathbf{b}_{II}\sqrt{r} \right\} \qquad (4.15)$$

For the CCI calculations, the span (Δa) was kept as $0.01a$. For the CCI without local smoothing, numerical integration as per Eq. (4.1) is performed over the span Δa. As the displacement fields and stress fields are non-polynomial in nature ahead of crack tip, sub-domain integration is preferred. The span Δa is divided into 5 sub-domains and 5-point Gauss integration scheme in each sub-domain is used to evaluate the integral.

In relation to evaluation of the M-integral, a square domain with an edge length of $0.25a$ centered at the crack tip is considered. For the displacement and stress methods, the COD and stress are evaluated at $0.01a$ ahead of the crack tip and $0.01a$ behind the crack tip respectively.

Table 4.1 shows the mode I and II SIFs obtained using different techniques. It is observed that the local smoothing technique reduces the error associated with the CCI by around 2.5%.

Table 4.1 Mixed-mode SIFs for edge crack subjected to shear traction.

SIF extraction techniques	$K_I(MPa\sqrt{m})$	$K_{II}(MPa\sqrt{m})$
CCI with local smoothing	34.01 (0.03%)	4.50 (-1.09%)
CCI without local smoothing	33.14 (-2.53%)	4.39 (-3.52%)
M-integral	33.72 (-0.82%)	4.48 (-1.54%)
Displacement method	34.77 (2.26%)	4.48 (-1.54%)
Stress method	34.79 (2.32%)	4.56 (0.22%)

Influence of nodal density

Table 4.2 shows the effect of nodal density on the SIFs obtained using the CCI techniques. Good results are obtained even with moderate nodal density (15×33).

Table 4.2 Mixed-mode SIFs for edge crack subjected to shear traction.

Nodal Density	CCI with local Smoothing		CCI without local smoothing	
	K_I	K_{II}	K_I	K_{II}
8×17	33.07 (-2.74%)	4.33 (-4.83%)	32.23 (-5.21%)	4.22 (-7.25%)
15×33	34.01 (0.03%)	4.50 (-1.10%)	33.14 (-2.53%)	4.39 (-3.52%)
29×65	34.48 (1.41%)	4.55 (0.00%)	33.64 (-1.06%)	4.44 (-2.42%)
36×81	33.91 (-0.27%)	4.48 (-1.54%)	33.01 (-2.91%)	4.36 (-4.18%)

The error in the SIFs does not monotonically reduce as the nodal density increases. This sort of observation has been also repeated by Xiaoying et al. (2012) and Gavete et al. (2002). Addition of nodes in the MMs involves both *h*- and *p*-adaptivity. This requires additional background cells for an accurate integration. This also increases the computational cost.

Influence of Gauss quadrature
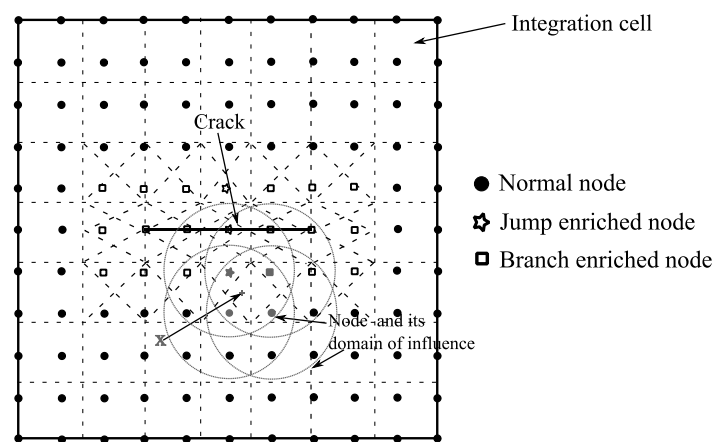
Fig. 4.6 XEFG discretization with enriched nodes around the crack.

The shape functions of the EFG/XEFG method are non-polynomial in nature. Additionally, the presence of enrichment terms requires a higher order Gauss quadrature.

Therefore, the region around the crack is divided into triangular cells to facilitate sub domain integration as shown in Fig. 4.6. It is recommended that a moderate order of quadrature, ($>11^{th}$ order), be used for integration near the crack tip.
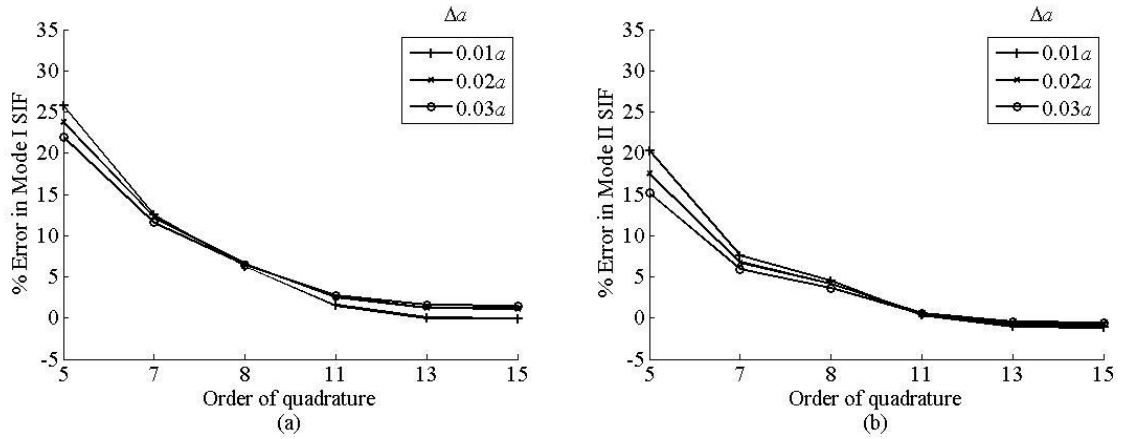
Fig. 4.7 Convergence of SIF with order of quadrature (a) Mode I. (b) Mode II.

Fig. 4.7 shows the convergence of the SIFs with increasing quadrature order for triangular cells. The mode I and mode II SIFs are obtained for six different orders of Gauss quadrature: 5, 7, 8, 11, 13 and 15. Three plots are shown in each figure that correspond to different values of virtual crack extension length, Δa. As the order of quadrature increases, the % error in SIF tends to zero.

Influence of nodal domain of influence (d_I)
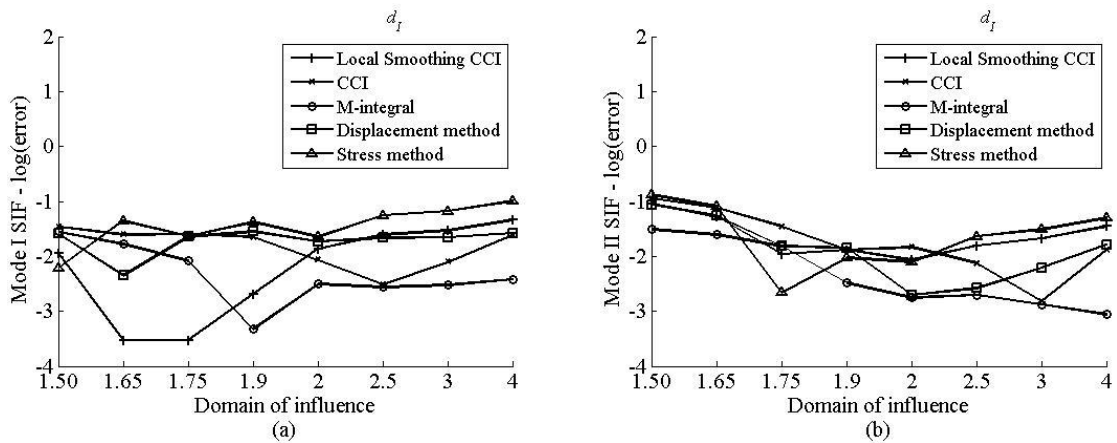
Fig. 4.8 Variation of SIFs with d_I (a) Mode I. (b) Mode II.

The optimal domain of influence/dilation parameter depends on the problem considered. It should be large enough to avoid ill conditioning of the moment matrix.

However, too large a value of d_I will result in smearing of the field solution (Rabczuk et al., 2004). In addition, it increases the bandwidth of the stiffness matrix. Fig. 4.8 shows variation of the mode I and mode II SIFs with dilation parameter. The SIFs error obtained using the CCI with local smoothing is minimum within the range of 1.65 to 2 times the nodal spacing.

Effect of fitting points on the SIFs

The effect of changing the location of the fitting points to model the displacement and traction field on the accuracy of the SIFs has been studied. The displacement variation is obtained according to Eq. (4.2). Table 4.3 shows the mode I and mode II SIFs, for different virtual crack extension lengths, calculated at random locations ahead of the crack tip for traction approximation. The relative standard error (RSE) is less than 0.26%. In Table 4.4, the SIFs are calculated by varying the fitting point locations for displacement approximation. The RSE is less than 0.066%. The traction variation is obtained according to Eq. (4.4).

Table 4.3 Effect of changing the fitting points for traction approximation on SIF.

Fitting points location	Δa							
	0.01a		0.02a		0.03a		0.05a	
	K_I	K_{II}	K_I	K_{II}	K_I	K_{II}	K_I	K_{II}
[0.25, 0.5, 0.75]	34.010	4.500	34.400	4.520	34.500	4.522	34.419	4.515
[0.25 0.75 0.9]	34.013	4.498	34.386	4.516	34.500	4.521	34.492	4.521
[0.1 0.3 0.8]	34.037	4.500	34.485	4.521	34.659	4.530	34.555	4.519
[0.4 0.5 0.6]	34.021	4.499	34.408	4.517	34.498	4.520	34.374	4.513
[0.5 0.65 0.95]	33.987	4.497	34.291	4.511	34.386	4.516	34.620	4.535
Rel. std error	0.048%	0.026%	0.180%	0.078%	0.252%	0.101%	0.258%	0.171%

Table 4.4. Effect of changing the fitting points for displacement approximation on SIF.

Fitting points location	Δa							
	0.01a		0.02a		0.03a		0.05a	
	K_I	K_{II}	K_I	K_{II}	K_I	K_{II}	K_I	K_{II}
[1/16,1]	34.034	4.499	34.440	4.517	34.554	4.521	34.402	4.509
[1/9,1]	34.031	4.499	34.436	4.517	34.550	4.521	34.404	4.512
[1/4,1]	34.010	4.500	34.400	4.520	34.500	4.522	34.418	4.515
[1/3,1]	34.023	4.499	34.429	4.519	34.551	4.523	34.431	4.517
[1/2,1]	34.020	4.500	34.438	4.519	34.556	4.525	34.457	4.521
Rel. std error	0.020%	0.010%	0.040%	0.022%	0.059%	0.029%	0.051%	0.066%

Effect of sub-domain integration on SIFs obtained by CCI

Table 4.5 and Table 4.6 show the effect of increasing the order of the Gauss quadrature and length of sub-domains on the mode I and mode II SIFs obtained by the CCI. The accuracy increases with increase in the number of sub-domains and order of Gauss quadrature. In order to limit the error to 2%, the stresses and displacements needs to be calculated at many points. To help in selecting the order of quadrature and number of subdomain, the errors below 2% given in bold in Tables 4.5 and 4.6. However, for all subsequent case studies 10 sub-domains along with 5th order Gauss quadrature is used to evaluate the CCI.

Table 4.5 % error in mode I SIF with varying order of Gauss quadrature and number of subdomains.

No of Sub-domains	Gauss points					
	1	2	4	5	7	10
1	-19.135%	-11.274%	-6.297%	-5.194%	-3.885%	-2.868%
2	-13.647%	-7.988%	-4.526%	-3.756%	-2.838%	-2.121%
5	-8.691%	-5.126%	-2.976%	-2.529%	**-1.921%**	**-1.465%**
10	-6.209%	-3.715%	-2.203%	**-1.865%**	**-1.459%**	**-1.156%**
20	-4.471%	-2.721%	**-1.671%**	**-1.421%**	**-1.153%**	**-0.924%**

50	-2.944%	**-1.847%**	**-1.191%**	**-1.038%**	**-0.856%**	**-0.697%**
100	-2.179%	**-1.409%**	**-0.929%**	**-0.815%**	**-0.712%**	**-0.653%**
200	**-1.659%**	**-1.112%**	**-0.744%**	**-0.674%**	**-0.638%**	**-0.485%**
500	**-1.171%**	**-0.838%**	**-0.629%**	**-0.535%**	**-0.547%**	**-0.497%**

Table 4.6 % error in mode II SIF with varying order of Gauss quadrature and number of subdomains.

No of Sub-domains	Gauss points					
	1	2	4	5	7	10
1	-20.470%	-12.495%	-7.398%	-6.268%	-4.927%	-3.886%
2	-14.905%	-9.130%	-5.585%	-4.796%	-3.855%	-3.121%
5	-9.846%	-6.200%	-3.998%	-3.516%	-2.916%	-2.451%
10	-7.305%	-4.752%	-3.207%	-2.857%	-2.444%	-2.134%
20	-5.525%	-3.736%	-2.659%	-2.404%	-2.130%	**-1.897%**
50	-3.963%	-2.842%	-2.171%	-2.013%	**-1.826%**	**-1.664%**
100	-3.182%	-2.393%	**-1.903%**	**-1.785%**	**-1.679%**	**-1.618%**
200	-2.648%	-2.086%	**-1.712%**	**-1.640%**	**-1.604%**	**-1.446%**
500	-2.149%	**-1.807%**	**-1.596%**	**-1.499%**	**-1.510%**	**-1.459%**

4.3.2   Center Crack in Finite Plate
Mode I

A plate with dimensions (Fig. 4.9(a)): $2w = 1$m and $L/2w = 2$ is subjected to tensile traction. The plate is discretized with 41×81 nodes as shown in Fig. 4.9(b) and the domain of influence is set at 1.75 times the nodal spacing.

It can be seen from Fig. 4.10 that the CCI with local smoothing consistently predicts the mode I SIF with a satisfactory level of accuracy, independently of the crack length. It is generally as accurate as the M-integral technique and significantly much simpler.
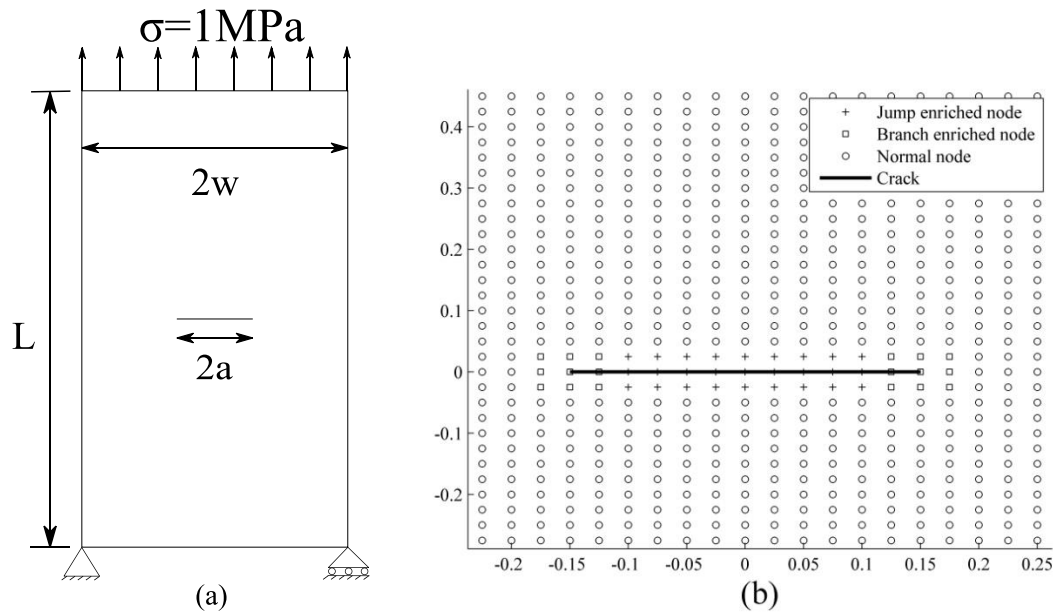
Fig. 4.9 (a) Mode I center crack subjected to tensile load. **(b)** Nodal Discretization.
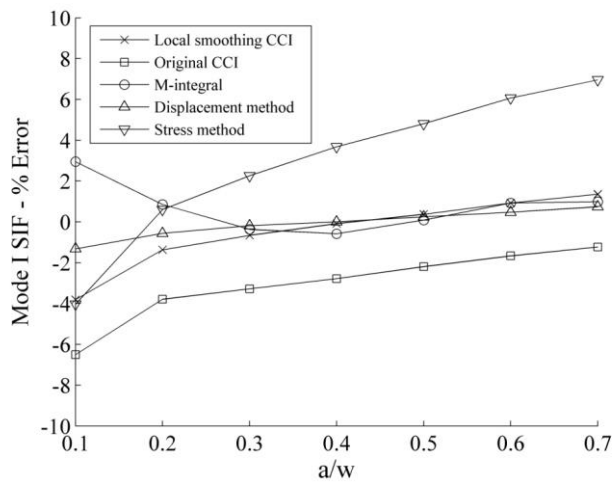
Fig. 4.10 Mode I SIF % error for various center crack lengths.

The mode I SIFs computed with the various techniques are shown in Table 4.7 along with relative error with respect to the analytical solution presented in (Murakami, 1987). K_I by the CCI technique without local smoothing has an error ranging from -6.51% to -1.23%. However, the error is significantly reduced to the range -3.81% to 1.36% by applying the local smoothing technique. The displacement method gives good results with an error band -1.32% to 0.74%, the stress method has the band -4.03% to 6.95%. The high band of error associated with the stress method is because the current XEFG method is based on the displacement approximation. The M-integral gives stable and accurate results with an error band -0.58% to 2.95%.

Table 4.7 Mode I SIFs for center crack in a finite plate using different techniques.

a/w	Murakami (1987)	$K_I(MPa\sqrt{m})$ and % *Error*				
		CCI with local smoothing	CCI without local smoothing	M-integral	Displacement method	Stress method
0.1	0.399	0.384 (-3.81%)	0.373 (-6.51%)	0.411 (2.95%)	0.393 (-1.32%)	0.383 -4.03%
0.2	0.574	0.567 (-1.36%)	0.553 (-3.79%)	0.579 (0.85%)	0.571 (-0.56%)	0.578 0.61%
0.3	0.727	0.722 (-0.66%)	0.703 (-3.28%)	0.724 (-0.37%)	0.725 (-0.18%)	0.743 2.26%
0.4	0.880	0.879 (-0.09%)	0.856 (-2.78%)	0.875 (-0.58%)	0.880 (0.00%)	0.913 3.67%
0.5	1.053	1.057 (0.37%)	1.030 (-2.19%)	1.054 (0.09%)	1.055 (0.25%)	1.103 4.81%
0.6	1.265	1.277 (0.92%)	1.244 (-1.67%)	1.277 (0.92%)	1.272 (0.47%)	1.342 6.07%
0.7	1.558	1.579 (1.36%)	1.539 (-1.23%)	1.573 (0.99%)	1.570) (0.74%)	1.666 6.95%

For smaller size of cracks, the two nodes corresponding to the crack tips influence each another. This leads to slightly erroneous estimates of the field variables and the SIF. The results are expected to improve with local node refinement near the crack tip.
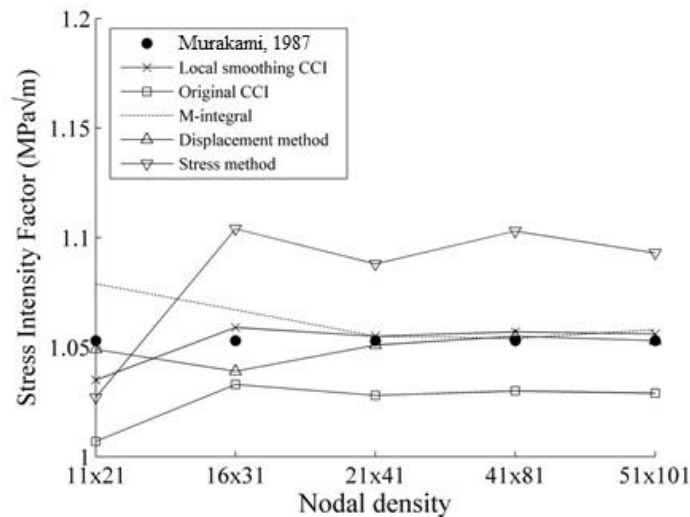
Fig. 4.11 SIF plot with different nodal density.

Fig. 4.11 shows the SIF plot with different nodal density for $a/w=0.5$. The SIFs are obtained using different techniques and compared with the reference results (Murakami, 1987). As seen from the plot, even the lower nodal density (11x21) gives fair results because

of the presence of enrichment functions. The oscillatory nature of SIF obtained using the stress method almost disappears when the CCI technique along with local smoothing scheme is employed. The displacement method also gives good results. The SIFs obtained using different techniques becomes stable with increase in the nodal density.

Mode II

The same plate is now subjected to shear load (Fig. 4.12(a)). The plate is discretized with 41×81 nodes and the domain of influence is again set at 1.75 times the nodal spacing.

Fig. 4.12(b) shows the variation in error in the mode II SIF by different techniques with crack length. The SIFs are obtained by the five techniques mentioned for the earlier case. The results show a trend similar to the case of mode I. Here, too, the error in the SIF by the original CCI method is significantly reduced, in most of the cases, by the application of the local smoothing technique.

(a)   (b)
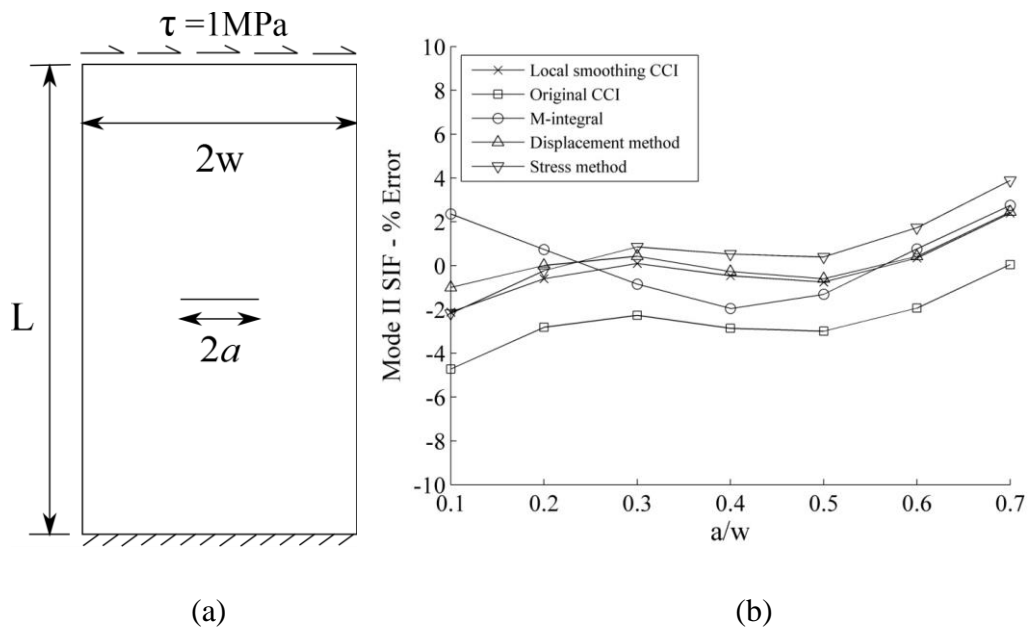
Fig. 4.12 (a) Mode II crack subjected to shear load. **(b)** Mode II SIF for various center crack lengths.

The deviation of the computed SIF by the stress and displacement method (Fig. 4.10 and Fig. 4.12(b)) corresponding to long cracks in plates of finite width may be due to the edge effect. When the crack tip is close to the free boundary, some interactions of the crack-tip stress field with the boundary, which can be free or loaded, is bound to happen and this can lead to errors. Similar situation is likely to happen even in the case of short edge cracks and

short internal cracks. The CCI or interaction integral technique may not get affected because of the underlying principle of the energy difference process and are preferable in the above cases. Out of the two, the CCI technique stands out because of the requirements of computation of stresses and displacements at a relatively few locations to obtain the SIFs.

Table 4.8 shows mode II SIFs and the errors associated with crack length for different techniques. The range of errors in the SIF calculation using different methods are: CCI with local smoothing -2.12% to 2.40%, CCI without local smoothing -4.72% to 0.05%, M-integral -1.96% to 2.75%, displacement method -1.00% to 2.45% and stress method -2.19% to 3.88%.

Table 4.8 Mode II SIFs for center crack in a finite plate using different techniques.

a/w	Murakami (1987)	$K_{II}(MPa\sqrt{m})$ and % *Error*				
		CCI with local smoothing	CCI without local smoothing	M-integral	Displacement method	Stress method
0.1	0.601	0.588 (-2.12%)	0.572 (-4.72%)	0.615 (2.36%)	0.595 (-1.00%)	0.588 (-2.19%)
0.2	0.845	0.840 (-0.60%)	0.822 (-2.82%)	0.852 (0.73%)	0.845 (0.01%)	0.843 (-0.23%)
0.3	1.045	1.046 (0.10%)	1.022 (-2.27%)	1.036 (-0.84%)	1.050 (0.43%)	1.054 (0.85%)
0.4	1.238	1.232 (-0.46%)	1.202 (-2.86%)	1.214 (-1.96%)	1.234 (-0.27%)	1.244 (0.53%)
0.5	1.429	1.418 (-0.75%)	1.386 (-2.99%)	1.410 (-1.31%)	1.420 (-0.60%)	1.434 (0.39%)
0.6	1.622	1.628 (0.35%)	1.591 (-1.94%)	1.635 (0.76%)	1.629 (0.42%)	1.650 (1.73%)
0.7	1.855	1.899 (2.40%)	1.856 (0.05%)	1.906 (2.75%)	1.900 (2.45%)	1.927 (3.88%)

Effect of Δa on SIF obtained by CCI with local smoothing

The effect of the virtual crack extension length, Δa, on the accuracy of the mode I and II SIFs, obtained using the CCI with local smoothing technique, for various centre crack lengths (0.1-0.7) are shown in Fig. 4.13. In order to restrict the error in the SIF within 3%, a range for Δa, $0.01a \le \Delta a \le 0.05a$, is recommended.

There can be two primary sources of error while computing the SIFs through the CCI. If Δa is too small, erroneous solutions are used to compute the SIFs. This will lead to poor solution. If Δa is too large, it may include the region outside the K-dominated region. This

too will lead to a poor solution. Therefore, neither a large nor a small value of Δa is advisable.
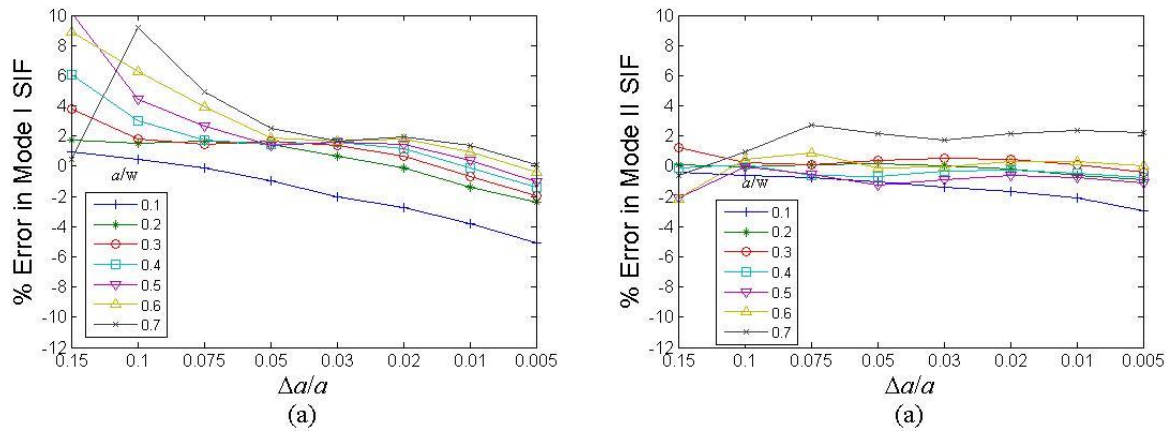
Fig. 4.13 Effect of virtual crack extension length on **(a)** Mode I SIF. **(b)** Mode II SIF.

4.3.3 Angled Crack Centrally Located in a Finite Plate
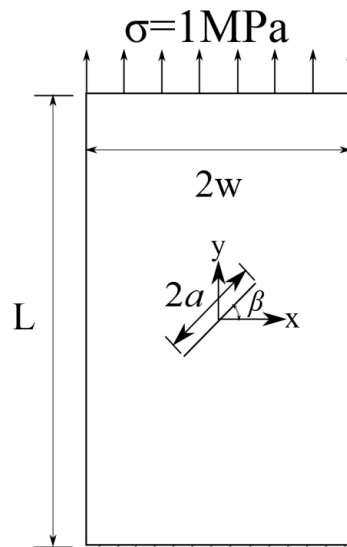
Fig. 4.14 Mixed-mode center crack subjected to tensile traction.

Fig. 4.14 shows a plate with dimensions $2w = 1$ m, $L/2w = 2$ and $a/w = 0.5$ and tensile loading of 1 MPa at the free end. The plate is discretized with 41×81 nodes. The centre crack is inclined at an angle β (in degrees) with x-axis.

As lower nodal density is used, a modified vector extrapolation described in Appendix D is used for the analysis. In this method, the sign needed for the jump enrichment at any generic point is calculated based on the level set values of the closest three nodes. Fig. 4.15 show the variation of mode I and II SIFs with crack orientation.
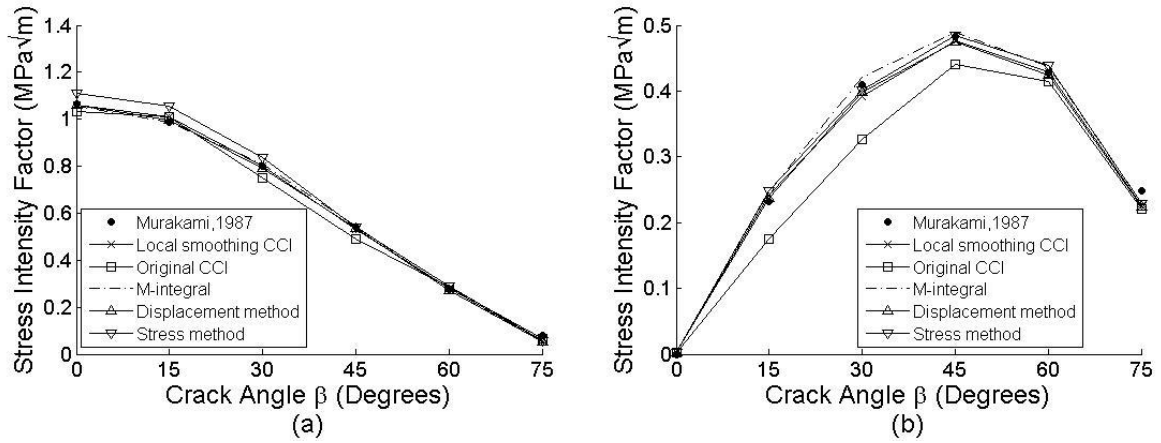
Fig. 4.15 Angle center crack subjected to tension **(a)** Mode I SIF. **(b)** Mode II SIF.

The results obtained by using the CCI in conjunction with local smoothing technique and M-integral are close and compare well with the results available in the literature. The CCI by itself gives inaccurate results for the mode II SIF. However, the local smoothing scheme improves the results. The results obtained by the displacement method are also good.

4.3.4   Mode I Crack Face with Pressure Loading

Fig. 4.16(a) shows a hollow cylinder, inner radius $r_1 = 1\,\text{m}$ and $r_2 / r_1 = 2$, with an inner radial crack of length a. The cylinder is subjected to an internal pressure p. Fig. 4.16(b) shows the variation of the mode I SIF with crack length.
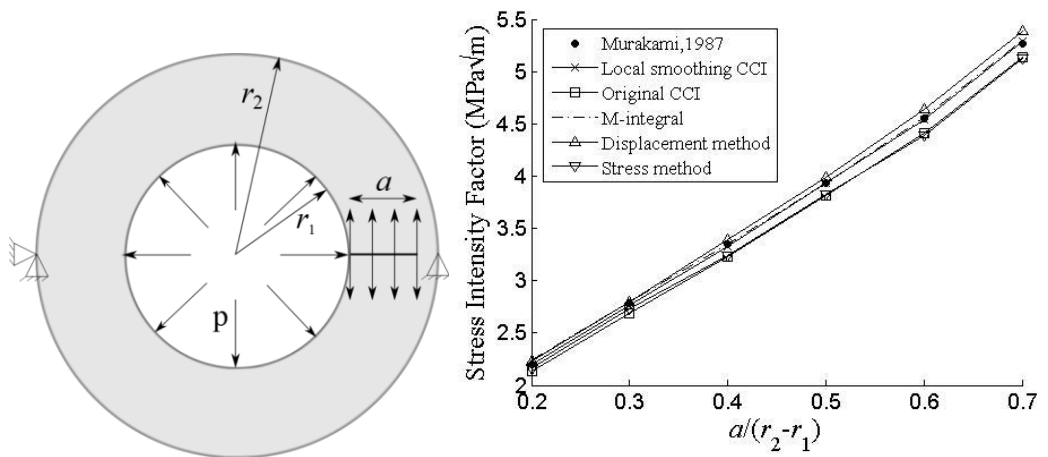
Fig. 4.16 (a) Hollow cylinder with inner radial crack subjected to pressure loading. (b) Mode I SIF for cylinder with an inner radial crack subjected to pressure.

The geometry is discretized with 20 nodes radially and 144 nodes circumferentially as shown in Fig. 4.17(a). The domain of influence varies along the radius in such a way that each

node has an average domain of influence of 1.75 times the nodal spacing. Fig. 4.17(b) shows the deformed cylinder, with crack face opening under the load. The CCI with local smoothing is evaluated by taking into account the pressure loading on the crack edges (Eq. (4.11)). Both the CCI with local smoothing and the M-integral technique give accurate results.

Fig. 4.18 shows the mode I SIF error variation with crack size by the various techniques. The CCI technique along with the local smoothing helps to improve the results. Further, the results by the CCI method with local smoothing are better than the popular M-integral technique.

(a)   (b)
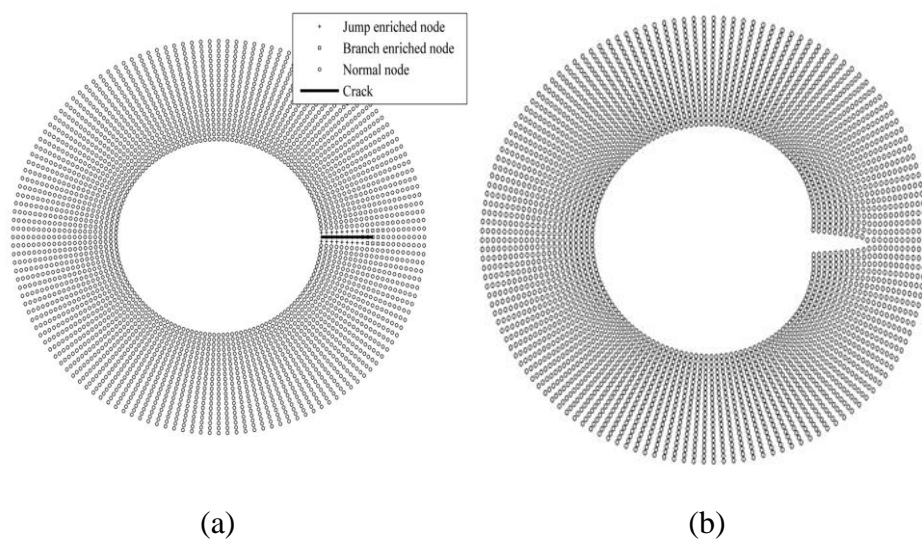
Fig. 4.17 Geometry **(a)** Nodal discretization with crack front. **(b)** Hollow cylinder's deformation due to pressure loading (scaled).
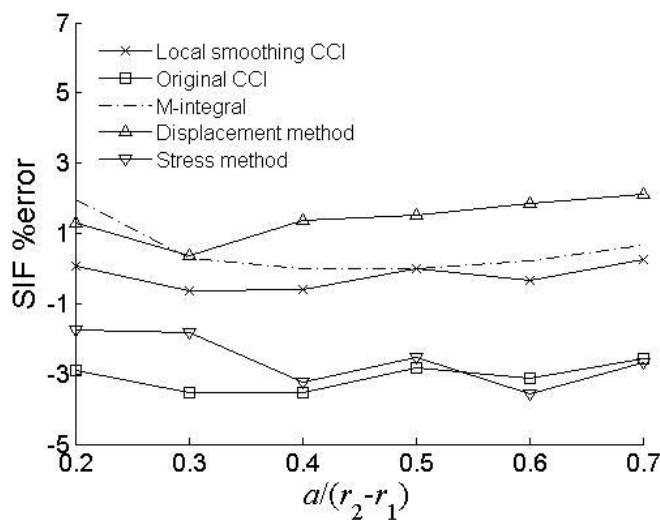
Fig. 4.18 Mode I SIF error for cylinder with an inner radial crack subjected to pressure.

Although there is deviation in the SIF calculated by the stress and displacement methods at higher crack lengths, the SIF obtained by the proposed local smoothing scheme does not deviate significantly.

4.3.5   Thermal Loading due to Linear Temperature Variation

Fig. 4.19 shows a plate with dimensions $w = 1\,\text{m}$ and $L/w = 2$. The geometry is fixed and thermally insulated at the top and bottom edges. A linearly variable temperature field, with extreme value $|T_o| = 100^o c$, is applied. The crack-to-width ratio (a/w) is varied from 0.1 to 0.6. The geometry is discretized with 21×81 nodes. The SIFs obtained are normalized with respect to $E\alpha T_0 \sqrt{w}/(1-v)$. Assuming plane strain conditions, the results are compared with those of Hellen *et al.* (1982) for coefficient of thermal expansion $\alpha = 13 \times 10^{-6}/^o C$. E and v are Young's modulus and Poisson's ratio respectively.
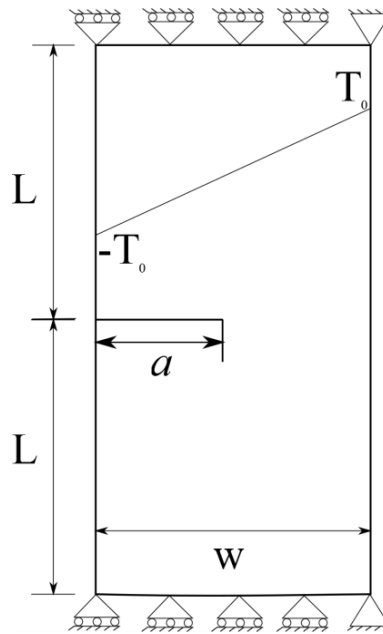
Fig. 4.19 Mode I crack with temperature varying linearly across the width.

The computed mode I SIFs are shown along with the theoretical results in Fig. 4.20. Fig. 4.21 shows the error plots for the SIFs obtained with crack length using different techniques. The SIFs obtained are compared with J-integral results by Hellen et al. (1982). The results obtained by the CCI with local smoothing technique match closely with the reference results. The CCI with local smoothing technique gives good results. Although the SIF obtained by the displacement method is inaccurate for $a/\text{w} = 0.7$, still the CCI-LS gives stable results.
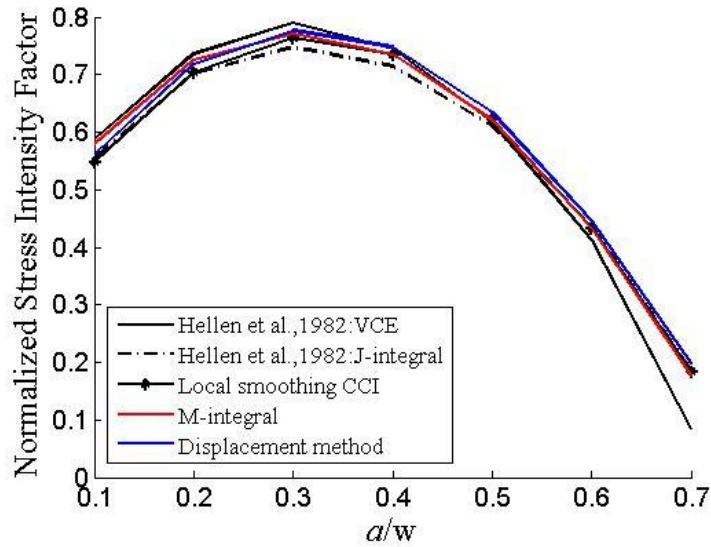
Fig. 4.20 Mode I SIF plot due to thermal load.
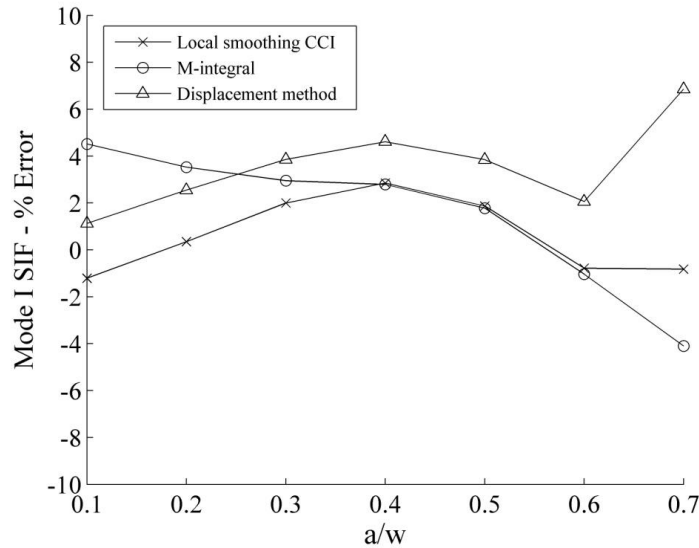
Fig. 4.21 Mode I SIF error plot due to thermal load.

4.3.6   Non Uniform Thermal Loading

Fig. 4.22 and Fig. 4.23 show an isothermal centre crack (temperature is constant on the crack face) and an adiabatic crack (crack faces are considered to be insulated) respectively involving a rectangular plate of dimensions: $w = 0.5$ m and $L/w = 1$. The geometry is discretized with 41×41 nodes. a/w ratio is varied from 0.1 to 0.6. The SIFs obtained are compared with the data of Murakami (1987) and Prasad et al. (1994). The coefficient of thermal expansion $\alpha = 13 \times 10^{-6} /^o c$.

The temperature field was enriched ahead of the crack tip as described by Marc (2008). The thermo-mechanical cases described in the following sections are solved by coupled thermo mechanical analysis (Wang & Zhang, 2011) rather than the two-step analysis, thermal analysis followed by mechanical analysis.

Mode I

The temperature of the center crack is maintained at $\Theta_1 = 0^o C$ and the periphery of the geometry is maintained at $\Theta_2 = 100^o C$ as shown in Fig. 4.22(a). The temperature is constant on the crack surface and the outer boundary of the geometry. Assuming plane strain conditions, the SIFs obtained were normalized with respect to $\alpha(\Theta_2 \text{-} \Theta_1)E\sqrt{2w}$. E and α are Young's modulus and coefficient of thermal expansion respectively.

<table>
<tr><td>(a)</td><td>(b)</td></tr>
</table>
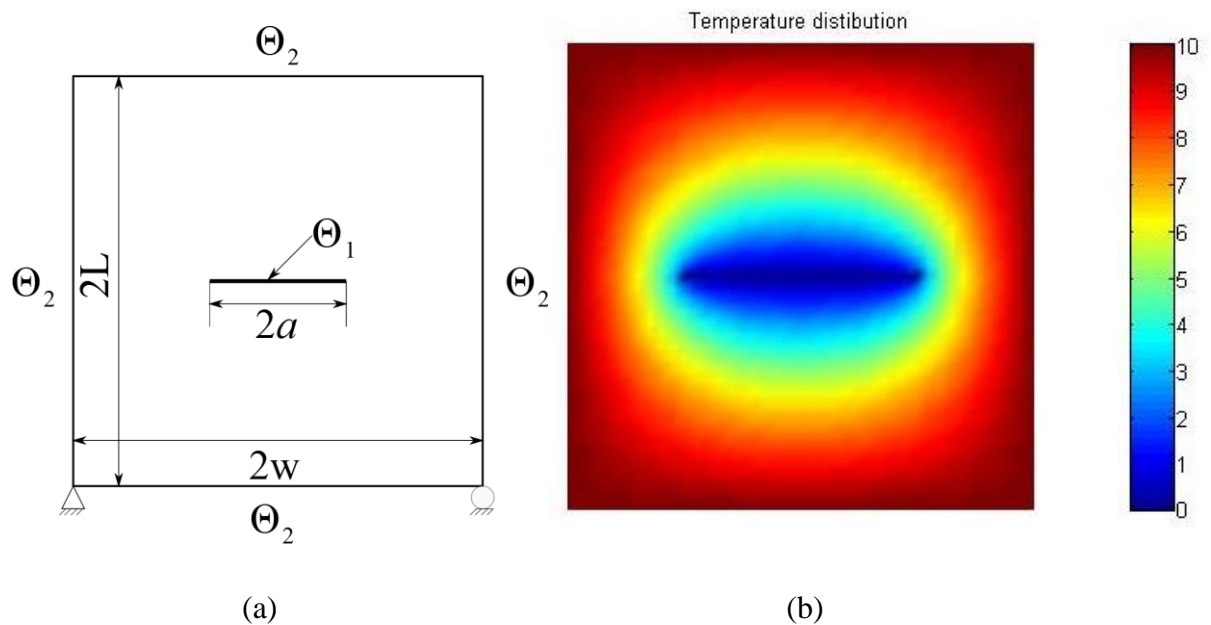
Fig. 4.22 (a) Mode I center crack. **(b)** Temperature distribution.

A modified absolute enrichment function is used to model the temperature field (Moës et al., 2003). The temperature distribution contour is shown in Fig. 4.22(b). Table 4.9 shows the comparison of the mode I SIF obtained using different methods along with the associated relative error with respect to the analytical solution presented by Prasad et al. (1994). In the present case, as the crack extends, the newly formed crack edges gets loaded normally due to finite temperature existing over the extended region. Eq.(4.14) is used to obtain the energy release rates and subsequently the SIFs.

Table 4.9 Mode I SIF for isothermal crack in a square plate.

a/w	Murakami (1987)	Prasad et al. (1994)	Normalized K_I			
			CCI with local smoothing	CCI without local smoothing	M-integral	Displacement method
0.1	0.271	0.268	0.262 (-2.24%)	0.254 (-5.22%)	0.280 (4.48%)	0.266 (-0.75%)
0.2	0.347	0.347	0.342 (-1.44%)	0.333 (-4.03%)	0.349 (0.58%)	0.346 (-0.29%)
0.3	0.406	0.401	0.396 (-1.25%)	0.385 (-3.99%)	0.397 (-1.00%)	0.401 (0.00%)
0.4	0.453	0.448	0.442 (-1.34%)	0.429 (-4.24%)	0.443 (-1.12%)	0.449 (0.22%)
0.5	0.491	0.491	0.489 (-0.41%)	0.475 (-3.26%)	0.488 (-0.61%)	0.493 (0.41%)
0.6	0.526	0.525	0.526 (0.19%)	0.511 (-2.67%)	0.523 (-0.38%)	0.530 (0.95%)

Mode II

(a)   (b)
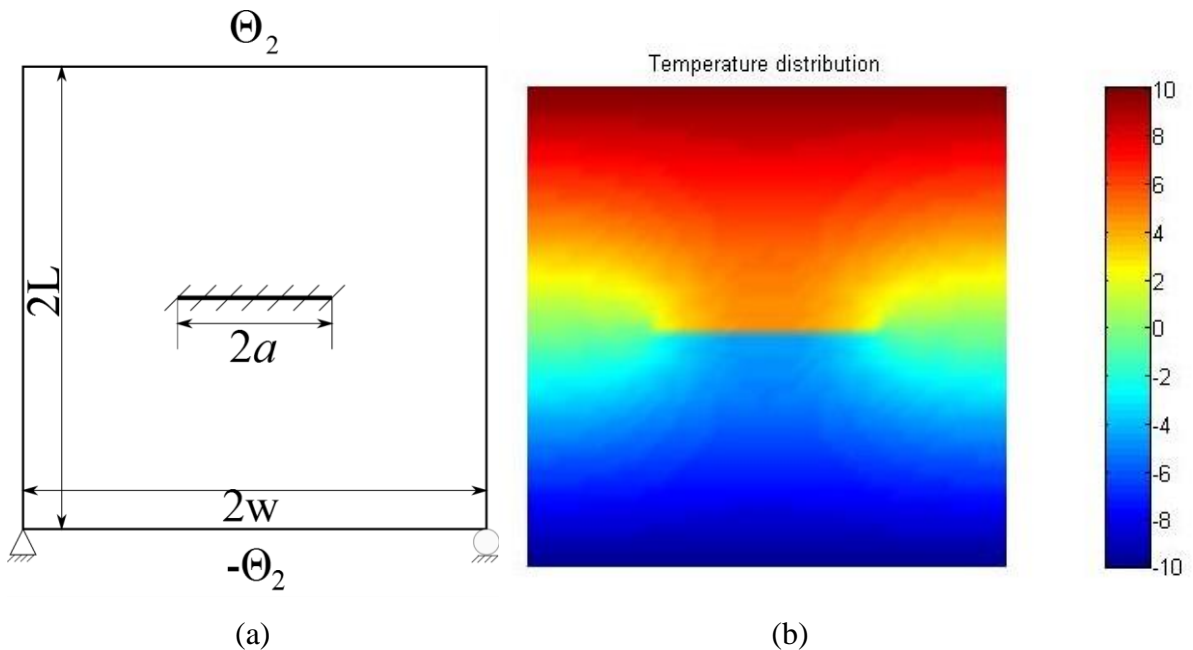
Fig. 4.23 (a) Mode II center crack; **(b)** Temperature distribution.

In this case, in addition to the anti-symmetry with respect to the x-axis, there is also symmetry about the y-axis passing through the center. Therefore, the COD decreases gradually from the crack tip and it becomes zero at the center. Table 4.10 shows the comparison of mode II SIF obtained using different methods along with the relative error with respect to the analytical solution presented by Prasad et al. (1994). The temperature distribution contour is shown in Fig. 4.23(b).

Table 4.10- Mode II SIF for adiabatic crack in a square plate.

a/w	Murakami (1987)	Prasad et al. (1994)	Normalized K_{II}			
			CCI with local smoothing	CCI without local smoothing	M-integral	Displacement method
0.1	0.021	0.018	0.019 (5.56%)	0.019 (5.56%)	0.019 (5.56%)	0.019 (5.56%)
0.2	0.053	0.054	0.053 (-1.85%)	0.052 (-3.70%)	0.053 (-1.85%)	0.053 (-1.85%)
0.3	0.094	0.095	0.094 (-1.05%)	0.092 (-3.16%)	0.093 (-2.11%)	0.093 (-2.11%)
0.4	0.141	0.141	0.140 (-0.71%)	0.137 (-2.84%)	0.137 (-2.84%)	0.139 (-1.42%)
0.5	0.188	0.191	0.189 (-1.05%)	0.186 (-2.62%)	0.186 (-2.62%)	0.188 (-1.57%)
0.6	0.247	0.243	0.243 (0.00%)	0.239 (-1.65%)	0.241 (-0.82%)	0.241 (-0.82%)

The SIFs obtained by the CCI with local smoothing technique and displacement method are in good agreement with the results available in the literature except for $a/w = 0.1$.

4.3.7 Curved crack in an infinite medium

A curved crack in a plate with width $w = 3$ m and length $L = 4$ m, under tension as shown in Fig. 4.24, is studied to demonstrate the effectiveness of the CCI with local smoothing. The plate is considered to be isotropic with Young's modulus $E = 300$ GPa and Poisson's ratio $v = 0.25$. Plane strain conditions are assumed.

The crack is a circular arc with radius $R = 0.425$ m centered at (0, 0.375). It subtends at an angle of $\beta = 28.0725^{o}$ at the center. For such a crack configuration ($a/w = 0.067$) in an infinite medium, the SIFs are given by Gdoutos (1993). The reference results are $K_I = 0.637$ MPa $\sqrt{m}$ and $K_{II} = 0.351$ MPa $\sqrt{m}$.

The plate dimensions are taken significantly larger compared to the crack dimensions to simulate conditions of an infinite medium. The plate is discretized with 61×81 nodes as shown in Fig. 4.25 and the domain of influence is set at 1.75 times the nodal spacing.
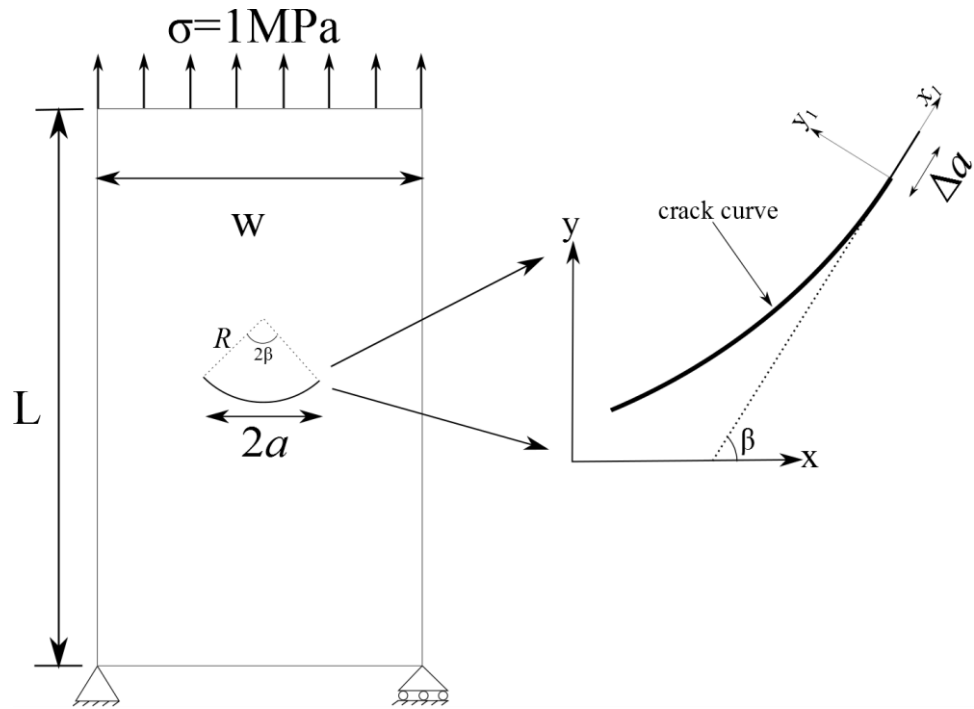
Fig. 4.24 Curved crack in a plate.
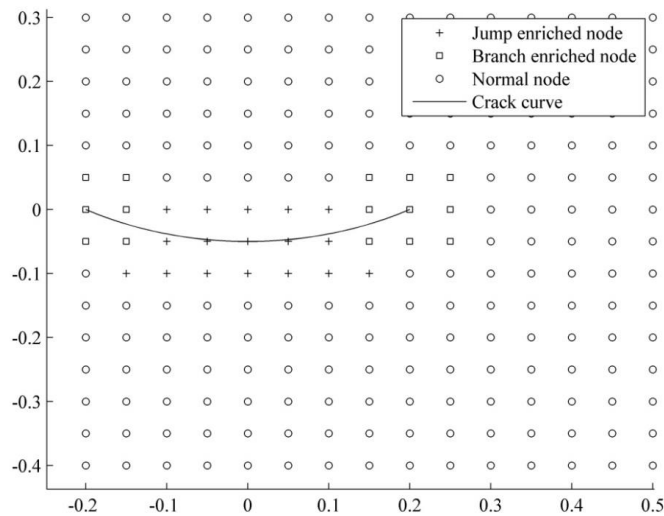
Fig. 4.25 Nodal discretization near the crack.

The CCI is calculated by considering a virtual crack extension Δa along the tangent at the crack tip (Fig. 4.24). Since Δa is small compared to the crack length, it can be taken to be collinear with a similar span behind the crack tip. The stresses and CODs in global coordinates x-y are transformed to the crack-tip local coordinates x_1-y_1 noting that Δa makes an angle β with the global x-axis. The CCI is calculated using these data.

Table 4.11 SIFs for a curved crack in an infinite medium.

SIF extraction techniques	$K_I(MPa\sqrt{m})$	$K_{II}(MPa\sqrt{m})$
CCI with local smoothing	0.656 (2.98%)	0.337 (-3.99%)
CCI without local smoothing	0.629 (-1.26%)	0.287 (-18.23%)
M-integral	0.647 (1.57%)	0.351 (0.00%)
Displacement method	0.633 (-0.63%)	0.333 (-5.13%)
Stress method	0.698 (9.58%)	0.340 (-3.13%)

Table 4.11 shows the mode I and II SIFs obtained using different techniques. The local smoothing technique reduces the error associated with CCI. As expected, M-integral gives good results. As the CCI with local smoothing gives acceptable SIFs for a curved crack, it can be also exploited to study the problems of crack propagation.

4.4 Functionally graded Materials (FGMs)

Functionally graded materials are characterized by pre-determined level of gradual changes in microstructure and material properties spatially. There is no sharp discontinuity in material microstructure and properties. They have been used as thermal barriers in weight-critical applications, in the nuclear industry and in bio-engineering applications (Cherradi et al., 1994; Mortensen & Suresh, 1995; Neubrand & Rode, 1997; Marin, 2005). Their failure is often due to cracks originating and propagating from inclusions and voids.

Delale *et al.* (1983) observed that the nature of crack tip asymptotic solutions, in non-homogenous materials with continuous and differentiable material properties, was identical to that of a solution for homogenous materials. Erdogan (1983) also pointed out that the square root nature of the stress singularity exists at the crack tip in a non-homogeneous medium with smoothly varying elastic properties. Furthermore Eischen (1987) examined mixed-mode crack problem in non-homogeneous materials using the FEM and confirmed the existence of square root singularity stress field around the crack tip. Taking advantage of the situation, it is sufficient to locally enrich the region around the crack tip in a non-homogenous medium by the crack tip solution for homogenous material.

Although, the FEM has been extensively used for modelling damage in the FGMs (Tilbrook et al., 2005; Li et al., 1999; Kim & Paulino, 2002), it involves extensive re-meshing for crack propagation studies, which is computationally costly. Over the past decade, the MMs have been utilized to study the behavior of FGMs (Ching & Yen, 2005; Gilhooley et al., 2008). Rao *et al.* (2003) used the EFG method to obtain the SIFs in a FGM with a crack.

In the next section, the SIFs are obtained for a number of crack problems using the CCI technique with local smoothing. The SIFs were also computed by other standard methods. All are compared with the solutions available in the literature.

4.5 *M*-integral for FGMs

The *M*-integral for FGMs is given by

$$M = \int_A (\sigma_{ij} u_{i,1}^{aux} + \sigma_{ij}^{aux} u_{i,1} - \sigma_{ik} \varepsilon_{ik}^{aux} \delta_{1j}) q_{,j} dA + \int_A (\sigma_{ij} u_{i,1}^{aux} + \sigma_{ij}^{aux} u_{i,1} - \sigma_{ik} \varepsilon_{ik}^{aux} \delta_{1j})_{,j} q dA \qquad (4.16)$$

The first term is identified as I_{nonh}. Since $(\sigma_{ik} \varepsilon_{ik}^{aux} \delta_{1j})_{,j} = \mathbb{C}_{ijkl,1} \varepsilon_{kl} \varepsilon_{ij}^{aux} + \sigma_{ij}^{aux} \varepsilon_{ij,1} + \sigma_{ij} \varepsilon_{ij,1}^{aux}$, the second term in Eq. (4.16) can be simplified to

$$\int_A (\sigma_{ij} u_{i,1}^{aux} + \sigma_{ij}^{aux} u_{i,1} - \sigma_{ik} \varepsilon_{ik}^{aux} \delta_{1j})_{,j} q dA = \int_A (\sigma_{ij,j} u_{i,1}^{aux} + \sigma_{ij} u_{i,1j}^{aux} + \sigma_{ij,j}^{aux} u_{i,1} + \sigma_{ij}^{aux} u_{i,1j}) q dA$$
$$- \int_A (\mathbb{C}_{ijkl,1} \varepsilon_{kl} \varepsilon_{ij}^{aux} + \sigma_{ij}^{aux} \varepsilon_{ij,1} + \sigma_{ij} \varepsilon_{ij,1}^{aux}) q dA \qquad (4.17)$$

Based on the way, second term of Eq. (4.16) is simplified, there are many formulations of *M*-integral available to compute SIFs in FGMs (Kim & Paulino, 2005).

4.5.1 Non-equilibrium formulation (M1)

In the non-equilibrium formulation, the actual and auxiliary states satisfy the compatibility condition ($u_{i,1j} = \varepsilon_{ij,1}$, $u_{i,1j}^{aux} = \varepsilon_{ij,1}^{aux}$). However, the actual state satisfies the equilibrium condition ($\sigma_{ij,j} = 0$) but the auxiliary state does not. This helps to simplify Eq. (4.16) to the following.

$$M = \int_A (\sigma_{ij} u_{i,1}^{aux} + \sigma_{ij}^{aux} u_{i,1} - \sigma_{ik} \varepsilon_{ik}^{aux} \delta_{1j}) q_{,j} dA + \int_A (\sigma_{ij,j}^{aux} u_{i,1} - \mathbb{C}_{ijkl,1} \varepsilon_{kl} \varepsilon_{ij}^{aux}) q dA \qquad (4.18)$$

4.5.2　Incompatibility formulation (M2)

In the incompatibility formulation, the actual state satisfies both the equilibrium ($\sigma_{ij,j} = 0$) and compatibility condition ($u_{i,1j} = \varepsilon_{ij,1}$) but the auxiliary state satisfies only the equilibrium condition ($\sigma_{ij,j}^{aux} = 0$). Thereby, the M-integral takes the form

$$M = \int_A (\sigma_{ij} u_{i,1}^{aux} + \sigma_{ij}^{aux} u_{i,1} - \sigma_{ik} \varepsilon_{ik}^{aux} \delta_{1j}) q_{,j} dA + \int_A (\sigma_{ij}(u_{i,1j}^{aux} - \varepsilon_{ij,1}^{aux}) - \mathbb{C}_{ijkl,1} \varepsilon_{kl} \varepsilon_{ij}^{aux}) q dA \qquad (4.19)$$

The M-integral for a mixed mode problem can also be expressed as follows.

$$M = \frac{(2K_I K_I^{aux} + 2K_{II} K_{II}^{aux})}{E_{tip}^*} \qquad (4.20)$$

where E_{tip}^* is E_{tip} for plane stress and $E_{tip}/(1-v_{tip}^2)$ for plane strain. E_{tip} and v_{tip} correspond to the values at the crack tip. K_I is evaluated from Eq.(4.20) by setting K_I^{aux} to unity and K_{II}^{aux} to zero, Similarly K_{II} is evaluated by setting K_{II}^{aux} to unity and K_I^{aux} to zero.

There is also another formulation based on the actual and auxiliary states satisfying the compatibility and the equilibrium conditions, but the auxiliary state does not strictly satisfy the constitutive relation of the FGM (Rao & Rahman, 2003). This formulation is called CCT formulation in this work. It is to be noted that both the actual and auxiliary states in the M1 and M2 formulation, that are discussed, satisfy the constitutive relation of the FGM.

4.6　Results for FGMs

4.6.1　Mode I edge crack under tensile traction

A plate with dimensions (Fig. 4.26(a)) $w = 1$ m and $L/w = 2$ (length-to-width) is subjected to tensile loading (σ_y). The plate is discretized with 21×41 regularly distributed nodes as shown in Fig. 4.26(b) .The elastic modulus varies exponentially.

$$E(x) = E_1 e^{(\eta x)} \qquad (4.21)$$

where $\eta = \log(E_2/E_1)$, $E_1 = E(0)$ and $E_2 = E(w)$. The value of E_1 is 1GPa . Although the elastic modulus varies, the variation in Poisson's ratio (v) can be considered negligible. Therefore v is kept constant with a value of 0.3. A plane strain condition is assumed. The

crack length a is varied from 0.2 to 0.6. The SIF for each a is calculated with different values of η, 0.1, 0.2, 5 and 10.
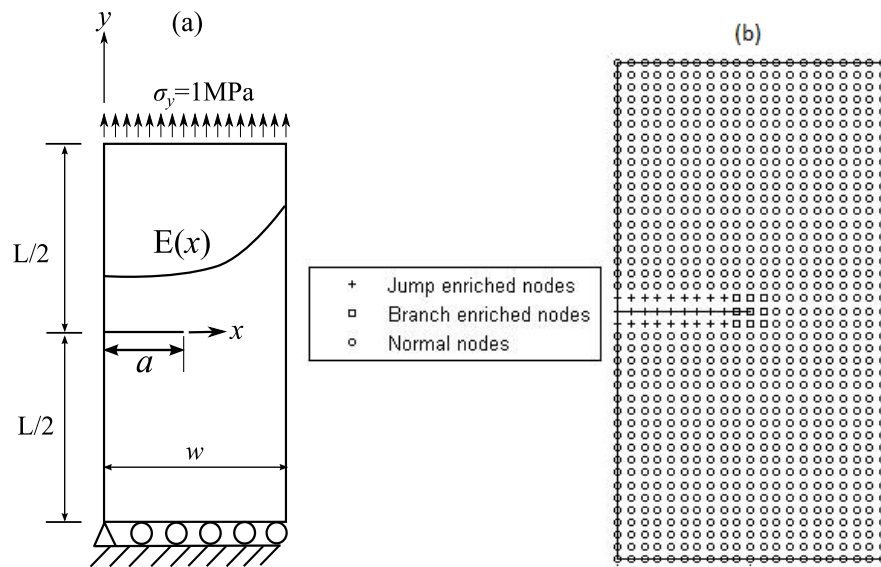
Fig. 4.26 (a) Edge crack subjected to constant tensile traction. **(b)** Nodal discretization.

The SIFs were obtained using five techniques: the CCI with local smoothing (CCI-LS), the CCI without local smoothing, the M-integral method (non-equilibrium formualtion) - M1, M-integral method (incompatibility formulation) - M2, and displacement method. Table 4.12 shows the comparision of the normalized mode I SIFs ($K_I / \sigma_y \sqrt{\pi a}$) obtained by the five methods with results available in the literature (Erdogan & Wu, 1997; Chen et al., 2000). While Erdogan & Wu (1997) obtained the results through analytical approach, Chen et al. (2000) obtained through EFG method.

The span Δa is kept as $0.02a$ for the CCI calculations. For the CCI without local smoothing, sub-domain integration is performed as the displacement and stress vary asymptotically near the crack tip. Δa is divided into 10 sub-domains and 5-point Gauss quadrature is used to evaluate the integral. For calculating M-integral, a square domain with an edge length of $0.25a$ centered at the crack tip is considered. For the displacement method, the COD is evaluated at $0.02a$ behind the crack tip. Unless specified, the above-mentioned parameters for SIF extraction techniques remain the same.

Table 4.12 Mode I SIFs for edge crack subjected to constant tensile traction.

a/w	η	Normalized mode I SIF						
		Erdogan & Wu (1997)	Chen et al. (2000)	CCI-LS	CCI	M1	M2	Displacement method
0.2	0.1	1.297	1.32	1.293	1.267	1.322	1.301	1.286
				-0.31%	-2.31%	1.93%	0.31%	-0.85%
	0.2	1.396	1.419	1.391	1.363	1.417	1.4	1.388
				-0.36%	-2.36%	1.50%	0.29%	-0.57%
	5	1.132	1.162	1.133	1.109	1.147	1.153	1.138
				0.09%	-2.03%	1.33%	1.86%	0.53%
	10	1.002	1.032	1.005	0.983	1.016	1.025	1.01
				0.30%	-1.90%	1.40%	2.30%	0.80%
0.3	0.1	1.864	1.865	1.865	1.83	1.866	1.83	1.85
				0.38%	-1.51%	0.43%	-1.51%	-0.43%
	0.2	1.85	1.849	1.849	1.814	1.844	1.818	1.838
				0.49%	-1.41%	0.22%	-1.20%	-0.11%
	5	1.37	1.39	1.385	1.357	1.364	1.38	1.384
				1.09%	-0.95%	-0.44%	0.73%	1.02%
	10	1.229	1.25	1.245	1.219	1.223	1.244	1.245
				1.30%	-0.81%	-0.49%	1.22%	1.30%
0.4	0.1	2.57	2.559	2.575	2.531	2.565	2.502	2.561
				0.19%	-1.52%	-0.19%	-2.65%	-0.35%
	0.2	2.444	2.449	2.46	2.418	2.441	2.399	2.449
				0.65%	-1.06%	-0.12%	-1.84%	0.20%
	5	1.748	1.775	1.777	1.743	1.732	1.761	1.774
				1.66%	-0.29%	-0.92%	0.74%	1.49%
	10	1.588	1.615	1.617	1.585	1.57	1.608	1.614
				1.83%	-0.19%	-1.13%	1.26%	1.64%
0.5	0.1	3.57	3.521	3.539	3.49	3.557	3.453	3.539
				-0.87%	-2.24%	-0.36%	-3.28%	-0.87%
	0.2	3.327	3.323	3.336	3.288	3.337	3.268	3.336
				0.27%	-1.17%	0.30%	-1.77%	0.27%
	5	2.366	2.413	2.411	2.369	2.355	2.406	2.409
				1.90%	0.13%	-0.46%	1.69%	1.82%
	10	2.176	2.223	2.22	2.181	2.158	2.225	2.219
				2.02%	0.23%	-0.83%	2.25%	1.98%
0.6	0.1	5.188	5.073	5.012	4.961	5.078	4.906	5.05
				-3.39%	-4.38%	-2.12%	-5.44%	-2.66%
	0.2	4.761	4.786	4.725	4.672	4.758	4.65	4.755
				-0.76%	-1.87%	-0.06%	-2.33%	-0.13%
	5	3.445	3.574	3.516	3.465	3.439	3.526	3.524
				2.06%	0.58%	-0.17%	2.35%	2.29%
	10	3.212	3.337	3.282	3.232	3.188	3.306	3.287
				2.18%	0.62%	-0.75%	2.93%	2.33%
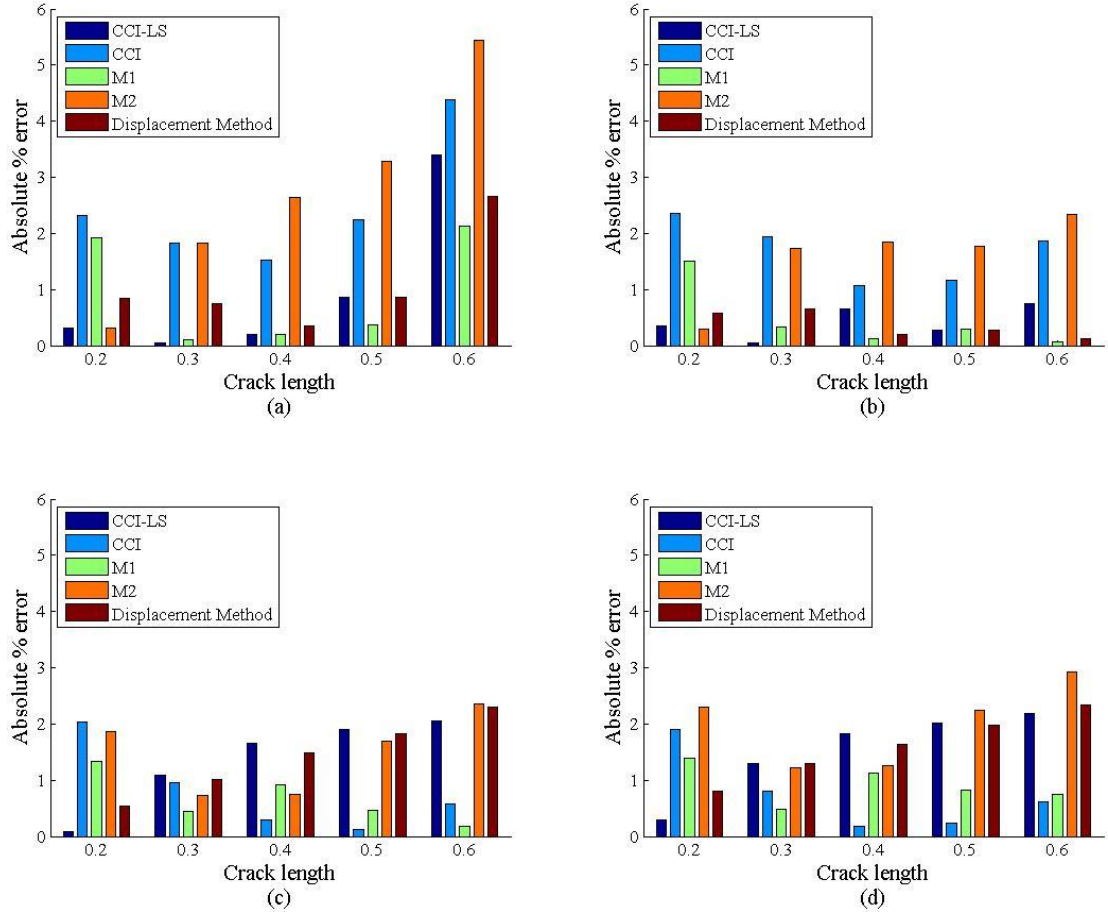
Fig. 4.27 Absolute % error for **(a)** η=0.1 **(b)** η=0.2 **(c)** η=5 **(d)** η=10.

Fig. 4.27 also shows the % error in K_I data compared with theoretical results (Erdogan & Wu, 1997). The CCI technique without local smoothing gives an error e_r in the range -4.38% and 0.62%. However, the error is slightly reduced by applying the local smoothing technique, e_r now lies between -3.39% and 2.18%. The errors e_r by the M1 and M2 integrals lie in the range -2.12% to 1.93% and -5.44% to 2.93% respectively. The displacement method has an error range e_r -2.66% to 2.33%. The errors are indicated below the SIFs, the highest absolute errors are underlined.

4.6.2 Angle crack in plate (Mixed Mode)

The plate with a crack has dimensions, width w=1m and a length-to-width ratio, $L/w = 2$. A normal stress of magnitude $\sigma_{22} = \bar{\varepsilon}\bar{E}\,e^{(\eta(x-0.5))}$, where $\bar{\varepsilon} = 0.001$, is applied on the top boundary of the plate. The plate is discretized with 21×41 nodes.
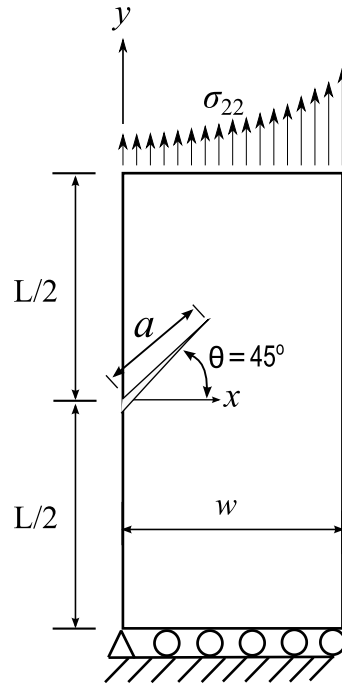
Fig. 4.28 Angle crack under mixed mode.

The crack is oriented at an angle of $45°$ with respect to the x axis with a normalized crack length of $a/w=0.4\sqrt{2}$. The elastic modulus varies exponentially.

$$E(x)=\bar{E}\,e^{(\eta(x-0.5))} \tag{4.22}$$

$\bar{E}$ is set at 1GPa. The mixed mode SIFs are calculated for the following values of parameter η: 0, 0.1, 0.25, 0.5, 0.75 and 1. The Poisson's ratio ν is kept constant at 0.3. A plane strain condition is assumed. The obtained mode I and II SIFs are normalized with respect to $\bar{\varepsilon}\bar{E}\sqrt{\pi a}$,

$$\hat{K}_I = \frac{K_I}{\bar{\varepsilon}\bar{E}\sqrt{\pi a}}$$
$$\hat{K}_{II} = \frac{K_{II}}{\bar{\varepsilon}\bar{E}\sqrt{\pi a}} \tag{4.23}$$

Table 4.13 and Table 4.14 show the mode I and II SIFs calculated for various η, at a fixed crack length, respectively. The results are compared with FEM results (Kim & Paulino, 2003) in the literature. In Table 4.13, it is observed that the SIF based on CCI results are significantly improved by the local smoothing technique.

- 106 -

Table 4.13 Normalized mode I SIF for angle crack under mixed mode.

η	Normalized mode I SIF						
	Eischen (1987)	Kim & Paulino (2003)	CCI-LS	CCI	M1	M2	Displacement method
0.00	1.438	1.451	1.409 -2.89%	1.332 -8.20%	1.437 -0.96%	1.436 -1.03%	1.446 -0.34%
0.10	-	1.396	1.355 -2.94%	1.281 -8.24%	1.380 -1.15%	1.382 -1.00%	1.391 -0.36%
0.25	-	1.316	1.279 -2.81%	1.209 -8.13%	1.300 -1.22%	1.304 -0.91%	1.312 -0.30%
0.50	-	1.196	1.163 -2.76%	1.099 -8.11%	1.178 -1.51%	1.187 -0.75%	1.192 -0.33%
0.75	-	1.089	1.059 -2.75%	1.001 -8.08%	1.070 -1.74%	1.081 -0.73%	1.085 -0.37%
1.00	0.984	0.993	0.966 -2.72%	0.913 -8.06%	0.973 -2.01%	0.987 -0.60%	0.989 -0.40%

K_I by the CCI method without local smoothing has a difference range (d_r) from -8.24% to -8.06%. However, d_r is significantly reduced to a narrow range -2.94% to -2.72% by the application of the local smoothing technique. The displacement method gives excellent results with d_r in the range -0.40% to -0.30%. d_r observed by the M1 and M2 integral methods are: -2.01% to -0.96% and -1.03% to -0.60% respectively.

In Table 4.14, d_r associated with the CCI method, -6.13% to -5.64%, is significantly reduced to -0.35 % to 0.25% by the CCI-LS technique. The performance of the M1 and M2 integral is good with d_r ranges of 0.75% to 1.32% and 1.32% to 4.23% respectively. The displacement method has d_r range of -1.55% to -1.13%.

Table 4.14 Normalized mode II SIF for angle crack under mixed mode.

η	Normalized mode II SIF						
	Eischen (1987)	Kim & Paulino (2003)	CCI-LS	CCI	M1	M2	Displacement method
0.00	0.605	0.604	0.602 -0.33%	0.567 -6.13%	0.612 1.32%	0.612 1.32%	0.595 -1.49%
0.10	-	0.579	0.577 -0.35%	0.544 -6.04%	0.586 1.21%	0.588 1.55%	0.570 -1.55%
0.25	-	0.544	0.543 -0.18%	0.511 -6.07%	0.550 1.10%	0.555 2.02%	0.536 -1.47%
0.50	-	0.491	0.490 -0.20%	0.462 -5.91%	0.496 1.02%	0.505 2.85%	0.484 -1.43%
0.75	-	0.443	0.444 0.23%	0.418 -5.64%	0.447 0.90%	0.460 3.84%	0.438 -1.13%
1.00	0.395	0.402	0.403 0.25%	0.379 -5.72%	0.405 0.75%	0.419 4.23%	0.397 -1.24%

4.6.3   Mode I edge crack under tensile traction
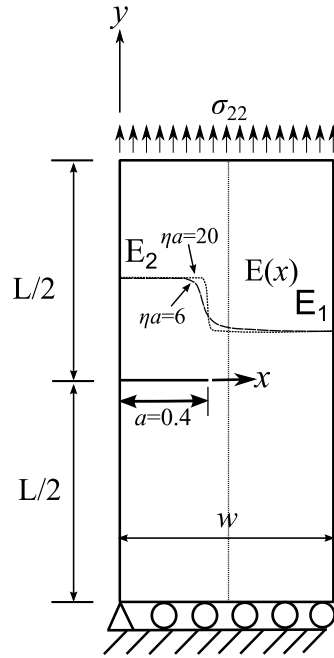
Fig. 4.29 Composite strip with mode I crack.

Consider the composite strip with mode I crack as shown in Fig. 4.29. The strip has dimensions, $w = 1$ m (width) and $L/w = 2$ (length-to-width). It has an edge crack of $a/w = 0.4$. The ν is kept constant 0.3. The variation of elastic modulus is given by

$$E(x) = \frac{E_1 + E_2}{2} + \frac{E_1 - E_2}{2} \tanh(x\eta - 0.4\eta) \qquad (4.24)$$

where $E_1 = 1$ GPa and $E_2/E_1 = 3$. As η increases, the discontinuity in elastic modulus becomes sharper at the crack tip. A plane strain condition is assumed. A tensile traction of $\sigma_{22} = \bar{\varepsilon}E(x)/(1-\nu^2)$, where $\bar{\varepsilon} = 0.001$, is applied on the top boundary to maintain uniform strain. The plate is discretized with 21×41 nodes. Table 4.15 shows the mode I SIFs obtained for different values of ηa. A square domain with an edge length of $0.1a$ centered at the crack tip is considered for the M-integral technique.

Good results are obtained by the XEFG method. The normalized SIFs $\left((1-\nu^2)K_I/\bar{\varepsilon}E(x=0)\sqrt{\pi a}\right)$ are compared in Table 4.15. The following are the error range e_r by the various methods -5.91% to 0.74% by the CCI-LS method, -6.67% to -0.91% by the CCI method, 0.66% to 3.20% by the M1 integral method, -6.70% to 0.66% by the M2 integral method and -6.07% to 0.56% by the displacement method. All the SIF extraction

techniques give rise to higher error as ηa increases. This may be because at higher ηa the material behaves more like a bi-material.

Fig. 4.30 shows the mode I SIFs obtained using the CCI method with local smoothing, and M1 and M2 techniques for various values for Dundurs' parameter. As material 1 becomes more complaint compared to material 2, the value of α increases; the normalized mode I SIF also increases. This suggests that the crack has more tendencies to penetrate into the compliant material that the stiffer material if the fracture toughness of both the materials are the same.
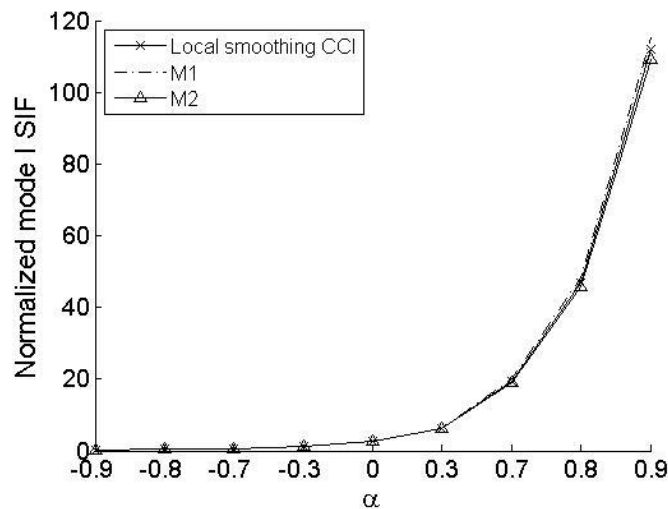
Fig. 4.30 Normalized mode I SIF as a function of the elastic mismatch for $\eta a = 6$.

Table 4.15 Normalized mode I SIF for composite strip.

ηa	Normalized mode I SIF#							
	Eischen (1987)	Rao & Rahman (2003)-CCT	Rao & Rahman (2003)-M2	CCI-LS	CCI	M1	M2	Disp. method
0	2.112	2.133	2.133	2.140 0.33%	2.100 -1.55%	2.147 0.66%	2.147 0.66%	2.133 0.00%
2	2.295	2.304	2.348	2.321 0.74%	2.283 -0.91%	2.341 1.61%	2.316 0.52%	2.317 0.56%
4	2.571	2.589	2.670	2.592 0.12%	2.553 -1.39%	2.633 1.70%	2.578 -0.42%	2.587 -0.08%
6	2.733	2.769	2.879	2.744 -0.90%	2.707 -2.24%	2.811 1.52%	2.723 -1.66%	2.738 -1.12%
20	3.228	3.314	3.579	3.118 -5.91%	3.093 -6.67%	3.420 3.20%	3.092 -6.70%	3.113 -6.07%

#The present results are compared with the reference SIF results obtained by CCT formulation by Rao & Rahman (2003).

4.6.4 Three point bending (TPB) specimen with mode I crack
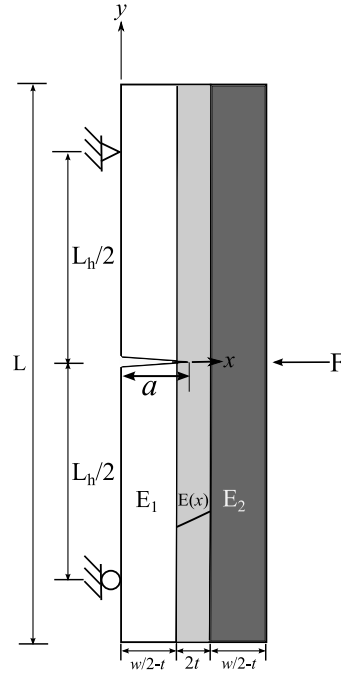
Fig. 4.31 Mode I crack in TPB specimen.

Fig. 4.31 shows a mode I crack in a TPB specimen of three material layers. A FGM layer that is sandwiched between the two layers of homogenous materials. The specimen has dimensions: $w = 1\,\mathrm{m}$ (width) and $L/w = 5.4$ (length-to-width) with a FGM layer of width $2t = 0.1\,\mathrm{m}$. The variation of elastic modulus is assumed as follows

$$E(x)=\begin{cases} E_2, & x > w/2+t \\ \dfrac{E_1+E_2}{2}+\dfrac{E_2\text{-}E_1}{2t}(x\text{-}w/2), & w/2\text{-}t \le x \le w/2+t \\ E_1, & x < w/2\text{-}t \end{cases} \tag{4.25}$$

A plane strain condition is assumed. A concentrated load $F = 1\,\mathrm{MPa}$ is applied (Fig. 4.31). The specimen is constrained at two locations that are equidistant from the *x-axis* such that the ratio, $L_h/w = 5$. The poisons ratio $v = 0.3$. The modulus E_1 is $1\,\mathrm{GPa}$. Three different crack lengths are chosen: $a/w = 0.45, 0.5$ and 0.55 such that the crack tip is either at the material interface or in the middle of the FGM layer. Normalized mode I SIFs as per $K_I\sqrt{w/2}/F$ are obtained for different E_2/E_1 ratios. The specimen is discretized with 21×41 nodes.

The span, Δa, is kept as $0.005a$ for the CCI calculations. A square domain with an edge length of $0.02a$ centered at the crack tip is used for the M-integral technique. The COD is evaluated at $0.005a$ behind the crack tip in the displacement method. Fig. 4.32 shows the absolute % error plot using different techniques compared against published results for different a/w ratios.

Table 4.16 Normalized mode I SIF for TPB specimen with $a/w = 0.45$.

E_2/E_1	Kim & Paulino (2003)	Rao & Rahman (2003) -CCT	Normalized mode I SIF#				
			CCI-LS	CCI	M1	M2	Displacement method
0.05	33.04	32.99	33.91	33.35	33.57	33.37	34.49
			2.63%	0.94%	1.60%	1.00%	4.40%
0.1	23.47	23.61	23.80	23.38	23.76	23.62	24.20
			1.41%	-0.38%	1.24%	0.64%	3.11%
0.2	17.36	17.28	17.38	17.07	17.45	17.36	17.66
			0.12%	-1.67%	0.52%	0.00%	1.73%
0.5	11.65	11.45	11.56	11.34	11.62	11.58	11.71
			-0.77%	-2.66%	-0.26%	-0.60%	0.52%
1	8.13	7.96	8.08	7.92	8.11	8.11	8.17
			-0.62%	-2.58%	-0.25%	-0.25%	0.44%
2	5.24	5.15	5.23	5.12	5.23	5.26	5.29
			-0.19%	-2.29%	-0.19%	0.38%	0.87%
5	2.54	2.51	2.59	2.53	2.54	2.60	2.62
			1.97%	-0.39%	0.00%	2.36%	3.12%
10	1.33	1.31	1.39	1.35	1.32	1.40	1.41
			4.51%	1.50%	-0.75%	5.26%	6.19%
20	0.66	0.66	0.70	0.68	0.63	0.70	0.72
			6.06%	3.03%	-4.55%	6.06%	8.82%

#The present results are compared with the reference SIF results obtained by Kim & Paulino (2003).

Table 4.16, Table 4.17 and Table 4.18 show normalized mode I SIFs obtained for various E_2/E_1 ratios. The results are compared with published data (Kim & Paulino, 2003; Rao & Rahman, 2003). Kim & Paulino (2003) obtained the results through FEM and Rao & Rahman (2003) obtained the results through EFG method. The following are the error range e_r for the SIFs for different a/w ratios, using the various methods (Fig. 4.32): -5.84% to 6.06% by the CCI-LS method, -8.38% to 4.37% by the CCI method, 0.00% to 4.95% by the M1 integral technique, 0.00% to 7.57% by the M2 integral, and 0.03% to 16.32% by the displacement method. Again, the local smoothing scheme improves the results obtained by the CCI technique. The SIFs obtained by the displacement method deviate at extreme ratios of E_2/E_1.

Table 4.17 Normalized mode I SIF for TPB specimen with $a/w = 0.5$.

E_2/E_1	Normalized mode I SIF						
	Kim & Paulino (2003)	Rao & Rahman (2003) -CCT	CCI-LS	CCI	M1	M2	Displacement method
0.05	31.12	31.53	32.92	32.48	30.98	30.42	32.32
			5.78%	4.37%	-0.45%	-2.25%	3.85%
0.1	23.92	23.96	24.69	24.33	23.66	23.27	24.25
			3.22%	1.71%	-1.09%	-2.72%	1.38%
0.2	18.32	18.36	18.56	18.26	18.12	17.87	18.33
			1.31%	-0.33%	-1.09%	-2.46%	0.03%
0.5	12.57	12.30	12.55	12.32	12.48	12.40	12.544
			-0.16%	-1.99%	-0.72%	-1.35%	-0.24%
1	9.47	9.21	9.42	9.22	9.44	9.44	9.51
			-0.53%	-2.64%	-0.32%	-0.32%	0.39%
2	7.32	7.34	7.24	7.09	7.31	7.36	7.40
			-1.09%	-3.14%	-0.14%	0.55%	1.02%
5	5.50	5.47	5.33	5.20	5.47	5.55	5.52
			-3.09%	-5.45%	-0.55%	0.91%	0.40%
10	4.59	4.62	4.37	4.25	4.55	4.63	4.57
			-4.79%	-7.41%	-0.87%	0.87%	-0.45%
20	3.94	3.99	3.71	3.61	3.93	4.00	3.93
			-5.84%	-8.38%	-0.25%	1.52%	-0.28%

Table 4.18 Normalized mode I SIF for TPB specimen with $a/w = 0.55$.

E_2/E_1	Normalized mode I SIF						
	Kim & Paulino (2003)	Rao & Rahman (2003) -CCT	CCI-LS	CCI	M1	M2	Displacement method
0.05	15.21	15.50	14.43	14.25	14.66	14.16	12.73
			-5.13%	-6.31%	-3.64%	-6.90%	-16.32%
0.1	13.73	13.40	13.49	13.30	13.05	12.69	12.54
			-1.75%	-3.13%	-4.95%	-7.57%	-8.68%
0.2	12.79	12.16	12.68	12.47	12.40	12.24	12.21
			-0.86%	-2.50%	-3.05%	-4.30%	-4.51%
0.5	11.76	11.29	11.76	11.55	11.66	11.62	11.69
			0.00%	-1.79%	-0.85%	-1.19%	-0.61%
1	11.15	10.85	11.11	10.89	11.13	11.13	11.22
			-0.36%	-2.33%	-0.18%	-0.18%	0.64%
2	10.62	10.44	10.49	10.28	10.62	10.63	10.73
			-1.22%	-3.20%	0.00%	0.09%	0.99%
5	9.96	9.93	9.73	9.53	9.96	9.99	10.05
			-2.31%	-4.32%	0.00%	0.30%	0.94%
10	9.50	9.59	9.24	9.04	9.50	9.53	9.57
			-2.74%	-4.84%	0.00%	0.32%	0.71%
20	9.12	9.27	8.86	8.67	9.11	9.14	9.16
			-2.85%	-4.93%	-0.11%	0.22%	0.38%

Fig. 4.32 Absolute % error for **(a)** $a/w = 0.45$ **(b)** $a/w = 0.5$ **(c)** $a/w = 0.55$.

4.7 Closure

The classical crack closure integral is augmented with a local smoothing technique to remove the abrupt variations in the computed stress and displacement fields near the crack tip. Two simple formulas, using tractions and displacements at predefined locations on the crack line, have been obtained as expressions for the mode I and mode II SIFs. The possibility of computation of the SIFs through the displacement and stress methods, within the framework of the XEFG, has been demonstrated.

The combined use of the CCI with local smoothing has given rise to simpler method of computation of the SIFs. This method is less tedious than the M-integral technique. Simple expressions for computation of the SIFs are presented. It gives rise to good accuracy consistently for remote loading, thermal loading, and crack face pressure loading. The CCI-LS technique also performed consistently well for a crack in FGMs when compared with results available in the literature.

Chapter 5   Modified Crack Closure Integral

5.1   Introduction

The modified crack closure integral (MCCI)* or virtual crack closure technique (VCCT) has been exploited abundantly in the FEM and, to a lesser extent, in the BEM, to extract the SIFs. Its adoption in the MMs is not that straightforward because it requires the knowledge of crack closure forces. In this chapter, a novel method to extract the nodal forces in the presence of regular nodal discretization in the EFG methods is described. The closure forces at the crack tip and at nodes ahead of it are multiplied with the opening displacements at the corresponding nodes behind the tip to obtain the strain energy release rates (SERRs). To bring out the special issues associated with the adoption, a number of case studies, involving crack edge and thermal loadings, are solved. Thereby the procedural details, effectiveness and accuracy obtainable are presented. In order to emphasize the effectiveness and accuracy of the method, the results obtained by the method are compared with those obtained by the popular M-integral technique, analytical solutions and, wherever possible, by the crack closure integral with local smoothing (CCI-LS) techniques described in the previous chapter.

5.2   MCCI for EFG method

Although the displacement method is a simple technique available to obtain the SIFs, their accuracy can be significantly improved by calculations involving energy release rates. This was clearly shown in the context of FEM (Maiti, 1992). There are many techniques available to calculate the potential energy release rate (PERR) using Eq. (4.1).

Direct Gauss integration method, Universal Crack Closure Integral (UCCI) technique (Singh et al., 1988), CCI-LS technique (Muthu et al., 2013), MCCI/VCCT (Rybicki & Kanninen, 1977; Raju, 1987; Sethuraman & Maiti, 1988) etc., are some of the alternatives through which PERR, and thereby SIFs, can be obtained. The MCCI technique is particularly convenient as it is relatively simple to implement. This technique was successfully applied in the realm of fracture mechanics in composites (Falzon et al., 1999). In addition, the SIFs are easily separated in a mixed mode problem.
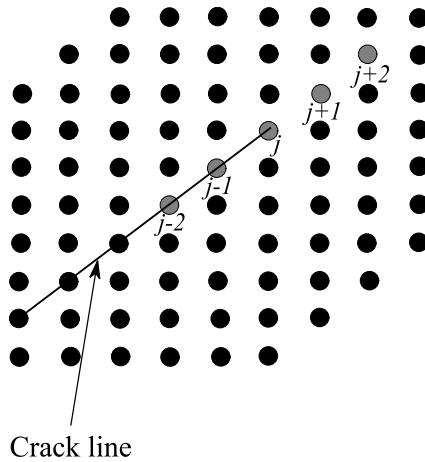
Fig. 5.1 Crack in a regular nodal discretization.

The MCCI/VCCT, in the FEM, requires the calculation of crack closure forces and corresponding CODs to find the SIFs in the context of the LEFM. In this chapter, a new approach for extracting the crack closure forces, for the application of the MCCI technique, within the framework of the EFG method is proposed. The CODs are extracted from the crack edge nodal displacement solution. Consequently, the PERR, which is a function of nodal forces and CODs, is obtained. Consider a crack at an arbitrary angle (Fig. 5.1). A regular nodal discretization where the nodes align with the crack line near the crack tip is used.

In order to compute the crack closure forces, the domain of influence (d_I) for a node j is split along the crack line as shown in Fig. 5.2(a). The stiffness matrix for one of the regions, either the upper or the lower one is obtained. This matrix is multiplied with the nodal displacement vector to obtain the crack closure/nodal reaction forces.

(a)   (b)
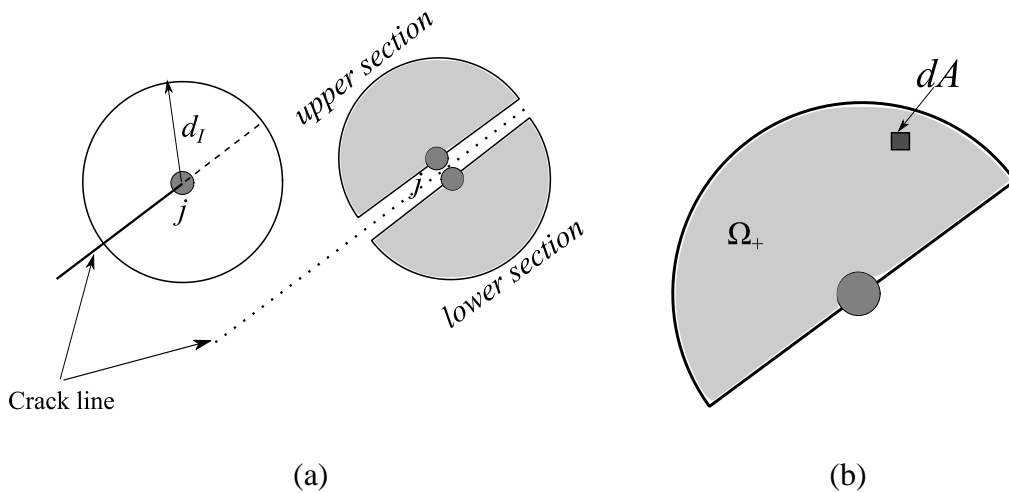
Fig. 5.2 (a) Splitting the domain of influence along the direction of the crack front. **(b)** An infinitesimal element in the upper section

- 115 -

Fig. 5.2(b) shows the upper section of the node j. The stiffness matrix for the upper region, denoted $\Omega+$, is computed by the following equation:

$$\mathbf{K}_{IJ}^{\Omega+} = \int_A \mathbf{B}_I^T \mathbb{C} \mathbf{B}_J \, t \, dA; \; I,J \in w_{\Omega+}(\mathbf{x}) \tag{5.1}$$

where $\mathbf{B}$ is a strain-displacement matrix, t is the thickness and A is the area enclosed by the upper or lower section (Fig. 5.2). Here, it is also a function of the crack front orientation. The set $w_{\Omega+}(\mathbf{x})$ includes only those nodes that are on and above the crack line. Similarly, the stiffness matrix, $\mathbf{K}_{IJ}^{\Omega-}$, for the lower section is computed by considering the nodes on and below the crack line.

The strain-displacement matrix, $\mathbf{B}$, for the classical EFG methods including the visibility and the diffraction method is given by

$$\mathbf{B} = \mathbf{B}^{std} = \begin{bmatrix} \Phi_{1,x} & 0 & ... & \Phi_{i,x} & 0 & ... & \Phi_{n,x} & 0 \\ 0 & \Phi_{1,y} & ... & 0 & \Phi_{i,y} & ... & 0 & \Phi_{n,y} \\ \Phi_{1,y} & \Phi_{1,x} & ... & \Phi_{i,y} & \Phi_{i,x} & ... & \Phi_{n,y} & \Phi_{n,x} \end{bmatrix} \tag{5.2}$$

where i indicates the node number lying either in the top or the bottom segment of the domain of influence of the current node j. For the XEFG method, the $\mathbf{B}$ matrix also comprises of extra terms due to the enrichment. It is given by

$$\mathbf{B} = [\mathbf{B}^{std} \mid \mathbf{B}^{enr}]$$
$$\mathbf{B}_{i,k}^{enr} = \begin{bmatrix} \Phi_{i,x}\Psi_k + \Phi_i\Psi_{k,x} & 0 \\ 0 & \Phi_{i,y}\Psi_k + \Phi_i\Psi_{k,y} \\ \Phi_{i,y}\Psi_k + \Phi_i\Psi_{k,y} & \Phi_{i,x}\Psi_k + \Phi_i\Psi_{k,x} \end{bmatrix} \tag{5.3}$$

where $\mathbf{B}_{i,k}^{enr}$ matrix comprises of the derivatives of the regular shape functions and the enrichment functions of the enriched nodes.

The integral in Eq. (5.1) is calculated by the numerical integration. To facilitate the integration either the top or the bottom segment of the circular domain of influence is subdivided into smaller triangles (Fig. 5.3). The Gauss point location to suit integration of 8th order complete polynomial (Dunavant, 1985), are indicated by '*'. X-Y is the global axis and x-y is the local axis at the crack tip; $+x$ points towards the direction of crack extension.
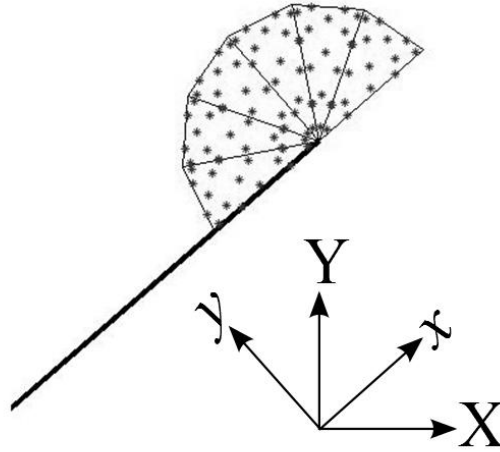
Fig. 5.3 Splitting of upper section into smaller triangles for numerical integration.

Even if the domain of influence is not circular, the top or the bottom regions of the crack line can be sub-divided for an accurate evaluation of the stiffness matrix. It is recommended to use higher order integration to calculate the crack forces accurately. The Gauss integration is carried out as follows.

$$\int_A \mathbf{B}_I^T \mathbb{C} \mathbf{B}_J t dA = \sum_i \mathbf{B}_I^T (\xi_i) \mathbb{C} \mathbf{B}_J (\xi_i) w_i \det J(\xi_i) t \tag{5.4}$$

where ξ_i is the Gauss point, w_i is the Gauss weight and $\det J(\xi_i)$ is the determinant of the Jacobian of the background triangular element at ξ_i. The nodal force vector is calculated by

$$\mathbf{K}^{\Omega+} \mathbf{U}^{\Omega+} = \mathbf{F} \tag{5.5}$$

where $\mathbf{U}^{\Omega+}$ is the nodal displacement vector of the nodes contained in $\Omega+$.
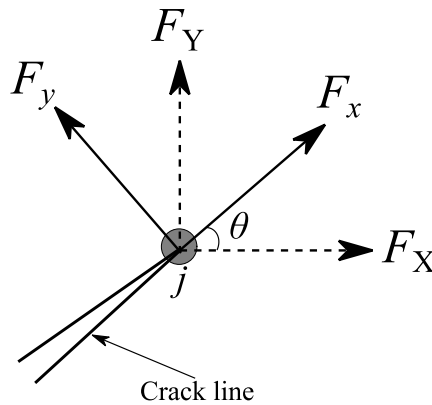
Fig. 5.4 Transformation of forces into local axis at the crack tip.

The nodal force vector can also be extracted at node j+1 by following the same procedure as mentioned above. The obtained forces are transformed to the local crack tip coordinates (Fig. 5.4) through the following relation:

$$\{\mathbf{F}\}_{xy} = [\mathbf{T}]\{\mathbf{F}\}_{XY}$$
$$\mathbf{T} = \begin{bmatrix} \cos\theta & -\sin\theta \\ \sin\theta & \cos\theta \end{bmatrix}$$

(5.6)

where $\{\mathbf{F}\}_{xy} = \{F^x, F^y\}$, $\{\mathbf{F}\}_{XY} = \{F^X, F^Y\}$ and θ is the angle at which the crack front is inclined to the X axis. In the XEFG method, contributions of additional forces due to branch enrichment are also taken into account.

Fig. 5.5 Crack closure forces and crack opening displacements.

The PERR are given by

$$G_I = \frac{1}{2\chi_{j,j-2}}[F_j^y v_{COD}^{j-2} + F_{j+1}^y v_{COD}^{j-1}]$$
$$G_{II} = \frac{1}{2\chi_{j,j-2}}[F_j^x u_{COD}^{j-2} + F_{j+1}^x u_{COD}^{j-1}]$$

(5.7)

where $\chi_{j,j-2}$ is the distance between j^{th} and j-2th nodes (Fig. 5.5). The denominator in Eq.(5.7), $\chi_{j,j-2}$, is analogous to the virtual crack extension length, Δa, used for MCCI/VCCT. In the FEM, Δa is the length along the crack line by which the crack is assumed to propagate.

A general MCCI equation for extracting the PERR, involving calculation of forces at n nodal points along the crack line can be written as

$$G_I = \frac{1}{2\chi_{j,j-n}} \sum_{i=0}^{n-1} F_{j+i}^{y} v_{COD}^{j-n+i}$$

$$G_{II} = \frac{1}{2\chi_{j,j-n}} \sum_{i=0}^{n-1} F_{j+i}^{x} u_{COD}^{j-n+i}$$

(5.8)

As n increases in Eq.(5.8), the accuracy of the PERR increases. This is demonstrated through a case study in a later section.

5.2.1 MCCI in the presence of crack face loading

In presence of crack face loading, the newly formed crack faces are also subjected to loading as shown in Fig. 5.6. Therefore, additional work has to be done to close the extended crack.
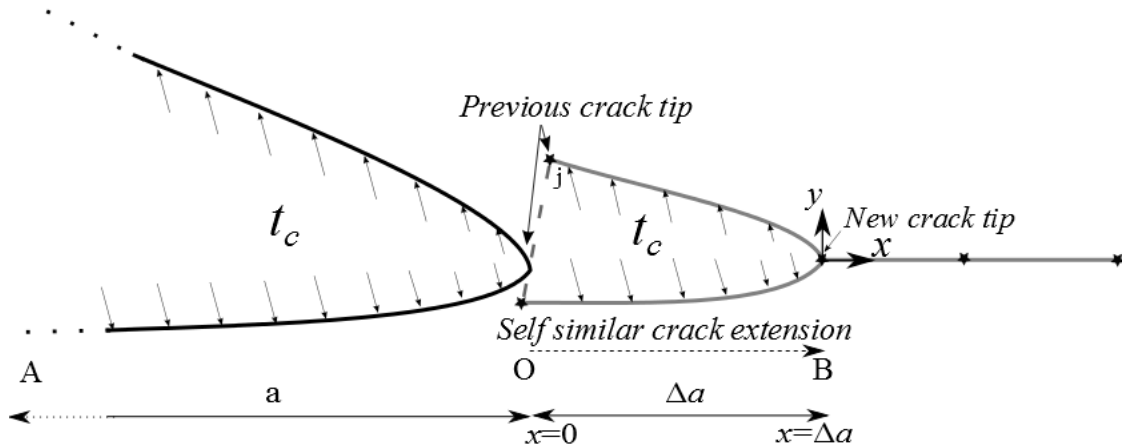
Fig. 5.6 Newly formed crack faces subjected to crack face loading.

The PERRs, in such a case, are then given by

$$G_I = \frac{1}{2\chi_{j,j-2}} [(F_j^{y} + F_{j-2}^{y}) v_{COD}^{j-2} + (F_{j+1}^{y} + F_{j-1}^{y}) v_{COD}^{j-1}]$$

$$G_{II} = \frac{1}{2\chi_{j,j-2}} [(F_j^{x} + F_{j-2}^{x}) u_{COD}^{j-2} + (F_{j+1}^{x} + F_{j-1}^{x}) u_{COD}^{j-1}]$$

(5.9)

where $\mathbf{F}_{j-1}$ and $\mathbf{F}_{j-2}$ are the nodal forces due to distributed load t_c on the crack faces.

5.2.2 MCCI in the presence of thermal loading

The mechanical strain, when thermal strain is present, is related to the total strain by

$$\varepsilon_{ij}^m = (\varepsilon_{ij}^t - \alpha^* \Delta T \delta_{ij}) \tag{5.10}$$

where ε_{ij}^m is the mechanical strain, ε_{ij}^t is the total strain, α^* is the coefficient of thermal expansion and ΔT is the temperature difference. Therefore, the resulting stiffness matrix is given by

$$\mathbf{K}_{IJ}^{mech} = \mathbf{K}_{IJ}^{total} - \mathbf{K}_{IJ}^{thermal}$$
$$\mathbf{K}_{IJ}^{total} = \int_A \mathbf{B}_I^T \mathbb{C} \mathbf{B}_J t dA;\ I,J \in w_{\Omega+}(\mathbf{x}) \tag{5.11}$$
$$\mathbf{K}_{IJ}^{thermal} = \int_A \mathbf{B}_I^T \mathbb{C} \alpha^* \begin{Bmatrix} \Delta T \\ \Delta T \\ 0 \end{Bmatrix} t dA$$

The resulting mechanical stiffness matrix, $\mathbf{K}_{IJ}^{mech}$, is then multiplied with the nodal displacement vector to obtain the residual nodal forces.

5.3 Accurate Extraction of the Nodal Force

Consider a bar of uniform cross section, A, of unit area and of unit length, L, as shown in Fig. 5.7. The bar is subjected to a point tensile load, P, of 10 MPa at its end. This problem is solved using 1D analysis with displacement (u_x) set to zero at the origin.
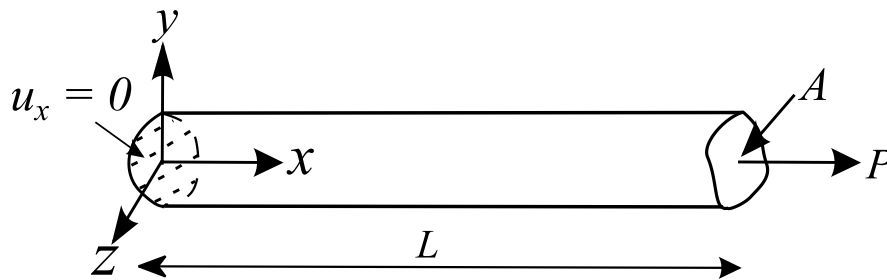
Fig. 5.7 Bar subjected to a point load at the end.

The bar is discretized with different nodal distributions. The domain of influence (d_I) of each node is constant and is set at $1.75\dfrac{L}{(n-1)}$ where n is the total number of nodes. Here n is equal to 11.

The force at the node of interest, j, can be extracted in two ways (*I* or *II*) as shown in Fig. 5.8. Either way, the stiffness matrix is established by the following relation

$$\mathbf{K} = \int_l \mathbf{B}^T \mathbb{C} \mathbf{B} A dx \qquad (5.12)$$

where $l = l_- = l_+ = 1.75 \dfrac{L}{2(n-1)}$. $\mathbb{C}$ is the Young's modulus, A is the area of the cross section and $\mathbf{B}$ is the standard strain-displacement matrix.

The goal here is to extract the force accurately at node located at $x=0.5$. Four nodal discretization arrangements, as shown in Fig. 5.9, are considered for an examination. The effect of location of the adjacent nodes around node, j, (darkened node) on the extraction of nodal force is studied. The first configuration (a) consist of equally spaced nodes while others (b), (c) and (d) have variable spacing.
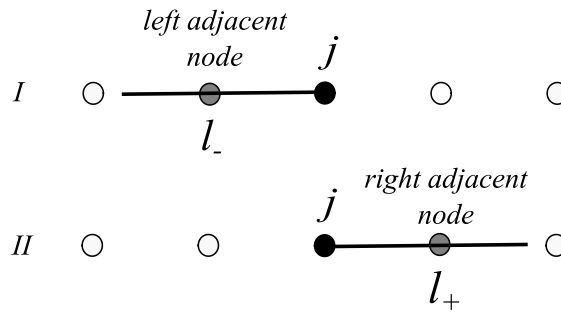
Fig. 5.8 Splitting the d_I for the node of interest j.

The force (F) at the node j is extracted using Eq. (5.5). Table 5.1 shows the force obtained for different configurations for an applied load P. It is clear that the error in computed forces F_I and F_{II} is zero for the configuration (a) with equally spaced nodes. The error is higher in the case of unstructured distribution of nodes (configuration (b), (c) and (d)). The averaged magnitude of the computed force (F) shows a relatively lower error. Therefore, for all subsequent studies, the average of two parts of forces has been used to compute the nodal force. It is given by

$$\mathbf{F} = \frac{1}{2}\left(\mathbf{K}^{l-}\mathbf{U}^{l-} - \mathbf{K}^{l+}\mathbf{U}^{l+}\right) \qquad (5.13)$$
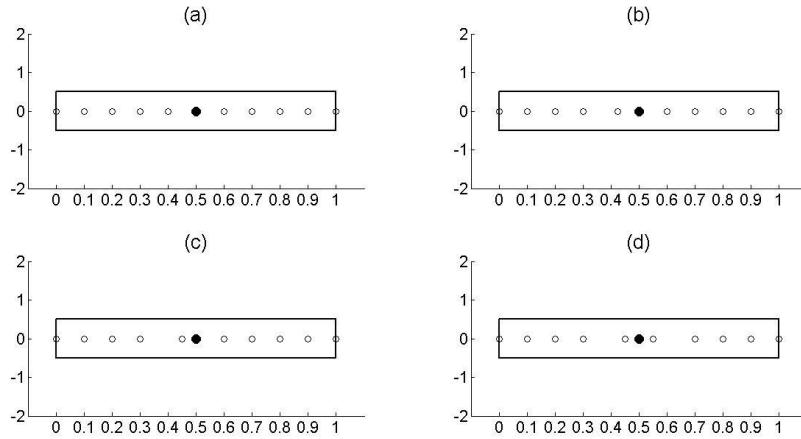
Fig. 5.9 Different nodal discretization.

Table 5.1 Force obtained for different nodal discretization.

Configuration	F_I (MN)	F_{II} (MN)	% error in F_I	% error in F_{II}	Average of F_I and $-F_{II}$ (F)	% error in F
(a)	10.0000	-10.0000	-0.0001%	-0.0001%	10.0000	0.0000%
(b)	10.0055	-9.9959	0.0552%	0.0414%	10.0007	0.0069%
(c)	10.1957	-9.9034	1.9575%	0.9658%	10.0496	0.4958%
(d)	10.1148	-10.1148	1.1478%	-1.1479%	10.1148	1.1478%

5.4 Results

In this section, the developed technique is applied to a number of crack problems including crack face pressure loading and thermal-mechanical loading. The PERR, and in turn the SIFs, computed using the proposed method and other standard methods are compared with the solutions available in the literature.

The SIFs are extracted using the four techniques: the MCCI technique, the M-integral method, the displacement method, and the stress method. The MCCI technique is employed here by calculating crack closure forces at the two nodes, in the direction along the crack line, and multiplying with the corresponding crack opening displacements. The M-integral is calculated using a square domain with edge length of $0.25a$. For displacement and stress methods, the COD and stress are evaluated at $0.02a$ behind the crack tip and at $0.02a$ ahead of the crack tip respectively.

5.4.1 Mixed-mode edge crack in finite plate

The dimensions of the plate are width $w = 1\,\text{m}$ and $L/w = 2$ (Fig. 5.10(a).) The plate is discretized with 41×81 nodes (Fig. 5.10(b)) and it is subjected to traction of $1\,\text{MPa}$ at the upper edge. The crack length a is varied from $0.1w$ to $0.8w$.. The domain of influence is set at 1.75 times the regular nodal spacing (δ). The materials are assumed to be isotropic with Young's modulus $E = 210\,GPa$ and Poisson's ratio $v = 0.3$. A Gauss integration of 8th order is used, in the background triangular cells, for the cases studied.
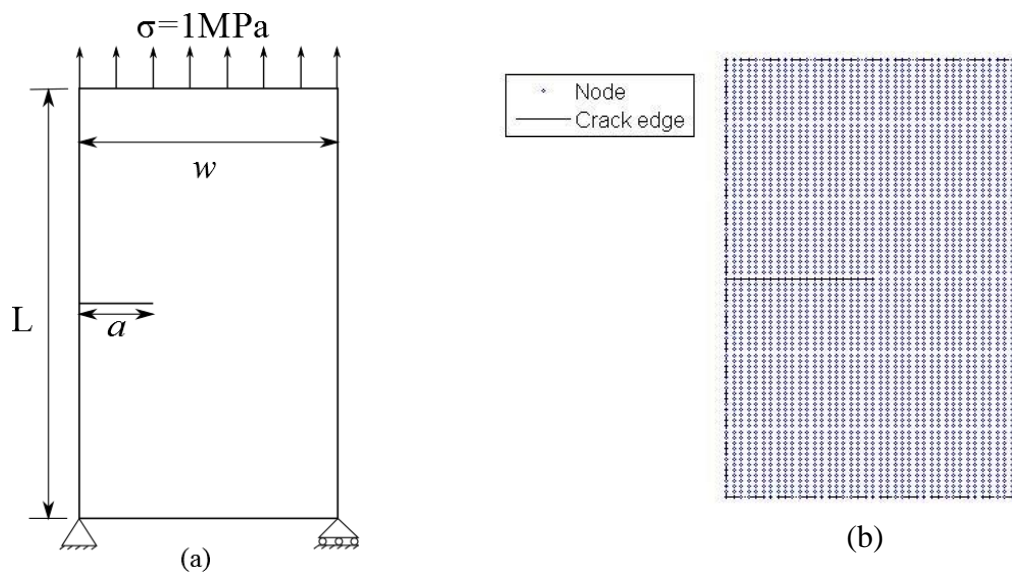
Fig. 5.10 Mode I edge crack **(a)** Geometry. **(b)** Nodal Discretization.

Table 5.2 and Table 5.3 show the mode I SIFs obtained using the four techniques through the visibility and diffraction methods respectively. The results obtained by the MCCI and M-integral methods are in good agreement with the reference results (Murakami, 1987) for $a/w \le 0.6$; and (Gross & Seelig, 2011) for $a/w > 0.6$. For better understanding, % error in the SIFs through the methods of visibility, diffraction and XEFG is plotted in Fig. 5.11(a), Fig. 5.11(b) and Fig. 5.12 respectively.

The stress method gives poor results in all cases. The displacement method too fails for the visibility and diffraction methods (Fig. 5.11(a) and Fig. 5.11(b)). However, the displacement method gives good results in the XEFG method (Fig. 5.12) because of the enrichment functions. Notably, the MCCI approach gives good results, for visibility and diffraction methods, despite poor accuracy of the computed COD. The results obtained by the CCI-LS technique using 37-point Gauss quadrature in the background cells to suit 13th order polynomial in the XEFG method are comparable with the results of the MCCI approach.

Table 5.2 Mode I SIFs for an edge crack using visibility method.

a/w	Murakami (1987) Gross & Seeli (2011)	$K_I(MPa\sqrt{m})$			
		MCCI	M-integral	Displacement method	Stress method
0.1	0.663	0.656	0.526	0.433	0.230
0.2	1.087	1.068	1.032	0.671	0.521
0.3	1.612	1.590	1.563	1.048	0.928
0.4	2.358	2.337	2.310	1.658	1.540
0.5	3.543	3.493	3.469	2.680	2.510
0.6	5.529	5.480	5.463	4.548	4.219
0.7	9.433	9.311	9.321	8.328	5.365
0.8	19.007	18.775	18.878	18.236	9.020

Table 5.3 Mode I SIFs for an edge crack using diffraction method.

a/w	Murakami (1987) Gross & Seeli (2011)	$K_I(MPa\sqrt{m})$			
		MCCI	M-integral	Displacement method	Stress method
0.1	0.663	0.655	0.537	0.282	0.207
0.2	1.087	1.066	1.038	0.639	0.467
0.3	1.612	1.587	1.570	1.032	0.837
0.4	2.358	2.332	2.318	1.645	1.397
0.5	3.543	3.488	3.481	2.661	2.292
0.6	5.529	5.464	5.473	4.506	3.859
0.7	9.433	9.294	9.336	8.264	4.815
0.8	19.007	18.701	18.860	18.051	7.978
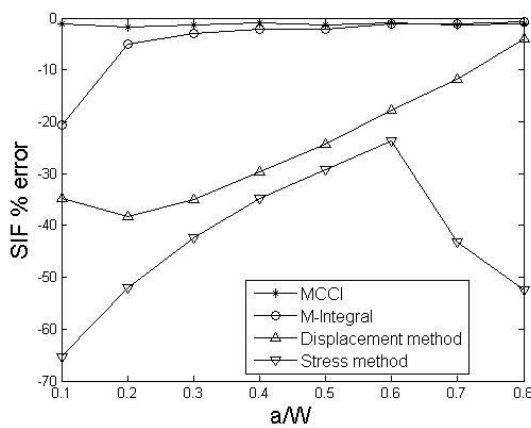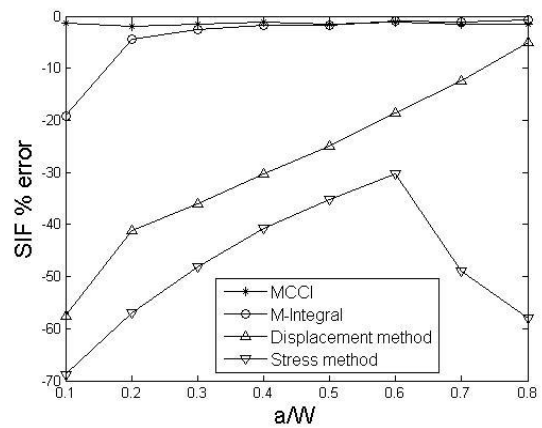
(a)　　　　　　　　　　　　　　(b)

Fig. 5.11 Mode I SIF % error using different techniques by **(a)** visibility method. **(b)** diffraction method.

Table 5.4 Mode I SIFs for an edge crack using XEFG method.

a/w	Murakami (1987) Gross & Seeli (2011)	$K_I(MPa\sqrt{m})$				
		MCCI	M-integral	Displacement method	Stress method	CCI-LS
0.1	0.663	0.662	0.682	0.687	0.782	0.674
0.2	1.087	1.074	1.086	1.108	1.222	1.099
0.3	1.612	1.595	1.634	1.644	1.816	1.639
0.4	2.358	2.340	2.377	2.405	2.691	2.408
0.5	3.543	3.498	3.536	3.579	4.007	3.590
0.6	5.529	5.471	5.555	5.581	6.261	5.610
0.7	9.433	9.281	9.454	9.504	10.574	9.540
0.8	19.007	18.541	18.912	19.337	21.173	19.202
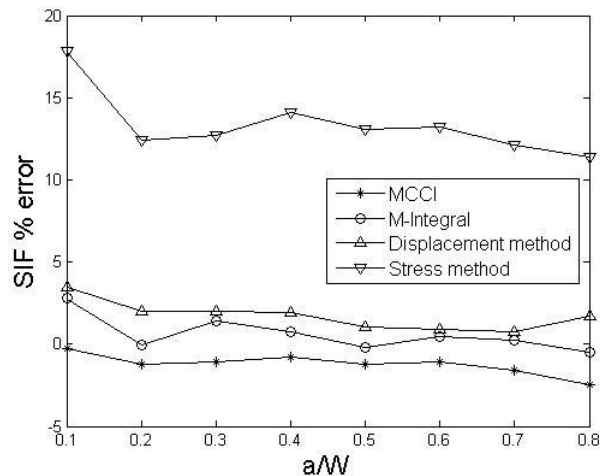
Fig. 5.12 Mode I SIF % error by XEFG method using different techniques.

Another notable feature is that the proposed technique performs better even for shorter cracks where the popular M-integral method gives inaccurate results; the errors are around 20% for the visibility and diffraction methods. In the XEFG method, the maximum error obtained by the CCI-LS technique, MCCI technique and the M-integral method is less than 2.1%, 2.5% and 2.9% respectively.

Number of nodes at which force is extracted

One of the important parameters to be considered is the number of nodes along the crack plane that need to be involved for an accurate estimation of the SIFs. Fig. 5.13 shows the accuracy of the SIF plotted against the number of nodes at which the forces are extracted for $a/w=0.5$.
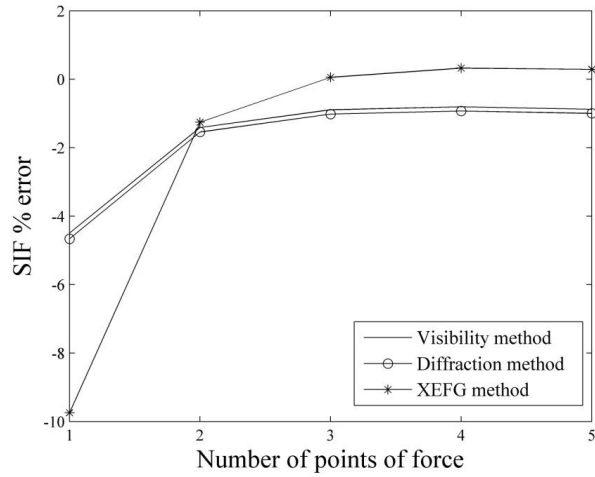
Fig. 5.13 Variation of error with number of nodes for extraction of force.

It is clear from the plot that at least two nodes are required to calculate the SIFs with error within 2 %. The error decreases marginally as the number of nodes, at which forces are extracted, are increased. In all the subsequent studies reported, the results are presented based on force extracted at two nodes. This is conservative and helps to minimize the computational effort.

Nodal density independency

It is reported (Belytschko et al., 1994; Ventura et al., 2002) that an increase in the nodal density helps to improve the accuracy of the SIFs. In this subsection, the effect of increasing the density of nodes, on the accuracy of the SIFs is studied. Fig. 5.14, Fig. 5.15 and Fig. 5.16 show the effect of increasing the number of nodes, in a regular manner, on all the techniques discussed using the methods of visibility, diffraction, and XEFG respectively.
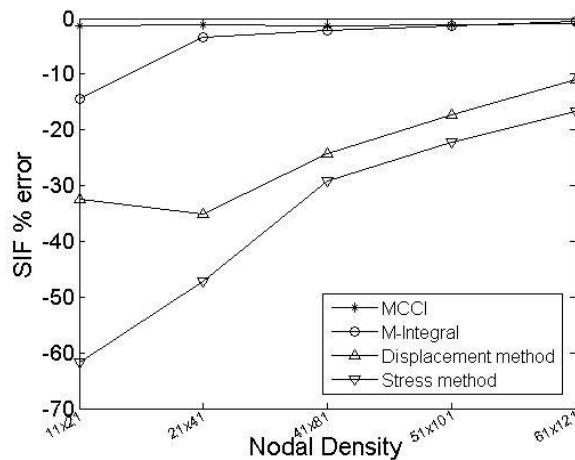
Fig. 5.14 Variation of % error in mode I SIF by visibility method for various nodal densities

$(a/w=0.5)$.

As the nodal density increases, the accuracy of the SIFs obtained through the displacement and stress methods via the non-enriched EFG method increases steadily. It is seen that the M-integral method does not give accurate results for very low nodal density. However, its accuracy improves and is steady for the subsequent nodal densities.
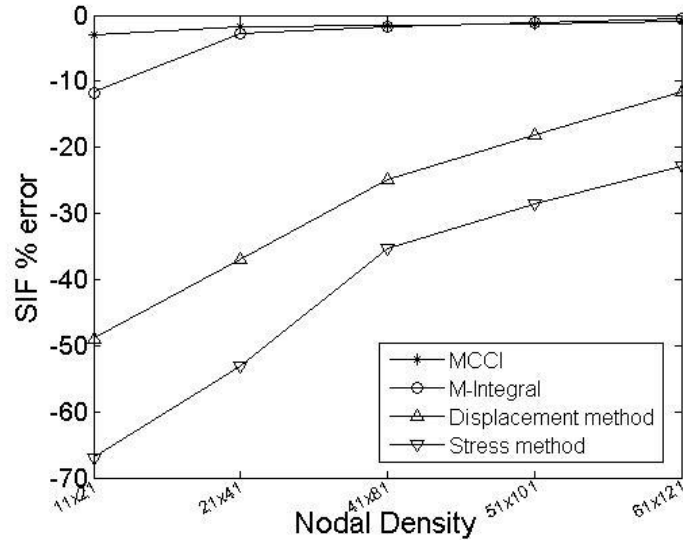
Fig. 5.15 Variation of % error in mode I SIF by diffraction method for various nodal densities (a/w=0.5).

The MCCI technique, even with low nodal density (11×21 nodes), gives accurate results. It is notable that it gives accurate results even if solution for the COD is poor. Perhaps, this is because the extracted force at the nodes compensate for the effect of inaccurate COD.
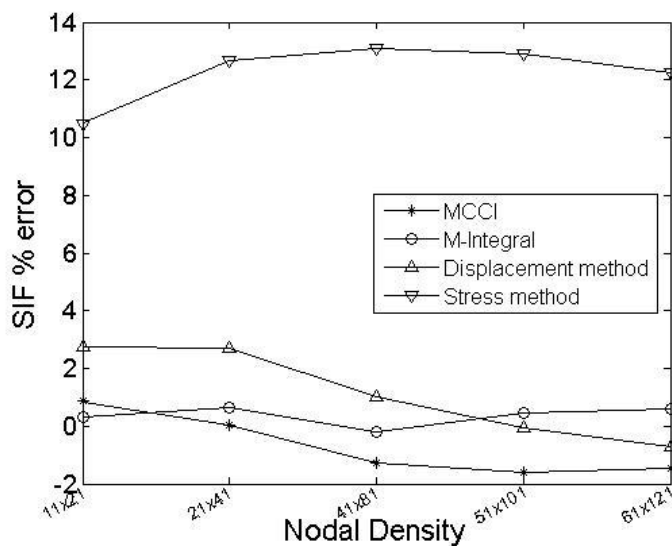
Fig. 5.16 Variation of % error in mode I SIF by XEFG method for various nodal densities (a/w=0.5).

In the case of the XEFG method, the SIFs obtained by the displacement method are accurate because of the presence of enrichment functions. No technique shows a reliable convergent behavior. However, the errors in the SIFs obtained by the M-Integral and MCCI techniques are within 2%.

Influence of order of Gauss quadrature
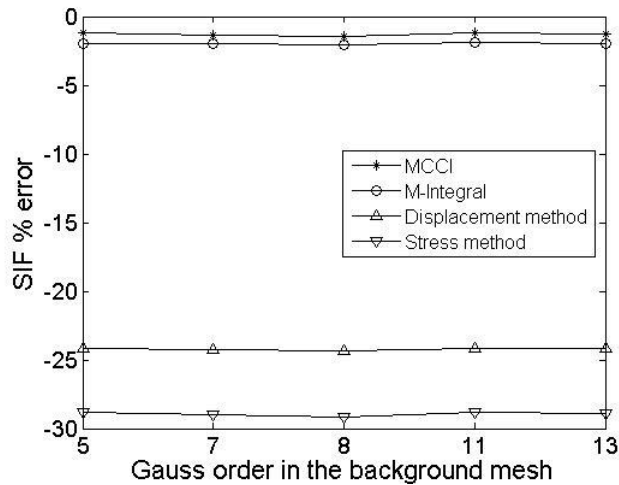
Fig. 5.17 Variation of % error in mode I SIF % by visibility method for various Gauss order (*a/w*=0.5).

Xiaoying *et al.* (2011) reported that an increased number of Gauss points around the crack tip improve the accuracy of the SIFs. The influence of increasing the Gauss quadrature order in the triangular cells around the crack on the accuracy using different techniques was investigated. Fig. 5.17 and Fig. 5.18 show the variation of % error in the SIFs obtained using the visibility and the diffraction method with a discretization of 21×41 nodes. It is clear that none of the SIF extraction techniques is affected significantly by the integration order in these two methods.

However, in the XEFG method, the SIFs obtained by the stress method and the CCI-LS method are significantly affected by the integration order (Fig. 5.19). The displacement method is affected slightly. As the integration points increase, the accuracy of the SIFs increases. The CCI-LS requires relatively higher order of Gauss quadrature for accurate computation of the SIFs. The M-integral and the MCCI technique are least affected by it.
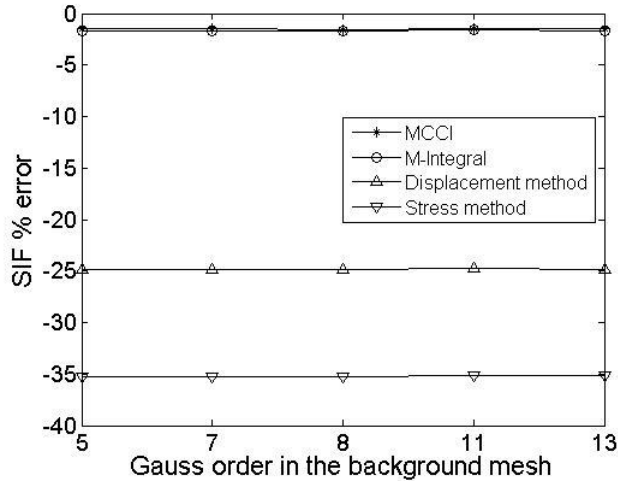
Fig. 5.18 % error in mode I SIF by diffraction method for various Gauss quadrature order (
$a/w=0.5$).
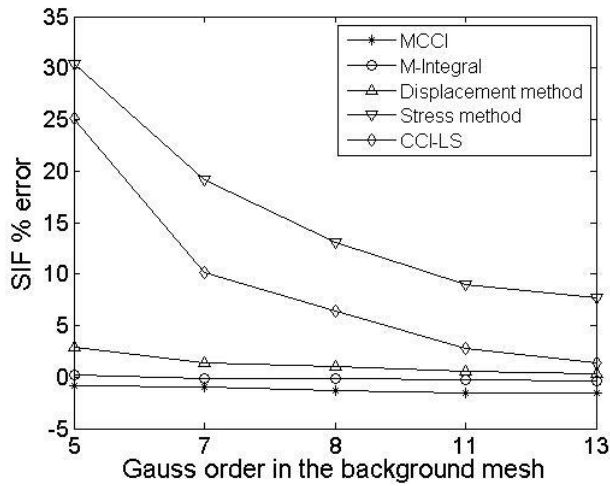
Fig. 5.19 Mode I SIF % error by XEFG method for various Gauss quadrature order
($a/w=0.5$).

Effect of domain of influence

Fig. 5.20 shows two different domains of influence (d_I) for the crack tip node. A larger d_I encompasses more nodes. A study was undertaken to explore the minimum number of nodes at which the force may be extracted to calculate the SIF accurately for variation of d_I.
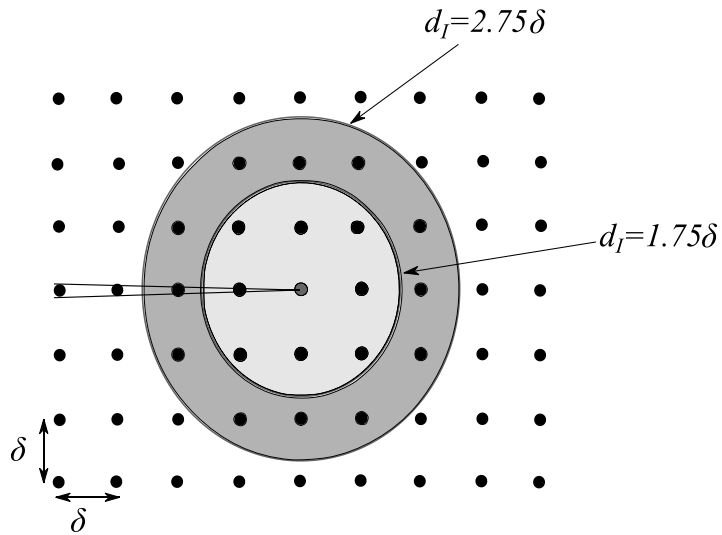
Fig. 5.20 d_I for a node at the crack tip.
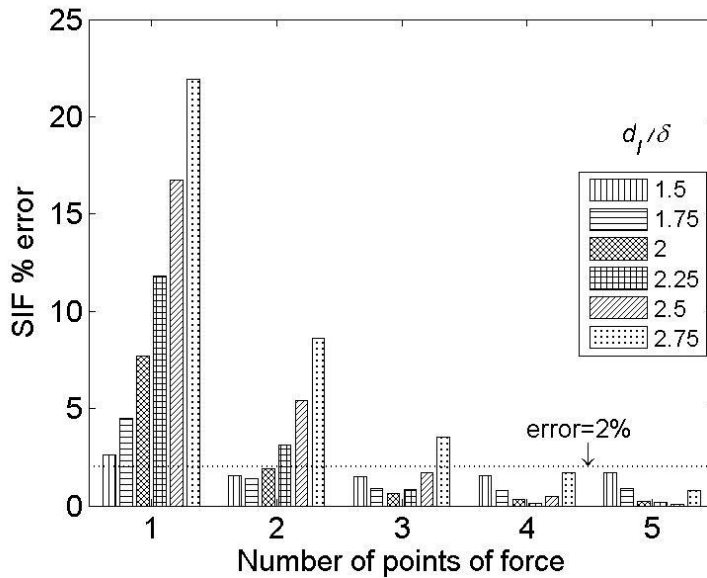
Fig. 5.21 Effect of d_I on % error in SIF and number of points for calculation of force by visibility method.

Fig. 5.21 and Fig. 5.22 show the effect of d_I and number of points for force calculation on the % error in the SIF. It is observed that as d_I/δ increases, closure forces should be computed at more nodes along the crack line for accurate calculation of the SIFs. A similar trend is also been observed in the XEFG method (Fig. 5.23).

To keep the absolute error in the computed SIF within certain level, the number of nodes at which the closure forces are to be calculated can be decided from these plots for a specific domain size d_I.
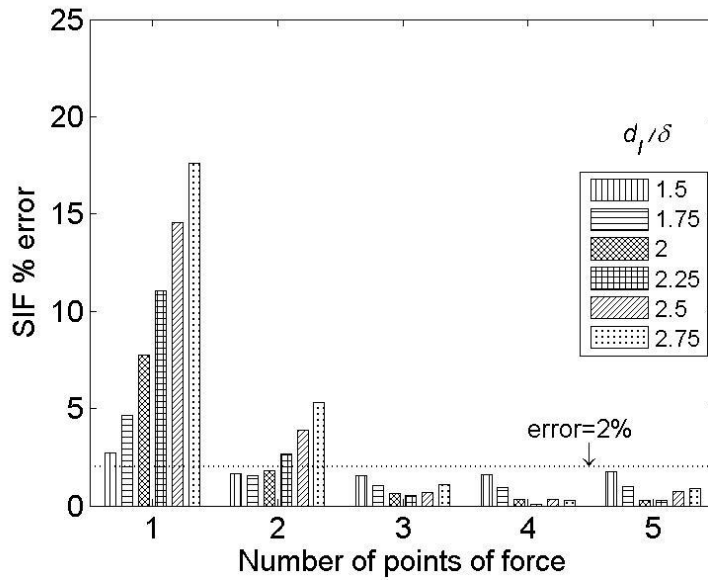
Fig. 5.22 d_I and number of force extraction points (diffraction method).
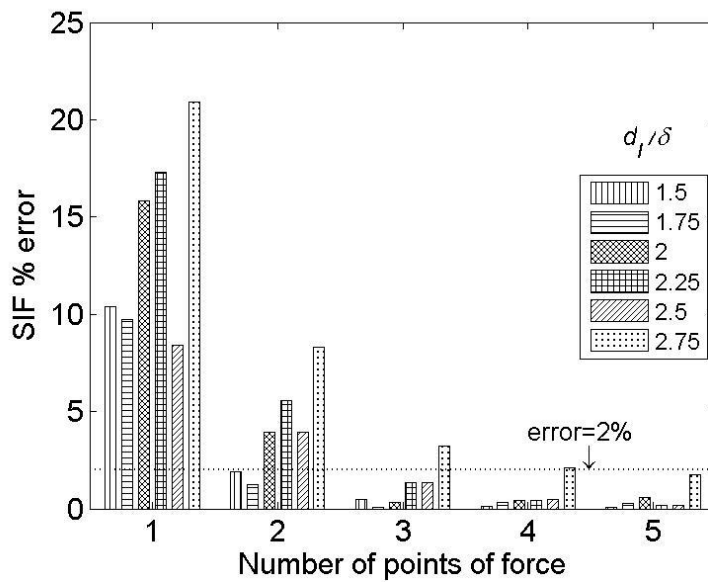
Fig. 5.23 d_I and number of force extraction points (XEFG method).

For all the case studies presented here d_I is taken as 1.75 times the nodal spacing. A higher value will result in smearing of the effect of field solution especially around the crack tip. However, d_I should be large enough to avoid any ill-conditioning of the moment matrix.

Local refinement
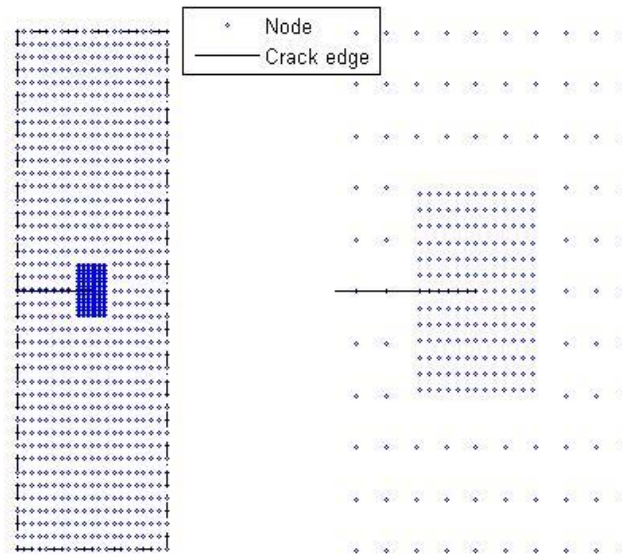
Fig. 5.24 Local refinement at the crack tip.

The effect of nodal refinement near the crack tip on the accuracy of the SIFs has also been examined. A typical nodal arrangement is shown in Fig. 5.24.

Table 5.5 Effect of local refinement on MCCI technique.

a/w	Murakami (1987) Gross & Seeli (2011)	Visibility		Diffraction		XEFG	
		(a)	(b)	(a)	(b)	(a)	(b)
0.1	0.663	0.656	0.661	0.655	0.660	0.662	0.675
		-1.104%	-0.371%	-1.170%	-0.434%	-0.081%	1.879%
0.2	1.087	1.070	1.072	1.069	1.071	1.065	1.080
		-1.536%	-1.362%	-1.684%	-1.518%	-2.033%	-0.626%
0.3	1.612	1.590	1.594	1.590	1.593	1.587	1.609
		-1.352%	-1.148%	-1.396%	-1.172%	-1.576%	-0.180%
0.4	2.358	2.336	2.341	2.335	2.340	2.328	2.364
		-0.941%	-0.734%	-0.988%	-0.759%	-1.285%	0.237%
0.5	3.543	3.503	3.513	3.497	3.507	3.477	3.535
		-1.132%	-0.855%	-1.298%	-1.019%	-1.854%	-0.234%
0.6	5.529	5.479	5.488	5.469	5.478	5.431	5.521
		-0.908%	-0.743%	-1.089%	-0.917%	-1.765%	-0.145%
0.7	9.433	9.336	9.349	9.317	9.331	9.246	9.402
		-1.033%	-0.892%	-1.232%	-1.080%	-1.979%	-0.330%
0.8	19.007	18.706	18.702	18.686	18.691	18.497	18.837
		-1.584%	-1.605%	-1.689%	-1.663%	-2.683%	-0.894%

Table 5.5 show the effect of refinement on the accuracy of the SIFs using the visibility, diffraction and the XEFGs method for crack sizes varying from $0.1w$ to $0.8w$. (a) and (b) corresponds to 13×13 and 17×17 nodes around the crack tip respectively. The nodes associated with a refinement are distributed regularly in the selected region (Fig. 5.24).

It is clear from the table that, as the refinement increases, the accuracy gets slightly better. While refining the zone with regular nodal arrangement near the crack tip, care must be taken to ensure that an intermediate node coincides with the crack tip and a row of nodes align with the direction of crack extension x. It is observed that the MCCI technique performs almost uniformly for all the crack-modelling techniques.

5.4.2 Centrally located angled crack in finite plate

Fig. 5.25(a) shows a geometry with dimensions $2w = 1\,\text{m}$, $L/2w = 2$ and $a/w = 0.5$. The plate is subjected to uniform tensile load of 1MPa on the edge. The plate is discretized with 41×81 nodes. The crack is inclined at an angle β (in degrees) with x-axis.

| (a) | (b) |
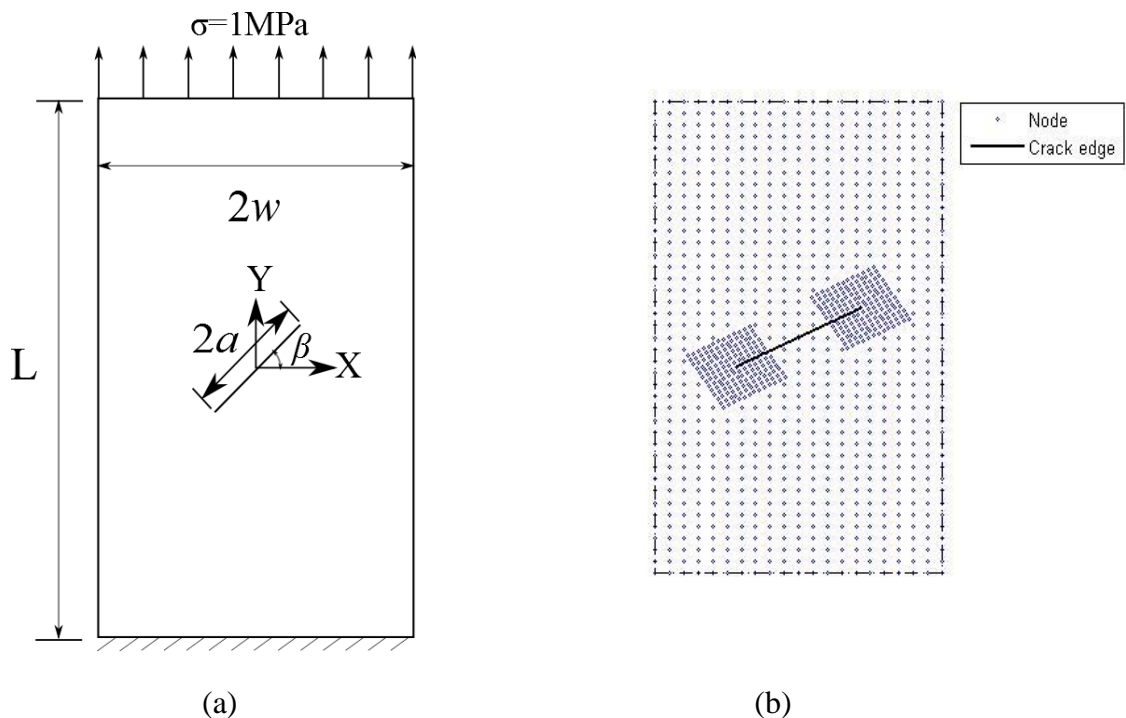
Fig. 5.25 (a) Mixed mode center crack subjected to tensile traction. **(b)** Nodal discretization for a mixed mode crack.

Fig. 5.25(b) shows the nodal discretization. A sub-region around the crack tips is refined with 13×13 nodes with $d_I = 1.75\delta$ where δ is the inter-nodal distance between the refined nodes.
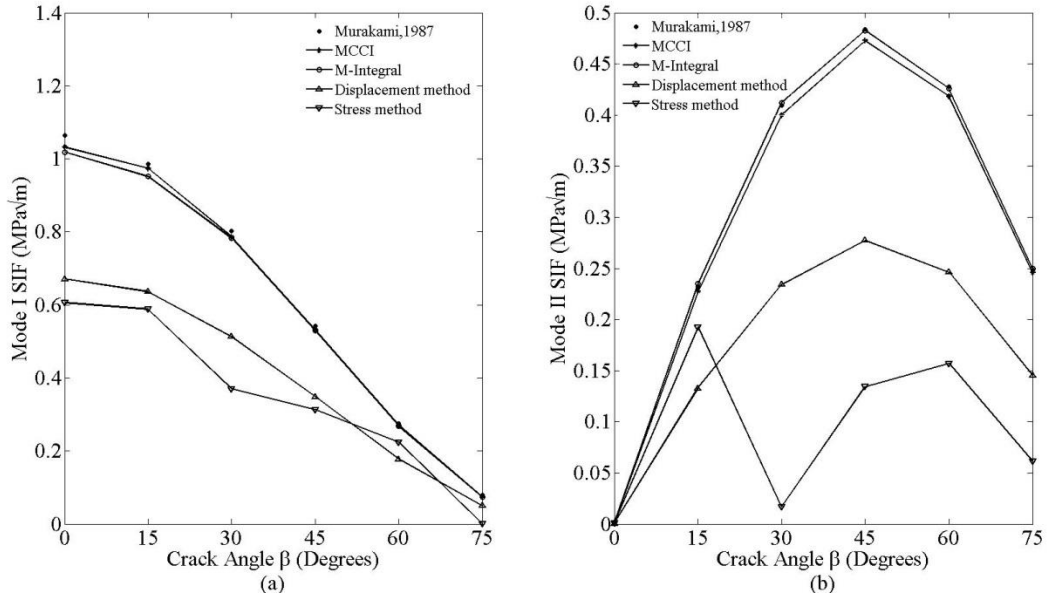
Fig. 5.26 Mixed mode SIFs by visibility method.
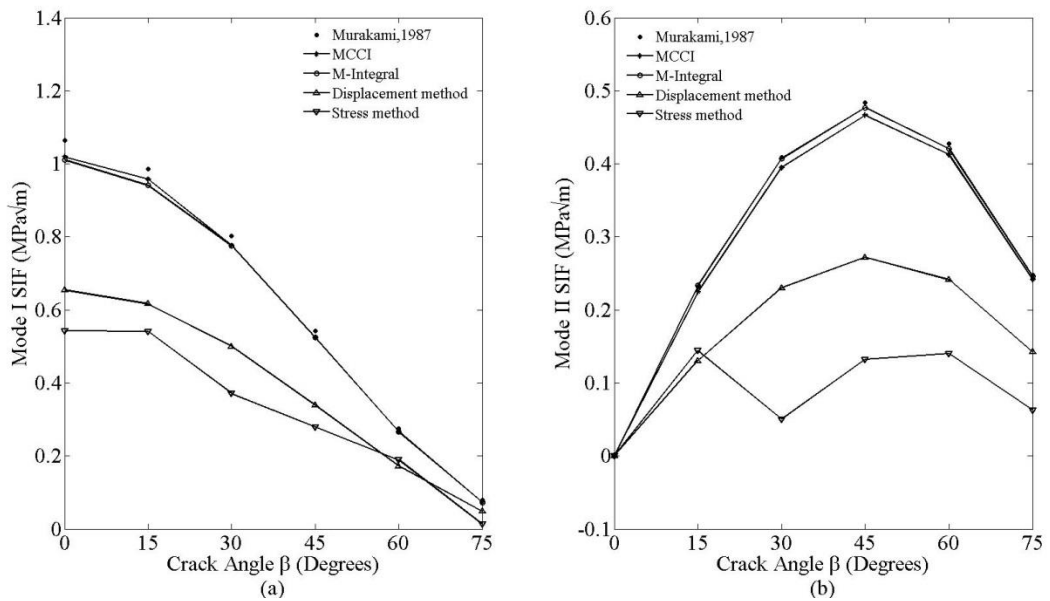
Fig. 5.27 Mixed mode SIFs by diffraction method.

The results obtained by various techniques are compared with the reference results available in (Murakami, 1987). Fig. 5.26 and Fig. 5.27 show the mode I and mode II SIFs obtained by all the extraction techniques using the visibility and diffraction methods respectively. The stress method and the displacement method yield poor results. The results by the M-integral and the MCCI techniques are in good agreement with the reference results.

Although, in the XEFG method, the displacement method gives satisfactory mode I SIF, the mode II SIFs are inaccurate (Fig. 5.28). The M-Integral and the MCCI technique consistently give accurate results for all the class of EFG methods.
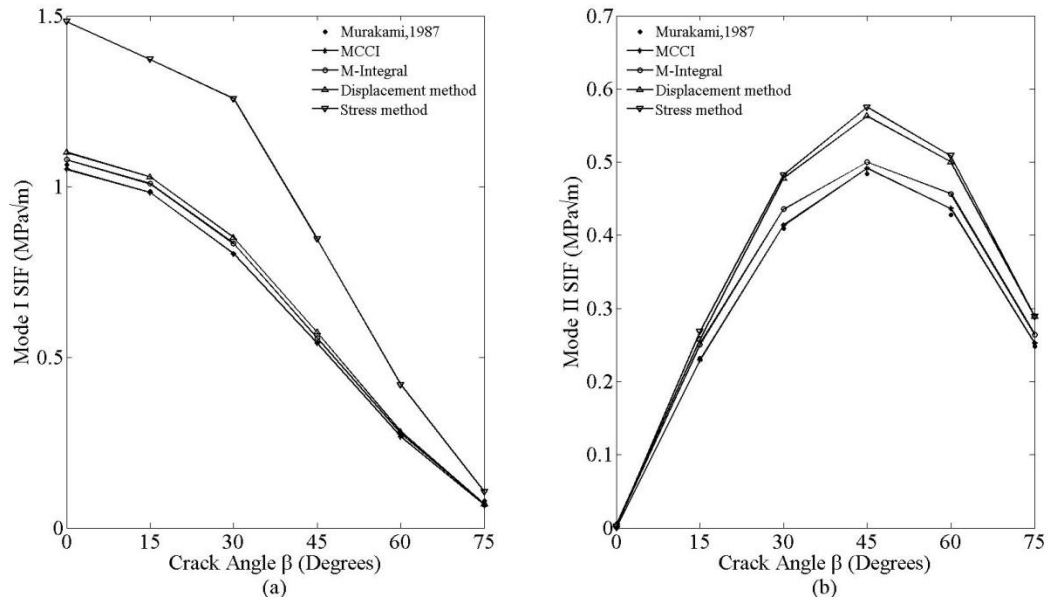
Fig. 5.28 Mixed mode SIFs by the XEFG method.

5.4.3 Mode I crack face pressure loading
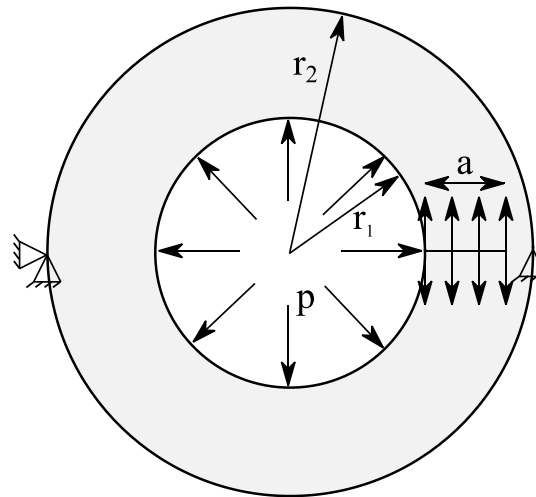
Fig. 5.29 Hollow cylinder with inner radial crack subjected to pressure loading.

Fig. 5.29 shows a hollow cylinder of inner radius $r_1 = 1\,\text{m}$ and $r_2 / r_1 = 2$ under internal pressure p. There is an inner radial crack of length a. This problem has been examined in (Muthu et al., 2013). The geometry is discretized with 25 nodes (radial) by 144 nodes (circumferential) as illustrated in Fig. 5.30. The region around the crack tip is refined with

13×13 nodes. The domain of influence d_I varies along the radius; spacing is 1.75 times the regular nodal spacing.
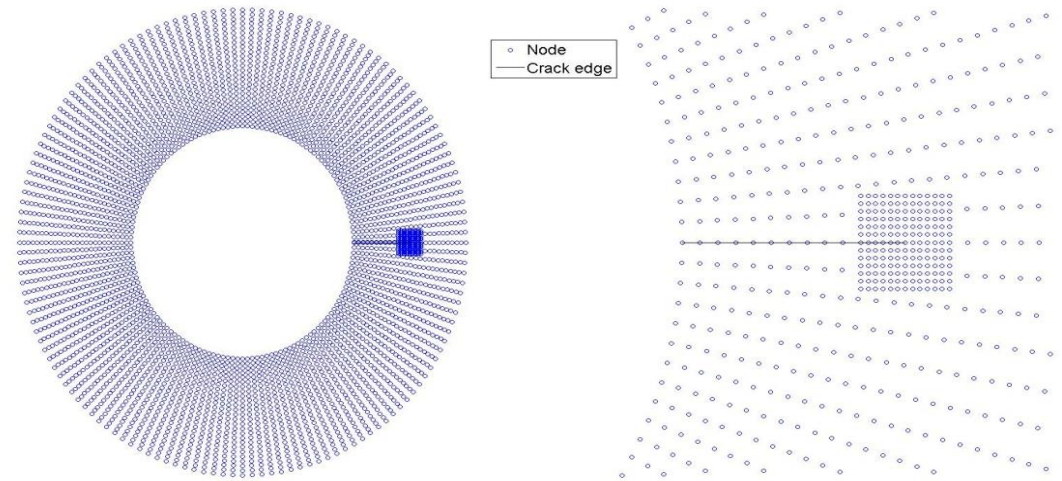
Fig. 5.30 Nodal discretization with local refinement at the crack tip.

The modified M-integral including the pressure loading on the crack edges is used for the SIF calculation. The MCCI, too, is calculated here by taking into account the pressure loading on the crack edges. The displacement method does not require any changes in the way the SIF is computed. Fig. 5.31, Fig. 5.32 and Fig. 5.33 show the % error in the SIFs calculated using the methods of MCCI, M-integral and displacement under crack modelling through the methods visibility, diffraction and XEFG.
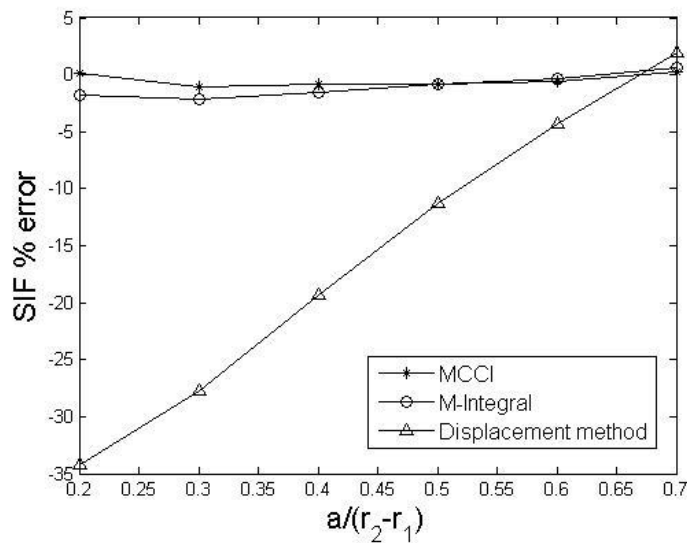
Fig. 5.31 SIF variation with crack length for loaded crack using visibility method.
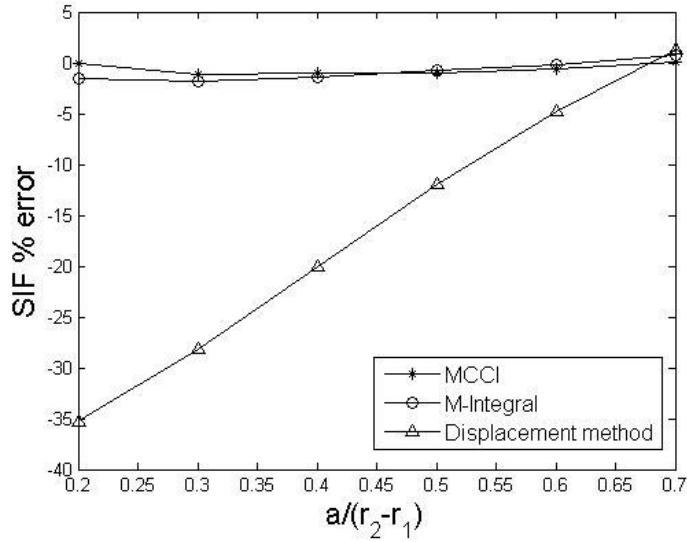
Fig. 5.32 SIF variation with crack length for loaded crack using diffraction method.

The results by the three methods are compared with the reference results (Murakami, 1987). It is observed that the displacement method gives inaccurate results with almost 35% error for the visibility and diffraction methods. In the XEFG method, the results are accurate based on the displacement method. Although the M-integral gives slightly erroneous results for $a/(r_2 - r_1) = 0.2$, it is still accurate for higher crack lengths. The proposed MCCI technique seems to perform significantly better in all the three cases.
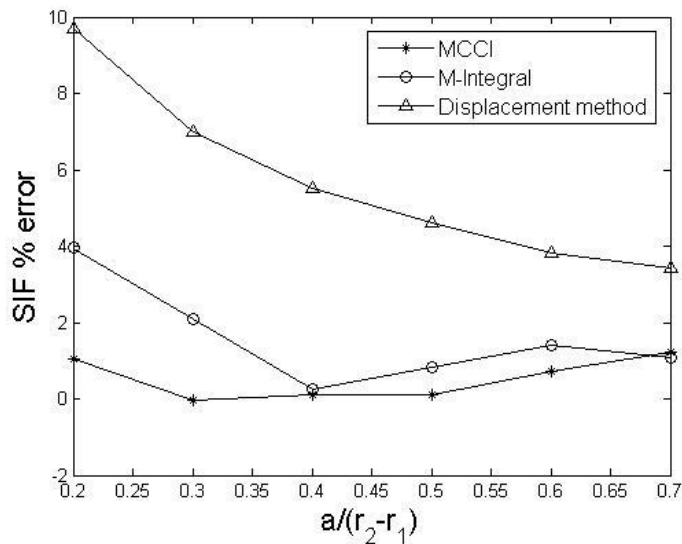
Fig. 5.33 SIF variation with crack length for loaded crack using XEFG method.

5.4.4 Thermal loading (linear temperature variation)

Fig. 5.34 shows a plate with dimensions $w = 1\,\text{m}$ and $L/w = 2$. The plate is fixed and thermally insulated at the top and bottom edges. This plate is subjected to a linearly variable temperature field varying from -100 and 100 degree Celsius as shown.
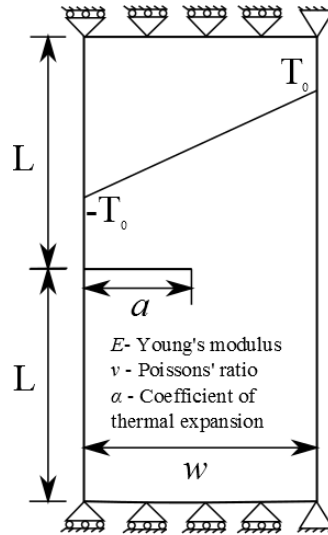
Fig. 5.34 Mode I crack with temperature varying linearly across the width.

The crack size to width ratio (a/w) was varied from 0.1 to 0.7 and the geometry was discretized with 41×161 nodes. The crack tip region was locally refined with 13×13 nodes. The SIFs computed were normalized with respect to $E\alpha T_0 \sqrt{w}/(1-v)$. Assuming plane strain conditions, the results are compared with those of Hellen *et al.* (1982). The coefficient of thermal expansion α is $13 \times 10^{-6}/^{o}C$.
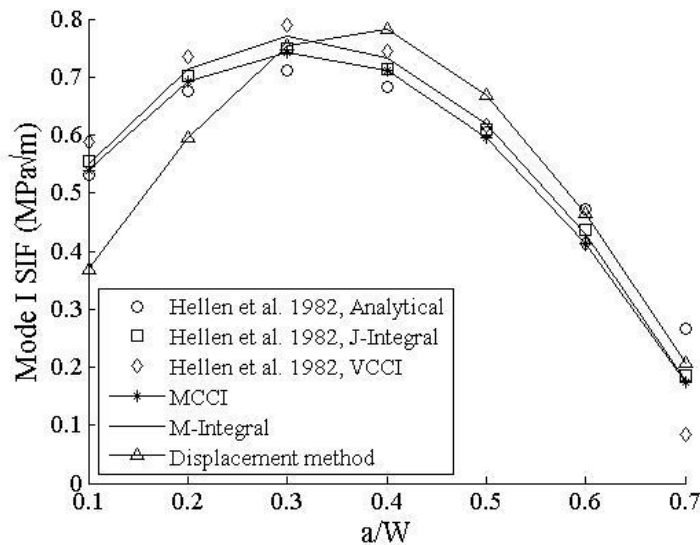
Fig. 5.35 Mode I SIF variation with crack length using the visibility method.

The computed mode I SIFs are compared with the reference results, in Fig. 5.35, Fig. 5.36 and Fig. 5.37 by the methods of visibility, diffraction and XEFG respectively.
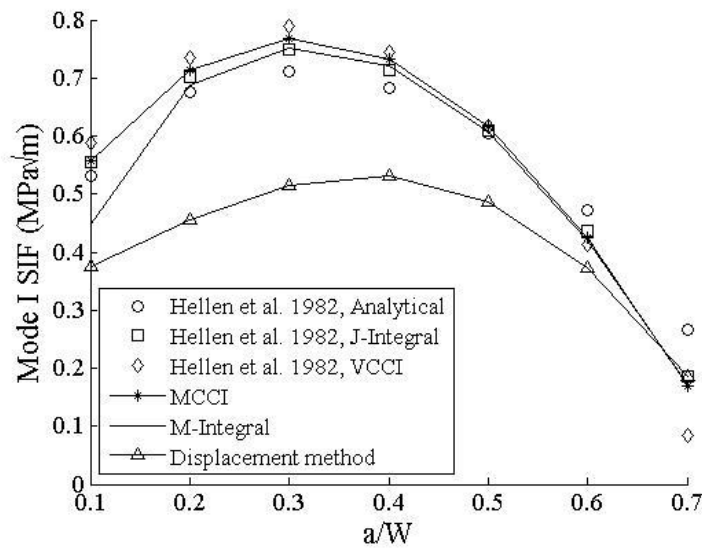
Fig. 5.36 Mode I SIF variation with crack length using the diffraction method.
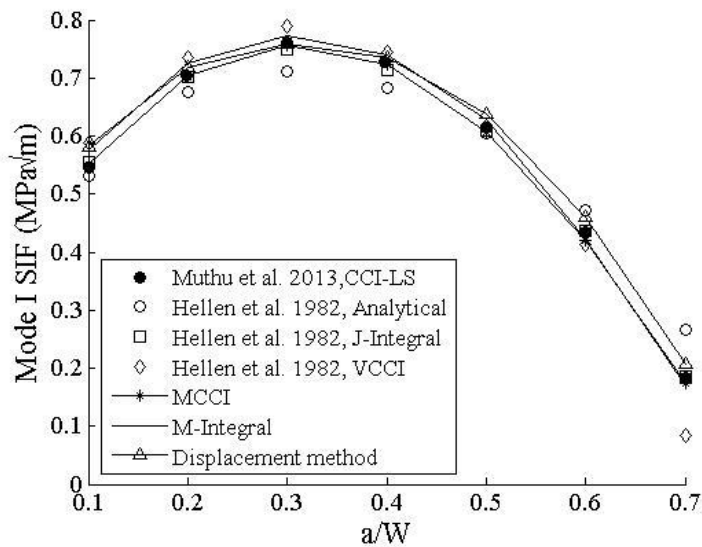
Fig. 5.37 Mode I SIF variation with crack length using the XEFG method.

The MCCI was calculated by considering the mechanical reaction force arising due to thermal load according to Eq. (5.11). The modified M-integral too takes into consideration of the thermal loading. The stress method is excluded from the results as it gave poor results. In the presence of enrichment functions, the displacement method yielded good results. The MCCI and M-integral techniques give satisfactory results and they are in better agreement with the published J-integral results.

5.5 Closure

A simple and accurate way of extracting the mixed-mode stress intensity factors within the framework of EFG method using the methods of visibility, diffraction, and the XEFG for crack modelling is presented. It involves computing crack closure forces only at two nodes, the crack tip, and a node ahead of it, and extraction of opening displacements at two nodes behind the crack tip. The effectiveness and special issues associated with the adoption of the MCCI/VCCT technique have been brought out through solutions to a variety of crack problems including crack face and thermal loadings. The study has facilitated a comparison of the performance of the classical displacement and stress methods, and the MCCI/VCCT, with the popular M-integral method, CCI-LS technique and the analytical solutions. The accuracy of the MCCI/VCCT is consistently good and is comparable to that of the M-integral method. The accuracy of the displacement method is acceptable only when it is employed in conjunction with the crack-tip enrichment functions.

Chapter 6   Crack Propagation through Composites

6.1 Introduction

Composite materials are often subjected to extreme mechanical and thermal loading conditions that make them susceptible to damage through crack formation. The material is non-homogenous, consisting of dissimilar materials or bi-materials separated by interfaces (Patrício & Mattheij, 2010). This issue is examined in this chapter. Studies on the modelling of fracture of composites range from nanoscale to macroscale. Useful insight into the study of fracture may be gained through analysis at the microscale. At this level, the constituent materials are represented separately.

A propagating crack at the microscale may often impinge on the bi-material interface at an angle. The associated singular stress field consists of two different orders of singularity, which may be either complex conjugates or real (Bogy, 1971; Zhen & Zhigang, 2007). In addition, a crack tip that meets an interface of two materials may grow along it or penetrate into the neighbouring material. The criterion for such a crack to kink into the neighbouring material is different from the criterion governing the crack propagation in a homogenous material. The development of a proper numerical method and an efficient approach to predict the angle of crack propagation, including kinking of an interface crack, can be very useful in the study of fracture of composites. This is also explored in this chapter.

Cotterell (1966), Williams *et al.* (1972), Finnie *et al.* (1973), Ewing *et al.* (1974), and Ueda *et al.* (1983) proposed the use of in-plane stress (T-stress) in the power series expansion of the stress distribution due to a crack, to determine the crack paths in metals under pure mode I loading. Several other investigators (Leevers et al., 1976; Hallback & Nilsson, 1994; Smith et al., 2001; Smith et al., 2006) have used the T-stress to predict the crack paths. Matvienko (2012) found good agreement between the predicted fracture angles and the experimental data for mixed-mode I/II crack growth through Guiting limestone. Ki (1994) studied the existing criteria for crack kinking out of the interface and recommended the inclusion of the T-stress. There are no studies on crack propagation through bi-materials within the framework of the MMs incorporating T-stress.

There are several criteria to determine the instantaneous angle of crack propagation when the crack is in a homogenous medium. However only few criteria have been proposed to predict this kinking angle in the case of an interface crack (Kang, 1994). The determination of the interface crack kinking angle, using the ERR criterion and $K_{II} = 0$ criterion, requires multiple case studies, which is computationally costly. In the MTS criterion given in reference (Yuuki & Xu, 1992), the first term of the eigenfunction expansion, or the singularity term, is only used to determine the angle of crack propagation. This angle corresponds to the direction of maximum tangential principal stress. The crack propagation angle given by the MTS criterion does not correspond to a principal direction when higher order terms are also used. In such a case, a direction separate from $\partial \sigma_{\theta\theta} / \partial \theta = 0$ and given by $\tau_{r\theta} = 0$ corresponds to the principal direction. This criterion, termed as zero shear stress criterion, or MTPS criterion (Maiti & Smith, 1983a), has been shown to be more accurate for homogenous materials. Application of such a criterion is convenient because it helps to avoid generating data for multiple cases to determine an interface crack kinking angle. Its application to bi-material interface cracks is also examined in this chapter.

6.2 Modified EFG method

The partition-of-unity scheme is attractive as it reproduces the asymptotic singular field around the crack tip. This is achieved by using Williams' crack-tip displacement solutions (Williams, 1952) as branch enrichment functions in a homogenous and isotropic material. The normal and enriched nodes are shown in Fig. 6.1. However, the branch enrichment functions $\xi^{enr}(r, \theta)$ depend on the nature of the problem considered and may not be suitable to study crack propagation in non-homogenous materials.
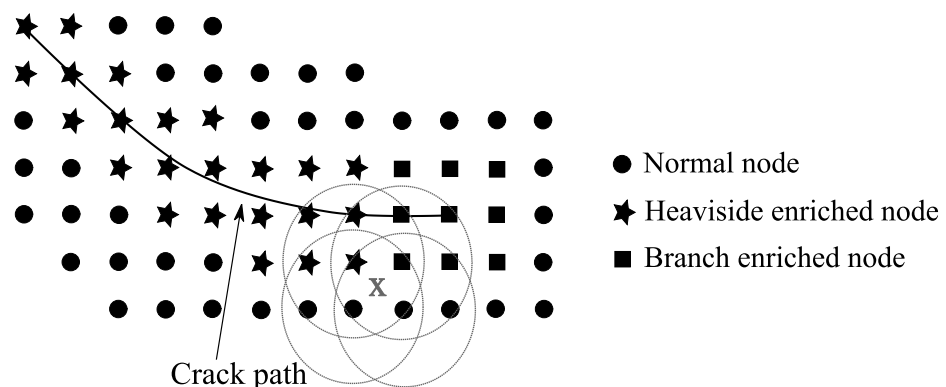
Fig. 6.1 Normal and enriched nodes.

In the second approach, the weight functions associated with each node that affects the crack are modified. The visibility and diffraction methods differ in the way the weight functions associated with nodes that influencing the crack tip are modified. These methods have been discussed in the section 3.8.1. However as the crack propagates more nodes are sometimes added along the crack line to avoid ill conditioning of the stiffness matrix.

A scheme combining the Heaviside function and the diffraction method of crack modelling is proposed in this chapter to study the crack propagation in non-homogenous materials. The diffraction method is used to model the crack tip region. The Heaviside function helps to avoid the need of adding additional nodes along the crack edges in a problem of mixed-mode crack propagation. Consequently, the displacement approximation in the case of a crack (strong discontinuity) and inclusion boundary (weak discontinuity) present in a geometry (Fig. 6.2) can be written in the following form.

$$\mathbf{u}(\mathbf{x}) = \sum_{I \in w(\mathbf{x})} \Phi_I(\mathbf{x})\mathbf{u}_I + \sum_{I \in w_j(\mathbf{x})} \Phi_I(\mathbf{x})\{\mathbf{a}_I H(f(\mathbf{x}))\} + \sum_{I \in w_c(\mathbf{x})} \Phi_I(\mathbf{x})\mathbf{c}_I \chi_I(\mathrm{x}) \qquad (6.1)$$

where function $\chi_I(\mathbf{x}) = F^I(\mathbf{x}) - F^I(\mathbf{x}_I)$, is employed for displacement continuity across the interface with $F^I(\mathbf{x}) = \sum_{I \in w_c(\mathrm{x})} |\zeta_I| \Phi_I(\mathbf{x}) - \left| \sum_{I \in w_c(\mathrm{x})} \zeta_I \Phi_I(\mathbf{x}) \right|$. ζ_I is the signed distance of node I from the interface (Moës et al., 2003). The set $w_c(\mathbf{x})$ consists of level set nodes enriched with displacement continuity function and $\mathbf{c}_I$ is the nodal degree-of-freedom corresponding to the enrichment functions.
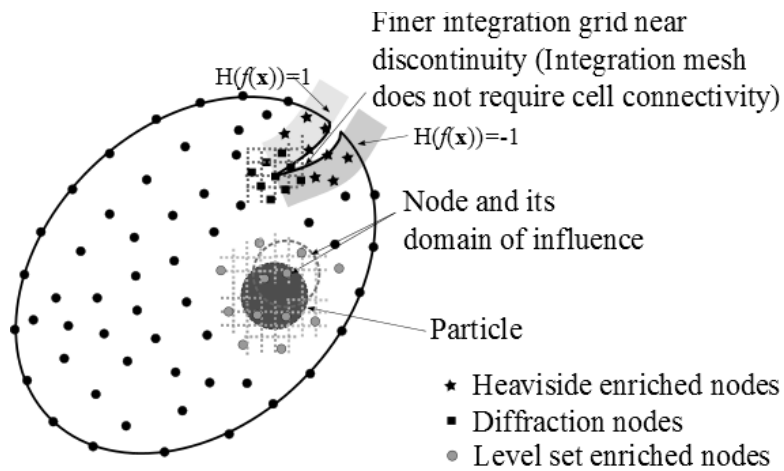
Fig. 6.2 Nodal discretization for geometry with a crack and an inclusion.

The routinely used polynomial basis $p = [1 \ x \ y]$ for the development of shape functions of the EFG method through the MLS technique is again employed. The cubic B-spline weight function with circular domain of influence is used. For accurate integration purposes, the background mesh that intersects the crack is subdivided into triangles (Fig. 6.3) using the simple mesh generator program developed by Persson and Strang (2004) such that no mesh crisscrosses the crack (Muthu et al., 2013). In the present work, in addition to the sub-triangulation, Gauss quadrature of order 13 has been employed in each triangular mesh close to the crack tip for good accuracy. The need for such high order of Gauss integration is illustrated by case studies in the result section.

The proposed method may not capture the order of singularity exactly. However, the higher order nodal shape functions ensures the accurate and easier computation of the SIFs. The computed SIFs are then used to describe the asymptotic stress field around the crack tip for predicting the direction of crack extension.
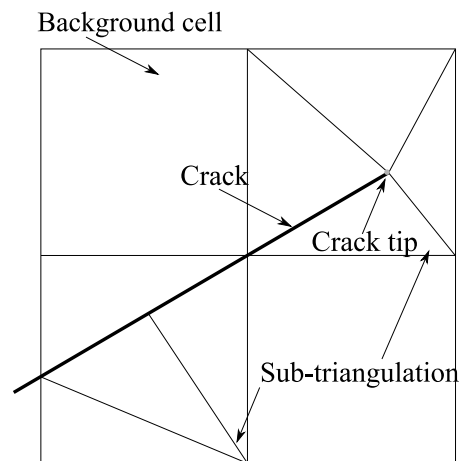
Fig. 6.3 Sub-triangulation for the background mesh.

6.2.1 Convergence study

A plate with dimensions: width $w = 1 \, \text{m}$, length to width ratio $L/w = 2$ with an edge crack ($a/w = 0.5$) is hsown in Fig. 6.4(a). It is subjected to tractions of 1MPa at the top and bottom edges. The domain of influence is set as 1.75 times the regular nodal spacing. The materials are assumed isotropic with Young's modulus $E = 210 \, \text{GPa}$ and Poisson's ratio $v = 0.3$. The actual SIF for this case is $3.543 \, \text{MPa} \sqrt{\text{m}}$ (Murakami, 1987).
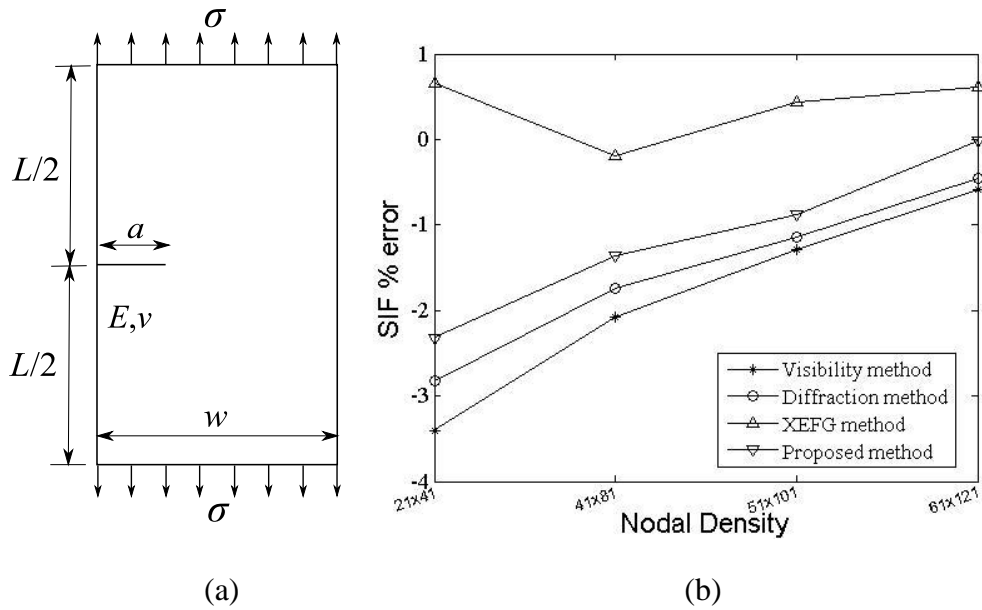
Fig. 6.4 (a) A finite plate with an edge crack subjected to uniform tensile load. **(b)** SIF % error with nodal density.

The % error in the computed SIF using the M-integral is plotted for various nodal discretization (Fig. 6.4(b)). This plot shows that the present method decreases the % error in SIF with increasing nodal density. It has better accuracy compared to the visibility and diffraction methods. The improvement in the accuracy may be attributed to the coupling of the diffraction method with the Heaviside enrichment function.
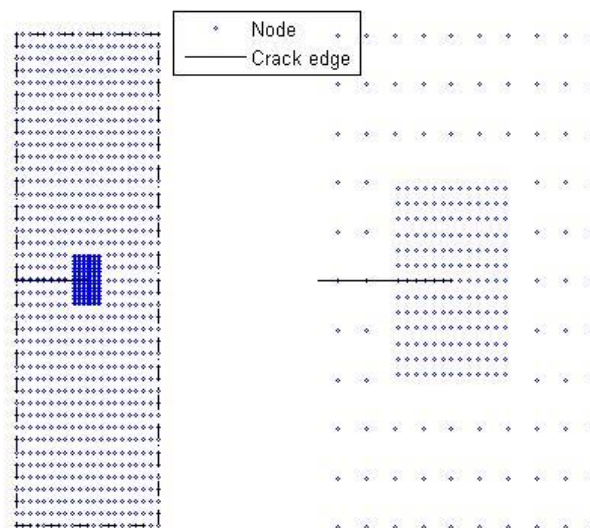
Fig. 6.5 Local refinement at the crack tip.

The XEFG method performs better compared to the proposed method owing to the crack tip enrichment functions. However, when a nodal refinement is used, in the proposed EFG method, in the region around the crack tip (Fig. 6.5), there is a significant improvement. Fig. 6.6 shows the convergence characteristics in terms % error in the SIF using a coarser nodal discretization of 21×41 with various refinements in the region around the crack tip. It is observed that even with a very low-density refinement 7×7, the % error becomes less than 2%. As the refinement increases, the error decreases and finally converges almost to the accurate solution. Thus, the proposed scheme helps to eliminate the need for enrichment functions and is advantageous especially for modelling crack propagation through the non-homogenous materials.
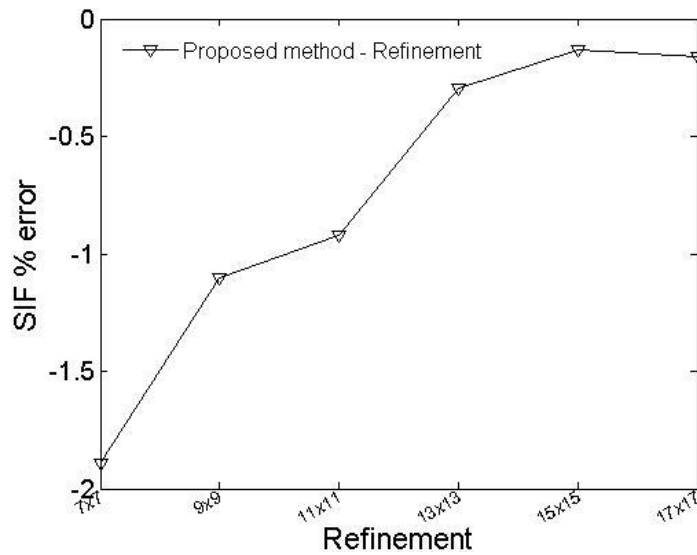
Fig. 6.6 % error in SIF with refinement in the region around the crack tip.

Selection of domain of influence (d_I)
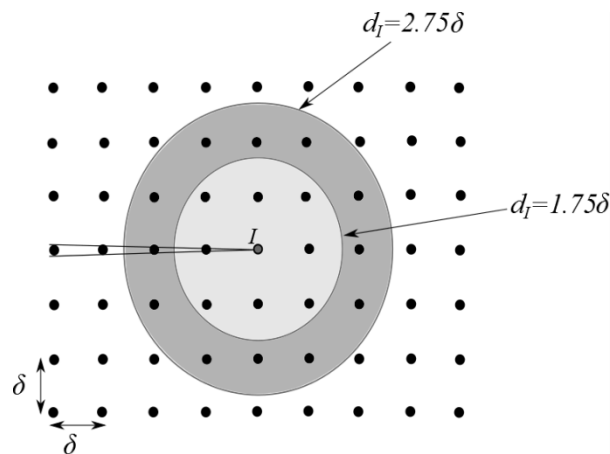
Fig. 6.7 d_I for regular nodal discretization.

In general, the nodal domain of influence (d_I) is a function of regular nodal spacing distance (δ) and scaling parameter $\bar{\alpha}$. A larger $\bar{\alpha}$ leads to larger number of nodes within the domain of influence of node I (Fig. 6.7). Different values of $\bar{\alpha}$ have been chosen by the previous investigators to model the crack (Organ et al., 1996; Muravin & Turkel, 2006; Muthu et al., 2014; Tuan & Fei, 2014).

To get the optimum values of the scaling parameter $\bar{\alpha}$, the error in SIF is plotted for various $\bar{\alpha}$ (Fig. 6.8). It is observed from the plot that the optimum value of the scaling parameter $\bar{\alpha}$ can range from 1.75 to 2.5. A higher value of $\bar{\alpha}$ will spread the effect of nodal weight function over a larger zone and increase the bandwidth of stiffness matrix. A very low value of $\bar{\alpha}$ will result in ill conditioning of the stiffness matrix. In the present study, the $\bar{\alpha}$ is chosen at 1.75 to keep the bandwidth of the global stiffness matrix without losing the accuracy.
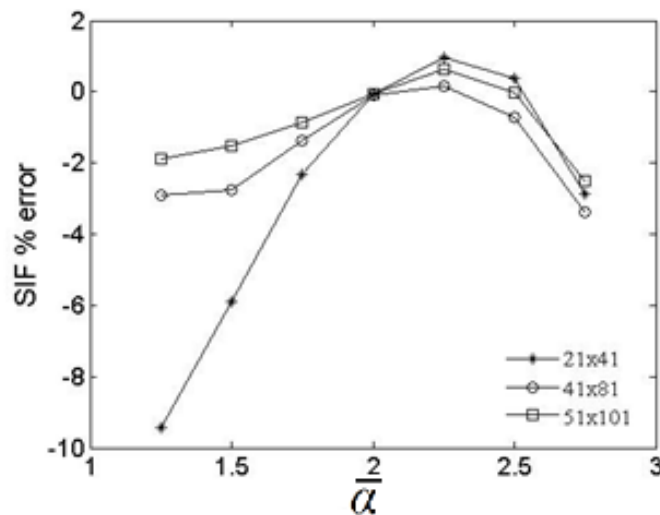
Fig. 6.8 Variation of SIF % error with domain of influence ($\bar{\alpha}$).

6.3   Criteria for prediction of direction of Crack propagation

Although the energy-based criterion can be used to determine both the kinking angle and the load leading to an initiation of kinking of an interface crack, it requires substantial computational effort. This is because the criterion requires multiple analyses to generate a variation of the ERR with possible kinking directions θ (Fig. 6.9(a) and Fig. 6.9(b)). In general, for an accurate computation of ERR, length Δa of the kinked crack is kept very small compared to the parent interface crack.
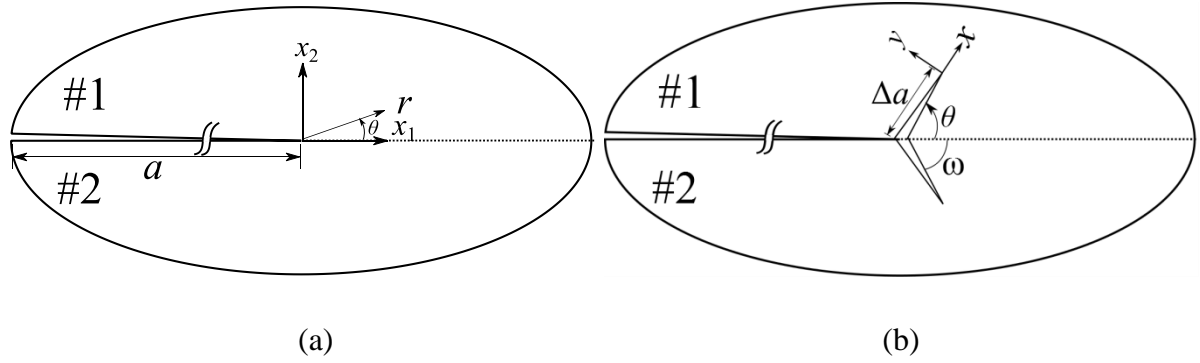
Fig. 6.9 (a) Interface crack. **(b)** Kinking of an interface crack.

Yuuki and Xu (1992), on the other hand, proposed that the interface crack would extend in the direction of maximum tangential/hoop stress given by the singularity term. They did not include T-stress in their analysis. For evaluation of tangential stress ($\sigma_{\theta\theta}$), a circle of finite radius is considered (Fig. 6.10). The orientation angle θ corresponding to $\sigma_{\theta\theta}^{\max}$ gives the kinking direction $\omega = \theta$. However, this criterion alone cannot determine whether the crack will kink into the material m or grow along the interface; this requires knowledge of the fracture toughness or fracture strength of the constitutive materials and the interface plus the values of ERRs along the direction ω and the interface.

The zero K_{II} criterion, proposed by Akisanya and Fleck (Akisanya & Fleck, 1992), stipulates that the interface crack kinks from the tip in the radial direction corresponding to $K_{II} = 0$. The mixed-mode SIFs of a kinked crack length Δa is related to the parent crack by (He & Hutchinson, 1989; Akisanya & Fleck, 1992).

$$K_I + iK_{II} = c\mathbf{K}(\Delta a)^{i\varepsilon} + \overline{d}\mathbf{K}(\Delta a)^{i\varepsilon} + gT_m\sqrt{\Delta a} \qquad (6.2)$$

where $\mathbf{K}$ is the complex SIF ($\mathbf{K} = K_1 + iK_2$). c, $\overline{d}$ and g are complex functions that are dependent on Dundurs' parameters α, β and kink angle ω.

The complex functions c, $\overline{d}$, g and the complex SIF $\mathbf{K}$ of the interface crack are substituted in Eq. (6.2) to determine ω. In the absence of c, $\overline{d}$ and g data, the kinked crack of length Δa is extended in various directions, θ. The kink angle ω corresponds to the direction at which mode II SIF at the tip of kinked crack Δa. This gives $\tau_{r\theta} = 0$ for the kinked crack, not the original crack. This is in a sense *a posteriori* stress field criterion.

Similar to the $\sigma_{\theta\theta}^{\max}$ criterion, this criterion too cannot determine whether the crack will penetrate or deflect without the knowledge of the individual fracture toughness of the constituent materials and the interface plus the ERRs along these directions.

In order to merge the advantages and overcome some of the difficulties, a criterion based on both the stress state and energy release rate is used here to predict the direction of kinking and the onset of crack propagation. According to the maximum tangential principal stress (MTPS) criterion, a crack extends in a radial direction corresponding to $\tau_{r\theta} = 0$ (Maiti & Smith, 1983a; Maiti & Smith, 1984). This is based on the classical Rankine's maximum principal stress theory. The crack propagates when the maximum tangential stress at the location reaches a critical value, a property of the material. This is similar to the $K_{II} = 0$ criterion, but with a difference. In the MTPS criterion, the determination of kink angle ω is based on the *a priori* stress field due to the parent interface crack. However, in $K_{II} = 0$ criterion, the kink angle ω is based on the main crack plus a kinked crack of length Δa.
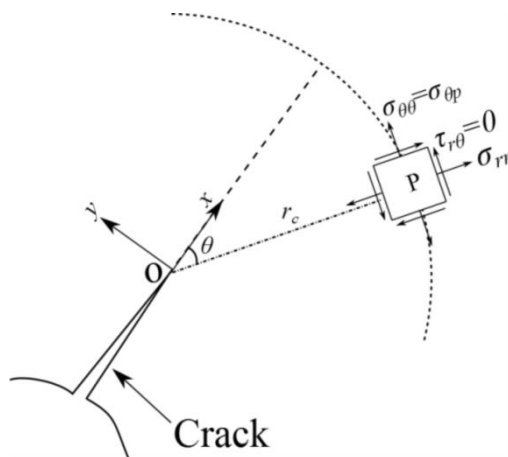
Fig. 6.10 Kinking angle of crack in homogenous medium.

Although the condition in terms of stress may ensure breaking of material ligament ahead of the crack tip, the availability of energy must be sufficient for creation of the new surfaces. This implies that the stress criterion may indicate the direction of possible extension; the actual occurrence is decided by the energy release rate and the fracture toughness of the material.

The advantages of combining the two criteria are: (1) It reduces the need of multiple analysis. The potential kink angle ω is obtained by a single analysis. (2) The effect of T-stress is included in the stress-based criterion.

6.4 Results

The proposed EFG method has been applied to a number of crack problems under mechanical or thermal loadings and the results are presented. A case study on a crack propagating towards a bi-material interface followed by further crack growth along the interface has also been presented.

6.4.1 Crack in orthotropic plate

Fig. 6.11(a) shows a square plate of *a/w*=0.1 with a center crack aligned along its axis of orthotropy. The plate is subjected to uniform tensile load of 1Pa. The material properties correspond to graphite-epoxy combination. A state of plane stress is assumed.
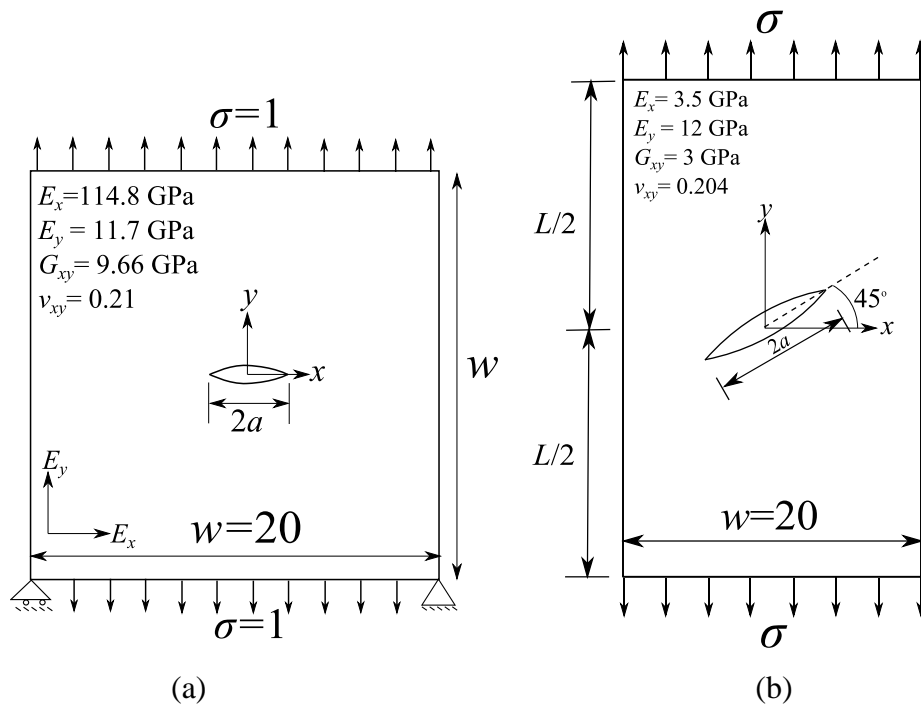
Fig. 6.11 Centre crack in orthotropic plate **(a)** Mode I. **(b)** Mixed mode.

A 9×9 nodal refinement is used at each crack tip. The mode I SIF obtained using M-integral is compared with the results published in the literature. The auxiliary functions for M-integral are adopted from Sih *et al.* (1965). A comparison of the normalized SIF, $\tilde{K}_I = K_I / \sigma\sqrt{\pi a}$, are presented in Table 6.1. The table shows that the results obtained using the proposed method reduces the need for higher nodal density if higher order Gauss integration is used. The result does not much improvement beyond Gauss quadrature involving 16 Gauss points in the background triangular cells.

Table 6.1 Comparison of normalized mode I SIF for a center crack in a finite orthotropic plate.

Method	DOFs	Elements	Background cells	Gauss points in the triangular cells	$\tilde{K}_I$
FEM (Kim & Paulino, 2003)	11702	2001	-	-	0.997
XFEM (Asadpoure et al., 2006)	4278	2025	-	-	1.018
XFEM (Asadpoure & Mohammadi, 2007)	4278	2025	-	-	1.020
XEFG (Ghorashi et al., 2011)	4035	-	1849	13	1.0045
Present Method – I	3644	-	1614	7	1.0416
Present Method - II	3644	-	1614	13	1.0161
Present Method - III	3644	-	1614	16	1.0072
Present Method - IV	3644	-	1614	37	1.0075
Present Method - V	3644	-	1614	48	1.0071

Table 6.2 Comparison of normalized mode I and II SIF for an angled crack in rectangular orthotropic plate.

Method	$\tilde{K}_I$	$\tilde{K}_{II}$
Sih et al. (1965), Analytical	0.5	0.5
Kim & Paulion (2003) – FEM	0.506	0.495
Asadpoure & Mohammadi (2007) – XFEM	0.514	0.519
Ghorashi et al. (2011) - XEFG	0.512	0.530
Atlurei et al. (1975) – FEM	0.484	0.512
Wang et al. (1980) - FEM	0.485	0.498
Present method	0.509	0.510

To further illustrate, an angled crack in a rectangular plate of $L/w = 2$ and $a = \sqrt{2}$ is considered as shown in Fig. 6.11(b). Results presented in Table 6.2 shows a good comparison

between the mixed mode SIFs obtained by the present method and the existing results in the literature.

6.4.2 Bi-material interfacial edge crack in finite plate

(a)   (b)
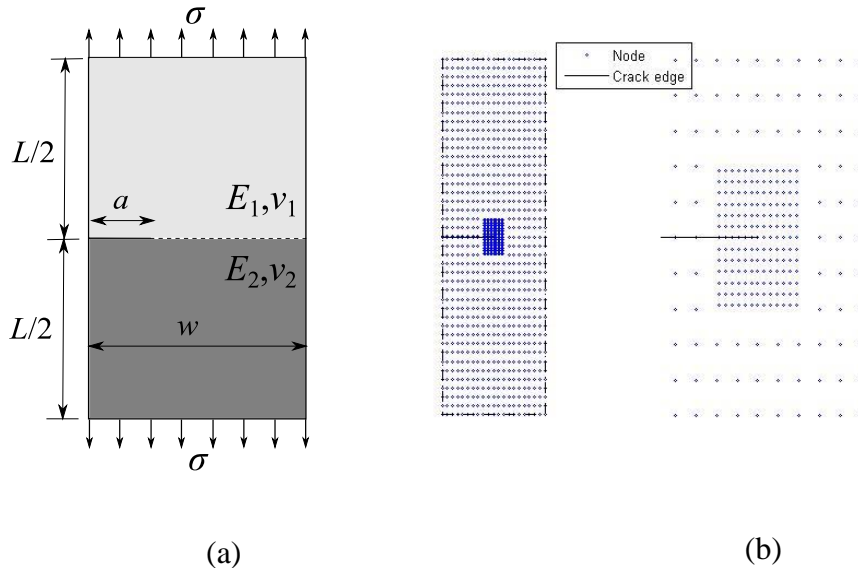
Fig. 6.12 (a) Interfacial edge crack in bi-material plate. **(b)** Nodal discretization.

A bi-material plate with an edge crack (Fig. 6.12(a)) with dimensions width $w = 1\,\text{m}$ and $L/w = 3$ is considered for the analysis using the proposed EFG method. The normal traction at the top and bottom edges is 1MPa. The plate is discretized with 21×61 nodes. The domain of influence is 1.75 times the nodal spacing. The material properties employed are: $E_2 = 205.8\,\text{GPa}$; three ratios of $E_1/E_2 = 1, 2$ and 100 are considered. The Poisson's ratio $v = 0.3$ is set for both materials. A state of plane stress condition is assumed. The region around the crack tip is refined with 13×13 nodes (Fig. 6.12(b)).

The normalized SIFs ($\mathbf{K}/\sigma\sqrt{\pi a}$) based on the proposed EFG method obtained for crack ratios (a/w) varying from 0.1 to 0.7 are compared (Fig. 6.13 and Fig. 6.14) with results available in the literature (Murakami, 1987; Matsumto et al., 2000; Mohit et al., 2011). These are also compared with those obtained by the XEFG method. Since the XEFG method incorporates special functions, the region around the crack tip was not refined with additional nodes.

The SIFs are obtained through the interaction integral using the crack tip auxiliary functions for the interface crack. A square domain of side length $0.125a$ centered on the crack tip is considered as the domain for the interaction integral. The results show that there

is an excellent agreement with the published results and with those obtained by the XEFG method.
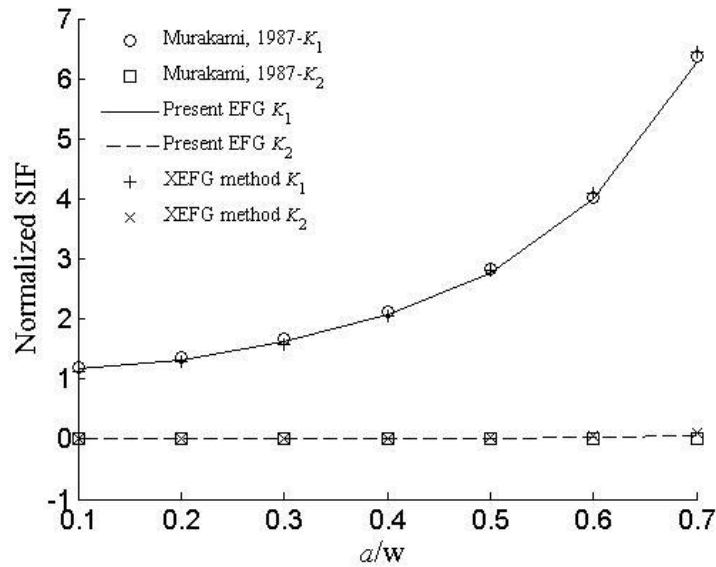
Fig. 6.13 Comparison of normalized SIFs for $E_1 / E_2 = 1$.

| (a) | (b) |
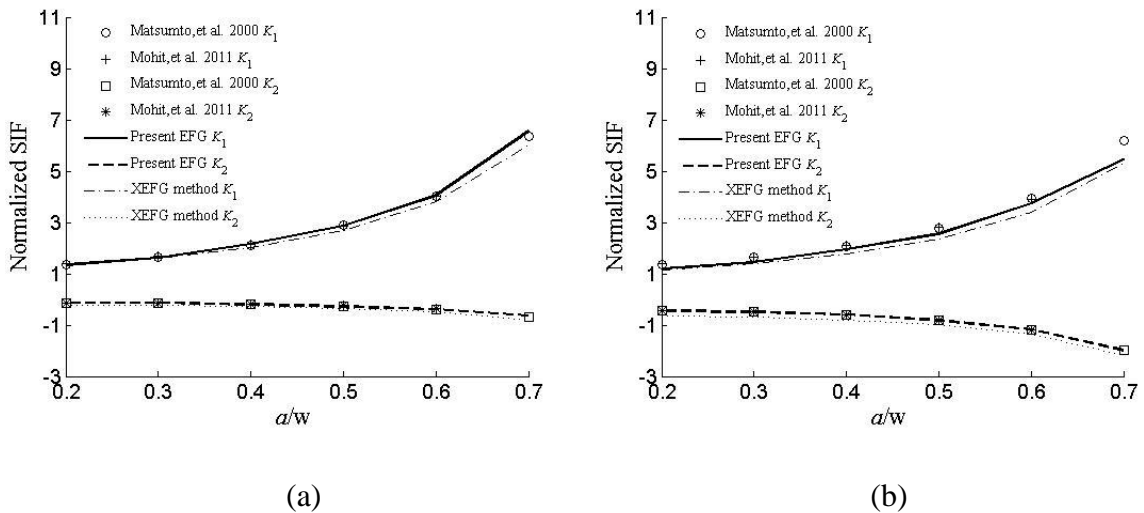
Fig. 6.14 Comparison of normalized SIFs for **(a)** $E_1 / E_2 = 2$ and **(b)** $E_1 / E_2 = 100$.

Fig. 6.14(a) and (b) show the similar comparisons of the normalized SIFs for $E_1 / E_2 = 2$ and $E_1 / E_2 = 100$ respectively. The results obtained by the proposed EFG method are in slightly in better agreement with those obtained through the XEFG method. This may be due to the refinement in the region around the crack tip. It is also observed that the computed SIFs deviate slightly from the published results, as the ratio of E_1 / E_2 increases.

The maximum difference with result of reference (Matsumto et al., 2000) is less than 15% with an average error of less than 5%. The difference is more in the case of K_I.

6.4.3 Bi-material disk subjected to thermal loading

Fig. 6.15 shows a bi-material disk subjected to uniform cooling $\Delta T = -5^{\circ}$C. The radius (r) of the disc is 20 mm and the crack length ($2a$) is $0.5r$. The upper material (1) is glass with $E_1 = 73$GPa, $\eta_1 = 8\text{e-}6/^{\circ}$C and $v_1 = 0.22$; and the lower material (2) is epoxy with $E_2 = 2.9$GPa, $\eta_2 = 73\text{e-}6/^{\circ}$C and $v_2 = 0.29$. A state of plane strain is assumed.
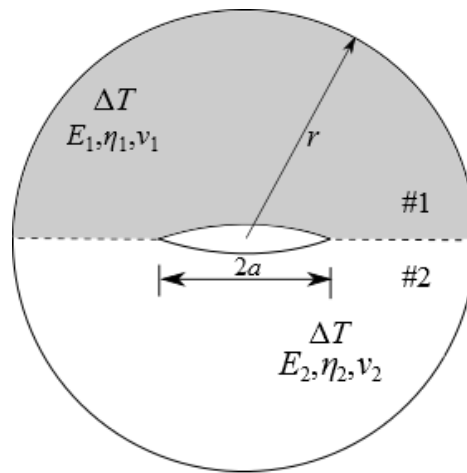
Fig. 6.15 Bi-material disc with central crack subjected to temperature change ΔT.

The complex SIF is calculated using the thermal interaction integral involving temperature. For the evaluation of the integral, a square domain with edge length of $0.25a$ is considered. The computed SIF is normalized through $\tilde{\mathbf{K}} = \left(K_1 + iK_2 \right) L^{i\varepsilon} / \sigma \sqrt{\pi a}$ where $\sigma = \dfrac{(1-v_1)\eta_1 - (1-v_2)\eta_2}{1/E_2^* - 1/E_1^*} \Delta T$ and $L = a$. Results presented in Table 6.3 show that the present method, devoid of enrichment functions, is able to give the SIFs close to the results of Pant. et al. (2010) based on enriched EFG method.

Table 6.3 Normalized complex SIF for central crack in a bi-material disc.

Normalized SIF	Banks-Sills & Dolev (2004)-FEM	Pant. et al. (2010)-EFG method	Present Method
$\tilde{K}_1$	-0.3466	-0.3523	-0.3574
$\tilde{K}_2$	0.2389	0.2342	0.2387

6.4.4 Crack approaching normal to material interface

Fig. 6.16 shows a bi-material panel with an internal crack: $a/w = 0.1$, $L/w = 3$, $w = 10\,\text{m}$, $\rho = \ln(10)/2w$ and $\sigma = 1\text{MPa}$. Material 1 is a functionally graded and material 2 is an isotropic and homogenous material. The modulus of material 1 varies with x and has value of E_o. The value of E_o is 1MPa. A state of plane strain is assumed. Poisson's ratio $v = 0.3$ is assumed for both the materials. Two cases are examined: Case (1) involves a sharp material discontinuity in Young's modulus at $x = 0$. While material 1 has the modulus of E_o at the interface $E(x = 0^-) = E_0$, material 2 has modulus $2E_o$ $E(x = 0^+) = 2E_0$. In Case (2) there is no discontinuity in the Young's modulus is considered at $x = 0$, but their derivatives are discontinuous. The moduli of both the materials are E_o.
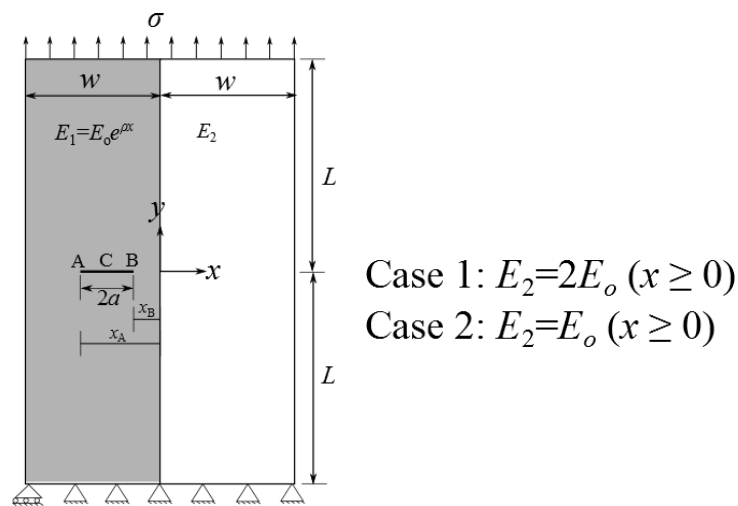
Fig. 6.16 Crack terminating normally to material interface

The normalized mode I SIFs ($K_I/(\sigma\sqrt{\pi a})$) for crack tip at A and B are plotted in Fig. 6.17(a) and Fig. 6.17(b) respectively as the location of crack center C is varied. Crack tip A and crack tip B meet the interface when $x_A/w=0$ and $x_B/w=0$ respectively. The interface is indicated by the dotted line.

Case (1) – The mode I SIF for the crack tip A increases gradually as the tip approaches the interface from the left. When the tip is at a distance of about $x_A/w = -0.2$, i.e., tip is away from the interface by the crack size, the SIF starts dropping slowly, then rises rapidly because of the influence of the stiffer material 2. It picks up the maximum value when $x_A/w \approx 0$. As soon as it moves into the material 2, the SIF has a sharp jump because of the material

influence. Subsequently it drops. For the tip B, the SIF reaches maximum when it is almost away from the interface by $x_B / w = -0.1$. On further movement towards the interface, it drops to a lower level. As it crosses the interface, the SIFs jump to higher level and it continues until it is away from the interface by a distance equal to the crack size. Then it drops.
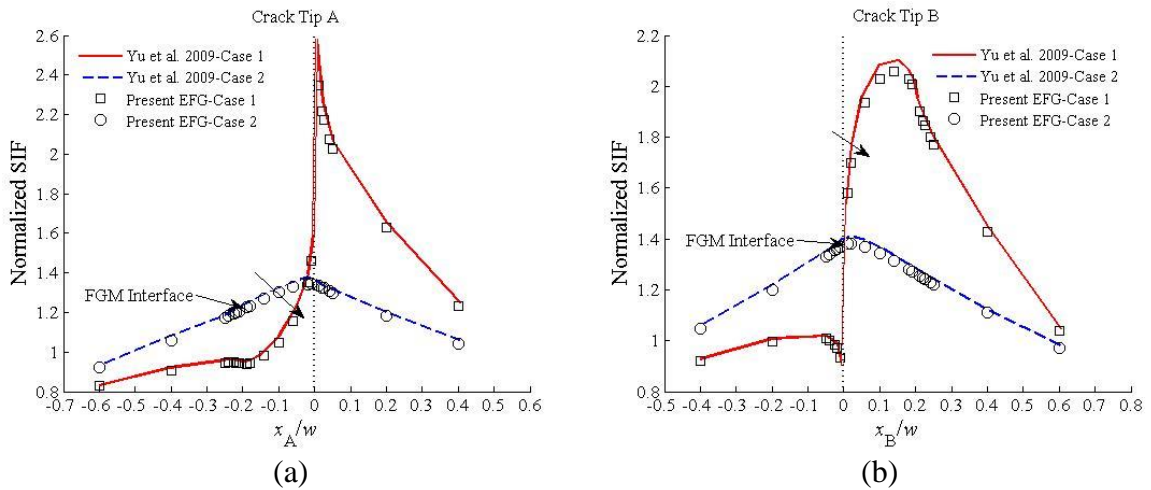
Fig. 6.17 Variation of normalized mode I SIFs with centre of crack *c/w* at **(a)** crack tip A and **(b)** crack tip B.

Case (2) – In the case of the interface with no discontinuity in the modulus, the SIFs for both the crack tip A and B increase until they meet the interface. As the crack cross the interface, the SIFs at both the tips start dropping. Such a case study was reported earlier by Guo & Noda (2008). The present observations on the SIF variation in for both the cases are in agreement with the results by Yu et al. (2009).

6.4.5 Crack normal to material interface
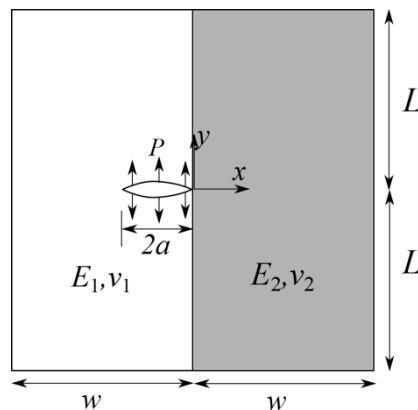
Fig. 6.18 Crack terminating normal to material interface.

Fig. 6.18 shows an internal crack subjected to pressure loading, P in a bi-material rectangular plate. The dimensions and loading are: $a/w = 1/9$, $L/w = 1$, $w = 9$in (0.2286m) and $P = 1$psi (6.895 kPa). A state of plane strain is assumed. Table 6.4 shows the properties of the materials used.

Table 6.4 Material properties.

Material	Young's modulus (E)	Poisson's ratio (ν)
Aluminum	10^7 psi (68.95 GPa)	0.3
Epoxy	0.45×10^6 psi (3.102 GPa)	0.35

Two cases were analyzed: In case (a), the crack is in the compliant material, epoxy. The ratio of μ_2 / μ_1 is 23.07. The value of order of singularity λ, in this case, is 0.6619. In case (b), the crack is in the stiff material, aluminium. The ratio of μ_2 / μ_1 is 0.043. The value of λ is 0.1752. The crack opening displacement (COD) profiles behind the interface tip, for the two cases, are compared with the published results (Cook & Erdogan, 1972; Maiti, 1992) in Fig. 6.19(a) and Fig. 6.19(b). The SIFs for the crack tip are obtained from the numerical COD solution using the following relation

$$K_1 = 2\sqrt{2}(\pi/r)^\lambda \lambda \mu^* v_{COD}$$
$$\mu^* = \mu_1 m \frac{(1-2\lambda)(m+\kappa_2)+(1+2\lambda)(1+m\kappa_1)}{(m+\kappa_2)(1+m\kappa_1)\sin \pi\lambda} \tag{6.3}$$

where v_{COD} is the COD, r is the radial distance from the crack tip and $m = \mu_2 / \mu_1$.

(a) (b)
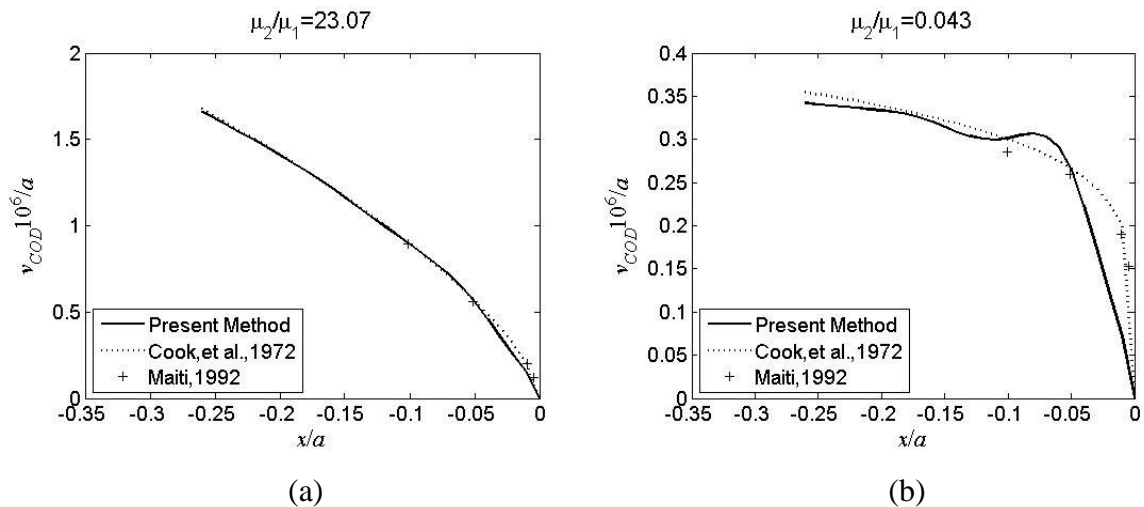
Fig. 6.19 COD profile of crack for **(a)** $\mu_2 / \mu_1 = 23.07$.**(b)** $\mu_2 / \mu_1 = 0.043$.

The COD profile for $\mu_2 / \mu_1 = 23.07$ is in good agreement with the published results when the crack is in the stiffer material; it deviated slightly from the existing results very close to the crack tip. The COD profile for $\mu_2 / \mu_1 = 0.043$ is found to oscillate close to the crack tip and gets stable after a distance of $0.1a$ from the crack tip. Such a discrepancy the results for $\mu_2 / \mu_1 = 0.043$ was already reported in the literature (Tracey & Cook, 1977; Maiti, 1992). Maiti's solution and Tracy *et al.*'s FEM results, differed by -12.5% and 9.97% with Cook and Erdogan's (1972) solution.

Hence, it is recommended that v_{COD} should be computed within a span of $0.1a$ to $0.2a$ behind the crack tip for determining the SIFs based on the displacement method. In the present studies v_{COD} values are computed at $0.1a$. Table 6.5 shows a comparison of SIF obtained by the proposed EFG method with the published results.

Table 6.5 Comparison of normalized SIF $K_I / P(\pi a)^{1-\lambda}$

Shear modulus ratio	$\mu_2 / \mu_1 = 23.07$		$\mu_2 / \mu_1 = 0.043$	
Singularity constant	$\lambda = 0.5$	$\lambda = 0.6619$	$\lambda = 0.5$	$\lambda = 0.1752$
Proposed EFG method (2014)	0.861 (2.16%)	4.147 (0.05%)	1.478 (0.14%)	0.048 (14.29%)
Maiti (1992)	0.880	4.149	1.476	0.042
Cook & Erdogan (1972)	0.882	-	1.355	0.048

6.4.6 Crack meeting at an oblique angle to the material interface

Fig. 6.20 shows an edge crack in a rectangular bimaterial plate inclined at an angle 20° to the *x*-axis. The dimension and loading details are: $L/w = 3, w = 0.5\,\mathrm{m}$ and $\sigma = 1\mathrm{MPa}$. Poisson's ratio, $v = 0.3$, is set for both the materials. A state of plane strain is assumed. The ratio of Young's moduli (E_1 / E_2) is 100. In this case, there are two orders of singularity: $\lambda_1 = 0.114$ and $\lambda_2 = 0.071$. A set of eight enrichment functions are needed for an accurate modelling using the XFEM or the XEFG method.

The crack opening displacement (v_{COD}) profiles, obtained using the proposed EFG method and the FEM are compared in Fig. 6.21(a). There is agreement between the two for $r > 0.01$. The EFG method is bound to The results are obtained with 2860 DOFs using the proposed EFG method. In the case of FEM, 995596 DOF and 165794 eight-node quadrilateral elements are employed in ANSYS to obtain the converged solution. A combination of very fine mesh near the crack tip (crack tip element size $-0.005a$) plus a

coarse mesh away resulted in higher degrees of freedom for the FEM analysis. The good performance of the proposed EFG method is attributed to higher order continuous shape functions.
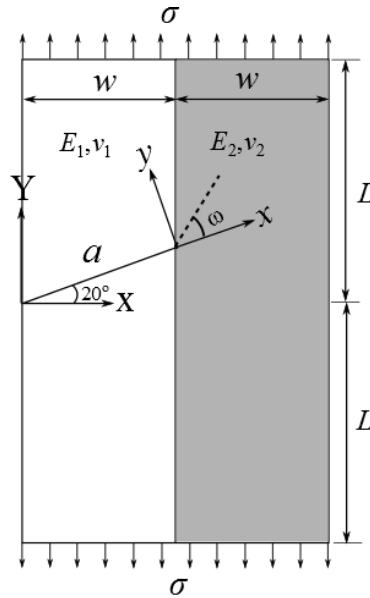
Fig. 6.20 Crack meeting at an angle to the bi-material interface.

The variation of the ERR ratio $G_{m\omega}/G_I$ with kinking angle θ is shown in Fig. 6.21(b). As θ increases, $G_{m\omega}/G_I$ increases till $\theta=-20^{\circ}$. Afterwards, it decreases steadily until it becomes aligned with the interface ($\theta=70^{\circ}$).

(a)   (b)
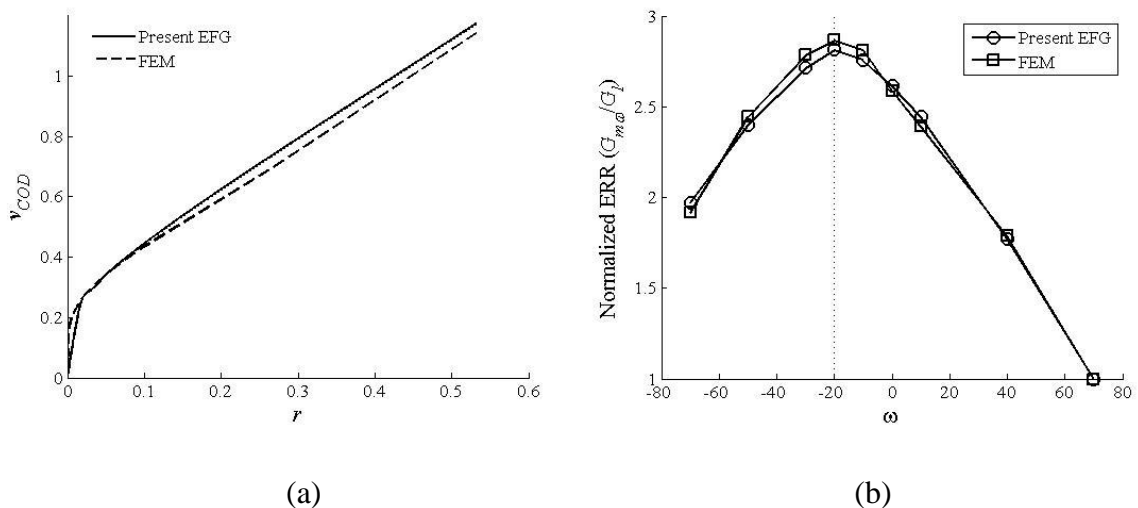
Fig. 6.21 (a) Crack opening displacement for oblique crack meeting biomaterial interface. **(b)** Variation of the normalized ERR $G_{m\theta}/G_I$ with kink angle θ.

This plot shows that the crack is likely to propagate along the radial direction $\theta=-20^{o}$ as this direction is associated with the maximum energy release rate. The crack will extend in the direction provided the $G_{m\omega}/G_I > \Gamma_f^m/\Gamma_f^I$ or if the interface fracture toughness is assumed to be tough. This is in agreement with the results published in the case of a tough interface (Sundararajan et al., 2014). Specifically, it will extend into the adjoining material if the interfacial fracture toughness is more than 0.36 times the fracture toughness for material $\left(\dfrac{\Gamma_f^I}{\Gamma_f^2} > \dfrac{1}{2.814} \approx 0.36\right)$.

6.4.7 T-stress for crack in bi-materials

The stress state for an interface crack of length, a, is given by

$$\sigma_{ij}^m = \frac{F_{ij}^m(\theta)}{\sqrt{r}}\mathrm{Re}\left[\mathbf{K}r^{i\varepsilon}\right] + \frac{G_{ij}^m(\theta)}{\sqrt{r}}\mathrm{Im}\left[\mathbf{K}r^{i\varepsilon}\right] + T_m\delta_{i1}\delta_{j1} + O(\sqrt{r}) \tag{6.4}$$

where $\mathbf{K} = K_1 + iK_2$ and T_m is the T-stress for material m, $m = 1$ and 2. T-stress is the first non-singular stress term of the William's eigenfunction expansion of a crack tip stress field. $F_{ij}^m(\theta)$ and $G_{ij}^m(\theta)$ are angular functions.

The same interaction integral used to compute the SIFs is invoked to determine the T-stress using appropriate selection of the auxiliary stresses (σ_{ij}^{aux}), strains (ε_{ik}^{aux}) and displacements (u_i^{aux}) (Sladek & Sladek, 1997). These auxiliary functions are given in Appendix E. The T-stress is related to the interaction integral by

$$T_m = \frac{IE_m^*}{f} \tag{6.5}$$

where T_m is the T-stress for material m and f is a point force applied. The same auxiliary solutions (i.e. assuming there will be only one material $m=1$) can also be used to determine the T-stress for a crack inside an isotropic material.

Two cases have been considered to illustrate the effectiveness of the proposed EFG method in evaluating T-stress. A state of plane strain condition is assumed. In case (a), a bi-material plate, with a center crack, subjected to a uniform tensile load σ is considered (Fig.

6.22(a)). The dimensions properties are: $L/w = 2$, $w = 1m$ and $v_1 = v_2 = 0.3$. The ratio of Young's moduli (E_1/E_2) is varied from 1 to 10. The T-stress is computed for three different crack length ratios (a/w): 0.15, 0.25 and 0.35.

Taking note of the suggestion of using a bigger integral domain (Hongjun et al., 2012) for T-stress calculation, a square domain with edge length of crack length a, is used. The T-stress obtained by the proposed approach is in good agreement (Fig. 6.23) with the published results (Sladek & Sladek, 1997) for various E_1/E_2 ratios. The computed T-stress is normalized by σ_o ($B = T/\sigma_o$), where

$$\sigma_o = [(K_1^2 + K_2^2)/\pi a]^{1/2} \tag{6.6}$$

(a)   (b)
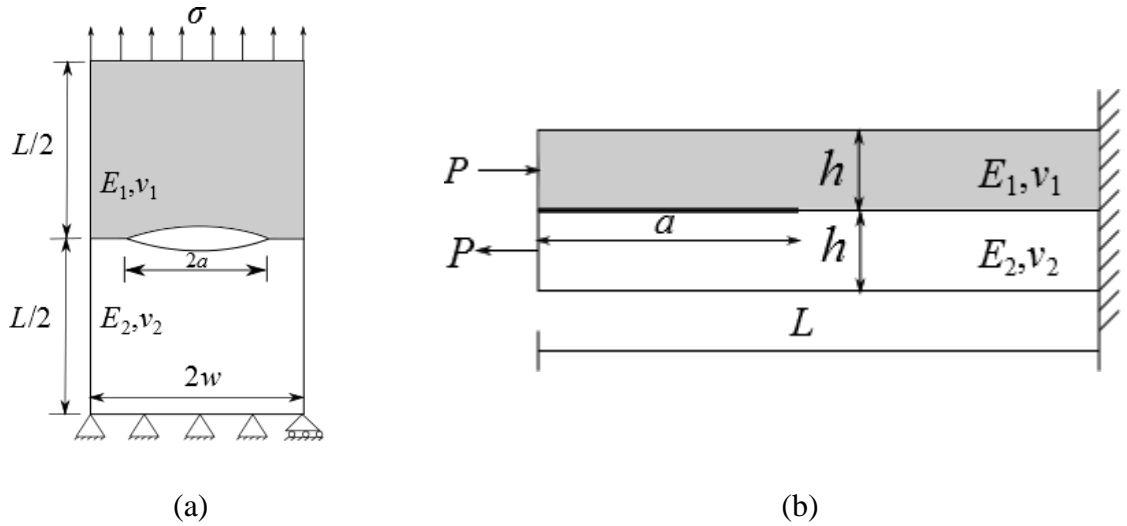
Fig. 6.22 (a) Centre crack in bi-material plate. **(b)** Edge crack in a bi-material strip.
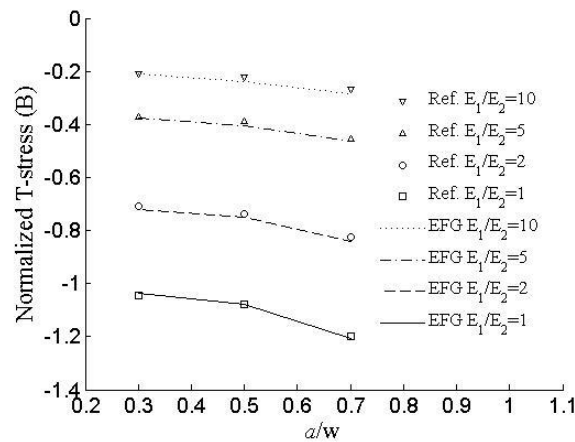
Fig. 6.23 Comparison of normalized T-stress with reference results Sladek et al. (1997) for centre crack in bi-material plate subjected to uniaxial tension.

A bi-material strip with an edge crack (Fig. 6.22(b)) is examined. The dimensions of the strip are: $a/L = 0.5$, $h/L = 0.1$ and $L = 10$m. The strip is subjected to point loads, $P = 1$MN, as shown in figure. The right end of the strip is fixed. Table 6.6 presents comparisons of normalized T-stress, $T/(P/h)$, with the published results (Hongjun et al., 2012; Kim & Vlassak, 2006) for different material combinations. The comparison shows a good agreement.

Table 6.6 Comparison of normalized T-stress for different material combinations for interafcecrack in bi-material strip.

E_1/E_2	v_1	v_2	α	β	$T/(P/h)$		
					Present EFG method	(Hongjun et al., 2012)	(Kim & Vlassak, 2006)
7/3	1/3	1/3	0.4	0.1	0.0709	0.0702	0.0709
20/9	1/4	1/8	0.4	0.2	0.0778	0.0773	0.0784
4	2/5	2/5	0.6	0.1	0.1301	0.1317	0.1310
4	1/4	1/4	0.6	0.2	0.1419	0.1410	0.1424

6.4.8 Interface crack kinking angle
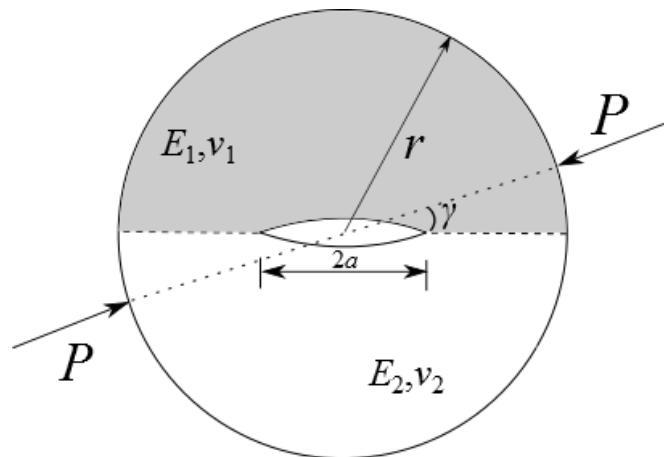
Fig. 6.24 Bi-material disc subjected to diametrical compression by point loads.

To predict the kink angle ω for an interface crack, a bi-material disc subjected to point loads, P, oriented at angle γ to the crack plane, is considered (Fig. 6.24). The dimensions are: $r = 40$mm and $a/r = 0.25$. The material properties are appropriately chosen to vary α and β.

The mode-mixity (ψ) is defined as

$$\psi = \tan^{-1}(K_2 / K_1) \tag{6.7}$$

Fig. 6.25 shows the variation of mode-mixity ($\hat{\psi}$), where $\hat{\psi} = -\psi$, with the compression angle γ for different material combinations. The variation of $\hat{\psi}$ with loading angle γ for different oscillation index ε, for $\alpha = 0$, is shown in Fig. 6.25(a). The results are similar to the results of Zhijia et al. (2013). This shows that, as γ increases, the crack experiences higher mode-mixity $\hat{\psi}$. $\hat{\psi}$ for a particular γ is found to depend on ε; it decreases as ε decreases. When $\varepsilon = 0$, $\hat{\psi}$ does not depend on Dundurs' parameter, α, (Fig. 6.25(b)). This suggests that the kinking angle ω is primarily dependent on ε. By means of extrapolation it is found that $\hat{\psi}=90^\circ$ occurs around $\gamma = 28^\circ$, for small ε ($|\varepsilon| \leq 0.01$). This is in close agreement with fracture test results of Atkinson *et al.* (1982).
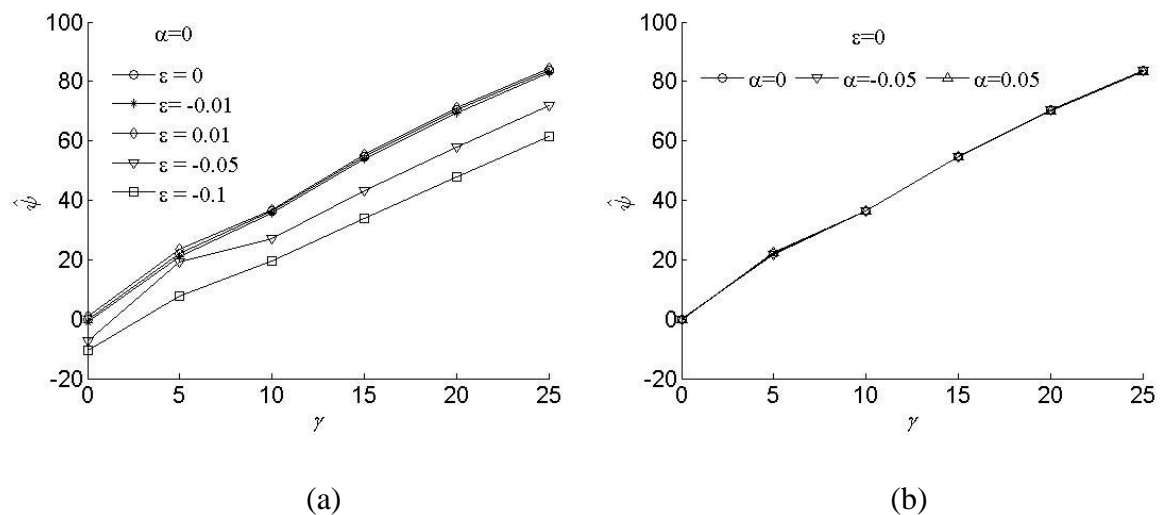
Fig. 6.25 Variation of mode-mixity $\hat{\psi}$ with compression angle γ for **(a)** $\alpha = 0$ and various ε **(b)** $\varepsilon = 0$ and various α.

The variation of interface crack kink angle, ω, with ψ for various α when $\beta = 0$ is shown in Fig. 6.26(a). This is plotted without consideration of T-stress. The present results are in good agreement with the results obtained using MTS criterion by Yuuki *et al.* (1992). They too showed that ω depended on ψ alone when $\varepsilon = 0$. However, He *et al.* (1989), using the energy-based approach, showed that ω was a function of ψ and α when $\varepsilon = 0$.

As expected, when the T-stress is included to predict ω, for the material combination $\alpha = 0$ and $\beta = 0$, ω is found to change with r/a ratio (Fig. 6.26 (b)). There is a maximum

difference of around 25° between the predicted kinking angle by plotting the stresses at $r/a = 0.0001$ and $r/a = 0.05$. Such a pattern was observed earlier for bi-materials (Kang, 1994) and functionally graded materials (Kim & Paulino, 2003). The T-stress is negative in this case and it decreases the magnitude of the kinking angle.

Another factor that contributes to the varying kinking angle, ω, with r/a ratios is the parameter ε. To illustrate the effect of ε, ω versus $\log_{10}(r/a)$ is plotted (Fig. 6.27(a)) for different ε at $\gamma = 15^{o}$ without considering the effect of T-stress. It is observed that the slope of the plot is higher for a higher oscillation index ε indicating that it plays an important role in determining the kinking angle.

(a)   (b)
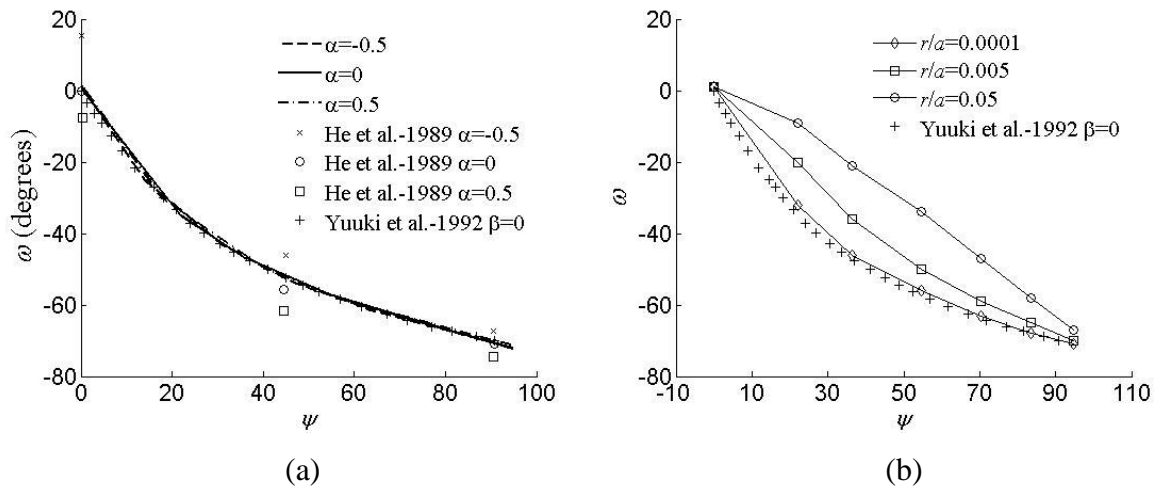
Fig. 6.26 Predicted kinking angle ω with ψ for **(a)** various α without the effects of T-stress for $\beta = 0$ and **(b)** various r/a with the effects of T-stress for $\alpha = \beta = 0$.

(a)   (b)
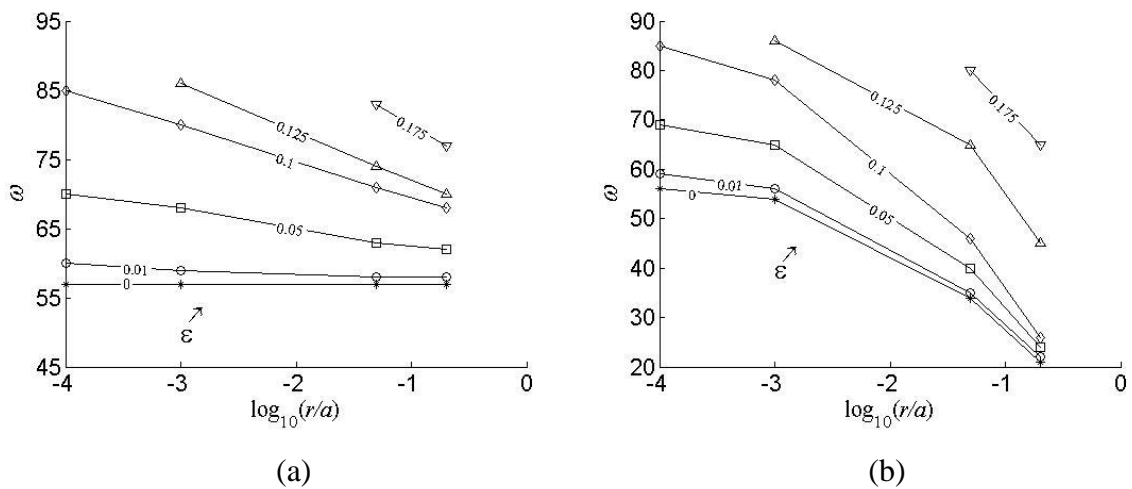
Fig. 6.27 Variation of kinking angle with r/a ratios for different material combinations **(a)** without T-stress. **(b)** with T-stress.

The predicted kinking angle changes significantly with the r/a ratio when the effect of T-stress is included (Fig. 6.27(b)). Both T-stress and ε affect ω at a particular r/a ratio. It is observed that the crack does not kink for certain r/a ratios for $\varepsilon > 0.1$ ($\varepsilon = 0.125$ and $\log_{10}(r/a) < -3$, $\varepsilon = 0.175$ and $\log_{10}(r/a) < -2$). This is because on such circles, the maximum tangential stress is compressive. Hence, the crack cannot extend as per the corollary of Swedlow (1976) given in connection with the MTS criterion that crack propagates in the direction corresponding to the maximum tensile stress. However, as r/a increases, the maximum tangential stress becomes tensile and kinking becomes a possibility. The kink angles significantly vary with r/a when ε is large $(\varepsilon > 0.1)$, which was also showed by Yuuki and Xu (1992).

6.4.9   Crack growth in presence of particle reinforcement

A crack of length a is assumed to be present in a square plate of side $L=2\,\text{m}$. The particle is of radius, $2r/L = 0.15$. The geometry is subjected to uniform tension of $\sigma = 1\,\text{MPa}$. Two arrangements of particles, Fig. 6.28(a) and Fig. 6.28(b), are studied. A state of plane strain condition is assumed. The particle material modulus is $E_p = 6.43 E_m$. The particle and matrix Poisson's ratio are: $v_p = 0.17$ and $v_m = 0.33$. These values correspond to silicon carbide (SiC) particle reinforcement in aluminum (Al) matrix.

(a)   (b)
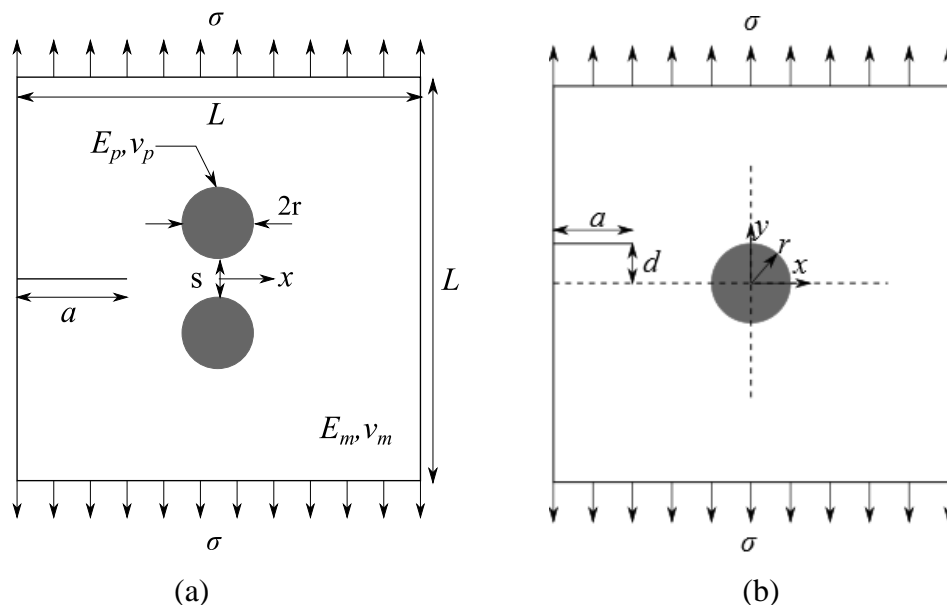
Fig. 6.28 (a) Cracked geometry with two particles. **(b)** Cracked geometry with single particle.

In the first case (Fig. 6.28(a)), the normalized energy release rate (G/G_o) is plotted as the crack propagates towards the particle starting from a crack size of $a/L = 0.4$. G is the

actual energy release rate (ERR) for a propagating crack and G_o is the ERR for the same geometry in the homogenous matrix of aluminium. A starter crack size of $a/L = 0.4$ is chosen based upon the previous work (Muthu et al., 2013), which showed that the particle effect on the crack tip stress field is insignificant when the distance of the crack tip from the center of the particle is more than $4r$. It is to be noted that the visibility method is used to model the crack tip in the previous work.

Inter-particle distance, S, is varied to show its effect on the propagation of mode I crack. As the crack approaches the particle, the effect of shielding, i.e. a decrease in G/G_o, and amplification, i.e. an increase in G/G_o, is observed to vary with S. Both the shielding and amplification effects are found to enhance with decreasing inter-particle distance (Fig. 6.29). The step-by-step crack advancement length and the finite radius r_c at which the shear stress is plotted are the same ($2r_c/L = 0.04$).
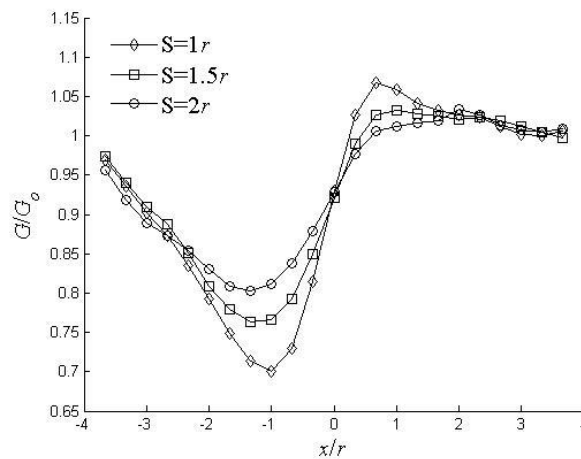
Fig. 6.29 Variation of normalized energy release rates with x/r for various S/r ratios for mode I crack in presence of two particles.

In the case of single particle reinforcement (Fig. 6.28(b)), the curved crack paths have also been determined. As the crack approaches the stiff particle, it gets repelled. The MTPS criterion, which includes the effect of the T-stress, has been employed to find the instantaneous angle of crack propagation, hence the crack paths (Fig. 6.30(a)).

The variation of normalized ERR ratio (G/G_o) is plotted with normalized crack tip position (x/r) with respect to the particle center in Fig. 6.30(b). The variation of the normalized ERRs as the crack propagated shows the shielding and the amplification effects.

It is observed that the shielding effect is more pronounced than the amplification effect in the material combination and the properties considered.

(a)   (b)
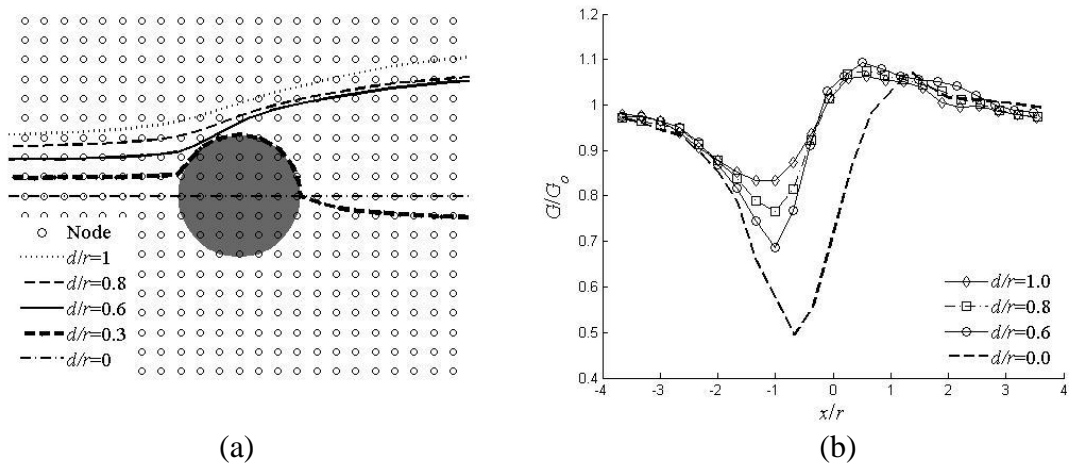
Fig. 6.30 (a) Crack paths for various d/r ratios. **(b)** Variation of normalized energy release with x/r for various d/r ratio.

This plot for $d/r \geq 0.6$ matches closely with results presented by Bush (1997) and Zhiyong et al. (2012). The crack experiences a shielding effect as it approaches the particle and amplification effect as it moves away from the particle. As d/r decreases, these effects increase. The shielding effect can lead to a toughening mechanism. It is observed that parameters like the inter-particle distance and the proximity of crack to the particle may lead to a toughening mechanism.

The shielding effect is highly enhanced for d/r=0 i.e. for a mode I crack approaching the particle. When this crack reaches the interface, it is likely to penetrate the particle along ω=0° if the interface fracture toughness is greater than 0.63 times the particle fracture toughness $\left(\Gamma_f^I > 0.63\Gamma_f^{SiC} \right)$. Otherwise, it would propagate along the interface. If the crack propagates fully through the particle, it may or may not kink into the aluminium matrix depending on the $\Gamma_f^I / \Gamma_f^{Al}$ ratio. The effect of the particle on the crack is reduced as it moves away from the particle.

For d/r=0.3 (Fig. 6.30(a)), the crack propagates through the aluminium matrix up to the interface and then extends along the interface. . The full extension is governed by the MTPS criteria in conjunction with the maximum energy release rate. It is observed that the crack approaches the particle at an angle close to 0^0 with respect to the interface. It propagates after that along the interface and kinks out of the particle-matrix interface. If

$\Gamma_f^I > 0.37\Gamma_f^{Al}$, the crack kinks into the relatively compliant ($\alpha = 0.71$) aluminium and extend as a normal crack in an isotropic and homogenous medium. The composite is assumed to contain no flaws. In reality, there may be flaws near the particle-matrix interface. These will influence extension of the crack.

The crack propagation in this particle-reinforced composite involves a wide spectrum of possibilities. Depending on the relative interface fracture toughness (Γ_f^I) with respect to the toughness of the two constituent materials and relative position of the crack with respect to the particle, fracture patterns may vary from interface cleavage/particle-matrix decohesion to particle breakage. The fracture toughness of the interface Γ_f^I varies with the contact time between the SiC particle and the molten Al matrix during the manufacturing stage (Tham et al., 2001). The possibility of occurrence of various patterns of crack propagation studied here may help to understand some practical situations.

It may be emphasized that an accurate modelling of variable order crack-tip singularity needs a special treatment. One method is to use the enrichment functions that are based upon the analytical solutions, which is only available for few cases. The other method is to develop novel shape functions that are able to account for the variable order singularity stress fields. The shape functions of quarter point element and variable order singularity elements of the FEM (Barsoum, 1976; Maiti, 1992) are examples. Notably, the proposed EFG method based on combination of h- (i.e. nodal spacing) and p- (i.e. order of approximating field function) refinements can be uniformly applied in all situations.

In the case of step by step analysis of crack propagation problems, in addition to the crack tip singularity there exists a variable order singularity at the knee depending on the knee angle. Both these singularities need to be modelled in such analysis. Since there is no technique available to take care of the variable order singularity in the EFG method, the proposed method can be applied without having to bother about the order of singularity at the knee or at the crack tip.

6.5 Closure

The proposed variant of the EFG method gives results of satisfactory accuracy with a reduced number of degrees of freedom. It is a feasible method to model crack propagation in any material, as it eliminates the need for enrichment functions to model a crack tip field. It

can be employed for evaluation of the various LEFM parameters with good accuracy. The SIFs obtained for a crack in the case of orthotropic material and bi-material interface crack under mechanical or thermal loading are in good agreement with the published results. The stress based MTPS criterion, that included T-stress, together with the energy-based approach reduces computational effort to determine the direction of kinking of an interface crack. The compressive T-stress is found to decrease the magnitude of the kinking angle. Both the T-stress and radial distance r_c from the crack tip at which the shear stress is evaluated affect the kinking angle.

In the case of particle-reinforced composites, a wide spectrum of crack propagation possibilities exists. The important factors are relative positions of initial crack with respect to the particle center, inter particle distance, and fracture toughnesses of the interface and the leading material. The tendency for a crack to grow along the interface or kink out of it depends on the relative standing of fracture toughness of the interface and that of the constituent materials.

Chapter 7   Multiple Interacting Cracks

7.1 Introduction

Multiple cracks originate in close proximity due to stress corrosion cracking (Kayama & Totsuka, 2002; Kayama & Kitamura, 2004), creep (Darzens et al., 2001), thermal fatigue, etc., in lap joints and rivets (Kebir et al., 2006), power plant components, nuclear power plant cooling systems (Seyedi et al., 2006), etc. An accurate assessment of life prediction requires the determination of the stress intensity factors (SIFs) under such situations.

Previously, Duflot *et al.* (2004; 2006) modelled multiple cracks by multiplying regular weight functions with square root of the distance from the crack tip. Singh *et al.* (2010) proposed a modified intrinsic meshfree method for modelling multiple cracks. They biased the enrichment by proximity of the Gauss point to a particular crack tip. Shi *et al.* (2013) demonstrated an accurate modelling of interacting cracks using partition-of-unity based EFG method. The enrichment functions used in the approaches above are dependent on crack geometry and material properties. Therefore, modelling an interface crack or a reentrant corner/wedge crack interacting with other cracks leads to difficulties. To overcome these, some of the difficulties, Barbieri *et al.* (2012) proposed the distance-based enriched weight function method. However, they did not validate their method for interacting cracks. Multiple crack weight (MCW) technique was introduced by Muravin & Turkel (2006) to model multiple interacting cracks. Calculating the parameters of this MCW technique is difficult in presence of many arbitrary oriented cracks.

In the present chapter, the level set method is used to determine the parameters of a modified MCW technique to model interacting cracks. This technique has been applied to study kinked cracks that involve reentrant corners and knee singularity. A general procedure to model many cracks using diffraction method is described. To illustrate the efficiency and accuracy of the proposed approach, a number of case studies, involving multiple crack interactions, crack-microcrack interactions, interface crack-microcrack interaction, double and triple kinked cracks have been solved. The M-integral/interaction integral is again used as the basis to compute the SIFs. The results are compared with reported results in the literature.

7.2 Multiple Crack weight (MCW)

In the diffraction method, that has been already discussed in Section 3.8.1, the weight function of a node that has crack tip in its domain (d_I), has its influence over a region dictated by the diffraction space associated with a point light source at the node and the crack acting as an opaque object. This ensures generation of smooth shape functions, which in turn ensures smooth strain field. In the case of single crack (Fig. 7.1), depending on a generic point location, $\mathbf{g} = (x, y)$, location of the crack tip ($\mathbf{x}^c$) and the nodal location $\mathbf{x}_I$, distance (d_r) between them is modified as per the relation

$$d_r = \left(\frac{s_1 + s_2(\mathbf{g})}{s_0(\mathbf{g})} \right)^{\lambda} s_0(\mathbf{g}) \tag{7.1}$$

where $s_0(\mathbf{x}) = \|\mathbf{g} - \mathbf{x}_I\|$. The parameter λ is 2. s_1 is the distance from the node I at location $\mathbf{x}_I$ to $\mathbf{x}^c$. $s_2(\mathbf{g})$ is the distance from ($\mathbf{x}^c$) to $\mathbf{g}$. In all the case studies in this chapter, a cubic weight function, $w(r)$ given in the following, is used

$$w(r) = \begin{cases} 2/3 - 4r^2 + 4r^3, & r \leq 0.5 \\ 4/3 - 4r + 4r^2 - 4/3r^3, & 0.5 < r \leq 1 \\ 0, & r > 1 \end{cases} \tag{7.2}$$

where $r = d_r / d_I$. Because of Eq. (7.1), the normal circular domain of influence is truncated as shown in Fig. 7.1. The shadow region, where $w(r) = 0$, near the crack is caused by the higher values of d_r.
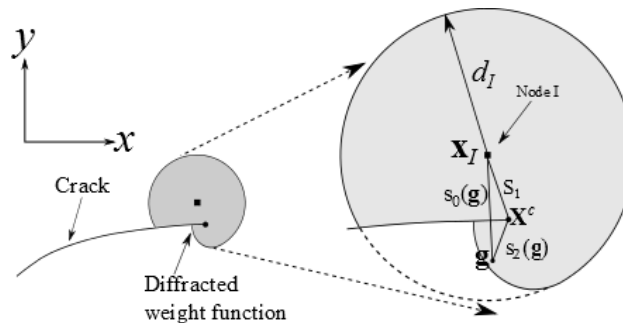
Fig. 7.1 Diffraction method for a single crack.

When multiple cracks are located in close proximity, it is necessary to use very high refinement to ensure that no two or multiple crack tips are influenced by a single node. On the other hand, the MCW technique enables coverage for multiple crack tips by a single node; this decreases the need for high nodal density. Modelling of multiple crack tips through diffraction method is possible because of higher order continuous nature of the EFG method shape functions derived using the MLS approach.

Fig. 7.2 shows a case of multiple interacting cracks where all the crack tips are located within d_I of a node I whose weight function is diffracted around each of the crack tips. In the MCW technique, s_1 in Eq. (7.1) is modified by

$$s_1 = \sum_{n_c=1}^{n} s_1^{n_c}$$

$$s_1^{n_c} = \begin{cases} \left\| \mathbf{x}_1^c - \mathbf{x}_I \right\|, & n_c = 1 \\ \left\| \mathbf{x}_{n_c}^c - \mathbf{x}_{n_c-1}^c \right\|, & n_c \neq 1 \end{cases} \tag{7.3}$$

$$s_2(\mathbf{g}) = \left\| \mathbf{g} - \mathbf{x}_{n_c}^c \right\|$$

where $\mathbf{x}_{n_c}^c$ is the location of crack tip n_c ($1 \leq n_c \leq n$). n is the total number of cracks whose tips are influenced by the node I. For instance, in Fig. 7.2, $s_1 = s_1^1 + s_1^2 + s_1^3$ and $s_2(\mathbf{g}) = \left\| \mathbf{g} - \mathbf{x}_3^c \right\|$. This definition is slightly different from what was used by Muravin and Turkel (2006).
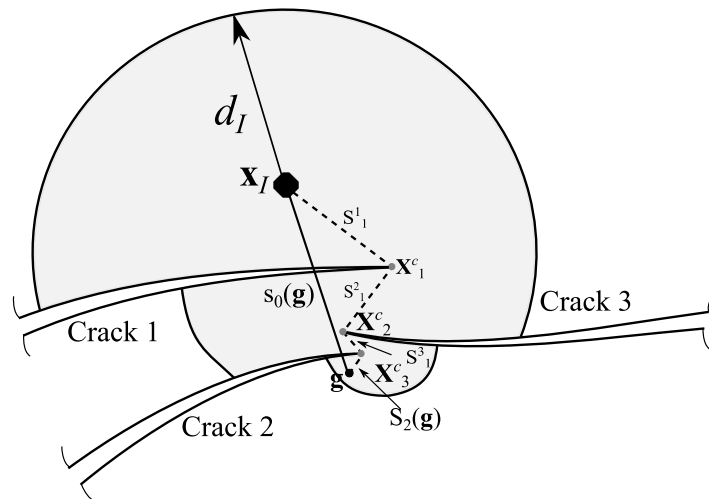
Fig. 7.2 Multiple crack weight (MCW) technique.

A method to compute the parameters s_1 and $s_2(\mathbf{g})$ is presented in the following. This is facilitated by the level set method, which are adopted in the MMs to help study problem of crack propagation.

7.3 Level set method

7.3.1 Level set description for a 2D crack
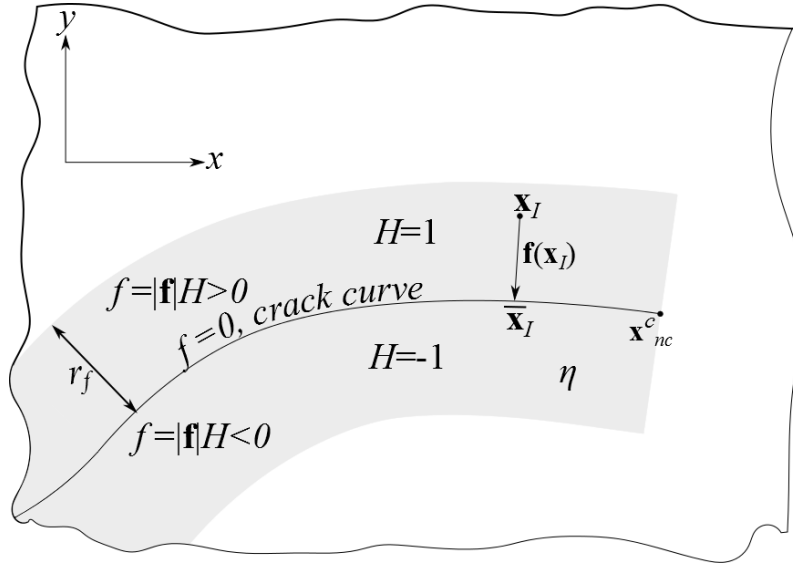
Fig. 7.3 Level set description for a crack.

The level set method is used to represent the crack location. This is facilitated by a signed distance function $f(\mathbf{x})$, which contains the signed normal distance from a grid point $\mathbf{x}$ to the crack. A crack is represented as a zero level set of the function $f(\mathbf{x})$ (Fig. 7.3). The endpoints of the crack, i.e. crack tip locations, are kept in store separately.

The sign of the level set function $f(\mathbf{x})$ is +ve if $\mathbf{x}$ lies above the crack and −ve if it lies below the crack. The sign information is given by $H(f(\mathbf{x}))$ where H is the Heaviside function. Since the area of interest is localized to the crack, the level set computations are restricted to the region that surrounds the crack. This region is called 'narrow band' and is indicated in grey colour (Fig. 7.3). In this work, the narrow band region is denoted by η. The crack is identified first and the level set functions are computed at the grid points in a predetermined region on both the sides of the crack. In the present work, the half size (r_f) of the narrow band is taken as $1.1d_I$ which is slightly bigger than the domain of influence for a regular meshfree node.

At every grid point $\mathbf{x}_I$ that lies in the narrow band, a vector level-set function $\mathbf{f}(\mathbf{x}_I)$ and the sign of the level set function $f(\mathbf{x}_I)$ is stored; for a 2D case, $\mathbf{f}(\mathbf{x}_I) = \Delta x_I \hat{i} + \Delta y_I \hat{j}$ where Δx_I and Δy_I are x and y components of the function $f(\mathbf{x})$. Then, the signed distance function $f(\mathbf{x})$ can be obtained using the relation: $f(\mathbf{x}_I) = \|\mathbf{f}(\mathbf{x}_I)\| H(f(\mathbf{x}_I))$. A compound object $\tilde{f}(\mathbf{x}_I)$ defined as $\tilde{f}(\mathbf{x}_I) = \{\Delta x_I, \Delta y_I, H(f(\mathbf{x}_I))\}^T$ is stored at grid point that lies inside the narrow band. If there are N grid points in the entire geometry, then the structure of the level set database is given by

$$\tilde{f} = \begin{bmatrix} . & \Delta x_i & . & . & . \\ . & \Delta y_i & . & . & . \\ . & H(f(\mathbf{x}_i)) & . & . & . \end{bmatrix}_{3 \times N} \quad i = \{1, 2, ..., N\} \tag{7.4}$$

Intially all information about level set grid points contains zeroes only. If any grid point is found to lie within the narrow band of a starter crack, then these grid points are activated and the object $\tilde{f}(\mathbf{x})$ is stored at these locations. Let p_η denote the set that consist of grid points inside η, then $\tilde{f}(\mathbf{x}_i) = \{0, 0, 0\}^T \forall i \notin p_\eta$. Consequently, if any element of the third row of the object $\tilde{f}$ is zero, then the corresponding grid point does lie in the narrow band region. As the crack extends, the new grid points that fall in the extended narrow band are activated with the level set data $\tilde{f}(\mathbf{x})$, which are easily obtained by some geometric relations for 2D problems (Ventura et al., 2002).
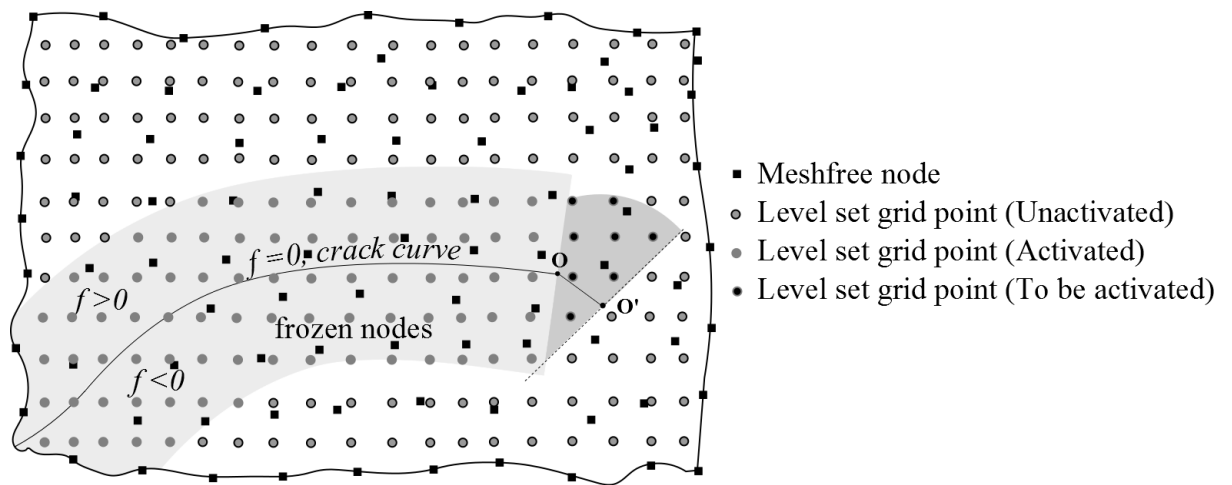
Fig. 7.4 Meshfree node and level set grid points.

- ■ Meshfree node
- ○ Level set grid point (Unactivated)
- ○ Level set grid point (Activated)
- ● Level set grid point (To be activated)

Generally, the levels set data are stored at the grid points that coincide with the meshfree nodes. Since coarser meshfree nodal discretization is used in this work, significant error can occur during activation of level set data in the new grid points (Ventura et al., 2002). Therefore, a background-refined arrangement of grid points with closer spacing, different from that of meshfree nodes, is used as storage locations (Fig. 7.4). As the crack grows from **O** to **O'**, new grid points are activated. These activated grid points will be added to the set p_η.

7.3.2   Level set for description for multiple cracks
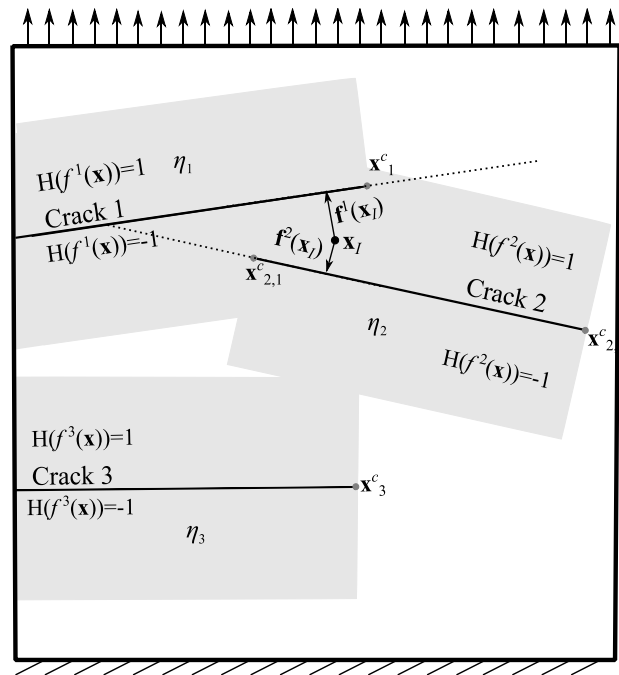
Fig. 7.5 Level set function for multiple cracks.

Fig. 7.5 shows the narrow band region for a set of three cracks 1, 2 and 3. The vector level-set distance function from a point $\mathbf{x}_I$ that is common to the narrow band of crack 1 and 2 is shown. The level set object $\tilde{f}(\mathbf{x}_I)$ for a three-crack system can be represented as $\tilde{f}(\mathbf{x}_I) = \left[[\tilde{f}^1(\mathbf{x}_I)] \quad [\tilde{f}^2(\mathbf{x}_I)] \quad [\tilde{f}^3(\mathbf{x}_I)]\right]^T$, where $\tilde{f}^3(\mathbf{x}_I) = \{0,0,0\}^T$ since $\mathbf{x}_I$ does not lie in the narrow band of crack 3. For a set of n cracks, the structure is given by

$$\tilde{f} = \begin{bmatrix} [\tilde{f}^1] \\ [\tilde{f}^2] \\ \vdots \\ [\tilde{f}^n] \end{bmatrix}_{3n \times N} \tag{7.5}$$

Eq. (7.5) is the extension of Eq.(7.4) for the multiple cracks. This level set structure contains the information about all the cracks in the given geometry through the grid points located in the narrow band region. The narrow band η for a set of n cracks is given by $\eta = \eta_1 \cup \eta_2 \cup ... \cup \eta_n$, where η_i is the narrow band region associated with crack i.

7.3.3 Extrapolating level set function to a generic point

During the evaluation of global stiffness matrix, it is necessary to determine the sign associated with a generic point such as Gauss point corresponding to a particular crack. This information is needed for Heaviside enrichment of the nodes that lie in the narrow band. An existing way is the use of the closest point projection (Ventura et al., 2002) technique for extrapolation. This is done by identifying the grid point $\mathbf{x}_I$ that is closest to the Gauss point $\mathbf{g}$. Then, the vector level-set distance function is extrapolated and the sign at $\mathbf{g}$ can be obtained using

$$\mathbf{v}_I = \mathbf{f}(\mathbf{x}_I) + (\mathbf{x}_I - \mathbf{g})$$
$$H(f(\mathbf{g})) = H(f(\mathbf{x}_I)) \operatorname{sign}\left(\mathbf{f}(\mathbf{x}_I) / \|\mathbf{f}(\mathbf{x}_I)\| . \mathbf{v}_I\right) \tag{7.6}$$

If the level set grid discretization is coarse or slope of the crack increases or the magnitude of the current crack advance vector is small, then the extrapolation according to Eq. (7.6) will be less precise. To increase the accuracy of the extrapolation, a procedure involving triangular coordinates is used as shown in Fig. 7.6. This is done by identifying three closest level-set grid points that form a triangle. The triangular or barycentric coordinates of Gauss point $\mathbf{g}$ is found; this technique is briefed in Appendix D. The signed level-set distance function $f(\mathbf{g})$ can be found using the following relation

$$f(\mathbf{g}) = L_1 f(\mathbf{x}_1) + L_2 f(\mathbf{x}_2) + L_3 f(\mathbf{x}_3) \tag{7.7}$$
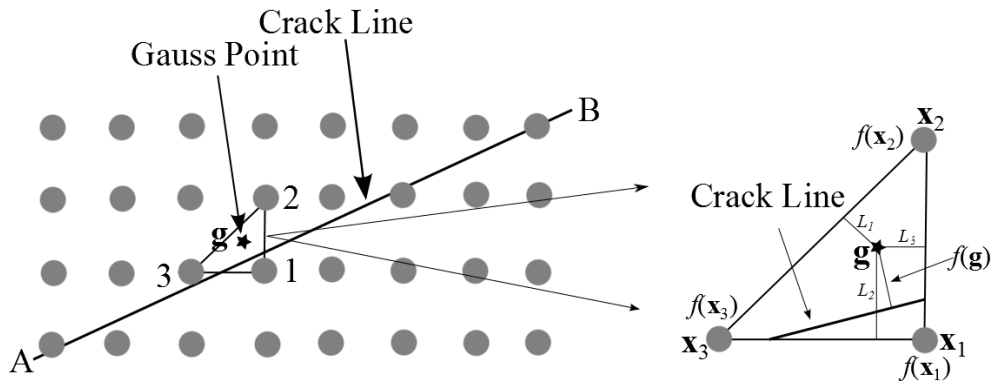
Fig. 7.6 Extrapolation based on triangular coordinates.

The sign at **g** is $H(f(\mathbf{g}))$. In the absence of three grid points that form a triangle, the 1D extrapolation described in Eq. (7.6) is used to determine the sign at **g**. This extrapolation described above can also be used in the case of a curved crack, because the segment of the curved crack lying within the triangle can be approximated to a straight segment.

7.4 Determination of diffracted region

In the diffraction method, a light ray emitted from a source node diffracts around the crack tip and some part of the region behind the crack would form the shadow region. Whether a generic point **g** falls in the shadow region or not depends upon the position of the crack tip, the source node and the location of **g**. Let line-of-sight (LOS) be a straight line drawn from a node I located at $\mathbf{x}_I$ to **g** (Fig. 7.7). Any crack extended infinitely, if it intersects the LOS, it is considered as a potential crack. Let P_c be defined as set of potential cracks labels. Whether a crack labelled n_c is a potential crack or not can be obtained through the following relation based on sign of the level-set distance function $f^{n_c}(\mathbf{x})$ corresponding to crack n_c.

$$H(f^{n_c}(\mathbf{x}_I)) \neq H(f^{n_c}(\mathbf{g})) \tag{7.8}$$

$H(f^{n_c}(\mathbf{s}))$ and $H(f^{n_c}(\mathbf{g}))$ can be obtained from Eq. (7.7). The inequality in Eq. (7.8) holds true only if node I and **g** lies on the opposite sides of a crack labeled n_c.
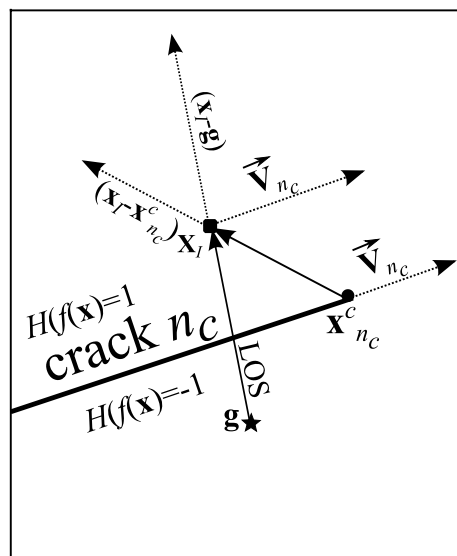
Fig. 7.7 Barrier crack.

Nevertheless, only some cracks in the set P_c truly intercept the LOS and create a shadow in part of the region around the crack tip. Such cracks are termed as barrier cracks in this work. The barrier cracks are always subset of potential cracks.

7.4.1 Single edge crack

Fig. 7.7 shows a single edge potential crack labelled n_c that is also a barrier crack; the LOS vector, $(\mathbf{x}_I - \mathbf{g})$, is intercepted by the crack. A potential crack will become a barrier for a particular $(\mathbf{x}_I, \mathbf{g})$ combination if the LOS vector $(\mathbf{x}_I - \mathbf{g})$ lies between the two vectors, crack front vector $\vec{\mathbf{V}}_{n_c}$ and $(\mathbf{x}_I - \mathbf{x}^c_{n_c})$. This is given by

$$
\begin{aligned}
\left[\vec{\mathbf{V}}_{n_c} \times (\mathbf{x}_I - \mathbf{g})\right] \bullet \left[\vec{\mathbf{V}}_{n_c} \times \left(\mathbf{x}_I - \mathbf{x}^c_{n_c}\right)\right] > 0 \\
\left[\left(\mathbf{x}_I - \mathbf{x}^c_{n_c}\right) \times (\mathbf{x}_I - \mathbf{g})\right] \bullet \left[\left(\mathbf{x}_I - \mathbf{x}^c_{n_c}\right) \times \vec{\mathbf{V}}_{n_c}\right] > 0
\end{aligned}
\tag{7.9}
$$

where $\times$ and $\bullet$ represents cross and dot product respectively. The first expression implies that the rotation direction from $\vec{\mathbf{V}}_{n_c}$ to $(\mathbf{x}_I - \mathbf{g})$ is same as from $\vec{\mathbf{V}}_{n_c}$ to $\left(\mathbf{x}_I - \mathbf{x}^c_{n_c}\right)$. The second expression implies that the rotation direction from $\left(\mathbf{x}_I - \mathbf{x}^c_{n_c}\right)$ to $(\mathbf{x}_I - \mathbf{g})$ is same as from $\left(\mathbf{x}_I - \mathbf{x}^c_{n_c}\right)$ to $\vec{\mathbf{V}}_{n_c}$. Both the expressions of Eq. (7.9) has to be valid for a potential crack to become a barrier crack.

Geomterically, Eq. (7.8) and Eq. (7.9) holds true only if $\mathbf{g}$ lies in the shadow region. Fig. 7.8(a) shows the Boolean of Eq. (7.8) for a source node I at $\mathbf{x}_I$ within its d_I. The ligher area indicates the region where Eq. (7.8) is false. However, the darker region denoted by A does not lie in shadow as any generic point is directly visible to node I. To make the region A lighted, Eq. (7.9) is invoked. The true shadow region is shown in Fig. 7.8(b). Any point in the darker region is not directly visible to the source node I; therefore weight function of node I gets diffracted in this region. In fact, the same conditions can also be used for application of the 'visibility' method of modelling a crack.

If a crack is a barrier, then $s_1 = \left(\mathbf{x}_I - \mathbf{x}^c_{n_c}\right)$ and $s_2(\mathbf{g}) = \left(\mathbf{g} - \mathbf{x}^c_{n_c}\right)$; $s_1 + s_2(\mathbf{g})$ is the shortest route from the node I to $\mathbf{g}$. If it is not a barrier crack, then

$s_1 + s_2(\mathbf{g}) = s_o(\mathbf{g}) = (\mathbf{x}_I - \mathbf{g})$. These values are substituted in Eq. (7.1) and Eq. (7.2) to get the profile of the weight function of the node I.

(a)　　　　　　　　　　　　　　　　　　(b)
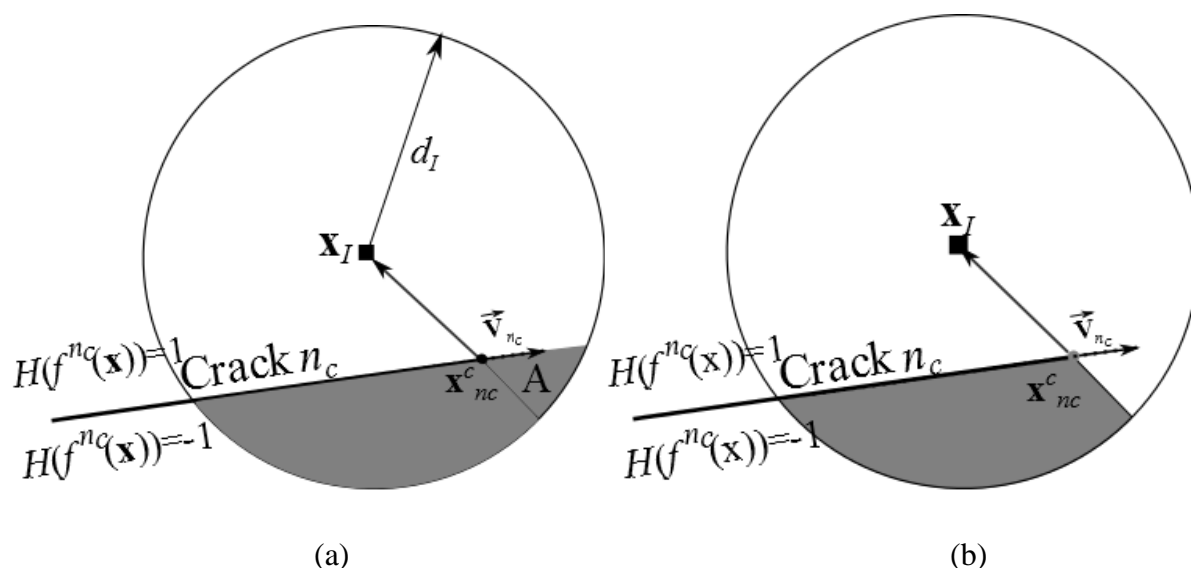
Fig. 7.8 (a) Boolean of Eq. (7.8). **(b)** Boolean of Eq. (7.8) and Eq. (7.9).

7.4.2   Double crack

In a single crack system, when a crack intercepts LOS, the shortest route has to pass through its tip. In the same way, in a multi crack system, when multiple cracks intercept LOS, the shortest route may have to pass through many crack tips of barrier cracks. Such tips are termed as junctions in this work. To determine whether the route passes through a particular tip depends on the location of the source node and/or the previous junctions.

Consider an example of a two-crack system, in which the node I at $\mathbf{x}_I$ has both the crack tips, $\mathbf{x}_1^c$ and $\mathbf{x}_2^c$ within its d_I (Fig. 7.9). In the first step, for $(\mathbf{x}_I, \mathbf{g})$ combination, both the cracks 1 and 2 are potential cracks, but crack 2 is not a barrier crack. The shortest route to the $\mathbf{g}$ has to first pass through the crack tip $\mathbf{x}_1^c$, as it is closer to the $\mathbf{x}_I$. Consequently, the route kinks at $\mathbf{x}_1^c$ and tries to reach to the point $\mathbf{g}$. Now, the crack tip $\mathbf{x}_1^c$ becomes the junction i.e. $\mathbf{x}_1^c$ behaves like a proxy source node.

A tip of a particular crack can behave only once as a junction; the shortest route cannot go through any junction more than once. Let L_c be a set consisting of crack labels whose tips behaved as junctions. Initially L_c will be a null set.
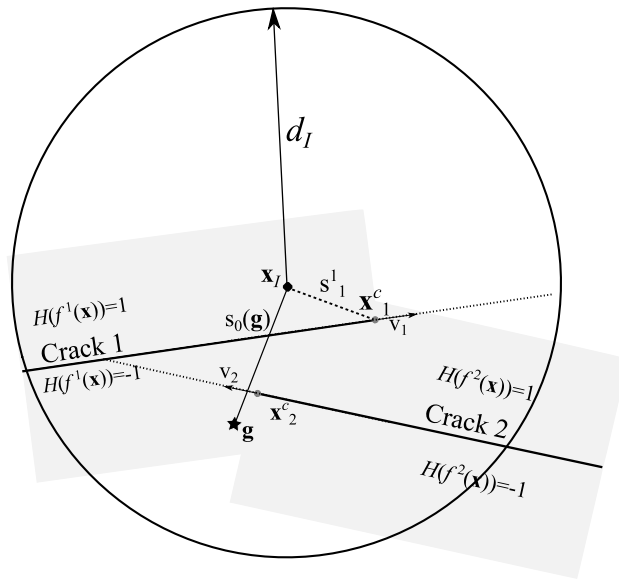
Fig. 7.9 A two-crack system.

Since $\mathbf{x}_1^c$ becomes a junction, the crack 1 is added to the set L_c. At this point, the problem is redefined i.e. to find the shortest distance between the junction $\mathbf{x}_1^c$ and $\mathbf{g}$. If a straight line is drawn from $\mathbf{x}_1^c$ to $\mathbf{g}$, it gets obstructed by the crack 2 and the shortest route to $\mathbf{g}$ will kink at $\mathbf{x}_2^c$ which becomes a junction (Fig. 7.10). As there are no cracks to intercept the LOS i.e. the ray from $\mathbf{x}_2^c$ to $\mathbf{g}$, $s_2(\mathbf{g})$ is computed. Therefore, the shortest route consists of distances s_1^1, s_1^2 and $s_2(\mathbf{g})$. It is to be noted that the crack 2 was not a barrier crack initially, but it becomes a barrier for the redefined problem.
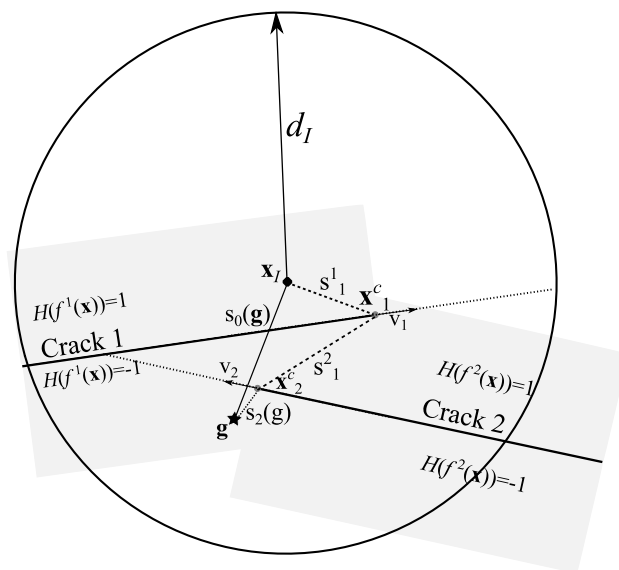
Fig. 7.10 Determination of shortest route from a crack tip junction.

7.4.3 Procedure to find the diffracted region in case of multiple cracks

The problem of determining the parameter $\mathbf{s}_1$ continues until there are no more cracks to obstruct the route. This principle to determine the shortest route from a source node to a generic point, in the case of many cracks, remains same as in the case of double cracks.

General procedure to find the diffracted region

1. Determine the family of potential cracks P_c such that $P_c \cap L_c = \varnothing$.

2. Sort the P_c, in the ascending order, based on the proximity of the node ($\mathbf{x}_I$) to the crack tips.

3. Loop through all the cracks in the sorted P_c.

   a. If a crack labeled n_c is a barrier crack, then obtain the new proxy node $\mathbf{x}_{n_\mathbf{c}}^c$ and compute $\mathbf{s}_1^n$ - (n here being the iteration number).

   b. Exit the loop when P_c is a null set or have run through all the cracks in P_c. Else, go back to step 1.

4. Calculate $\mathbf{s}_2(\mathbf{g})$ in the end.

Example - A five crack system

To illustrate this procedure, a five-crack arrangement with the location of source node $\mathbf{x}_I$ and Gauss point $\mathbf{g}$ is shown in Fig. 7.11. In the first iteration, a LOS is obstructed by crack 1, 4 and 5. Since crack 1 is the closest, the route gets kinked at $\mathbf{x}_1^c$, which becomes the new junction for the next iteration (Fig. 7.11(a)). In the second iteration, the LOS from $\mathbf{x}_1^c$ to $\mathbf{g}$ is gets obstructed first by crack 3; crack 2 does not interrupt LOS. So, the route gets kinked again at the tip $\mathbf{x}_3^c$ (Fig. 7.11(b)). In the third iteration, the LOS from $\mathbf{x}_3^c$ to $\mathbf{g}$ gets obstructed by crack 5. Therefore, the route gets kinked at the tip $\mathbf{x}_5^c$ and finally there is no obstruction for the LOS from $\mathbf{x}_5^c$ to $\mathbf{g}$ (Fig. 7.11(d)).
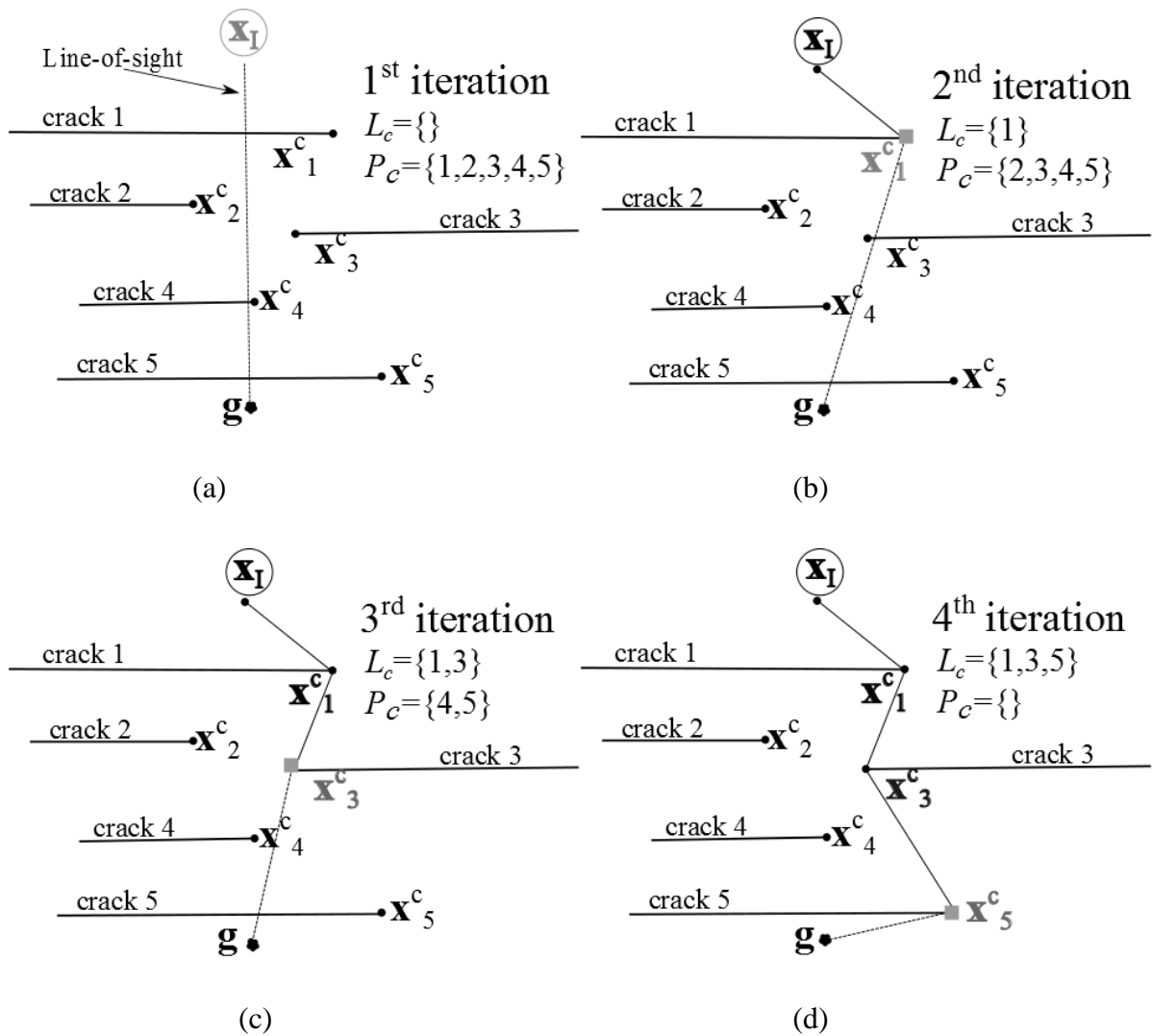
Fig. 7.11 Shortest distance between node and a sampling point **(a)** Iteration 1 **(b)** Iteration 2 **(c)** Iteration 3 **(d)** Iteration 4.

7.4.4 Test cases

Fig. 7.12(a) and Fig. 7.12(b) show the diffracted regions in the case of an arrangement of two parallel cracks and four cracks respectively. The solid black line indicates a crack. The grey and black asterisk markers indicate the region with non-zero and zero weight function associated with source node denoted by **s** respectively. The zero weight-function regions correspond to the shadow region cast by the crack. For effective working of the procedure given in Section 7.4.3, it should be ensured that no source node contains both the crack tips of a single crack in its domain of influence.

In the second case (Fig. 7.12(b)), the source node **s** is located just below the crack 1. Therefore, the region below the crack 1 is lit i.e. it has non-zero value of the weight function.

The region above the crack 1 close to its tip has also non-zero weight function due to diffraction.

(a)   (b)
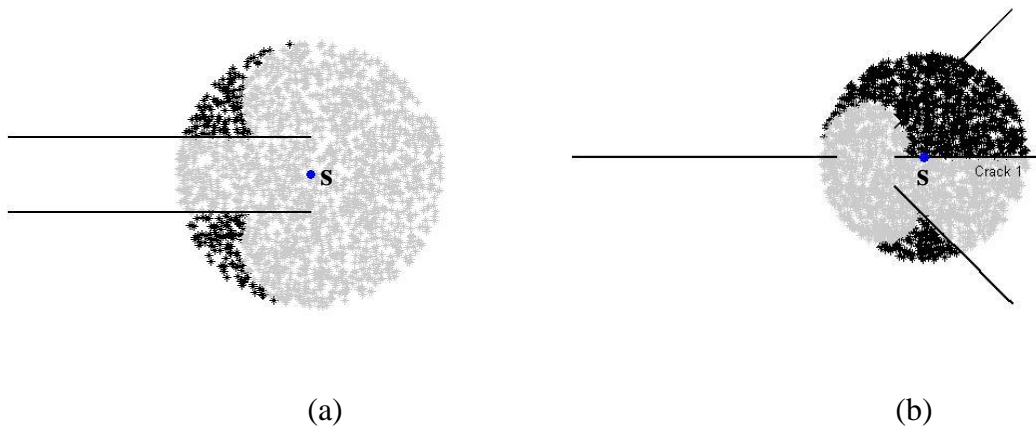
Fig. 7.12 Diffracted region in **(a)** an arrangement of two parallel cracks. **(b)** an arrangement of four cracks.

To illustrate further, a case of multiple cracks, which are close to each other, with the diffracted regions, is shown in Fig. 7.13.
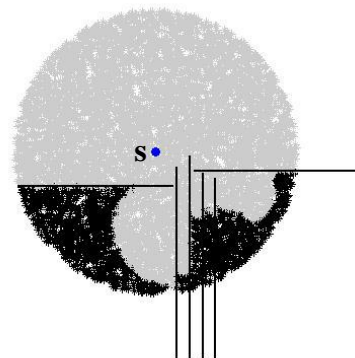
Fig. 7.13 Diffracted region in an arrangement of multiple cracks.

7.4.5 Kinking of a crack

Eq. (7.9) is not applicable for kinked cracks because of the the complexity in determining the diffracted region (Fig. 7.14(a) and (b)). In the case of kinked crack, even the segments between two kink junctions can affect the LOS. . In other words, the kinks of the same crack can act as a barrier for the LOS. In order to determine the shortest route, it becomes necessary to check if the LOS from a source node or a kink point including crack tip

such as $\mathbf{x}^{c,k}$ $\left(k=\{0,1,2,...,n\}\right)$ to a generic point is obstructed by the segments between two kinks.

(a)   (b)
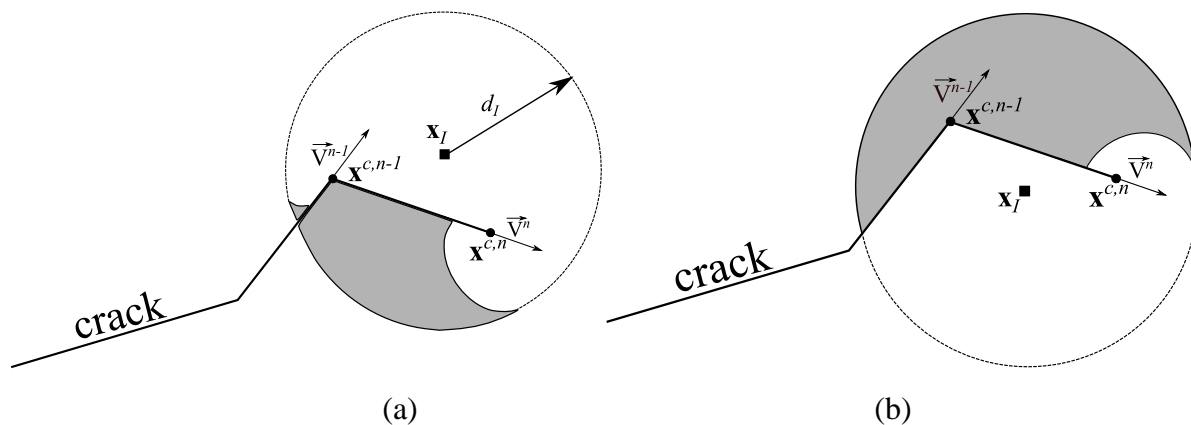
Fig. 7.14 Diffraction in case of kinked crack.

We define the kth kink vector $\vec{\mathrm{V}}_k = \mathbf{x}^{c,k} - \mathbf{x}^{c,k-1}$ and express the kth kink segment in the parametric form as $\mathbf{x}^{c,k-1} + t(\mathbf{x}^{c,k} - \mathbf{x}^{c,k-1})$, where t is a scalar parameter. Similarly, the LOS can also be expressed in the parametric form as $\mathbf{s} + u(\mathbf{g}-\mathbf{s})$, where $\mathbf{s}$ can be a source node or kink points and u is a scalar parameter. If the kth kink segment intersects the LOS, then $\mathbf{x}^{c,k-1} + t(\mathbf{x}^{c,k} - \mathbf{x}^{c,k-1}) = \mathbf{s} + u(\mathbf{g}-\mathbf{s})$ (Fig. 7.15). The parameters t and u can be solved and expressed as

$$t = \left(\mathbf{x}_I - \mathbf{x}^{c,k-1}\right) \times \left(\mathbf{g}-\mathbf{s}\right) \Big/ \left(\left(\mathbf{g}-\mathbf{s}\right) \times \left(\mathbf{x}^{c,k} - \mathbf{x}^{c,k-1}\right)\right)$$
$$u = \left(\mathbf{x}_I - \mathbf{x}^{c,k-1}\right) \times \left(\mathbf{x}^{c,k} - \mathbf{x}^{c,k-1}\right) \Big/ \left(\left(\mathbf{g}-\mathbf{s}\right) \times \left(\mathbf{x}^{c,k} - \mathbf{x}^{c,k-1}\right)\right)$$

(7.10)
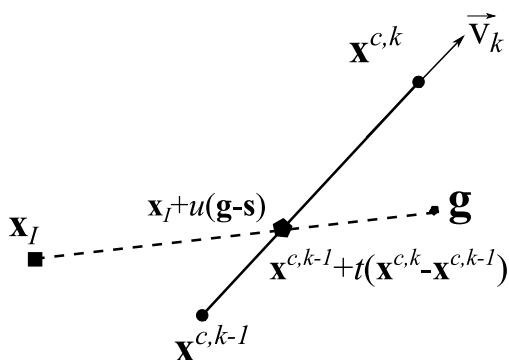
Fig. 7.15 Intersection of two line segments.

Fig. 7.16 shows an example of multiple kinking crack labelled 1. The LOS from $\mathbf{x}_I$ to $\mathbf{g}$ is intercepted by the kink located at $\mathbf{x}^{c,n-2}$. Geometrically, this means that the kink

segments $\vec{V}_{n-1}$ and $\vec{V}_{n-2}$ intersects the LOS, and $\mathbf{x}^{c,n-2}$ is located below the LOS. Whether the LOS is intercepted by a kink vector $\vec{V}_k$ can be found by the condition $0 \le t \le 1$ and $0 \le u \le 1$ of Eq. (7.10). Moreover, the sign of the $\mathbf{g}$ ($H(f^1(\mathbf{g}))$) is required to know if a kink points acts as a junction.
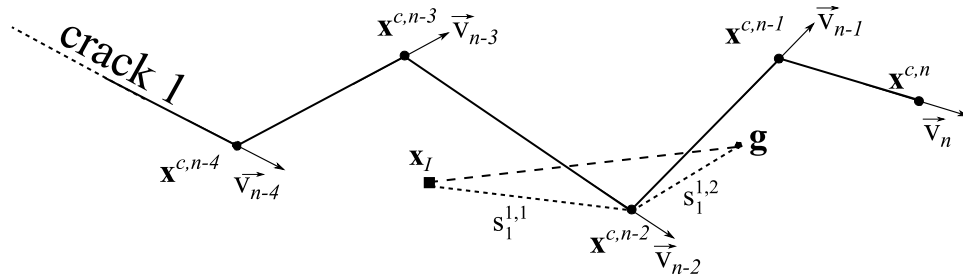
Fig. 7.16 Step-by-step crack propagation; $\mathbf{g}$ is below the crack.

Consider Fig. 7.17, where the sign of the $\mathbf{g}$ is +ve. The kink segments $\vec{V}_{n-2}$ and $\vec{V}_{n-3}$ intersects the LOS. $\mathbf{x}^{c,n-3}$ is located above the LOS, and therefore behaves as a junction. In both the cases, the shortest route becomes $s_1 = s_1^{1,1} + s_1^{1,2}$. The positioning of kink location $\mathbf{x}^{c,k}$ $(k = \{0,1,2,...,n\})$ with respect to the LOS and the sign of $\mathbf{g}$ with respect to the crack, will determine if $\mathbf{x}^{c,k}$ can act as a junction.
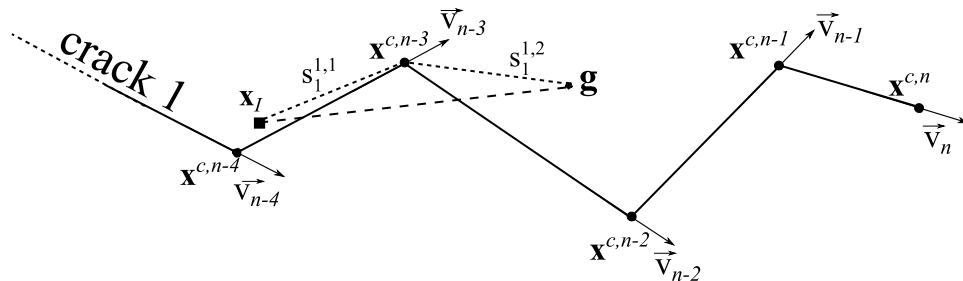
Fig. 7.17 Step-by-step crack propagation; $\mathbf{g}$ is above the crack.

In the case of multiple kinks within a d_I of node at $\mathbf{x}_I$, a particular kink location $\mathbf{x}^{c,k}$ $(k = \{0,1,2,...,n\})$ acts as a junction only if it satisfies $0 \le t \le 1$ and $0 \le u \le 1$ (Eq. (7.10)) and the following condition.

$$H(\ell(\mathbf{x}^{c,k})) = H(f^{n_c}(\mathbf{g})) \tag{7.11}$$

where ℓ is equation of the LOS given by the form $y\text{-}mx\text{-}b = 0$; m is the slope and b is the y-intercept.

For kinked cracks, the general procedure described in Section 7.4.3 is modified by taking into account of the intra-crack barriers due to kinks. Based on this, the diffracted region for a single and double kinked crack is shown in Fig. 7.18(a) and Fig. 7.18 (b) respectively.

<div align="center">(a)   (b)</div>
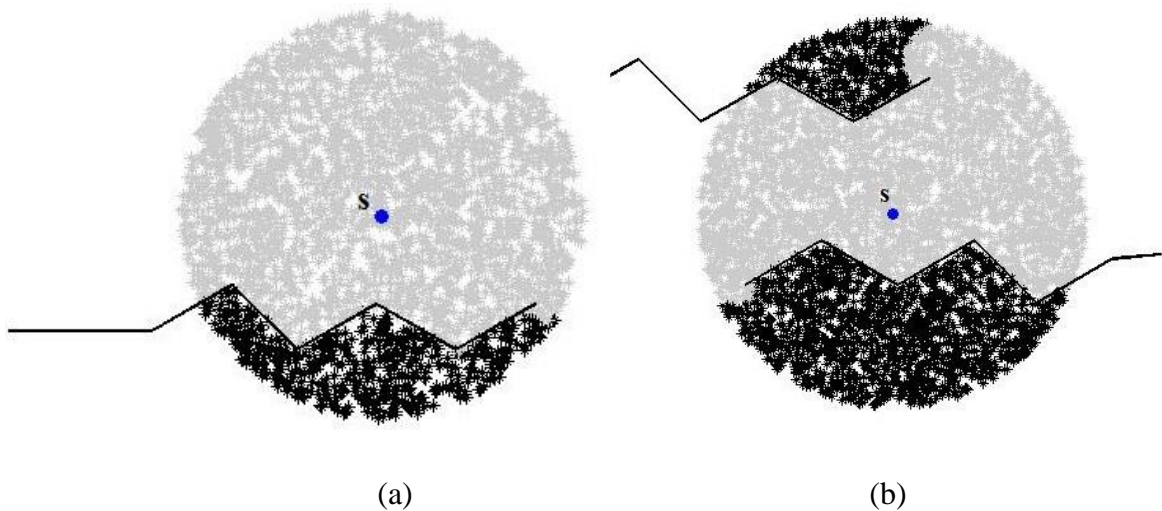
Fig. 7.18 Diffraction region in case of **(a)** single crack. **(b)** double crack.

In case of kinking crack, there is also a knee singularity at the kink in addition to the crack tip singularity. In order to capture this interaction effect, the diffraction node's influence is restricted to two kink locations. The procedure described in this section may also be used for the straight cracks, but is computationally cumbersome to the procedure described in Section 7.4.3

7.5   Results

The modified EFG method presented in Section 6.2 has been applied to a number of problems involving interacting cracks. The nodal domain of influence (d_I) is set to 1.75 times the regular nodal spacing. The SIFs are obtained using the interaction integral technique in all the case studies reported in this section and the results are compared with those in the literature.

7.5.1   Double edge cracks

Fig. 7.19(a) shows a finite plate with double-edge collinear cracks. The plate is subjected to tensile traction of 1MPa. A state of plane strain is assumed. The SIFs are calculated for two plate geometries $L/w = 1$ and $L/w = 3$ with crack length-to-width ratio of $a/w = 0.8$ and $a/w = 0.9$. The computed mode I (K_I) and mode II (K_{II}) SIFs is normalized

by $\sigma\sqrt{\pi a}$: $\hat{K}_I = K_I /(\sigma\sqrt{\pi a}), \hat{K}_{II} = K_{II} /(\sigma\sqrt{\pi a})$. Unless specified, the materials are assumed to be isotropic with Young's modulus $E = 210 GPa$ and Poisson's ratio $v = 0.3$.
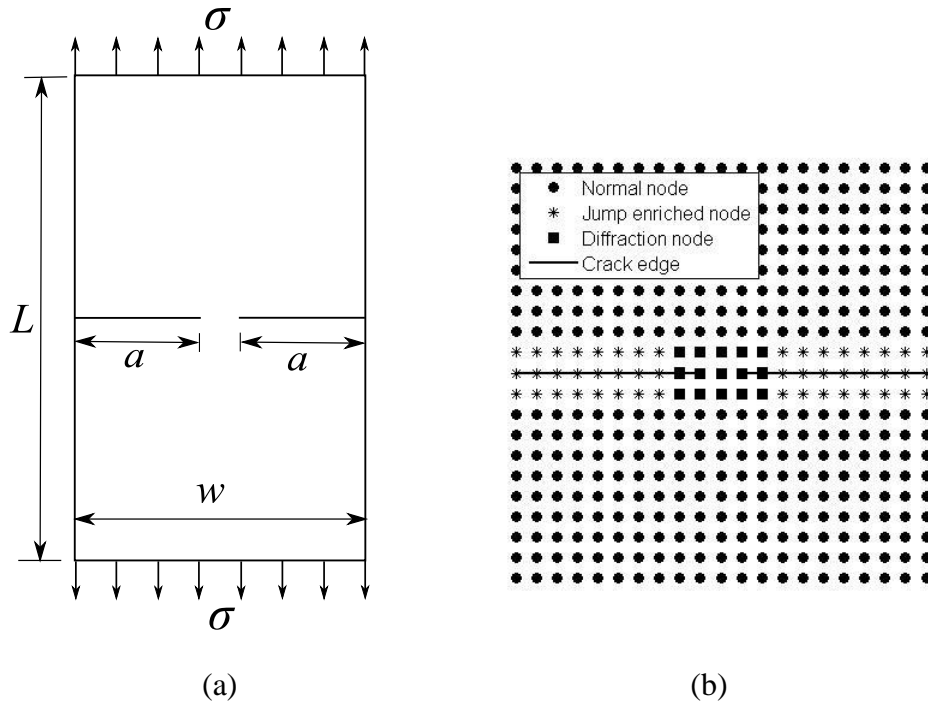
Fig. 7.19 (a) Double-edge collinear cracks. **(b)** Nodal Discretization.

Regular nodal discretizations of 21×21 (Fig. 7.19 (b)) nodes for $L/w = 1$ and 21×61 nodes for $L/w = 3$ are used. This is similar to the nodal discretization used by Muravin *et al.* (2006). However, the bandwidth of the resulting stiffness matrix in the present case is lower than the latter due to lower value of d_I. The present proposed method does not require higher value of d_I due to the utilization of Heaviside enrichment function to model discontinuity of the displacement across the crack edges. However, the classical EFG method, where only visibility or diffraction method is used, needs extra nodes along the crack edges or higher value of d_I to avoid ill conditioned stiffness matrix.

The normalized mode I SIF ($\hat{K}_I$) is compared with the results obtained by the EFG method and the analytical solutions of Bowie (1964). The error is computed based on the results of Muravin & Turkel (2006). The comparison in Table 7.1 shows that there is an excellent agreement though coarser nodal discretization and low d_I is employed in the present study.

Table 7.1 Comparsion of normalized SIF for double-edge cracks.

a/w	L/w	$\hat{K}_I$ (Muravin & Turkel, 2006)	$\hat{K}_I$ (Bowie, 1964)	$\hat{K}_I$ Present Method	% Error*
0.8	1	1.6111	1.5806	1.6085	-0.161 %
0.8	3	1.5497	1.5649	1.5454	-0.278 %
0.9	1	2.1326	2.1133	2.1231	-0.446 %
0.9	3	2.1016	2.1133	2.0993	-0.109 %

* % error is with respect to results based on Muravin and Turkel (2006) results.

7.5.2 Four neighbouring cracks

In this example (Fig. 7.20(a)), a finite plate has four cracks whose crack tips lie in close proximity. The plate is subjected to a tensile load of 1MPa. A state of plane strain is assumed. The SIFs are calculated for $L = 4$ and crack length-to-width ratio $a/w = 0.45$. There is a strong interaction amongst the four crack-tip singular stress fields. In order to capture such a complex field accurately, the classical EFG needs a fine nodal discretization in the region encompassing the crack tips. However, the MCW function reduces the complexities involved.

(a)   (b)
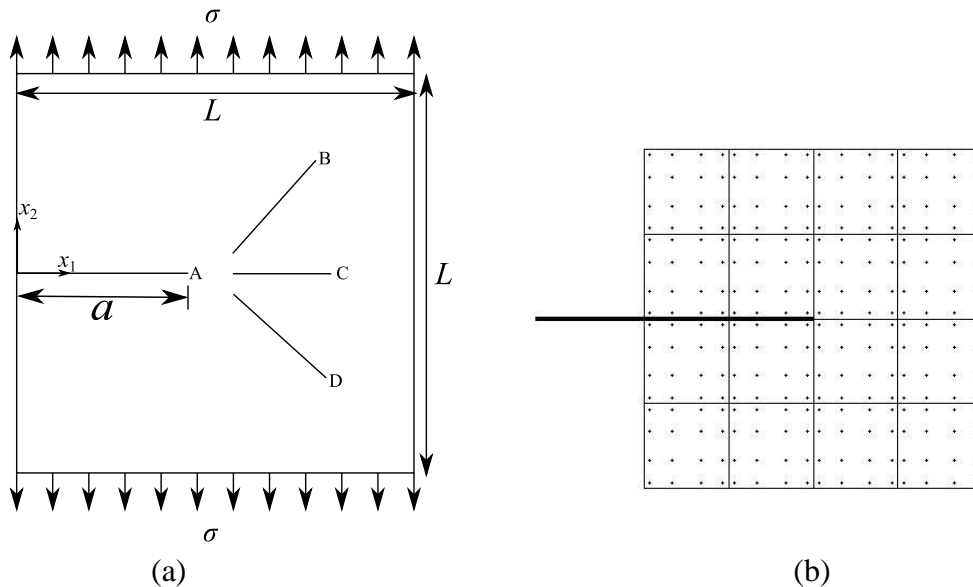
Fig. 7.20 (a) Finite plate with four cracks under uniform tensile loading. (b) Interaction integral domain with Gauss points.

The end coordinates of cracks B, C and D are (2.2,0.2),(3,1); (2.2,0),(3.2,0); and (2.2,-0.2),(3,-1) respectively. The singular stress field at the tip of edge crack A interacts strongly with the neighbouring crack-tip stress fields of crack B, C and D. The SIFs are obtained using interaction integral whose integral domain is a square of edge length $0.2a$. The distribution of Gauss points for numerical integration is indicated by dots (Fig. 7.20(b)).

Table 7.2 shows comparison of the computed normalized mode I SIFs at the tip of crack A with the published data by Muravin & Turkel (2006) for three nodal discretizations. It is to be noted that satisfactory results are obtained even with a very coarse nodal density and low d_I.

Table 7.2 Comparison of normalized SIFs for edge crack interacting with three neighbouring cracks.

Nodal Discretization	$\hat{K}_I$ (Muravin & Turkel, 2006)	$\hat{K}_I$ Present Method	% Error
21×21		2.7789	-0.793 %
41×41	2.80114	2.7963	-0.171 %
81×81		2.802	0.032 %

7.5.3 Cross cracks and star cracks

Fig. 7.21(a) and Fig. 7.21(b) show cross cracks and star cracks in a square plate of size $w = 4$ subjected to bi-axial loads. The normalized mode I SIFs are obtained for various a/w ratios. In order to increase the accuracy and capture the singular field accurately in this case, the region around the crack tip is slightly refined. This process is not cumbersome as in the case of mesh-based methods.
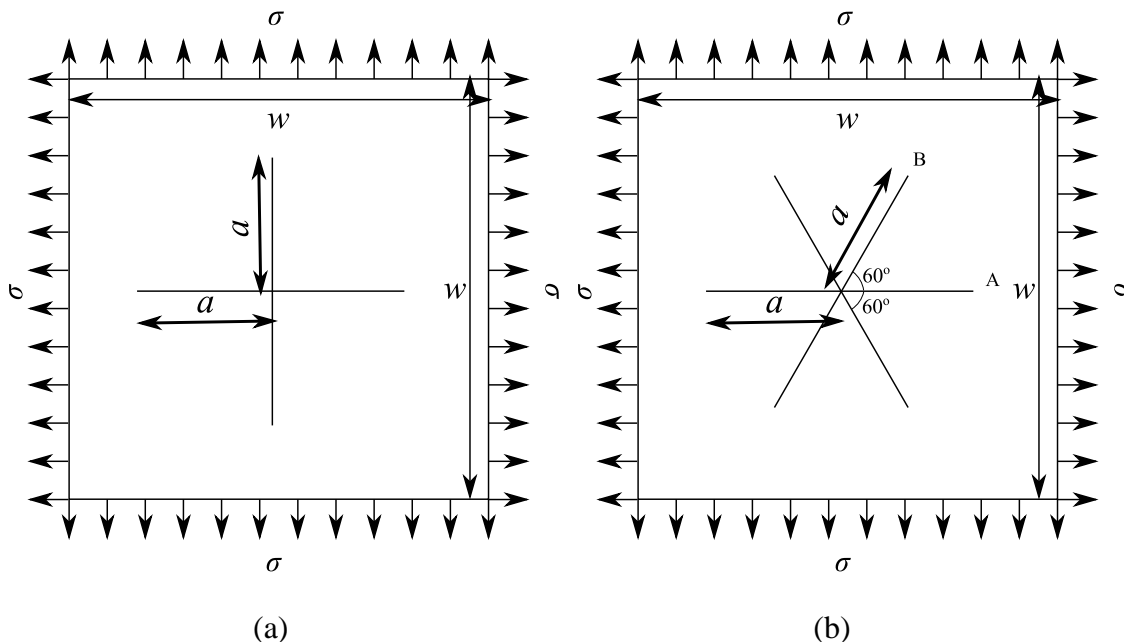
Fig. 7.21 (a) Cross cracks. **(b)** Star cracks.

Table 7.3 shows a comparison of the computed normalized mode I SIF ($\hat{K}_I$) for the case of cross cracks. The present results are in good agreement with the results obtained by

an enriched meshfree method based on the reproducing kernel particle method (RKPM) (Barbieri et al., 2012).

Table 7.3 Comparison of normalized SIFs for cross cracks in square plate.

a/w	$\hat{K}_I$ (Cheung et al., 1992)	$\hat{K}_I$ (Barbieri et al., 2012)	$\hat{K}_I$ Present Method	% error*
0.1	0.8641	0.8655	0.8563	-1.059 %
0.2	0.88	0.8837	0.8837	-0.002 %
0.3	0.9092	0.9126	0.9132	0.060 %
0.4	0.9537	0.967	0.9583	-0.901 %
0.5	1.0223	1.037	1.0273	-0.938 %
0.6	1.13	1.145	1.1361	-0.781 %
0.7	1.2866	1.33	1.3182	-0.884 %
0.8	1.4857	1.65	1.6550	0.300 %
0.9	-	2.44	2.4650	1.025 %

* % error is with respect to the results of Barbieri et al. (2012)

Fig. 7.22 shows the comparison of the normalized SIFs for a star crack with the results obtained using the EFG method (Muravin & Turkel, 2006) and XFEM (Daux et al., 2000). $\hat{K}_I^A$ $\left(K_I^A / \sigma\sqrt{\pi a} \right)$ denotes the normalized mode I SIF for crack tip A. $\hat{K}_I^B$ $\left(K_I^B / \sigma\sqrt{\pi a} \right)$ and $\hat{K}_{II}^B$ $\left(K_{II}^B / \sigma\sqrt{\pi a} \right)$ denotes the normalized mode I and mode II SIFs for crack tip B. The comparison shows that the obtained SIFs are in good agreement with the published numerical results.
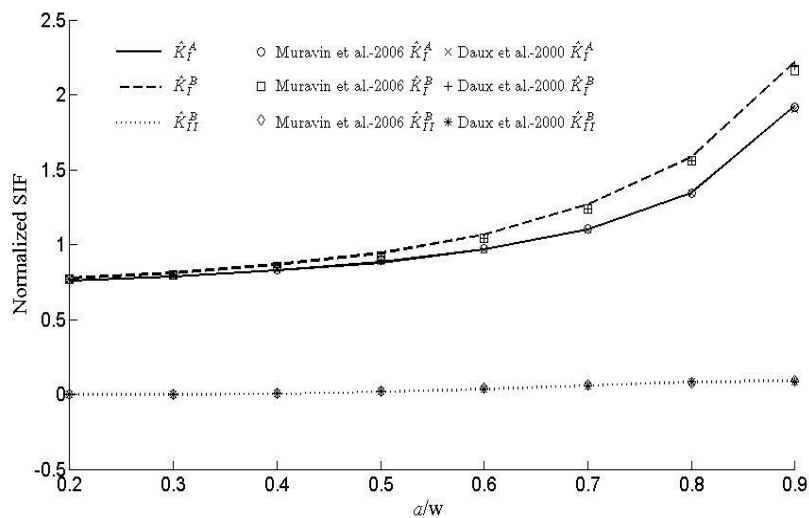
Fig. 7.22 Variation of normalized SIFs for star crack with a/w .

It is observed that the accuracy of the SIFs increase and converge as we increase the density of the nodes in the region around the crack tip.

7.5.4 Crack-microcrack interaction

Fig. 7.23(a) shows two stacked microcracks interacting with a macro edge crack in a plate under uniform tensile load. The results are obtained for various h/l ratios. Only the semi-stack height (h) is varied. The geometric specifications are: $w = 20\,\text{mm}$, $L/w = 5$, $a/w = 0.5$ and $2l/a = 0.05$.

(a)   (b)
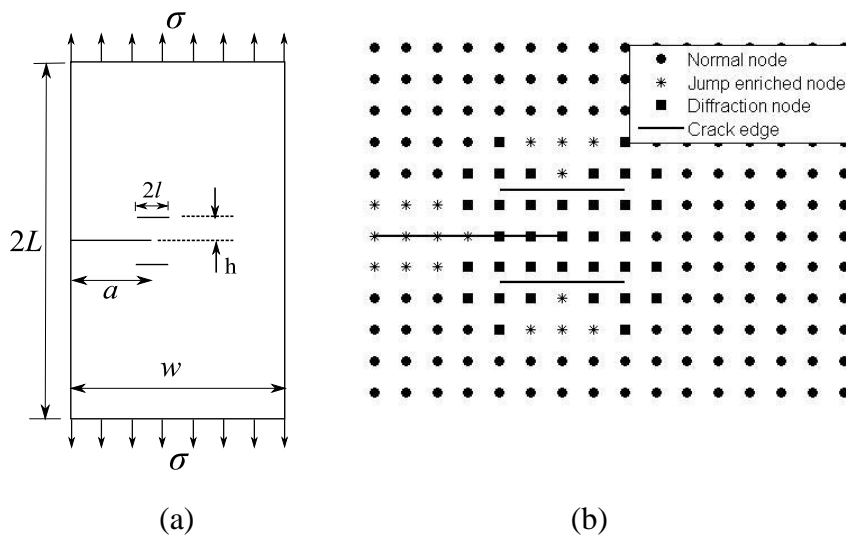
Fig. 7.23 (a) Single edge crack with two stacked micro cracks.**(b)** Nodal discretization.

The region encompassing the microcracks is refined (Fig. 7.23(b)) to increase the accuracy of the normalized SIF (K_I/K_{I0}), where K_{I0} is the mode I SIF of the macro crack without the microcracks.
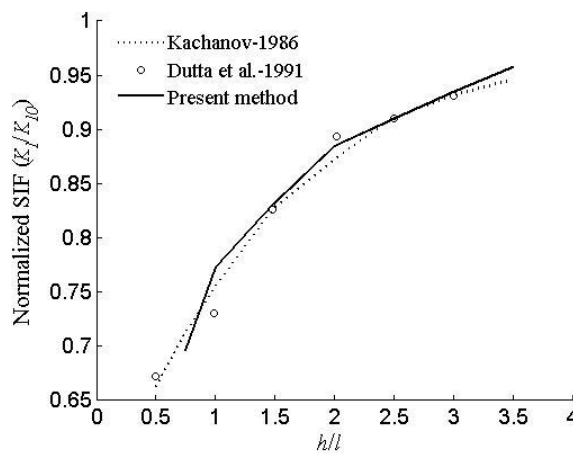
Fig. 7.24 Comparison of variation of normalized mode I SIF with h/l ratio.

Fig. 7.24 shows that the obtained SIF agrees satisfactorily with the exiting results in the literature (Kachanov, 1986; Dutta et al., 1991). There is a shielding effect at the macrocrack tip when the distance between the macrocrack and the microcracks are small. The shielding effect decreases with the increase in h/l ratio and vanishes beyond the distance of $3.5 h/l$.

7.5.5 Interface crack-microcrack interaction

Fig. 7.25(a) shows an interface crack interacting with a microcrack in a bi-material plate subjected to uniform tensile load. The geometric specifications of the plate are: $w = 150 \, \text{mm}$, $L/w = 4/3$, $a/w = 2/15$, $c/a = 0.2$ and $h = 1.27 \, \text{mm}$. The material properties of the ceramic-metal bi-material plate correspond to S45C steel ($E_1 = 206 \, \text{GPa}$, $v_1 = 0.3$) and Si$_3$N$_4$ ($E_2 = 304 \, \text{GPa}$, $v_2 = 0.27$). For analysis, plane stress conditions are assumed in this case.
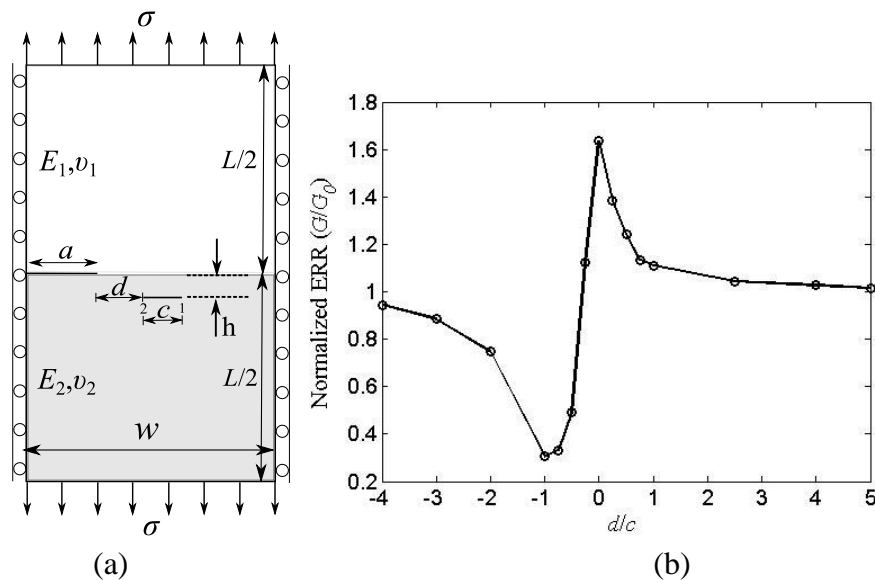
Fig. 7.25 (a) Bimaterial plate with interface crack and micro cracks under tensile loading. **(b)** Normalized ERR variation with d/c ratio.

The complex SIF ($K_1 + iK_2$) associated with the interface crack is obtained using the interaction integral (Sukumar et al., 2004). The energy release rate for the interface crack is related to complex SIF by

$$G = \frac{1}{E^*} \frac{K_1^2 + K_2^2}{\cosh^2(\pi\varepsilon)}$$

$$1/E^* = 1/E_1^* + 1/E_2^*$$

(7.12)

where E^* is E for plane stress and $E/(1-v^2)$ for plane strain and β is one of the Dundurs' parameters.

Fig. 7.25(b) shows the variation of the normalized energy release rate (ERR) G/G_0 with d/c ratio. G_0 is the ERR of the interface crack in the absence of a microcrack. As the microcrack approaches the interface crack tip from the left, the shielding effect is observed. G/G_0 reaches a minimum when the crack tip 1 is close to the interface crack tip. The ratio G/G_0 amplifies rapidly as d/c increases and reaches a maximum when the crack tip 2 coincides with the interface crack tip. Then, it decreases and reaches close to unity after $d/c > 4$.

The effect of shielding or amplification is experienced by the interface crack even when the micro crack is at distances h, which is several times its length l. Similar trends were also observed by Ouinas et al. (2010).

7.5.6 Double and triple kinked cracks
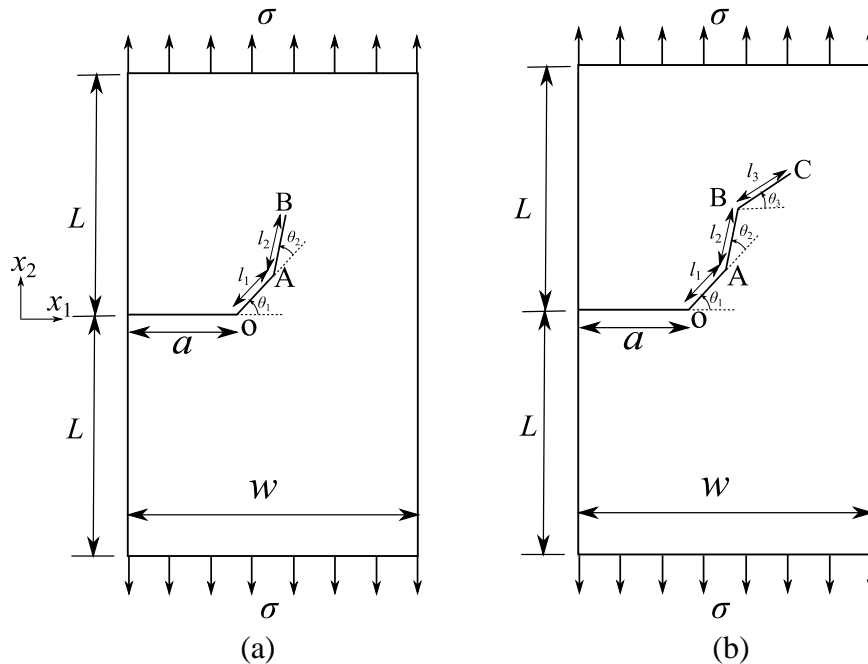
Fig. 7.26 (a) Double kinked cracks. **(b)** Triple kinked cracks.

$$a = 1\,\text{mm}, \ a/w = 0.5, \ L/w = 2 \text{ and } l_1 = l_2 = l_3 = 0.04a.$$

Fig. 7.26(a) and Fig. 7.26(b) show double and triple kinked cracks in rectangular plates under tension. These kinds of zigzag cracks may develop due to stress corrosion cracking. They can also come due to extension of a mixed mode crack. It involves the interaction of knee point singular fields with the crack tip singular field. In the first case (Fig. 7.26 (a)), the first kink OA makes an angle $\theta_1 = 45^o$ with x_1-axis. The second kink AB makes an angle θ_2 with OA. Fig. 7.27 shows the variation of normalized mode I

$\left(K_I / \sigma\sqrt{\pi a} \right)$ and mode II SIFs $\left(K_{II} / \sigma\sqrt{\pi a} \right)$ with θ_2 obtained using nodal discretization strategies such that the diffraction nodes affect one kink and two kinks locations. The results obtained by both the strategies are in agreement with each other except at the extremities of the plot. Perhaps, this may be due to the interaction of kink singularity field with the crack tip singularity field.
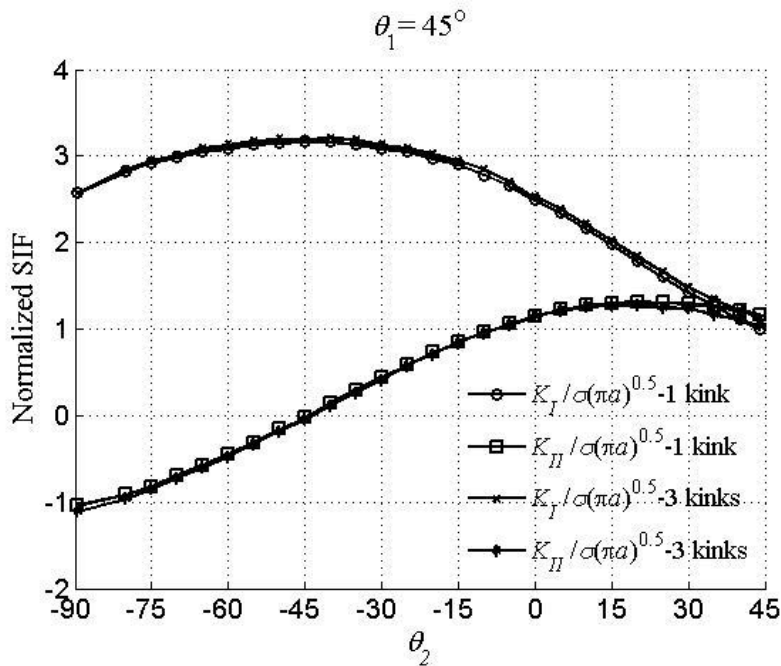
Fig. 7.27 Normalized mode I and mode II SIF of double kinked crack with θ_2.

The normalized mode I SIF reaches its maximum at $\theta_2 = -45^o$ where the mode II SIF is zero. This agrees with the maximum tangential stress (MTPS) criterion which dictates that crack will propagate in the direction of zero shear stress or $K_{II} = 0$. As the kink AB propagates at an angle -45° and the whole crack becomes pure mode I crack.

Fig. 7.28 shows the variation of normalized mode I and mode II SIFs at the tip C with θ_3 for three values of θ_2. It is observed from each subplot that the maximum value of mode I occurs when $K_{II} = 0$ at the tip C. This is the angle in which the crack is likely to propagate further.
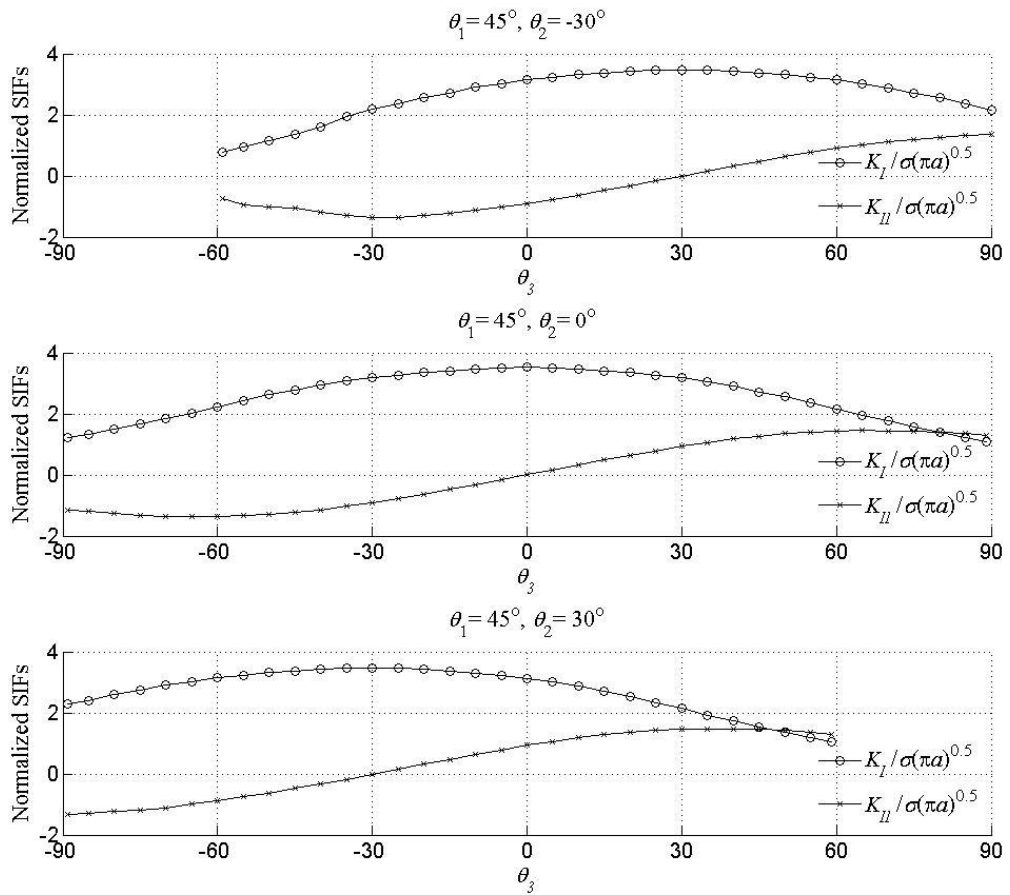
Fig. 7.28 Variation of normalized mode I and mode II SIFs for triple kinked crack problem with θ_3.

7.5.7 Multiple crack propagation
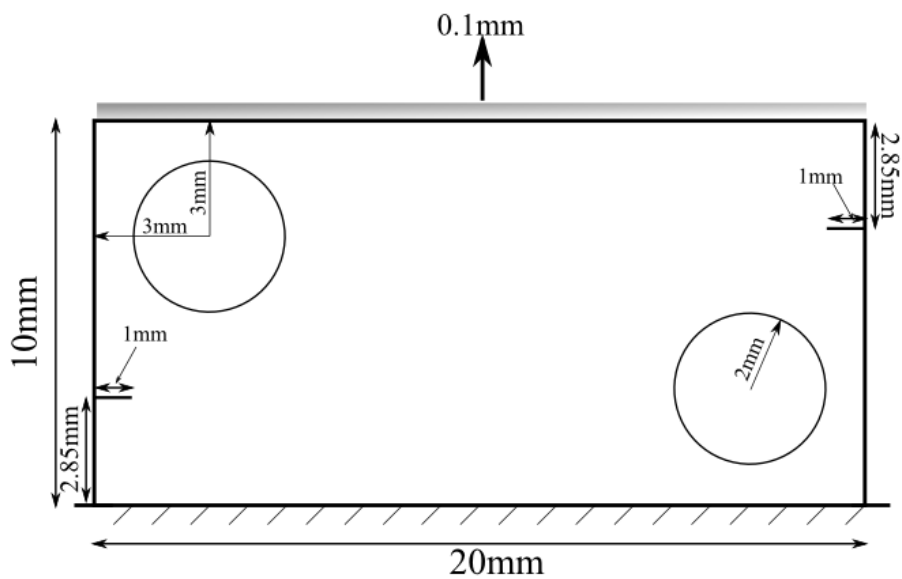
Fig. 7.29 Plate with two holes and two cracks subjected to tensile displacement.

Fig. 7.29 shows a plate subjected to displacement at the top edge. The plate has two holes and two symmetrical cracks. The material properties are $E=2\times10^5$ N/mm^2 and $v = 0.3$. This problem has been previously studied using FEM (Bouchard et al., 2003; Khoei et al., 2008) and XFEM (Geniaut & Galenne, 2012). The holes are modelled using level set enrichment. MTPS criterion is used to determine the angle of crack propagation. The crack extension length or kink length is set to 0.5mm. Two sets of nodal configuration are used: 40×20 and 32×16 with refinement at the crack tip using 9×9 nodes such that diffraction node influences atleast one kink point.
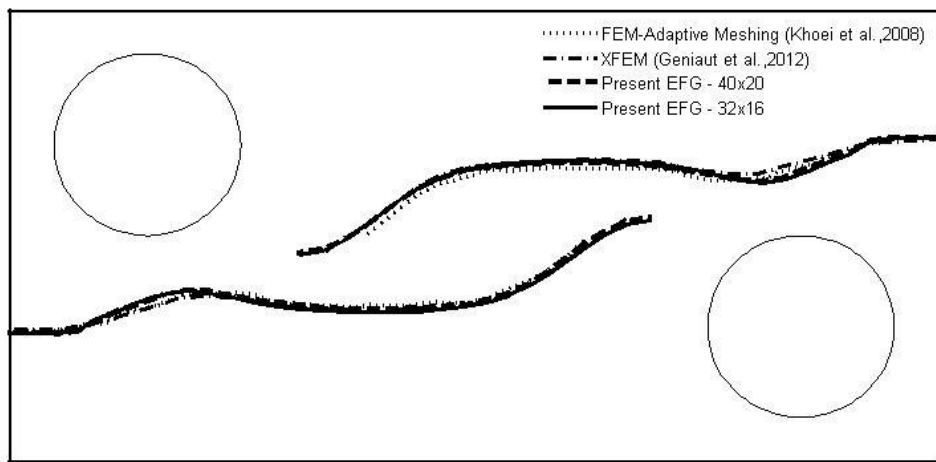
Fig. 7.30 Crack propagation in a plate with two holes.

Fig. 7.30 shows the crack paths, predicted by the present EFG method, are in good agreement with those obtained using FEM and XFEM. Initially, the crack is attracted by the nearest hole and then at certain point, the two cracks are close enough to interact. This interaction effect leads to repulsion of the crack, which is well captured by the present method. Although the nodal degrees of freedom of the EFG method is significantly lower than that of the mesh-based methods, the results are accurate to higher order continuous nature of the EFG shape functions. Further, the nodal degrees of freedom are reduced by the usage of the diffraction methodology for kinked cracks.

7.6 Closure

In this chapter, the proposed variant of the EFG method is combined with the level set method to model problems of interaction of multiple cracks. A general procedure is given to determine the parameters of the diffraction method, which plays significant role in modelling

these problems, and help to reduce the need for high refinement in the region containing the crack tips. A number of case studies have been presented involving crack-crack, crack-microcrack and interface crack-microcrack interactions. The computed SIFs based on the proposed EFG method are in good agreement with the published results. The proposed method has been applied to study cases involving double and triple kinked cracks. It can be employed along similar lines to examine problems of crack propagation through any medium.

Chapter 8 Conclusion

8.1 Introduction

In this chapter, a general discussion on the results and suggestion for the future work is presented. This is followed by major conclusion of the study. Finally, the contributions of the present work are given.

8.2 Observations and Discussions

The main thrust of the work is accurate modelling of crack in isotropic, orthotropic, functionally graded materials and bi-materials using the element-free Galerkin (EFG) method. One of the objectives was to compute the SIFs accurately using the simplest methodology possible within the EFG method. The popular interaction integral is routinely used within the framework of the meshfree methods (MMs) and guarantees stress intensity factors (SIFs) of satisfactory accuracy. However, it involves auxiliary functions that are obtained through analytical solutions. Implementing this integral when crack faces are subjected to mechanical or thermal loading requires special attention. On the other hand, the crack closure integral augmented by the local smoothing technique (CCI-LS) gives SIFs of accuracy on par with interaction integral, that too with minimal computational efforts.

It is observed that the crack-tip stress field obtained through the EFG method does not vary smoothly ahead of the crack tip despite using enrichment functions. The local smoothing function in the CCI-LS technique helps to smooth the stress field solution by eliminating the numerical error and gives the SIFs of good accuracy. Unlike FEM, the stresses and displacements can be extracted at any point in the domain due to higher order continuous shape functions of the EFG method. This gives a wide possibility of integral spans (Δa) for computing the SIFs through CCI-LS. It is recommended that a span of $0.01a \leq \Delta a \leq 0.05a$ be used to restrict the error within 3%. Further, the mode separation is easy using the CCI-LS technique. Problems including crack face loading, thermal loading and curved crack are solved easily. It also gives satisfactory results for a crack in functionally graded materials (FGMs).

Classical SIF extraction methods like displacement and stress methods have been also investigated to compute the SIFs using the EFG method. The computational efforts involved

in these methods are minimal and are even less than the CCI-LS technique. However, the accuracy of the SIFs obtained depends on parameters such as the nodal density and enrichment functions.

In order to reduce the error associated with numerical integration, higher order Gauss integration was employed in the background triangular cells surrounding the crack tip. Secondly, a regular nodal discretization was used to minimize the non-polynomial behaviour of the EFG method shape functions. Error control during numerical integration is a challenging issue in the MMs. Suitable procedures that generate a higher order polynomial-like shape functions would be beneficial.

The modified crack closure integral (MCCI) or virtual crack closure technique (VCCT), which finds frequent application in FEM has also been developed for the EFG method. Since this technique necessitates computation of the crack closure forces lying ahead of the crack tip along the crack plane, a novel way has been proposed to extract the nodal forces using regular nodal discretization. This involves computing the local stiffness matrix at the nodes, corresponding to its semi domain of influence and its multiplication with the nodal displacement vector. This method guarantees the SIFs of very good accuracy despite low nodal density in the region around the crack tip. This is because the MCCI is based on an energy approach. Similar to the CCI, this method also enables easier mode separation, but differs in the way it is done. This method gives total energy release rate (ERR) associated with the singularity term plus other higher order terms of the Williams' eigenfunction expansion, while the interaction integral or CCI-LS technique gives the ERR only due to the singularity term alone.

The MCCI can also be easily extended to extract SIFs for a crack in orthotropic media and bimaterial interfaces. Computing the nodal forces is currently not possible for an irregular nodal discretization in the EFG method. This needs further investigation. Further study is also needed to compute the SIFs using MCCI when the crack is close to a material interface.

The present work also focused on modelling crack propagation in non-homogenous materials. The usage of partition-of-unity based approaches like extended element-free Galerkin (XEFG) method poses difficulties when it comes to modelling crack propagation through the non-homogenous materials. This is because the enrichment functions have to be modified depending on the location of the crack tip, type of material and loading. In addition,

it becomes difficult to use the XEFG method for a new problem that has no analytical solution. To overcome these difficulties, a variant of the EFG method, that combines Heaviside function and diffraction method, was proposed to handle the problem of varying order of singularity. In general, the case studies using coarser nodal discretization show good agreement with the other reported results based on the analytical solutions and the FEM. This is attributed to the shape functions of the EFG method that are capable of reproducing a higher order variation of the field variables.

Currently, there are no established techniques to determine the order of singularity for a variable order singular stress field; thus extracting the 'stress intensity factors' for such cases are difficult. This needs further examination.

When a crack propagates through composites, it often encounters the material interfaces and sometimes grows as an interface crack. The T-stress is found to influence the instantaneous angle of further crack propagation. In order to include the effect of T-stress, the maximum tangential principal stress (MTPS) criterion has been used. It is shown to be different from the popular MTS criterion. A criterion based on both the stress and the ERR is proposed to predict the crack propagation direction and onset of extension of an interface crack. This combination greatly reduces the computational effort. The case study that shows crack meandering around the particle in particle-reinforced composites demonstrates the scope and effectiveness of the method.

To model multiple interacting cracks, a procedure based on level sets within the EFG method, using diffraction method, has been suggested. To store the level set data, a background grid comprising of closely spaced nodes is constructed. In the case of continuously kinking crack, the singularity points like the adjacent knee and the crack tip, the interaction is accommodated implicitly. This method reduces the need for high nodal density at the crack tips.

8.3   Conclusions

The main conclusions of this thesis are as follows:

1.   The % error in the SIFs obtained using the crack closure integral (CCI) technique in conjunction with local smoothing technique (CCI-LS) is less than 3%, when compared to the theoretical results, if a span of Δa for integration, $0.01a \le \Delta a \le 0.05a$, where a is the crack

length, is chosen. The local smoothing, on average, reduces the error in the SIF obtained through the original CCI method by 2.5% in the case of isotropic materials. In the case of functionally graded materials, the reduction is up to 6.5%.

2.   The CCI-LS technique allows an easy way of mode separation, with less computational effort.

3.   In both the isotropic and functionally graded materials, the displacement method gives results of an average error less than 4% using XEFG method. This is attributed to the presence of enrichment functions that ensure higher order displacement variation in the region around the crack tip.

4.   The performance of the stress method is poor, among all the SIF extraction techniques, even in the presence of enrichment functions. The maximum error in the SIF increased up to 9.58% in few cases when compared to the published results.

5.   The modified crack closure integral (MCCI) guarantees SIFs of very good accuracy even with low nodal density for both the enriched and non-enriched EFG methods. Similar to the CCI-LS technique, the MCCI technique also enables easier mode separation.

6.   In general, the accuracy of the SIFs increases with increase in the number of nodes at which the closure forces are extracted. For practice, it is sufficient to compute the closure forces at two nodes ahead of the crack tip to restrict the error within 2%.

7.   The SIFs obtained by the classical displacement method is poor when a crack is modelled by the visibility or diffraction methods. The error sometimes is more than 50%. This decrease in the accuracy is due to the absence of enrichment functions. The stress method always gives inferior accuracy; error in the SIFs crossed 60% especially for short edge cracks.

8.   In spite of the poor displacement solution, the MCCI gives good results. This is because it is based on an energy approach. The same holds true for the interaction integral which gives good results in spite of poor stress distribution ahead of the crack tip.

9.   An efficient variant of the EFG method was developed to model crack propagation in non-homogenous materials. This method gives results of satisfactory accuracy without the enrichment functions. This is due to the higher order continuous nature of the EFG method shape functions.

10.   The MTPS criterion combined with the maximum energy release rate criterion reduces the computational effort to handle any crack propagation study.

11.   The factors that affect the kinking angle of an interface crack are the T-stress, radius of the contour and the oscillation index. The negative T-stress is found to decrease the magnitude of the kinking angle.

12.   A wide spectrum of crack propagation possibilities in a single particle reinforced composite has been shown. The crack path is dependent on distance of the crack tip from the particle, and the interface and the adjoining material toughness.

13.   A procedure to model multiple interacting cracks was developed. It yielded accurate results despite lower nodal density.

14.   The procedure developed to handle multiple cracks has been extended to model repeated kinking connected with a propagating crack. The accuracy obtained with reduced number of degrees of freedom is satisfactory.

15.   The variation of shielding and amplification of the energy release rate for a macro-crack with its position of a particle inclusion or a micro-crack is in line with the published results.

8.4   Thesis Contributions

This thesis has contributed to the field of fracture mechanics by:

1. demonstrating the usefulness of the displacement and stress methods for the extraction of the SIF through the EFG method,

2. developing expressions based on the CCI in conjunction with local smoothing technique to compute the SIFs for cracks with edge, or thermal, loading in isotropic and functionally graded materials,

3. developing a MCCI technique to extract the SIFs with good accuracy within the framework of the EFG method,

4. developing a form of the EFG method combining the diffraction method and the Heaviside function to analyze problems of variable order singularity,

5. showing the computational advantage of the combined MTPS and energy release rate criterion to determine the kinking of an interface crack,

6. showing the influence of the T-stress on the kinking angle of an interface crack,

7. developing a scheme using the level sets to model multiple interacting cracks, and, above all,

8. extending the scope of the EFG method.

Appendix A

For an isotropic and homogenous material, the auxiliary stress solution is given by

$$\sigma_{11}^{aux} = \frac{1}{\sqrt{2\pi r}}\left\{ K_I^{aux}\operatorname{Cos}\frac{\theta}{2}(1-\operatorname{Sin}\frac{\theta}{2}\operatorname{Sin}\frac{3\theta}{2}) - K_{II}^{aux}\operatorname{Sin}\frac{\theta}{2}(2+\operatorname{Cos}\frac{\theta}{2}\operatorname{Cos}\frac{3\theta}{2}) \right\}$$

$$\sigma_{22}^{aux} = \frac{1}{\sqrt{2\pi r}}\left\{ K_I^{aux}\operatorname{Cos}\frac{\theta}{2}(1+\operatorname{Sin}\frac{\theta}{2}\operatorname{Sin}\frac{3\theta}{2}) + K_{II}^{aux}\operatorname{Sin}\frac{\theta}{2}\operatorname{Cos}\frac{\theta}{2}\operatorname{Cos}\frac{3\theta}{2} \right\} \quad \text{(A.1)}$$

$$\sigma_{12}^{aux} = \frac{1}{\sqrt{2\pi r}}\left\{ K_I^{aux}\operatorname{Cos}\frac{\theta}{2}\operatorname{Sin}\frac{\theta}{2}\operatorname{Cos}\frac{3\theta}{2} + K_{II}^{aux}\operatorname{Cos}\frac{\theta}{2}(1-\operatorname{Sin}\frac{\theta}{2}\operatorname{Sin}\frac{3\theta}{2}) \right\}$$

The auxiliary displacement solution is given by

$$u_1^{aux} = \frac{1}{2\mu}\sqrt{\frac{r}{2\pi}}\left\{ K_I^{aux}\operatorname{Cos}\frac{\theta}{2}(\kappa\text{-}1+2\operatorname{Sin}^2\frac{\theta}{2}) + K_{II}^{aux}\operatorname{Sin}\frac{\theta}{2}(\kappa+1+2\operatorname{Cos}^2\frac{\theta}{2}) \right\}$$

$$\quad \text{(A.2)}$$

$$u_2^{aux} = \frac{1}{2\mu}\sqrt{\frac{r}{2\pi}}\left\{ K_I^{aux}\operatorname{Sin}\frac{\theta}{2}(\kappa+1-2\operatorname{Cos}^2\frac{\theta}{2}) + K_{II}^{aux}\operatorname{Cos}\frac{\theta}{2}(\kappa\text{-}1-2\operatorname{Sin}^2\frac{\theta}{2}) \right\}$$

where μ is the Shear modulus and κ is the Kolosov's constant of the material.

Appendix B

For an orthotropic and homogenous material, the auxiliary stress solution is given by

$$\sigma_{11}^{aux} = \frac{K_I}{\sqrt{2\pi r}}\operatorname{Re}\left[\frac{s_1 s_2}{s_1-s_2}\left(\frac{s_2}{\sqrt{\cos\theta+s_2\sin\theta}} - \frac{s_1}{\sqrt{\cos\theta+s_1\sin\theta}} \right) \right] +$$

$$\frac{K_{II}}{\sqrt{2\pi r}}\operatorname{Re}\left[\frac{1}{s_1-s_2}\left(\frac{s_2^2}{\sqrt{\cos\theta+s_2\sin\theta}} - \frac{s_1^2}{\sqrt{\cos\theta+s_1\sin\theta}} \right) \right]$$

$$\sigma_{22}^{aux} = \frac{K_I}{\sqrt{2\pi r}}\operatorname{Re}\left[\frac{1}{s_1-s_2}\left(\frac{s_1}{\sqrt{\cos\theta+s_2\sin\theta}} - \frac{s_2}{\sqrt{\cos\theta+s_1\sin\theta}} \right) \right] +$$

$$\frac{K_{II}}{\sqrt{2\pi r}}\operatorname{Re}\left[\frac{1}{s_1-s_2}\left(\frac{1}{\sqrt{\cos\theta+s_2\sin\theta}} - \frac{1}{\sqrt{\cos\theta+s_1\sin\theta}} \right) \right]$$

$$\sigma_{12}^{aux} = \frac{K_I}{\sqrt{2\pi r}}\operatorname{Re}\left[\frac{s_1 s_2}{s_1-s_2}\left(\frac{1}{\sqrt{\cos\theta+s_1\sin\theta}} - \frac{1}{\sqrt{\cos\theta+s_2\sin\theta}} \right) \right] +$$

$$\frac{K_{II}}{\sqrt{2\pi r}}\operatorname{Re}\left[\frac{1}{s_1-s_2}\left(\frac{s_1}{\sqrt{\cos\theta+s_1\sin\theta}} - \frac{s_2}{\sqrt{\cos\theta+s_2\sin\theta}} \right) \right]$$

$$\quad \text{(B.1)}$$

The auxiliary displacement solution is given by

$$u_1^{aux} = K_I \sqrt{\frac{2r}{\pi}} \, \text{Re}\left[\frac{1}{s_1 - s_2}\left(s_1 p_2 \sqrt{\cos\theta + s_2 \sin\theta} - s_2 p_1 \sqrt{\cos\theta + s_1 \sin\theta}\right)\right] +$$

$$K_{II} \sqrt{\frac{2r}{\pi}} \, \text{Re}\left[\frac{1}{s_1 - s_2}\left(p_2 \sqrt{\cos\theta + s_2 \sin\theta} - p_1 \sqrt{\cos\theta + s_1 \sin\theta}\right)\right]$$

$$u_2^{aux} = K_I \sqrt{\frac{2r}{\pi}} \, \text{Re}\left[\frac{1}{s_1 - s_2}\left(s_1 q_2 \sqrt{\cos\theta + s_2 \sin\theta} - s_2 q_1 \sqrt{\cos\theta + s_1 \sin\theta}\right)\right] +$$

$$K_{II} \sqrt{\frac{2r}{\pi}} \, \text{Re}\left[\frac{1}{s_1 - s_2}\left(q_2 \sqrt{\cos\theta + s_2 \sin\theta} - q_1 \sqrt{\cos\theta + s_1 \sin\theta}\right)\right]$$

(B.2)

where p_i and q_i are given by

$$p_i = \mathbb{C}_{11} s_i^2 + \mathbb{C}_{12} - \mathbb{C}_{16} s_i \quad i = 1, 2$$

$$q_i = \mathbb{C}_{12} s_i + \frac{\mathbb{C}_{22}}{s_i} - \mathbb{C}_{26} \quad i = 1, 2$$

(B.3)

Appendix C

The auxiliary displacement field can be written as

$$u_i = \begin{cases} \dfrac{1}{4\mu_1 \cosh(\pi\varepsilon)} \sqrt{\dfrac{r}{2\pi}} f_i(r, \theta, \varepsilon, \kappa_1) & (\text{upper-half plane}) \\ \dfrac{1}{4\mu_2 \cosh(\pi\varepsilon)} \sqrt{\dfrac{r}{2\pi}} f_i(r, \theta, \varepsilon, \kappa_2) & (\text{lower-half plane}) \end{cases} \quad (i = 1, 2) \quad \text{(C.1)}$$

To extract K_I, the functions f_1 and f_2 are

$$f_1 = D + 2\delta \sin\theta \sin\varphi \equiv D + T_1, \quad f_2 = -C - 2\delta \sin\theta \cos\varphi \equiv -C - T_2 \quad \text{(C.2)}$$

To extract K_2, the functions f_1 and f_2 are

$$f_1 = -C + 2\delta \sin\theta \cos\varphi \equiv -C + T_2, \quad f_2 = -D + 2\delta \sin\theta \sin\varphi \equiv -D - T_1 \quad \text{(C.3)}$$

where $C = \beta' \gamma \cos\dfrac{\theta}{2} - \beta \gamma' \sin\dfrac{\theta}{2}$, $\quad D = \beta \gamma \cos\dfrac{\theta}{2} + \beta' \gamma' \sin\dfrac{\theta}{2}$ and δ is given by

$$\delta = \begin{cases} e^{-(\pi-\theta)\varepsilon} & (\text{upper-half plane}) \\ e^{(\pi+\theta)\varepsilon} & (\text{lower-half plane}) \end{cases} \quad \varphi = \varepsilon \log r + \frac{\theta}{2} \quad \text{(C.4)}$$

β and β' are given by

$$\beta = \frac{0.5\cos(\varepsilon\log r) + \varepsilon\sin(\varepsilon\log r)}{0.25 + \varepsilon^2}$$

$$\beta' = \frac{0.5\sin(\varepsilon\log r) - \varepsilon\cos(\varepsilon\log r)}{0.25 + \varepsilon^2}$$

(C.5)

γ and γ' are given by

$$\gamma = \kappa\delta - \frac{1}{\delta}, \quad \gamma' = \kappa\delta + \frac{1}{\delta}, \quad \kappa = \begin{cases} \kappa_1 & \text{(upper-half plane)} \\ \kappa_2 & \text{(lower-half plane)} \end{cases}$$

(C.6)

The auxiliary strain components can be obtained from

$$\varepsilon_{ij}^{\text{aux}} = \frac{1}{2}\left(u_{i,j}^{\text{aux}} + u_{j,i}^{\text{aux}}\right), \quad (i,j = 1,2)$$

(C.7)

The derivatives of T_1 and T_2 defined in Equations (C.2) and (C.3) can be written as

$$T_{1,r} = \frac{\varepsilon T_2}{r}, \quad T_{1,\theta} = \varepsilon T_1 + \frac{T_2}{2} + T_3$$

$$T_{2,r} = \frac{\varepsilon T_1}{r}, \quad T_{2,\theta} = \varepsilon T_2 - \frac{T_1}{2} + T_4$$

(C.8)

where $T_3 = 2\delta\cos\theta\sin\varphi$ and $T_4 = 2\delta\cos\theta\cos\varphi$. Defining $E = \beta'\gamma'\cos\frac{\theta}{2} - \beta\gamma\sin\frac{\theta}{2}$ and

$F = \beta\gamma'\cos\frac{\theta}{2} + \beta'\gamma\sin\frac{\theta}{2}$, then

$$C_{,r} = \frac{\varepsilon D}{r}, \quad C_{,\theta} = -\frac{F}{2} + \varepsilon E$$

$$D_{,r} = -\frac{\varepsilon C}{r}, \quad D_{,\theta} = \frac{F}{2} + \varepsilon F$$

(C.9)

The derivatives of auxiliary displacements can be written as

$$u_{1,1}^{\text{aux}} = A\left(Bf_{1,1} + \frac{r_{,1}f_1}{4\pi B}\right), \quad u_{1,2}^{\text{aux}} = A\left(Bf_{1,2} + \frac{r_{,2}f_1}{4\pi B}\right)$$

$$u_{2,1}^{\text{aux}} = A\left(Bf_{2,1} + \frac{r_{,1}f_1}{4\pi B}\right), \quad u_{2,2}^{\text{aux}} = A\left(Bf_{2,2} + \frac{r_{,2}f_2}{4\pi B}\right)$$

(C.10)

where A and B are given by

$$A = \begin{cases} \dfrac{1}{4\mu_1 \cosh(\pi\varepsilon)} & \left(\text{upper half-plane}\right) \\[3mm] \dfrac{1}{4\mu_2 \cosh(\pi\varepsilon)} & \left(\text{lower half-plane}\right) \end{cases} \qquad B = \sqrt{\dfrac{r}{2\pi}} \qquad \text{(C.11)}$$

The derivatives of the functions f_1 and f_2 are given by

$$\begin{aligned}
f_{1,\alpha} &= -D_{,\alpha} + T_{1,\alpha}, \quad f_{2,\alpha} = -C_{,\alpha} - T_{2,\alpha} \quad (\alpha = r, \theta) \\
f_{1,\alpha} &= -C_{,\alpha} + T_{2,\alpha}, \quad f_{2,\alpha} = -D_{,\alpha} + T_{1,\alpha} \quad (\alpha = r, \theta) \\
f_{1,1} &= f_{1,r} r_{,1} + f_{1,\theta} \theta_{,1}, \quad f_{1,2} = f_{1,r} r_{,2} + f_{1,\theta} \theta_{,2} \\
f_{2,1} &= f_{2,r} r_{,1} + f_{2,\theta} \theta_{,1}, \quad f_{2,2} = f_{2,r} r_{,2} + f_{2,\theta} \theta_{,2}
\end{aligned} \qquad \text{(C.12)}$$

The auxiliary stresses (σ_{ij}^{aux}) can be obtained from the auxiliary strains using the Hooke's law.

Appendix D

In order to calculate the global stiffness matrix, the signed distance at node I is extrapolated to any generic point p. This is done by identifying the closest point close to p as shown in Fig. 8.1(a). Then the signed distance is projected as shown in Fig. 8.1(b), which is given by

$$\begin{aligned}
f(\mathbf{x}_p) &= f(\mathbf{x}_I) + (\mathbf{x}_I - \mathbf{x}_p) \\
\mathrm{H}(f(\mathbf{x}_p)) &= \mathrm{H}(f(\mathbf{x}_I)) \, \mathrm{sign}(f(\mathbf{x}_p).\hat{f}(\mathbf{x}_I))
\end{aligned} \qquad \text{(D.1)}$$

where $f(\mathbf{x}_I)$ is the signed vector distance function from the crack line and I is the closest node to p. $\hat{f}(\mathbf{x}_I)$ is the normalized vector distance.
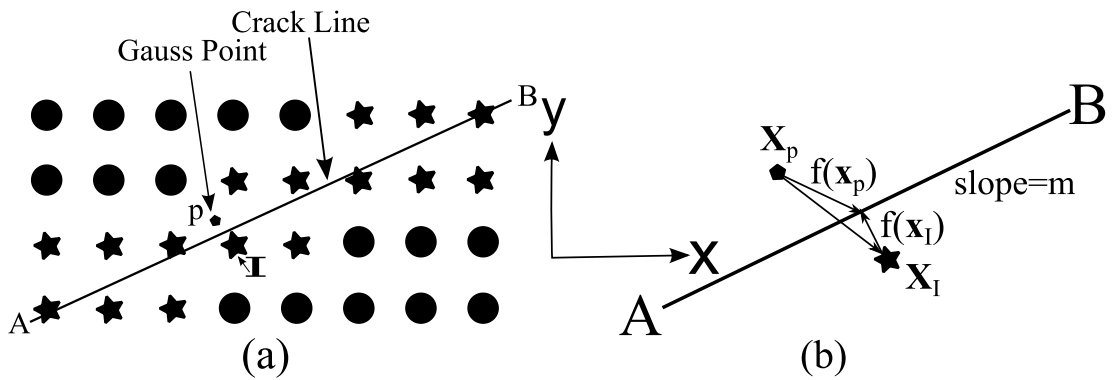
Fig. 8.1 (a) Gauss point p near the crack line; **(b)** Vector extrapolation.

If the slope m of the crack (AB) line increases, then the extrapolation according to Eq. (D.1) will be less precise when lower nodal density is used. In the face of higher slope, the extrapolation method has been modified.
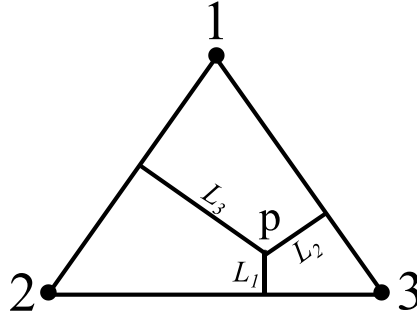
Fig. 8.2 Triangular coordinates of a point p inside a triangle.

For any generic point p, the closest three neighbouring nodes that surround the point p are identified as shown in Fig. 8.2. Then the distance from the point p and it's sign are calculated by

$$f(\mathbf{x}_p) = L_1 f(\mathbf{x}_1) + L_2 f(\mathbf{x}_2) + L_3 f(\mathbf{x}_3)$$
$$H(f(\mathbf{x}_p)) = sign(f(\mathbf{x}_p))$$

(D.2)

where L_i in Eq. (D.2) are the triangular/barycentric coordinates of the point p. If three nodes that form a triangle are not identified, then the vector extrapolation from the closest point method is used.

Appendix E

The auxiliary displacement (u_i^{aux}), stresses (σ_{ij}^{aux}) and strains (ε_{ij}^{aux}) to determine T-stress are defined by

$$u_1^{aux} = -\frac{E^\# f}{E_o \pi}\left(2\ln\frac{r}{d} + (1+v_o)\sin^2\theta\right)$$

$$u_2^{aux} = -\frac{E^\# f}{E_o \pi}\left((1-v_o)\theta - (1+v_o)\sin\theta\cos\theta\right)$$

$$\sigma_{11}^{aux} = -E^\# \frac{2f}{r\pi}\cos^3\theta$$

(E.1)

$$\sigma_{22}^{aux} = -E^\# \frac{2f}{r\pi}\cos\theta\sin^2\theta$$

$$\sigma_{22}^{aux} = -E^\# \frac{2f}{r\pi}\cos^2\theta\sin\theta$$

where f is a point force applied for auxiliary fields, d is a reference length and

$$E^{\#} = \frac{E_o}{E_1^* + E_2^*}, E_o = E_m^* \forall \mathbf{x} \in \text{material } m$$

$$v_o = v_m^* \forall \mathbf{x} \in \text{material } m \qquad \text{(E.2)}$$

$$v_m^* = \begin{cases} v_m & \text{plane stress} \\ \dfrac{v_m}{1 - v_m} & \text{plane strain} \end{cases}$$

The auxiliary strains are obtained using

$$\varepsilon_{ij}^{aux} = S_{ijkl}(\mathbf{x})\sigma_{kl}^{aux} \qquad \text{(E.3)}$$

where $S_{ijkl}(\mathbf{x})$ is the compliance matrix at the point $\mathbf{x}$.

References

Akisanya, A.R. & Fleck, N.A., 1992. Analysis of a wavy crack in sandwich specimens. *International Journal of Fracture*, 55, pp.29-45.

Akisanya, A.R. & Fleck, N.A., 1997. Interfacial cracking from the free-edge of a long bi-material strip. *International Journal of Solids and Strcutures*, 34, pp.1645-65.

Aliabadi, M.H. & Rooke, D.P., 1991. *Numerical Fracture Mechanics*. Dordrecht, The Netherlands: Kluwer Academic Publisher.

Aluru, N.R., 2000. A point collocation method based on reproducing kernel approximations. *International Journal of Numerical Methods in Engineering*, 47, pp.1083-121.

Amit, K.C. & Jeong, H.K., 2008. Interaction integrals for thermal fracture of functionally graded materials. *Engineering Fracture Mechanics*, 75, pp.2542-65.

Anderson, T.L., 1995. *Fracture mechanics—fundamentals and applications*. 2nd ed. Boca Raton, Florida: CRC Press.

Asadpoure, A. & Mohammadi, S., 2007. Developing new enrichment functions for crack simulation in orthotropic media by the extended finite element method. *International Journal for Numerical Methods in Engineering*, 69, pp.2150-72.

Asadpoure, A., Mohammadi, S. & Vafai, A., 2006. Modelling crack in orthotropic media using a coupled finite element and partition of unity methods. *Finite Element in Analysis and Design*, 42, pp.1165-75.

Askes, H., Wells, G.N. & De Borst, R., 2003. Numerical and computational methods. In Milne, I., Karihaloo, B.L. & R.O.:, R. *Comprehensive Structural Integrity*. Elsevier Pergamon.

Atkinson, C., Smelser, R.E. & Sanchez, J., 1982. Combined mode fracture via the cracked Brazilian disk test. *International Journal of Fracture*, 18, pp.279-91.

Atluri, S.N., Kobayashi, A.S. & Nagasaki, M.A., 1975. Finite element program for fracture mechanics analysis of composite material. *Fracture Mechanics of Composites ASTM STP*, 593, pp.86-98.

Atluri, S.N. & Shen, S., 2002. *The Meshless Local Petrov-Galerkin (MLPG) Method*. Stuttgart: Tech Science Press.

Atluri, S.N. & Zhu, T., 1998. A new meshless local Petrov–Galerkin (MLPG) approach in computational mechanics. *Computational Mechanics*, 22, pp.117-27.

AZoM.com, 2015. *Azo Materials*. [Online] Available at: http://www.azom.com/article.aspx?ArticleID=1592#_The_Origin_of [Accessed 9 February 2015].

Babuška, I., Banerjee, U. & Osborn, J.E., 2002. *Survey of meshless and generalized finite lement methods: A unified approach*. Technical Report. TICAM.

Banks-Sills, L. & Dolev, O., 2004. The conservative M-integral for thermal-elastic problems. *International Journal of Fracture*, 125, pp.1149-70.

Barbieri, E., Petrinic, N., Meo, M. & Tagarielli, V.L., 2012. A new weight-function enrichment in meshless methods for multiple cracks in linear elasticity. *International Journal for Numerical Methods in Engineering*, 90, pp.177-95.

Bardenhagen, S.G., Brackbill, J.U. & Sulsky, D., 2000. The material-point method for granular materials. *Computer Methods in Applied Mechanics and Engineering*, 187, pp.529-41.

Barsoum, R.S., 1976. On the use of isoparametric finite elements in linear fracture mechanics. *Internatiional Journal of Numerical Methods in Engineering*, 10, pp.25-37.

Belytschko, T. & Black, T., 1999. Elastic crack growth in finite elements with minimal remeshing. *International Journal of Numerical Methods in Engineering*, 45, pp.601-20.

Belytschko, T. et al., 1996. Meshless Methods: An Overview and Recent Developments. *Computer Methods in Applied Mechanics and Engineering*, 139, pp.3-47.

Belytschko, T., Liu, W.K. & Moran, B., 2000. *Nonlinear Finite Elements for Continua and Structures*. New York, USA: John Wiley and Sons Ltd.

Belytschko, T., Lu, Y.Y. & Gu, L., 1994. Element-free Galerkin methods. *International Journal of Numerical Methods in Engineering*, 37, pp.229-56.

Belytschko, T., Organ, D. & Krongauz, Y., 1995. A coupled finite element-element-free Galerkin method. *Computational Mechanics*, 17, pp.186-95.

Belytschko, T. & Xiao, S.P., 2004. A bridging domain method for coupling continua with molecular dynamics. 193, pp.1645-69.

Bogy, D.B., 1971. On the plane elastostatic problem of a loaded crack terminating at a material interface. *Journal of Applied Mechanics*, 38, pp.911-18.

Bonet, J. & Kulasegaram, S., 2000. Correction and stabilization of smooth particle hydrodynamics methods with application in metal forming simulations. *International Journal of Numerical Methods in Engineering*, 47, pp.1189-214.

Bonet, J. & Lok, T., 1999. Variational and momentum preservation aspects of smooth particle hydrodynamic formulations. 180, pp.97-115.

Bordas, S. & Moran, B., 2006. Enriched finite elements and level sets for damage tolerance assessment of complex structures. *Engineering Fracture Mechanics*, 73, pp.1176-201.

Bordas, S. et al., 2008. An extended finite element library. *International Journal of Numerical Methods in Engineering*, 71, pp.703-32.

Bouchard, P.O., Bay, F. & Chastel, Y., 2003. Numerical modelling of crack propagation: automatic remeshing and comparison of different criteria. *Computer Methods in Applied Mechanics and Engineering*, 192, pp.3887-908.

Bouhala, L. et al., 2013. An XFEM crack-tip enrichment for a crack terminating at a bi-material interface. *Engineering Fracture Mechanics*, 102, pp.51-64.

Bowie, O.L., 1964. Rectangular tensile sheet with symmetric edge cracks. *Journal of Applied Mechanics*, 31, pp.208-12.

Brezzi, F., 1974. On the existence, uniqueness and approximation of saddlepoint problems arising from Lagrange. *RAIRO - Analyse numérique*, R-2, pp.129-51.

Bush, M.B., 1997. The interaction between a crack and a particle cluster. *International Journal of Fracture*, 88, pp.215-32.

Cerkovnik, M. & Akhtar, W., 2013. Inclusion of ccrack face pressure in reference stress for thick walled risers ansd flowlines. In *Proceedings of the ASME 2013 32nd International Conference on Ocean, Offshore and Arctic Engineering*. Nantes, France, 2013.

Chang, K.J., 1981. On the maximum strain criterion-a new approach to the angled crack problem. *Engineering Fracture Mechanics*, 14, pp.107-24.

Chang, X., Liu, J. & Li, S., 2011. EFG Virtual Crack Closure Technique for the Determination of Stress Intensity Factor. *Advanced Materials Research*, 250-253, pp.3752-58.

Chan, S.K., Tuba, I.S. & Wilson, W.K., 1970. On the finite element method in linear fracture mechanics. *Engineering Fracture Mechanics*, 30, pp.227-31.

Chen, D.H., 1994. A crack normal to and terminating at a bimaterial interface. *Engineering Fracture Mechanics*, 49, pp.517-32.

Chen, J.S., Pan, C. & Wu, C.I., 1997. Large Deformation Analysis of Rubber based on a Reproducing Kernel Particle Method. *Computational Mechanics*, 211, pp.211-27.

Chen, J.S. & Wang, H.P., 2000. New Boundary Condition Treatments in Meshfree Computation of Contact Problems. *Computer Methods in Applied Mechanics and Engineering*, 187, pp.441-68.

Chen, J., Wu, L. & Du, S., 2000. Element free Galerkin methods for fracture of functionally graded material. *Key Engineering Materials*, 487-492, pp.183-87.

Cherepanov, G.P., 1979. *Mechanics of brittle fracture*. New York: McGraw-Hill.

Cherradi, N., Kawasaki, A. & Gasik, M., 1994. Worldwide trends in functional gradient materials research and development. *Composites Engineering*, 8, pp.883-94.

Cheung, Y.K., Woo, C.W. & Wang, Y.H., 1992. A general method for multiple crack problems in a finite plate. 10, pp.335-43.

Ching, H.K. & Yen, S.C., 2005. Meshless local Petrov-Galerkin analysis for 2d functionally graded elastic solids under mechanical and thermal loads. *Composites Part B: Engineering*, 36, pp.223-40.

Cook, T.S. & Erdogan, F., 1972. Stresses in bonded materials with a crack perpendicular to the interface. *International Journal of Engineering Science*, 10, pp.677-97.

Cotterell, B., 1966. Notes on Paths and Stability of Cracks. *International Journal of Fracture Mechanics*, 2, pp.526-33.

Courant, R., Friedrichs, K.O. & Lewy, H., 1928. Über die partiellen Differenzengleichungen der Mathematischen Physik. *Mathematische Annalen*, 100, pp.32-74. English translation,

with commentaries by Lax, P.B., Widlund, O.B., Parter, S.V., in IBM J. Res. Develop. 11 (1967).

Darzens, S., Chermant, J.L. & Vicens, J., 2001. Microcracking mechanism in a SiCf–SiBC composite creep-tested in argon. *Journal of microscopy*, 20, pp.230-37.

Daux, C. et al., 2000. Arbitrary branched and intersecting cracks with the extended finite element method. *International Journal for Numerical Methods in Engineering*, 48, pp.1741-60.

Delale, F. & Erdogan, F., 1983. The crack problem for a nonhomogeneous plane. *Journal of Applied Mechanics*, 50, pp.609-14.

Dilts, G.A., 2000. Moving least square particle hydrodynamics. I. Consistency and stability. *International Journal of Numerical Methods in Engineering*, 44, pp.1115-55.

Dilts, G.A., 2000. Moving least square particle hydrodynamics. II. Conservation and boundaries. *International Journal of Numerical Methods in Engineering*, 48, pp.1503-24.

Dolbow, J. & Belytschko, T., 1999. Numerical integration of the Galerkin weak form in meshfree methods. *Computational Mechanics*, 23, pp.219-30.

Duarte, C.A. & Oden, J.T., 1996. An h-p adaptive method using clouds. *Computer Methods in Applied Mechanics and Engineering*, 139, pp.237-62.

Duflot, M., 2006. A meshless method with enriched weight functions for three-dimensional crack propagation. *International Journal for Numerical Methods in Engineering*, 65, pp.1970-2006.

Duflot, M. & Nguyen-Dang, H., 2004. A meshless with enriched weight functions for fatigue crack growth. *International Journal for Numerical Methods in Engineering*, 59, pp.1945-2001.

Dunant, C. et al., 2007. Architecture trade-offs of including a mesher in an object-oriented extended finite element code. *Europian Journal of Computational Mechanics*, 16, pp.237-58.

Dunavant, D.A., 1985. High degree efficient symmetrical Gaussian quadrature rules for the triangle. *International Journal for Numerical Methods in Engineering*, 21, pp.1129-48.

Dundurs, J., 1969. Edge-bonded dissimilar orthogonal elastic wedges. *ASME Journal of Applied Mechanics*, 36, pp.650-52.

Dutta, B.K., Maiti, S.K. & Kakodkar, A., 1991. Analysis of crack-microcrack inetractions and doubly kinked cracks using multiple singular points elements. *Engineering Fracture Mechanics*, 38, pp.215-23.

Eischen, J.W., 1987. Fracture of nonhomogeneous materials. *International Journal of Fracture*, 34, pp.3-22.

Erdogan, F., 1983. Stress intensity factors. *Journal of Applied Mechanics*, 50, pp.992-1002.

Erdogan, F. & Sih, G.C., 1963. On crack extension in plates under plane loading and transverse shear. *Transaction of ASME, Journal of Basic Engineering*, pp.519-27.

Erdogan, F. & Wu, B.H., 1997. The surface crack problem for a plate with functionally graded properties. *Journal of Applied Mechanics*, 64, pp.449-56.

Ewing, P.D. & Williams, J.G., 1974. Further observations on the angled crack problem. *International Journal of Fracture*, 10, p.135.

Falzon, B.G., Hitchings, D. & Besant, T., 1999. Fracture mechanics using a 3D composite element. *Composite Structures*, 45, pp.29-39.

Fernández-Méndez, S. & Huerta, A., 2004. Imposing essential boundary conditions in mesh-free methods. 193, pp.1257-75.

Finnie, I. & Saith, A., 1973. A note on the angled crack problem and the directional stability of cracks. *International Journal of Fracture*, 9, pp.484-86.

Fleming, M.A., 1997. *The element free Galerkin method for fatigue and quasi-static fracture*. PhD thesis. Northwestern University.

Fleming, M., Chu, Y.A., Moran, B. & Belytschko, T.., 1997. Enriched element-free Galerkin methods for crack tip fields. *International Journal for Numerical Methods in Engineering*, 40, pp.1483-504.

Fries, T.P. & Matthies, H.G., 2004. Informatikbericht Nr.: 2003-3 *Classification and Overview of Meshfree Methods*. Brunswick: Technical University, Braunschweig.

Gavete, L., Cuesta, J.L. & Ruiz, A., 2002. A numerical comparison of two different approximations of the error in a meshless method. *European Journal of Mechanics*, 21, pp.1037-54.

Gdoutos, E., 1993. *Fracture Mechanics*. Boston: Kluwer Academics Publishers.

Geniaut, S. & Galenne, E., 2012. A simple method for crack growth in mixed mode with X-FEM. *International Journal of Solids and Structures*, 49, pp.2094-106.

Ghorashi, S.S., Mohammadi, S. & Sabbagh-Yazdi, S.R., 2011. Orthotropic enriched element free Galerkin method for fracture analysis. *Engineering Fracture Mechanics*, 78, pp.1906-27.

Gilhooley, D.F. et al., 2008. Two-dimensional stress analysis of functionally graded solids using the MLPG method with radial basis functions. *Computational Materials Science*, 41, pp.467-81.

Gingold, R.A. & Monaghan, J.J., 1977. Smoothed particle hydrodynamics - theory and application to non-spherical stars. *Monthly Notices of the Royal Astronimical Society*, 181, pp.375-89.

Gosz, M. & Moran, B., 2002. An interaction energy integral method for computation of mixed-mode stress intensity factors along non-planar crack fronts in three dimensions. *Engineering Fracture Mechanics*, 69, pp.299-319.

Gravouil, A., Moës, N. & Belytschko, T., 2002. Non-planar 3D crack growth by the extended finite element and level sets.Part II: level set update. *International Journal for Numerical Methods in Engineering*, 53, pp.2569-86.

Griffith, A.A., 1921. Phenomena of rupture and flow in solids. *Philosophical Transactions of the Royal Society of London, Series A*, 221, pp.163-98.

Gross, D. & Seelig, T., 2011. *Fracture mechanics: with an introduction to micromechanics*. Springer.

Guiamatsia, I., Falzon, B.G., Davies, G.A.O. & Lannucci, L., 2009. Element-free Galerkin modelling of composite damage. *Composites Science and Technology*, 69, pp.2640-48.

Gunther, F.C. & Liu, W.K., 1998. Implementation of Boundary Conditions for Meshless Methods. *Computer Methods in Applied Mechanics and Engineering*, 163, pp.205-30.

Guo, L.C. & Noda, N., 2008. Fracture mechanics analysis of functionally graded layered structures with a crack crossing the interface. *Mechanics of Materials*, 40, p.8199.

Hallback, N. & Nilsson, F., 1994. Mixed-mode I/II fracture behaviour of an aluminium alloy. *Journal of Mechanics of Physics and solids*, 42, pp.1345-74.

Han, W. & Meng, X., 2002. Some studies of the reproducing kernel particle method. In Meshfree Methods for Partial Differential Equations. *Lecture Notes in Computational Science and Engineering*, 26, pp.193-210.

Hegen, D., 1996. Element-free Galerkin methods in combination with finite element approaches. *Computer Methods in Applied Mechanics and Engineering*, 135, pp.143-66.

He, M.Y. & Hutchinson, J.W., 1989. Kinking of a crack out of an interface. *Journal of Applied Mechanics*, 56, pp.270-78.

Hellen, T.K., Cesari, F. & Maitan, A., 1982. The application of fracture mechanics in thermally stressed structures. *International Journal of Pressure Vessels and Piping*, 10, pp.181-204.

Hellen, T.K., Cesar, I.F. & Maitan, A.., 1982. The application of fracture mechanics in thermally stressed structures. *International Journal of Pressure Vessels and Piping*, 10, pp.181-204.

Hongjun, Y., Linzhi, W. & Hui, L., 2012. T-stress evaluations of an interface crack in the materials with complex interfaces. *International Journal of Fracture*, 177, pp.25-37.

Huber, O., Nickel, J. & Kuhn, G., 1993. On the decomposition of the J-integral for 3d crack problems. *International Journal of Fracture*, 64, pp.339-48.

Hutchinson, J.W. & Suo, Z., 1992. Mixed mode cracking in layered materials. *Advances in Applied Mechanics*, 29, pp.63-191.

Inglis, C.E., 1913. Stress in a plate due to the presence of cracks and sharp corneres. *Transaction of theInstitue of Naval Architectures*, 55, pp.219-41.

Irwin, G.R., 1948. Fracutre dynamics. In *Fracturing of metals*. Clevland: American Society for Metals. pp.147-66.

Jin, Z.H. & Noda, N., 1994. Crack tip singular fields in nonhomogeneous materials. *Jounrla of Applied Mechanics*, 61, pp.738-40.

Johnson, G.R., 1994. Linking of Lagrangian Particle Methods to Standard Finite Element Methods for High Velocity Impact Copmutations. *Nuclear Engineering and Design*, 150. Post-SMIRT Impact IV Seminar.

Johnson, G.R. & Beissel, S.R., 1996. Normalized smoothing functions for sph impact computations. *International Journnal of Numerical Methods in Engineering*, 39, pp.2725-41.

Kachanov, M., 1986. On crack-microcrack interactions. *International Journal of Fracture*, 30, pp.65-72.

Kaljevic, I. & Saigal, S., 1997. An improved element free Galerkin formulation. *International Journal of Numerical Methods in Engineering*, 40.

Kang, K.J., 1994. Criteria for kinking out of interface crack. *Engineering Fracture Mechanics*, 49, pp.587-98.

Kayama, M. & Kitamura, T., 2004. A simulation on growth of multiple small cracks under stress corrosion. *International Journal of Fracture*, 130, pp.787-801.

Kayama, M. & Totsuka, N., 2002. Influence of interaction between multiple cracks on stress corrosion crack propagation. *Corrosion Science*, 44, pp.2333-52.

Kebir, H., Roelandt, J.M. & Chambon, L., 2006. Dual boundary element method modelling of aircraft structural joints with multiple site damage. *Engineering Fracture Mechanics*, 73, pp.418-34.

Khoei, A.R., Azadi, H. & Moslemi, H., 2008. Modeling of crack propagation via an automatic adaptive mesh refinement based on modified superconvergent patch recovery technique. *Engineering Fracture Mechanics*, 75, pp.2921-45.

Kim, J.H. & Paulino, G.H., 2002. Finite element evaluation of mixed mode stress intensity factors in functionally graded materials. *International Journal for Numerical Methods in Engineering*, 53, pp.1903-55.

Kim, J.H. & Paulino, G.H., 2003. Mixed-mode J-integral formulation and implementation using graded finite elements for. *Mechanics of Materials*, 35, pp.107-28.

Kim, J.H. & Paulino, G.H., 2003. The interaction integral for fracture of orthotropic functionally graded materials: evaluation of stress intensity factors. *International Journal of Solids and Structures*, 40, pp.3967-4001.

Kim, J.H. & Paulino, G.H., 2003. T-stress, mixed-mode stress intensity factors, and crack initiation angles in functionally graded materials: a unified approach using the interaction integral method. *Computer Methods in Applied Mechanics and Engineering*, 192, pp.1463-94.

Kim, J.H. & Paulino, G.H., 2005. Consistent Formulations of the Interaction Integral Method for Fracture of Functionally Graded Materials. *Journal of Applied Mechanics*, 72, pp.351-64.

Kim, J.H. & Vlassak, J.J., 2006. T-stress of a bi-material strip under generalized edge loads. *International Journal of Fracture*, 142, pp.315-22.

Kitagawa, H., Okamura, H. & Ishikawa, H., 1976. Application of J-integral to mixed-mode crack problems. *Transaction of JSME*, 760, pp.46-48.

Krysl, P. & Belytschko, T., 1997. Element-free Galerkin method: convergence of the continuous and discontinuous shape functions. *Computer Methods in Applied Mechanics and Engineering*, 148, pp.257-77.

Kumar, P., 2013. *Elements of Fracture Mechanics*. New Delhi: McGraw Hill.

Labossiere, P.E.W., Dunn, M.L. & Cunningham, S.J., 2002. Application of bimaterial interface corner failure mechanics to silicon/glass anodic bonds. *Journal of the Mechanics and Physics of Solids*, 50, pp.405-33.

Lancaster, P. & Salkauskas, K., 1981. Surfaces generated by moving least square methods. *Mathematics of Computation*, 37, pp.141-58.

Leevers, P.S., Radon, J.C. & Culver, L.E., 1976. Fracture trajectories in a biaxially stressed plate. *Journal of Mechanics and Physics of Solids*, 24, pp.381-95.

Lekhnitskii, S.G., 1963. *Theory of an anisotropic elastic body*. Sann Francisco: Holden-Day.

Libersky, L.D. et al., 1993. High strain Lagrangian hydrodynamics. *Journal of Computational Physics*, 109, pp.67-75.

Liu, G.R., 2010. *Meshfree Methods: Moving Beyond the Finite Element Method*. 2nd ed. Boca Raton, Florida: CRC Press.

Liu, G.R. & Gu, Y.T., 2001. A point interpolation method for two-dimensional solids. *International Journal of Numerical Methods in Engineering*, 50, pp.937-51.

Liu, W.K., Jun, S. & Zhang, Y.F., 1995. Reproducing kernel particle methods. *International Journal of Numerical Methods in Engineering*, 20.

Li, C., Zou, Z. & Duan, Z., 1999. Stress intensity factors for functionally graded solid cylinders. *Engineering Fracture Mechanics*, 63, pp.735-49.

Lu, Y.Y., Belytschko, T. & Gu, L., 1994. A New Implementation of the Element Free Galerkin Method. *Computer Methods in Applied Mechanics and Engineering*, 113, pp.397-414.

Lucy, L.B., 1977. Numerical approach to testing of fission hypothesis. *Astronomical Journal*, 82.

Lu, M.C. & Erdogan, F., 1983. Stress intensity factors in two bonded elastic layers containing cracks perpendicular to and on the interface-I. *Engineering Fracture Mechanics*, 18, pp.491-506.

Maiti, S.K., 1992. A multicorner variable order singularity triangle to model neighbouring singularities. *International Journal for Numerical Methods in Engineering*, 35, pp.391-408.

Maiti, S.K., 1992. Finite element computation of crack closure integrals and stress intensity factors. *Engineering Fracture Mechanics*, 41, pp.339-48.

Maiti, S.K., Mukhopadhyay, N.K. & Kakodkar, A., 1997. Boundary element method based computation of stress intensity factor by modified crack closure integral. *Computational Mechanics*, 19, pp.203-10.

Maiti, S.K. & Smith, R.A., 1983a. Comparison of the criteria for mixed mode brittle fracture based on the preinstability stress-strain field Part I: Slit and elliptical cracks under uniaxial tensile loading. *International Journal of Fracture*, 23, pp.281-95.

Maiti, S.K. & Smith, R.A., 1983b. Comparison of the criteria for mixed mode brittle fracture based on the pre-instability stress-strain field Part II: Pure shear and uniaxial tensile loading. *International Journal of Fracture*, 24, pp.5-22.

Maiti, S.K. & Smith, R.A., 1984. Criteria for brittle fracture in biaxial tension. *Engineering Fracture mechanics*, 19, pp.793-804.

Marc, D., 2008. The extended finite element method in thermo-elastic fracture mechanics. *International Journal of Numerical methods in Engineering*, 74, pp.827-47.

Marin, L., 2005. Numerical solution of the Cauchy problem for steady-state heat transfer in two dimensional functionally graded material. *International Journal of Solids and Structures*, 42, pp.4338-51.

Matsumto, T., Tanaka, M. & Obara, R., 2000. Computation of stress intensity factors of interface cracks based on interaction energy release rates and BEM sensitivity analysis. *Engineering Fracture Mechanics*, 65, pp.683-702.

Matthew, C.W., Glaucio, H.P. & Robert, H.D., 2005. Interaction integral procedures for 3-D curved cracks including surface tractions. *Engineering Fracture Mechanics*, 72, pp.1635-63.

Matvienko, Y.G., 2012. Maximum Average Tangential Stress Criterion for Prediction of the Crack Path. *International Journal of Fracture*, 176, pp.113-18.

Moës, N., Cloirec, M., Cartraud, P. & Remacle, J.-F., 2003. A computational approach to handle complex microstructure geometries. *Computer Methods in Applied Mechanics and Engineering*, 192, pp.3163-77.

Mohammadi, S., 2012. *XFEM fracture analysis of composites*. 1st ed. Chichester, West Sussex: John Wiley and Sons.

Mohammed, I. & Liechti, K.M., 2000. Cohesive zone modeling of crack nucleation at bimaterial corners. *Journal of the Mechanics and Physics of Solids*, 48, pp.735-64.

Mohit, P., Singh, I.V. & Mishra, B.K., 2011. Evaluation of mixed mode stress intensity factors for interface cracks using EFGM. *Applied Mathematical Modelling*, 35, pp.3443-59.

Monaghan, J.J., 1982. Why particle methods work. *SIAM Journal of Scientific and Statistical Computing*, 3(3), pp.422-33.

Moran, B. & Shih, C.F., 1987. Crack tip and associated domain integrals from momentum and energy-balance. *Engineering Fracture Mechanics*, 27, pp.615-42.

Mortensen, A. & Suresh, S., 1995. Functionally graded metals and metal-ceramic composites: Part 1 Processing. *International Material Reviews*, 30, pp.83-93.

Moës, N., Gravouil, A. & Belytschko, T., 2002. Non-planar 3D crack growth by the extended finite element and levelsets. Part I: Mechanical model. *International Journal for Numerical Methods in Engineering*, 53, pp.2549-68.

Mukherjee, Y.X. & Mukherjee, S., 1997. On Boundary Conditions in the Element free Galerkin Method. *Computational Mechanics*, 19, pp.264-70.

Mukhopadhyay, N.K., Maiti, S.K. & Kakodkar, A., 1999. Modified crack closure integral based computation of SIFs for thermoelastic problems through BEM. *Nuclear Engineering and Design*, 187, pp.277-90.

Munz, C.D., Schneider, R. & Voss, U., 1999. A finite volume particle-in-cell method for the numerical simulation of devices in pulsed power technology. *SURVEYS ON MATHEMATICS FOR INDUSTRY*, 8, pp.243-57.

Murakami, Y., 1987. *Stress intensity factors handbook*. Oxford: Pergamon Press.

Muravin, B. & Turkel, E., 2006. Multiple crack weight for solution of multiple interacting cracks by meshless numerical methods. *International Journal for Numerical Methods in Engineering*, 67, pp.1146-59.

Muthu, N., Falzon, B.G., Maiti, S.K. & Khoddam, S., 2013. Modelling Crack Propagation in Particle-Reinforced Composites using the Element-Free Galerkin Method. In *International Conference in Composite Materials'19*. Montreal, 2013.

Muthu, N., Maiti, S.K., Falzon, B.G. & Guiamatsia, I., 2013. A comparison of stress intensity factors through crack closure integral and other approaches using eXtended element-free Galerkin method. *Computational Mechanics*, 52, pp.587-605.

Muthu, N., Maiti, S.K., Falzon, B.G. & Khoddam, S., 2014. Modified crack closure integral for extracion of SIFs in meshfree methods. *Finite Element in Analysis and Design*, 78, pp.25-39.

Nayroles, B., Touzot, G. & Villon, P., 1992. Generalizing the Finite Element Method: Diffuse Approximation and Diffuse Elements. *Computational Mechanics*, 10, pp.307-18.

Nelson, M.M., Surjya, K.M. & Wenyi, Y., 2014. Analysis of Cracks in Bimaterials/Composites with Variable Order Singularity using Meshless Method. In *World Congress on Computational Mechanics*. Barcelona, 2014.

Neubrand, A. & Rode, J., 1997. Gradient materials: An overview of a novel concept. *Zeitschrift Fur Metallkunde*, 88, pp.358-71.

Nguyen, V.P., Rabczuk, T., Bordas, S. & Duflot, M., 2008. Meshless methods: A review and computer implementation aspects. *Mathematics and Computers in Simulation*, 79, pp.763-813.

Nguyen, V.P., Timon, R., Stéphane, B. & Marc, D., 2008. Meshless methods: A review and computer implementation aspects. *Mathematica and computers in simulation*, 79, pp.763-813.

Nicolas, M., John, D. & Ted, B., 1999. A finite element for crack growth without remeshing. *International Journal of Numerical Methods in Engineering*, 46, pp.1103-18.

Nikishkov, G.P..A.S.N., 1987. Calculation of fracture-mechanics parameters for an arbitrary 3-dimensional crack, by the equivalent domain integral method. *International Journal for Numerical Methods in Engineering*, 24, pp.1801-21.

Nisitani, H. & Chen, D.H., 1987. *Body Force Method*. Tokyo: Baifukan. in Japanese.

Nisitani, H. & Chen, D.H., 1992. Body force method. In Aliabadi, M..B.C. *Advance in Boundary Element Methods for Fracture Mechanics*. Southampton, Boston: Computational Mechanics Publications. Ch. 4.

Noguchi, H., Kawashima, T. & Miyamura, T., 2000. Element free analyses of shell and spatial structures. *International Journal of Numerical Methods in Engineering*, 47, pp.1215-40.

Onate, E. et al., 1996. A stabilized finite point method for analysis of fluid mechanics problems. *Computer methods in applied mechanics and engineering*, 139, pp.315-46.

Organ, D., Fleming, M., Terry, T. & Belytschko, T., 1996. Continuous meshless approximations for non-convex bodies by diffraction and transparency. *Computational Mechanics*, 18, pp.225-35.

Osher, S. & Sethian, J.A., 1988. Fronts propagating with curvature dependent speed: algorithms based on Hamilton–Jacobi formulations. *Journal of Computational Physics*, 79, pp.12-49.

Ouinas, D. et al., 2010. Interaction effect crack-interfacial crack using finite element method. *Materials and Design*, 31, pp.375-81.

Pant., M., Singh, I.V. & Mishra, B.K., 2010. Numerical simulation of thermo-elastic fracture problems using element free Galerkin method. *International Journal of Mechanical Sciences*, 52, pp.1745-55.

Parks, D.M., 1974. A stiffness derivative finite element technique for determination of crack tip stress intensity factors. *International Journal of Fracture*, 10, pp.487-502.

Patrício, M. & Mattheij, R.M.M., 2010. Crack paths in compsoite materials. *Engineering Fracture Mechanics*, 77, pp.2251-62.

Persson, P.O. & Strang, G., 2004. A simple mesh generator in MATLAB. *SIAM Review*, 46, pp.329-45.

Portela, A., Aliabadi, M.H. & Rooke, D.P., 1992. The dual boundary element method - effective implementation for crack problems. *International Journal for Numerical Methods in Engineering*, 33, pp.1269-87.

Prasad, N.N.V., Aliabadi, M.H. & Rooke, D.P., 1994. The dual boundary element method for thermo-elastic crack problems. *International Journal of Fracture*, 66, pp.255-72.

Qing, W..R., Yu, W..D. & Tina, T..Y.U., 2009. Numerical modeling of concrete hydraulic fracturing with extended finite element method. *Science in China Series E: Technological Sciences*, 52, pp.559-65.

Rabczuk, T., 2013. Computational Methods for Fracture in Brittle and Quasi-Brittle Solids: State-of-the-Art Review and Future Perspectives. *ISRN Applied Mathematics*, 2013. Article ID 849231.

Rabczuk, T. & Belytschko, T., 2006. Application of meshfree methods to static fracture of reinforced concrete structures. *International Journal of Fracture*, 137, pp.19-49.

Rabczuk, T., Belytschko, T., Fernandez-Mendez, S. & Huerta, A., 2004. Meshfree Methods. *Encyclopedia of Computational Mechanics*.

Rabczuk, T., Xiao, S.P. & Sauer, M., 2000. Coupling of meshfree methods with finite elements: Basic concepts and test results. *Communications in numerical methods in engineering*, 00, pp.1-36.

Raju, I.S., 1987. Calculation of strain-energy release rates with higher order and singular finite elements. *Engineering Fracture Mechanics*, 28, pp.251-74.

Rao, B.N. & Rahman, S., 2003. Mesh-free analysis of cracks in isotropic functionally graded materials. *Engineering Fracture Mechanics*, 70, pp.1-27.

Reedy, E.D., 2000. Connection between interface corner and interfacial fracture analyses of an adhesively-bonded butt joint. *International Journal od Solids and Structures*, 37, pp.2429-42.

Rice, J.R., 1968. A path independent integral and the approximate analysis of strain concentration by notches and cracks. *Journal of Applied Mechanics*, 35, pp.379-86.

Rice, J.R., 1988. Elastic fracture mechanics concepts for interfacial cracks. *Journal of Applied Mechanics*, 55, pp.98-103.

Rigby, R.H. & Aliabadi, M.H., 1998. Decomposition of the mixed-mode J-integral revisited. *International Journal of Solids and Structures*, 35, pp.2073-99.

Ronald, K., 2002. ICASE Report No. 2002-10 *The Virtual Crack Closure Technique: History, Approach and Applications*. Hampton: National Aeronautics and Space Administration.

Roylance, D., 2001. *Introduction to fracture mechanics.* Cambridge, MA: Massachusetts Institute of Technology.

Rybicki, E.F. & Kanninen, M.F., 1977. A finite element calculation of stress intensity factors by a modified crack closure integral. *Engineering Fracture Mechanics*, 9, pp.931-38.

Sauer, M., 2000. *Adaptive Koppling des netzfreien SPH-Verfahrens mit finiten Elementen zur Berechnung von Impaktvorgaengen*. Dissertation. Universitaet der Bundeswehr Muenchen.

Sethian, J.A., 1999. *Level Sets Methods & Fast Marching Methods: Evolving Interfaces in Computational Geometry,Fluid Mechanics, Computer Vision and Materials Science*. Cambridge, U.K.: Cambridge University Press.

Sethuraman, R. & Maiti, S.K., 1988. Finite element based computation of strain energy release rate by modified crack closure integral. *Engineering Fracture Mechanics*, 30, pp.227-31.

Seyedi, M., Taheri, S. & Hild, F., 2006. Numerical modeling of crack propagation and shielding effects in a striping network. *Nuclear engineering and design*, 236, pp.954-64.

Shanmugavel, P. et al., 2012. An Overview of Fracture Analysis in Functionally Graded Materials. 68, pp.412-39.

Shaofan, L. & Liu, W.K., 2008. Meshfree and particle methods and their applications. 55, pp.1-34.

Shi, J., Ma, W. & Li, N., 2013. Extended meshless method based on partition of unity for solving multiple crack problems. *Meccanica*, 48, pp.2263-70.

Sih, G.C., 1974. Strain Energy Density Factor Applied to Mixed Mode Crack Problems. *International Journal of Fracture*, pp.305-21.

Sih, G.C., Paris, P.C. & Irwin, G.R., 1965. On cracks in rectilinearly anisotropic bodies. *International Journal of Fracture*, 1, pp.189-203.

Singh, R., Carter, B.J., Wawrzynek, P.A. & Ingraffea, A.R., 1988. Universal crack closure for SIF estimation. *Engineering Fracture Mechanics*, 60(133-146).

Singh, I.V., Mishra, B.K. & Mohit, P., 2010. A modified intrinsic enriched element free Galerkin method for multiple cracks simulation. *Materials and Design*, 31, pp.628-32.

Sladek, J. & Sladek, V., 1997. Evaluations of the T-stress for interface cracks by the boundary element method. *Engineering Fracture Mechanics*, 56, pp.813-25.

Smith, D.J., Ayatollahi, M.R. & Pavier, M.J., 2001. The role of T-stress in brittle fracture for linear elastic materials under mixed-mode loading. *Fatigue and Fracture of Engineering Materials and Structures*, 24, pp.137-50.

Smith, D.J., Ayatollahi, M.R. & Pavier, M.J., 2006. On the consequences of T-stress in elastic brittle fracture. *Proceedings of the Royal Society A: Mathematical, Physical and Engineering Science*, 462, pp.2415-37.

Stolarska, M., Chopp, D.L., Moës, N. & Belytschko, T., 2001. Modelling crack growth by level sets in the extended finite element method. *International Journal of Numerical Methods in Engineering*, 51, pp.943-60.

Sukumar, N., Chopp, D.L. & Moran, B., 2002. Extended finite element method and fast marching method for three-dimensional fatigue crack propagation. *Engineering Fracture Mechanics*, 70, pp.29-48.

Sukumar, N., Huang, Z.Y., Prévost, J.H. & Suo, Z., 2004. Partition of unity enrichment for bimaterial interface cracks. *International Journal for Numerical Methods in Engineering*, 59, pp.1075-102.

Sundararajan, N., Chongmin, S. & Salim, B., 2014. Numerical evaluation of stress intensity factors and T-stress for interfacial cracks and cracks terminating at the interface without asymptotic enrichment. *Computer Methods in Applied Mechanics and Engineering*, 279, pp.86-112.

Swedlow, J.L., 1976. Criteria for growth of the angled crack. *Cracks and Fracture, ASTM STP 601, American Society for Testing and Materials*, pp.506-21.

Terry, T.G., 1994. *Fatigue crack propagation modeling using the element free galerkin method*. M.S. Thesis. Northwestern University.

Tham, L.M., Gupta, M. & Cheng, L., 2001. Effect of limited matrix-reinforcement interfacial reaction on enhancing the mechanical properties of aluminium-silicon carbide composites. *Acta Materialia*, 49, pp.3243-53.

Tilbrook, M.T., Moon, R.J. & Hoffman, M., 2005. Finite element simulations of crack propagation in functionally graded material under flexural loading. *Engineering Fracture Mechanics*, 72, pp.2444-267.

Timoshenko, S.P., 1953. *History of Strength of Materials*. New York: McGraw-Hill.

Timoshenko, S. & Goodier, J.N., 1970. *Theory of Elasticity*. 3rd ed. New York: McGraw-Hill.

Tracey, D.M. & Cook, T.S., 1977. Analysis of power type singularities using finite elements. *International Journal for Numerical Methods in Engineering*, 11, pp.1225-33.

Tuan, B.M. & Fei, C.Y., 2014. Analysis and prediction of crack propagation in plates by the enriched free Galerkin method. *International Journal of Mechanical Engineering and Applications*, 2, pp.78-86.

Ueda, Y., Ikeda, K., Yao, T. & Aoki, M., 1983. Characteristics of brittle fracture under general combined modes including those under bi-axial tensile loads. *Engineering Fracture Mechanics*, 18, pp.1131-58.

Valentin, S.R., Stepan, V.L., Ignaas, V. & Larissa, G., 2015. Modelling evidence of stress concentration mitigation at the micro-scale in polymer composites by the addition of carbon nanotubes. *Carbon*, 82.

Ventura, G., Budyn, E. & Belytschko, T., 2003. Vector level sets for description of propagating cracks in finite elements. *International Journal of Numerical Methods in Engineering*, 58, pp.1571-92.

Ventura, G., Xu, J.X. & Belytschko, T., 2002. A vector level set method and new discontinuity approximations for crack growth by EFG. *International Journal of Numerical Methods in Engineering*, 54, pp.923-44.

Wang, S.S., Yau, J.F. & Corten, H.T., 1980. A mixed mode analysis of rectilinear anisotropic solids using conservation laws of elasticity. *International Journal of Fracture*, 16, pp.247-59.

Wang, S. & Zhang, H., 2011. Partition of unity-based thermomechanical meshfree method for two-dimensional crack problems. *Archive of Applied Mechanics*, 81.

Watwood, V.B., 1969. The finite element method for prediction of crack behavior. *Nuclear Engineering and Design*, 11.

Wen, P.H. & Aliabadi, M.H., 1995. A contour integral for the evaluation of stress intensity factors. *Applied Mathematical Modelling*, 19, pp.450-55.

Westergaard., 1939. Bearing pressure and cracks. *Journal of Applied Mechanics*, 6, pp.49-53.

Williams, M.L., 1952. Stress singularities resulting from various boundary conditions in angular corners of plates in extension. *Transactions ASME: Journal of Applied Mechanics*, 4, pp.526-28.

Williams, J.G. & Ewing, P.D., 1972. Fracture under complex stress-the angled crack problem. *International Journal of Fracture*, 8, pp.441-46.

Wilson, W.K., 1969. *Combined Mode Fracture Mechanics*. PhD Thesis. PA: University of Pittsburgh.

Wu, H.C., 1974. Dual failure criterion for plane concrete. *Journal of Engineering Mechanics, Divison ASCE*, 100, pp.1167-81.

Wu, H.C. & Chang, K.J., 1978. Angled elliptic notch problem in compression and tension. *Journal of Applied Mechanics*, 45, pp.258-62.

Xiaoying, Z., 2010. *Meshless methods: theory and application in 3D fracture modelling with level sets*. PhD Thesis. Durham University.

Xiaoying, Z., Charles, A. & Stéphane, B., 2011. Accurate fracture modelling using meshless methods, the visibility criterion and level sets: Formulation and 2D modelling. *International Journal of Numerical Methods in Engineering*, 86, pp.249-68.

Xiaoying, Z., Claire, H. & Charles, A., 2012. On error control in the element-free Galerkin method. *Engineering Analysis with Boundary Elements*, 36, pp.351-60.

Yau, J.F., Wang, S.S. & Corten, H.T., 1980. A mixed-mode crack analysis of isotropic solids using conservation laws of elasticity. *Journal of Applied Mechanics*, 47, pp.335-41.

Yuuki, R. & Xu, J.X., 1992. Stress based criterion for an interface crack kinking out of the interface in dissimilar materials. *Engineering Fracture Mechanics*, 41, pp.635-44.

Yu, H.J. et al., 2009. Investigation of mixed-mode stress intensity factors for nonhomogeneous materials using an interaction integral method. *International Journal of Solids and Structures*, 46, pp.3710-24.

Zak, A.R. & Williams, M.L., 1963. Crack point singularities at a bi-material interface. *Journal of Applied Mechanics*, 31.

Zhen, Z. & Zhigang, S., 2007. Split singularities and the competition between crack penetration and debond at a material interface. *International Journal of Solids and Structures*, 44, pp.4559-73.

Zhijia, S., Youtang, L. & Hongyan, D., 2013. Consistent Mode Mixity for the Interface Crack of the Bimaterial Disc under Diametric Compression Loading. *Applied Mechanics and Materials*, 345, pp.268-71.

Zhiyong, W., Li, M., Linzhi, W. & Hongjun, Y., 2012. Numerical simulation of crack growth in brittle matrix of particle reinforced composites using the XFEM technique. *Acta Mech Solida Sinica*, 25, pp.9-21.

Zhuang, X., Augarde, C. & Mathisen, K.M., 2012. Fracture modeling using meshless methods and level sets in 3d: framework and modeling. *International Journal for Numerical Methods in Engineering*, 92, pp.969-98.

Acknowledgement

Publications out of this thesis

1. N. Muthu, S.K. Maiti, B.G. Falzon, I. Guiamatsia. "Computation of stress intensity factors in functionally graded materials using partition-of-unity meshfree method" *The Aeronautical Journal*, 1253-1277; **116(1186)**:2012.

2. N. Muthu, S.K. Maiti, B.G. Falzon, I. Guiamatsia. "A Comparison of Stress Intensity Factors Obtained Through Crack Closure Integral and Other Approaches using Extended Element-Free Galerkin Method" *Computational Mechanics*, 587-605; **52**: 2013.

3. N. Muthu, B.G. Falzon, S.K. Maiti, S. Khoddam. "Modified Crack Closure Integral for Extraction of SIFs in Meshfree Methods" *Finite Element in Analysis and Design*, 25-39; **78**: 2014.

4. N. Muthu, S.K. Maiti, B.G. Falzon, Wenyi Yan. "Crack Propagation in Non-homogenous materials: Evaluation of Mixed-Mode SIFs, T-stress and Kinking angle using a variant of EFG Method" *Engineering analysis with Boundary Elements* (Under review).

5. N. Muthu, S.K. Maiti, B.G. Falzon, Wenyi Yan. "A Procedure for Modelling Interaction of Cracks using Level Set Method within the framework of the EFG method" (To be submitted).

6. N. Muthu, B.G. Falzon, S.K. Maiti, S. Khoddam. "Modelling Crack Propagation in Particle-Reinforced Composites using the Element-Free Galerkin Method" in *Proceedings of International Conference in Composite Materials*, Montreal, 2013.

7. Nelson M. Muthu, Surjya K. Maiti and Wenyi Yan. "Analysis of Cracks in Bimaterials/Composites with Variable Order Singularity using Meshless Method" in `*Proceedings of World Congress on Computational Mechanics,* Barcelona, 2014

8. N. Muthu, B.G. Falzon, S.K. Maiti, W. Yan "Micromechanical modelling of non-homogenous materials using meshless methods" in *Proceedings of International Conference in Composite Materials*, Copenhagen, 2015.